In Search of Inflation: Tools for Cosmic Microwave Background Polarimetry

Kevin Thomas Crowley

A Dissertation
Presented to the Faculty
of Princeton University
in Candidacy for the Degree
of Doctor of Philosophy

Recommended for Acceptance
by the Department of
Department of Physics
Adviser: Professor Suzanne T. Staggs

September 2018

Abstract

The pursuit of knowledge of the early universe via the properties of the cosmic microwave background (CMB) is now being guided by the need to perform measurements of large-scale polarization patterns at a part in 100 million. In addition to confirming the CDM concordance model shaped by the CMB, such studies pursue evidence of primordial tensor perturbations, which themselves could elucidate a period of inflation in the early universe. These tensor perturbations are imprinted on the CMB polarization as divergence-free patterns, known as B-modes. To make these demanding polarization measurements, increased instrumental sensitivity and control of systematics is required. As part of the Advanced ACTPol (AdvACT) project, high-density detector arrays of thousands of highly-sensitive bolometers were deployed on the Atacama Cosmology Telescope (ACT). The Atacama B-mode Search (ABS) instrument featured a polarization modulator system to control systematics and gain access to large-scale anisotropy modes otherwise masked by changing signals in the atmosphere. We describe aspects of these technologies, and their impact on CMB polarization studies.

In this thesis, I begin by presenting the standard model of the universe and discuss the promise of CMB polarization measurements. This motivates a discussion of current technologies progressing to an introduction of arrays of multiplexed bolometers. I discuss generic bolometer models involving superconducting thermistors, known as transition-edge sensors (TESes). These models are then compared to data on bolometer sensitivity and response acquired for AdvACT devices. I next describe the principle of polarization modulation using a continuously-rotating half-wave plate (CRHWP), including the signal injected into bolometer data thereby. I present a pipeline developed to investigate and remove this signal. Initial results from the 2017 run of silicon metamaterial CRHWPs on ACT are shown. Finally, I describe the maximum-likelihood pipeline developed as part of the ABS collaboration to con-

strain the parameter describing the power in primordial tensor perturbations, the tensor-to-scalar ratio r. The final published results for ABS are discussed. I conclude by considering the future development of high-sensitivity focal planes in the context of systematic error control, specifically detector non-linearity, for the Simons Observatory set of instruments, which are in the design phase.

Acknowledgements

Many people, through their hard work, care, and support, are responsible for my producing this set of pages. Thanking them all is a tall task, but also the least I can do.

I'll begin with those cosmology students and scientists with whom I was so fortunate to share lab time and tight spaces in Jadwin. Sara Simon helped bring me on board to the ABS project and was always ready to help with any questions; indeed, she still is today, and I am tremendously grateful to her. Patty Ho filled a similar role on the ACT side, but circumstances also conspired to demand some careful wafer vacuum lowering, wafer pinning, and fridge mounting from us. Her positive attitude and fearless affect in the lab has been crucial in seeing the ACT team through tricky times. Yaqiong Li gets a special shoutout for her dedication and fortitude, especially in some of the all-day bonder sessions, when the only sound besides thousands of hydraulic swooshes was our conversation about old movies and Chinese sci-fi. Steve Choi has always led with a forthrightness and sincere desire to make things better that I appreciate. Maria Salatino, who has moved on, is remembered fondly (U2 playing in the lab less so!); new students, Sarah Marie Bruno, Erin Healy, and others, I am looking forward to tracking all your exciting progress from afar. The original runners of the lab that I interacted with, Emily Grace, Christine Pappas, and others, I appreciate all your help in bringing me up to speed and teaching me most of what I know about cryostats, readout, and the rest.

Outside collaborators in ACT and ABS are so numerous that to elaborate them all here would double my page count! I wish to highlight the respect and affection I feel for Brian Koopman, Jason Stevens, Nick Cothard, Pato Gallardo, and all of the Cornell MUX team led by Mike Niemack (who also been a stalwart and appreciated supporter of my detector work). Shawn Henderson deserves his own sentence for reminding me that anything even getting close to working is something to cele-

brate, and for answering all my unceasing questions about MCE business. The team I've been so fortunate to visit at NIST and see elsewhere, Jay Austermann (who introduced me to Velma and hit the town with me in Kurume), Brad Dober (the king of the unexpected and lucky invite), Shannon Duff, Doug Bennett, Joe Fowler, Randy Doriese, and others made those trips to Boulder something to look forward to. Matthew Hasselfield deserves a whole paean to himself, for training up myself, and simultaneously a ton of other people, to do anything useful with field data, and for being one of the sharpest eyes in the room when my misshapen plots got aired out at telecons. A big thanks to you, man; sorry about that In-N-Out pepper challenge.

To the administrators and staff I was fortunate enough to work with regularly in Jadwin: Ted Lewis, Darryl Johnson, Todd Antonakos, Julio Lopez, Stephanie Rumphrey, Sumit Saluja (all those disks!), and others, thank you for all your hard work. To Steve Lowe in the student shop, and Bill Dix, Glenn Atkinson, and the pro shop team: thanks for being unfailingly on-time and supportive. Bert Harrop, the whole ACT team owes you a debt of gratitude for all your work on our array integration. I always enjoy coming round to your office. Angela Lewis, hauling sandwiches was a great privilege, as was working with you.

A whole other stream of experiences took place in South America. Lucas Parker is responsible for breaking me in to work at 17,000 feet, and for being a swell guy to share the mountain with. Mark Devlin, watching you drop lightning rods from 20 m up is about as memorable an experience as I've ever had. Thanks for all your support and candor. To the engineers who slog it out for many months to make our work possible, and had to ferry my automatic transmission-only butt up the road, a personal and permanent thanks: Felipe Rojas Aracena, Federico Nati, Felipe Carrero, Max Fankhanel. Y'all are spectacular.

There are a whole bunch of friends to thank: to physics folks who never had to see me drop screws all over the lab: Farzan, Stevie, Will, and others. Thanks for

making Jadwin in general a fun place to be. My original Pton roommate Jordan is now essentially an extension of my brain; you're a gem buddy, never forget it. The basement gang, and most especially Sama, Mattias, and Jamal, the music flows through you and buoys us all. I'll storm PREX or hit a drum with you guys anytime. Summer softball plays are some of my sweetest memories of genteel guys and gals like Kenan, Zach, Anne, and *mon capitain* Tom, all of whom I'm pretty grateful I got to hang with outside the hall of physics. And to the 201 crew(s): Zander&Charlie (the originals), Ugne, Jose, Alex, and the incomparable Kyle: you all were a big part of keeping me going through many tough weeks. I'm extremely grateful to have lived with you all.

And now, the incalculably big thank yous: to Lyman Page, who never said anything about me falling asleep during my first ACT telecons and has unfailingly supported my efforts across all projects since then. To Akito Kusaka, who, despite my first-year eagerness to quibble over every detail, remains an exceptionally thoughtful and helpful mentor. To Hannes Hubmayr, who has always encouraged my efforts to play around with these TESes, and who I am grateful to consider a friend and mentor. And to my adviser Suzanne Staggs, who brought me into CMB work and has gently pushed and pulled me into all that I've done, supported my efforts, given me food for thought, caught out my errors and shown me how to do better, and been a great person to work for and with: Thank you.

Finally, it's down to the family. Cat, you may not care about this stuff, but you're a fantastic sister and maybe one day, an even better playwright. Mom and Dad, your wisdom in grown-up matters shows itself more and more each day; you've never not been around to talk things through, and I owe you everything. Noelle, my partner, no matter how hairy things got on your end, you always made room in your heart and mind to make me feel special and loved. I only hope I supported you nearly as well as you've done for me. I'm as lucky as can be to have you with me. Thank you.

To Mom and Dad, for their support,

and Noelle, for everything. I love you.

Contents

List of Tables

List of Figures

0.1 Related Work

Some of the work in this dissertation has been presented at conferences and published. The sections in this work that contain content from these conferences and publications have been modified and/or expanded for this dissertation. I list all such presentations and publications below, along with a description of my work with regard to these public exhibition of results. I also indicate publications and presentations being drawn from in the body of the dissertation where relevant. All publications and presentations discussed below benefited from collaborative editing with the respective coauthors.

In the case of the following, the content in these presentations was only presented at the conference.

- Poster presentation, Oct. 2015, ESA 36th Antenna Workshop, Title: "Characterization of Multichroic Pixels for Advanced ACTPol."

  I presented this work on the behalf of the Advanced ACTPol Collaboration. I was responsible for the text and organization of these early detector measurements from NIST (J. Austermann) and Princeton (S.P. Ho, J. Kuan). It is relevant to this dissertation solely as the source of Fig. 2.5 produced by S.P. Ho.

- Poster presentation, September 2016, 12th Workshop on Low-Temperature Electronics, Title: "Electrothermal Modelling of Single-Crystal Si Harpstring Bolometer for PIXIE."

  I presented this work on behalf of the Goddard collaboration working on PIXIE bolometers. This content is discussed in Appendix B, where it represents the achievements of measurement campaigns on PIXIE bolometers at Princeton.

In the cases below, the content in these presentations was presented at the conference and subsequently published.

- Poster presentation, June 2016, SPIE Astronomical Telescopes and Instrumentation, Title: "Data-Driven Electrothermal and Noise Modeling of TES Detectors in Multichroic Arrays for Advanced ACTPol."

  I presented this work in concert with S. Choi on behalf of the Advanced ACTPol collaboration. I produced about half of the figures and text.

- Proceeding, Title: "Characterization of AlMn TES Impedance, Noise, and Optical Effciency in the First 150 mm Multichroic Array for Advanced ACTPol." Crowley, K.T.; Choi, S.K.; et al. 2016. [15].

  This article is part of the conference proceedings showing in detail the work presented in the poster. As co-first author, I produced all figures and text in Section 3, and was responsible for the overall drafting of the article. This work is expanded upon in Ch. 3.

- Poster presentation, July 2017, Low-Temperature Detectors (LTD) 17, Title: "Advanced ACTPol TES Device Parameters & Noise Performance in Fielded Arrays."

  I presented this work on behalf of the Advanced ACTPol collaboration. I was responsible for all figures except where indicated, and all text. This work is expanded upon in Ch. 3.

- Proceeding, Title: "Advanced ACTPol TES Device Parameters and Noise Performance in Fielded Arrays." Crowley, K.T. et al. [14]. 2017.

  As sole first author, I produced all figures and text in this article. This article contains some of the results on Advanced ACTPol array noise seen in Ch. 3, where it is also expanded upon.

- Oral presentation, June 2018, SPIE Astronomical Telescopes and Instrumentation, Title: "Characterizing AlMn Bolometers for Advanced ACTPol (AdvACT)."

  I presented my work on detailed characterization of TES bolometer data acquired at NIST on behalf of the Advanced ACTPol collaboration. This presentation was solely produced by myself except where indicated, and described the work discussed in Ch. 3 on these data.

- Proceeding, Title: "Electrothermal Characterization of AlMn Transition Edge Sensor Bolometers for Advanced ACTPol." 2018.

  This article is in preparation and about to be submitted as a conclusion to the data presented in the oral presentation above. As sole first author, I contributed all text and figures where not otherwise indicated in the article.

In the case of the ABS science results paper:

- Journal article, Title: "Results from the Atacama B-Mode Experiment." Kusaka, A.; Appel, J.; Essinger-Hileman, T.; et al. 2018. [68]

  My work was not previously presented at a conference. I drafted the text of Sections 4, 6.1, and 6.5. My main contribution to the ABS results are in Sec. 6.5 of that paper and Ch. 5 of this dissertation, where they are presented in more detail.

Chapter 1

Introduction

1.1 The ΛCDM Model

In modern physical cosmology, across the diverse landscape of measurement techniques and objects of study, a common model has emerged to explain the energy contents of the universe. The initiation of this model was the discovery of the Friedmann-Lemaitre-Robertson-Walker solutions (FLRW) [37] [76] [109] [129] to Einstein's equations in general relativity (GR). Given the assumption of a homogeneous, isotropic universe when coarse-grained on the largest (tens of megaparsecs (Mpc) to gigaparsecs (Gpc)) scales, a concept now given the name the "cosmological principle," the FLRW solutions describe dynamic universes whose evolution is described by a scale factor $a(t)$, where t is the coordinate time. This scale factor can be used as the clock for all cosmological time, and it evolves according to the energy content of the universe. In general, the FLRW solutions can be classified according to the curvature of the space-time in the universe. All of this can be seen in the Friedman equation for a in terms of the Hubble parameter, $H(t) \equiv \dot{a}/a$, where $\dot{a}$ is the time derivative of a:

$$H^2 + \frac{K}{a^2} = \frac{8\pi G}{3}\rho. \tag{1.1}$$

Here ρ is the total energy density, G is Newton's gravitational constant, and K is a parameter describing the curvature of spacetime. The energy density, ρ, has the following dependence on a and a_0, the latter being the present day value of the scale factor (conventionally normalized to 1):

$$\rho = \frac{3H_0^2}{8\pi G}\left[\Omega_\Lambda + \Omega_M\left(\frac{a_0}{a}\right)^3 + \Omega_R\left(\frac{a_0}{a}\right)^4\right] \tag{1.2}$$

where Ω_i indicates the energy density of the component i as a fraction of the critical density required to avoid a collapsing universe at present, $\rho_c = 3H_0^2/8\pi G$, with H_0 the value of $H(t)$ at present. Here $i = M$ corresponds to the sum of energy density from the mass of matter, including particles in the Standard Model, like baryons, and any dark matter, $i = R$ denotes the energy density of radiation and any other relativistic species (including neutrinos in the early universe) for which energy is redshifted away by the expansion of space, and $i = \Lambda$ is discussed below.

Given the FLRW universe as a background spacetime, one can compute the evolution of perturbations to the spacetime given generic energy components and some spectrum of primordial perturbations. Beyond baryonic matter with standard interactions according to the four forces, and the radiation component comprised of all relativistic species, studies of the cosmic microwave background (CMB) have identified and constrained the amount of both dark matter ($\Omega_{\rm DM}$) and dark energy (Ω_Λ) [101].Signatures of dark energy and dark matter have also been identified using astrophysical probes of objects like galaxies (reviews in [4] [120]), clusters of galaxies (review in [3]), supernovae hosted in galaxies (the most recent experimental results [112]), and weak lensing of older source galaxies by intervening matter (see review [56] and recent experimental results [22]). In the case of supernovae, careful calibration of observations of Type-Ia supernovae is performed in order to use them as standard candles with well-defined luminosity. Comparing their luminosity to their apparent

brightness gives a measurement of their distance, which, combined with measurements of their redshift, then allows estimation of $H(t)$ for the redshift ranges over which the supernovae may be observed.

With regard to these dark energy densities, the dark matter component, called"cold dark matter" and making up the CDM part of ΛCDM, interacts with regular matter only gravitationally, and primarily constitutes spherical halos within which luminous astrophysical objects like stars and galaxies are embedded. In the case of dark energy, we usually mean some unknown energy source which, at the present moment, is producing an accelerating universe ($\ddot{a} > 0$). Acting as a negative pressure which resists the collapsing of the universe, dark energy is critical in supporting the current best understanding of the universe's evolution. The label Λ refers to the simplifying assumption that this energy density may be a true cosmological constant, existing at a constant value regardless of the increase of a [102].

Throughout this evolution, the assumption of a thermal history in which the temperature of the universe followed a monotonically decreasing trajectory, in accordance with the increasing scale factor and expanding volume of the universe, has proven to have considerable explanatory power. The program of predicting the remnant atomic species based on the nuclear and atomic physics relevant to the large energy range explored by the expanding, adiabatically-cooling early universe is known as Big Bang nucleosynthesis. It has been validated by observation in combination with the probe of early-universe behavior provided by CMB measurements [17]. In addition, as we will discuss in the next section, the thermal timeline relevant for understanding the pattern of minute anisotropies in the CMB can also rest comfortably in the unified ΛCDM picture.

Beyond the details of a roughly homogeneous, cooling, expanding universe in GR, the simplifying assumption of "scale-invariant" perturbations to the matter density,

velocity, particle species distributions, and other parameters has proven to be validated by most observational data. In fact, the perturbations exhibit a mild red tilt, meaning their amplitudes decrease with decreasing spatial scale. This small deviation appears to describe the behavior of the dominant density perturbations across all measurable scales [101] [22].

Inflation There are thus (at least!) two mysteries as to how the universe got the way it is. First, what component or property of the universe sources the necessary nearly scale-invariant primordial perturbations in the first instants after the Big Bang? Second, how is it that the universe's thermal history appears completely isotropic? That is, despite the existence of a horizon beyond which no particle obeying GR could have traveled in a finitely-old universe, why is it that the available evidence of the thermal evolution, and indeed current temperature, of the CMB, which defines the temperature of the mostly-empty present-day universe, is the same in every direction?

The latter problem, known as the horizon problem, has an interesting counterpart based on the relative change of the terms in Eq. 1.2 with changing scale factor a. We can write a contribution of the curvature to the energy density by moving the term K/a^2 to the right hand side of Eq. 1.1. This results in an $\Omega_K = -K/a^2H_0^2$. If we imagine tracing this value back in time, we find that for it to be negligible today, which is supported by the combination of available cosmological probes [101], it would have to be so small relative to the other energy contents of the universe as to suggest a need for fine-tuning of the universe. That is, without any reason to assume that a universe emerging from a Big Bang should have Ω_K tuned to be negligible through cosmic history, we would be surprised to find that our universe's being this way is a chance occurrence.

An enticing way to wrap up these and other interesting puzzles about why the universe appears the way it does can be explained by a broad category of early universe models that fall under the rubric of "inflation" [48] [80] [121]. Inflation

posits a brief period of exponential evolution of the scale factor with constant H. This is conceptually similar to the de Sitter cosmological solution for GR [21], which corresponds to a universe with the only energy density being a positive cosmological constant, and where spacetime has a constant positive curvature. While the Λ-like expansion of the universe in the present day is thus analogous, the scale of the energies needed to drive inflation, and to explain the current amount of accelerating expansion in the universe, are extremely different. It is also not certaint whether dark energy is fully described by a cosmological constant Λ.

To effect the simplest models of inflation, it is assumed that there exists a quantum field, the "inflaton", which experiences a potential that dominates the energy density of all space in an extremely homogeneous condition. When the energy density of a patch of space is dominated by the potential energy density of a quantum field, its expansion behavior can well mimic de Sitter-like expansion. Given the energy density ρ of the quantum field ϕ, with appropriate field units, is $\rho_\phi = 1/2\dot{\phi}^2 + V(\phi)$, we can anticipate that if $V \gg 1/2\dot{\phi}^2$, ρ is approximately constant, and the universe can achieve nearly-exponential expansion. It can be shown for GR and Eq. 1.1 that:

$$\dot{H} = 4\pi G\dot{\phi}^2. \tag{1.3}$$

We also see that for a small value on the right-hand side of Eq. 1.3, we can treat the Hubble parameter H as approximately constant.

However, the potential-driven expansion of space has an effect on the quantum field, which begins to evolve through the potential. In order to account for the horizon and flatness puzzles it was designed to explain, the duration of the exponential expansion must result in a specific amount of increase in the scale factor. Written as

the number of "e-foldings" N_*, where:

$$N_* \approx \ln\left(\frac{a_{\rm end}}{a_{\rm begin}}\right), \tag{1.4}$$

the end of inflation, when the term $1/2\dot{\phi}^2$ in the energy density is no longer negligible, should occur after $N_* = 50$-60 e-foldings.

We can sharpen our discussion above by putting conditions on parameters that help determine how slowly the inflaton evolves through its potential. These "slow-roll" parameters are:

$$\epsilon = \frac{1}{2}\left(\frac{V'}{V}\right)^2, \tag{1.5a}$$

$$\eta = \frac{V''}{V}. \tag{1.5b}$$

These parameters themselves evolve as the inflaton moves through its potential. Inflation ends when $\epsilon \sim 1$. If both ϵ and η are sufficiently small, then, given some semiclassical approximations describing the effect of inflation on the quantum perturbations sourced by the inflaton as it progresses, it is possible to write down simple, approximate expressions in which ϵ, especially, defines the characteristic amplitude and spectral index of the nearly-scale-invariant perturbations we see today. These perturbations would further define an observable universe which was initially a causally-connected region of space before inflation (explaining why the temperature of space should be so uniform) and with a curvature diluted by the astronomical factor $1/e^{2N_*}$ (explaining why our universe is flat at present).

1.2 The Cosmic Microwave Background

In this section, we provide an overview of the early-universe physics relevant to interpretation of CMB observations, specifically studies of the anisotropies present in the CMB. We begin by discussing how primordial matter perturbations source effec-

tive temperature and polarization anisotropies in the photon-baryon fluid near the epoch of recombination. We then elaborate how these anisotropies evolve and discuss the methods for recovering information about them from data. Finally, we describe the set of astrophysical foregrounds, emission components which dominate the sky brightness and/or polarization, that have been revealed by recent CMB polarization observations. These signals are playing an important role in the design considerations of current- and future-generation CMB instruments.

Primordial Perturbations and the CMB. Below, we describe the relation between primordial perturbations and the temperature and polarization anisotropies measurable in the CMB today. Weinberg's text *Cosmology* [133] provides an excellent review and is a good reference for much of the material discussed.

As discussed with regard to inflation in Sec. 1.1, the early universe featured perturbations, in variables like the energy density ρ and the velocity v, about the mean values defining the background spacetime. These perturbations are treated by expanding the FLRW equations to linear order in the context of GR. They can be separated into scalar, vector, and tensor perturbations according to tensor analysis of generic perturbations to the metric and the stress-energy tensor. The coupling of all sources of stress-energy to each other in the early universe ensures that these perturbations will affect the photon energy distribution that characterized the CMB.

Such perturbations are a distinct component of CMB physics from the study of the spectral characteristics of the CMB [32] [47] [33]. These experiments have established that the CMB is a blackbody to the level of the temperature anisotropies [one part in $\mathcal{O}(10^5)$], to be introduced shortly. We briefly note that the temperature of the CMB thus established, $T_{\rm CMB} = 2.73$ K [31], is a reflection of the thermodynamic nature of the universe's expansion. The CMB is "cooling" as a result of the cosmological redshift of the bath of thermal radiation present in the baryon-photon plasma in the early universe. This redshift, called z, can be determined at anytime in the past

$t < t_0$, when the scale factor was smaller, as:

$$1 + z = a_0/a(t). \tag{1.6}$$

From arguments based on the form for the number density of photons in equilibrium with matter at temperature T, we can recover that, when the CMB has ceased interacting with matter, its spectrum retains the form of the Planck blackbody distribution, but with a temperature $T(z) = T_L \frac{1+z}{1+z_L}$, where the subscript L stands for an idealized, instantaneous time of last scattering.

According to the above argument, CMB photons are thus distributed as a perfect blackbody. However, the primordial perturbations affecting the energy density have the small, one part in 100,000-level effect on the CMB mentioned above. In order to fully calculate the perturbations to the CMB due to physics near the time of last scattering, or "recombination" (referring to the universe becoming electrically neutral due to the combining of electrons and protons into hydrogen atoms), a full treatment of the perturbations to the CMB number density in phase space is required. In these expressions, a natural decomposition arises where perturbations to the CMB energy distribution are written as $T(x,t) = \bar{T} + \Delta T(x,t)$ with $\bar{T}$ the average.

The temperature anisotropy, $\Delta T(x,t)$, effectively describes the number density fluctuation at that position as a temperature fluctuation. Conceptually, it is positive or negative depending on the presence of matter overdensities or underdensities, respectively, for "adiabatic" perturbations, the dominant mode of perturbations. We can consider this as due to the fact that the photons of the CMB are tightly coupled to free electrons by Thomson scattering in this era. Recombination begins when the timescale on which CMB photons scatter from ionized matter falls below the Hubble expansion timescale $\sim 1/H(t)$.

We now prepare to describe how these temperature anisotropies are studied. Consider that there is some "primordial power spectrum" of fluctuations, particularly for scalar perturbations. These result in a power spectrum of temperature fluctuations, which we can estimate in principle from the autocorrelation between the temperature anisotropy $\Delta T(\hat{n})$ measured in some direction $\hat{n}$ on the celestial sphere, and some $\Delta T(\hat{n}')$. In terms of what has been previously discussed, $\Delta T(\hat{n})$ measured today is $T(\hat{n}) - T_{\rm CMB}$, and we can write its decomposition into spherical harmonics as:

$$\Delta T(\hat{n}) = \sum_{\ell m} a_{\ell m} Y_\ell^m(\hat{n}), \tag{1.7}$$

When we then take the covariance, we can define the angular power for a given multipole moment ℓ, C_ℓ, as:

$$\langle \Delta T(\hat{n}) \Delta T(\hat{n}') \rangle = \sum_{\ell m} C_\ell Y_\ell^m(\hat{n}) Y_\ell^{-m}(\hat{n}'), \tag{1.8}$$

where angle brackets indicate an ensemble average over all possible realizations of the anisotropies given the ΛCDM cosmology. We can also write:

$$\langle a_{\ell m} a * \ell' m' \rangle = \langle a_{\ell m} a_{\ell' -m'} \rangle = \delta_{\ell \ell'} \delta_{m m'} C_\ell, \tag{1.9}$$

with δ the Kronecker delta, and with the first equality following from the real-valued nature of the anisotropies.

However, these averages cannot be performed, as they would require observing the CMB from multiple positions in the universe. We thus form the measured quantity $C_\ell^{\rm meas}$ as the average of the estimator in Eq. 1.9 over the spherical harmonic index m, under the assumption that the CMB has no preferred direction, and thus can be

described by the 1-D spectrum C_ℓ independent of m.

$$C_\ell^{\rm meas} = \frac{1}{2\ell+1}\sum_m a_{\ell m}a_{\ell -m}. \tag{1.10}$$

We can then see how the finite number of independent spherical-harmonic modes used to form an estimate of $C_\ell^{\rm meas}$ for each multipole moment determines the signal variance on the measurement, known as "cosmic variance," which goes as $\sqrt{2/(2\ell+1)}C_\ell$ assuming Gaussian distribution of the primordial perturbations [64].

This compression of the information in the anisotropies into a single 1-D power spectrum has been extremely important for cosmology. From exploration of these data alone, the ΛCDM model can be powerfully constrained. Given the many degeneracies between parameters, a limited set of six free parameters describing our universe in the ΛCDM framework has been used to nearly completely describe the structure of $C_\ell^{\rm meas}$ [101]. The connection between CMB spectra and these parameters is provided by numerical software [115] [77] [7] designed to output realizations of power spectra given these parameters as input. The signal recovered in the power spectrum indicates the presence of acoustic waves in the primordial baryon-photon plasma, arising from the opposing forces of gravity, under which photons are dragged with matter towards overdensities and away from underdensities, and radiation pressure, which resists the aggregation of high numbers of photons.

If we assume a perfectly scale-invariant perturbation spectrum (i.e., flat in wavevector k space), we recover a spectrum C_ℓ which goes as $C_\ell \propto (\ell(\ell+1))^{-1}$. It is therefore common to rescale C_ℓ by this factor, with an additional numerical constant, to recover a spherical-harmonic power spectrum that is also flat with multipole moment [100]. The typical quantity to plot is $\hat{C}_\ell = \frac{\ell(\ell+1)}{2\pi}C_\ell$ and we use this convention in Ch. 5.

CMB Polarization. Generation of linear polarization of the CMB via the same spectrum of primordial perturbations falls naturally out of the study of the evolution of these perturbations given the energy contents of the early universe. The results are most easily expressed in terms of the components of linear polarization in the Stokes vector $\{I, Q, U, V\}$, where linear polarization is defined by the two components Q and U. Non-zero values of these components are sourced from scalar perturbations according to local quadrupole moments of the CMB distribution around a free electron, according to Thomson scattering. The total amplitude of linear polarization $p = \sqrt{Q^2 + U^2}$ has a ratio with the pure CMB intensity of $p/I \lesssim 10$ %. There is expected to be no generation of circular polarization V of CMB photons due to Thomson scattering in the early universe.

Since Q and U are related by a 45° rotation of the polarization, they can be combined into two complex polarization quantities $Q \pm iU$, which admit of a spherical-harmonic decomposition using spin-2 harmonics [62]:

$$(Q \pm iU)(\hat{n}) = \sum_{\ell m} a^{\pm 2}_{\ell m \pm 2} Y^m_\ell(\hat{n}). \tag{1.11}$$

However, it is more common to form two scalar fields, labeled $E(\hat{n})$ (since curl-free, like a classical electric field) and $B(\hat{n})$ (since divergence-free, like a magnetic field), from the polarization quantities. This is done according to a global transformation, most easily written according to the spin-2 $a^{\pm 2}_{\ell m}$ quantities [114]:

$$a^E_{\ell m} = -\frac{(a^{+2}_{\ell m} + a^{-2}_{\ell m})}{2}, \tag{1.12a}$$

$$a^B_{\ell m} = \frac{(a^{+2}_{\ell m} - a^{-2}_{\ell m})}{2}. \tag{1.12b}$$

It is the case that these coefficients can be recovered as the decomposition of a particular combination of Q and U according to the standard, spin-0 spherical harmonics.

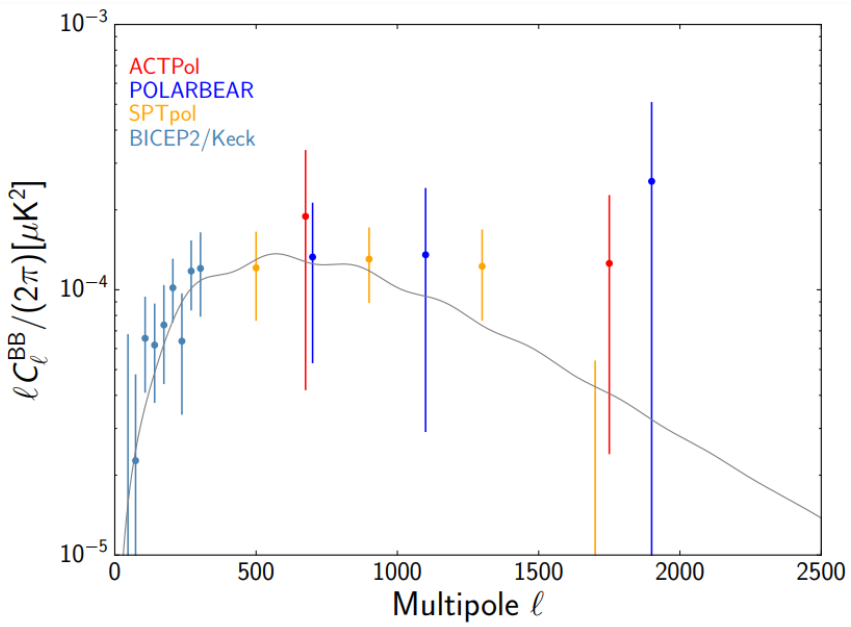

Figure 1.1: Recent measurements of C_ℓ^{BB} from the ground, including the two-season nighttime-only data from the ACTPol experiment. Figure taken from [82].

We can then form the power spectra C_ℓ^{EE} and C_ℓ^{BB} of CMB polarization in a rotation-independent way. Primordial scalar perturbations only contribute power to the C_ℓ^{EE} spectrum. In this case, the polarization signal is 90° out-of-phase with the signal sourced by the acoustic waves and seen in the temperature power spectrum [106].

However, tensor perturbations, identified with primordial gravitational waves in the early universe, contribute power to both polarization spectra. Thus, gravitational waves of a sufficient amplitude may induce a measurable signal in C_ℓ^{BB} at multipole moments around $\ell = 100$. This signal is parametrized by the tensor-to-scalar ratio r, which describes the ratio of the amplitudes of the power spectrum of tensor perturbations in k-space to those of the primordial scalar perturbation power spectrum at a given pivot scale k'. In modeling the perturbations induced by inflation, an approximation for r can be written in terms of the slow-roll parameter ϵ from Eq. 1.5a assuming $k' = 0.002$ Mpc^{-1}:

$$r \approx 16\epsilon = 8\left(\frac{V'}{V}\right)^2. \tag{1.13}$$

Another mechanism for generating C_ℓ^{BB} is gravitational lensing, which distorts E-mode signal into B-mode. Recent ground-based measurements of the C_ℓ^{BB} spectrum consistent with lensing are summarized in Fig. 1.1, which includes the most recent published results for the ACTPol experiment [82], to be discussed in Sec. 1.4.1. This lensing signal represents an obstruction to measuring the primordial signal, but can be "cleaned" given a measurement of the lensing potential sourcing the B-modes [84].

Polarized Foregrounds. The example of lensing of the CMB polarization signal described above gives an example of an inflation-confounding signal due to large-scale structure in the universe. However, our existence within the Milky Way galaxy presents its own serious challenges to performing studies of the polarization of the CMB. Polarized signals at millimeter-wave frequencies arise from free-electron synchroton radiation, the dominant foreground in both temperature and polarization at long wavelength, and from thermal emission of dust in the galaxy. The role of the latter in interfering with measurements of r has been highlighted by the necessity of removing an expected signal sourced by dust in the analysis of data from the BICEP2/Keck experiment [6].

A representation of the results on polarized foregrounds as reported by Planck [103] is shown in Fig. 1.2. We have used the Planck Legacy Archive values of parameters describing the foreground spectral indices, polarizaton amplitudes, and dust temperature when making the figure. Here, "polarization" refers to the polarization amplitude $p = \sqrt{Q^2 + U^2}$. Despite the amplitude of the foregrounds being greater than the CMB across these frequencies, the distinct frequency dependence of these foreground sources should make it possible to clean these signals from a multi-frequency map set. It is clear that this is now a critical aspect of unveiling the potential primordial signal in C_ℓ^{BB}. The desire to measure the CMB at multiple frequencies internal to individual experiments has driven some recent instrumentation development, to be discussed in the next section.

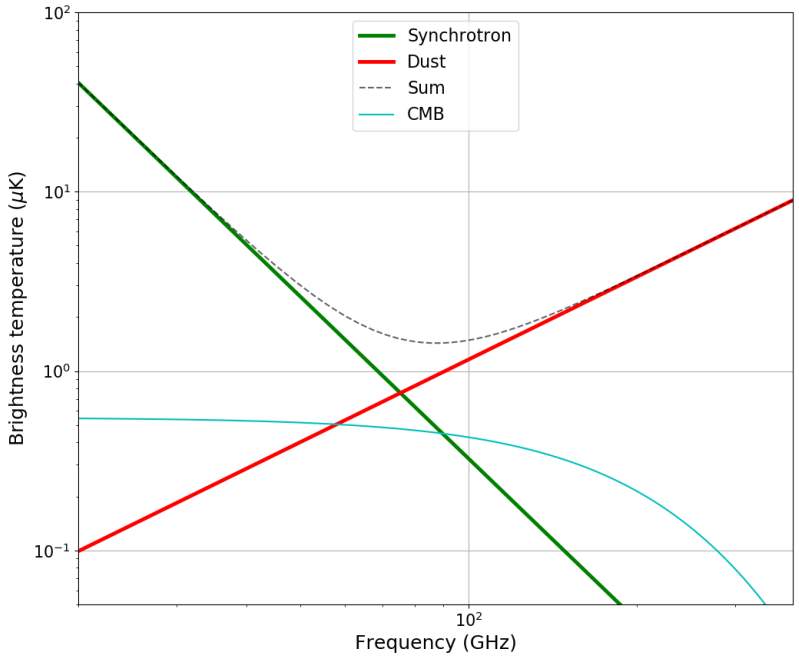

Figure 1.2: Brightness temperature in Raleigh-Jeans units of the two dominant sources of polarized foregrounds as measured by Planck [103]. "Polarization" here refers to the polarization amplitude $p = \sqrt{Q^2 + U^2}$. Here we assume a power law index β_s for synchrotron of -3, a greybody spectrum for thermal dust with dust temperature $T_d = 21$ and index $\beta_d = 2.5$, and a CMB temperature $T_{\rm CMB} = 2.73$ K. The dust and synchrotron amplitudes come from Table 5 in *Planck* Collaboration X, 2016 [103] for maps from the 30 GHz (synchrotron) and 353 GHz (thermal dust) channels. We approximate the RMS value of the CMB polarization anisotropies as 0.55 μK. It is apparent that the foregrounds dominate the overall CMB polarization signal across the entire range of frequencies, which span the Planck channels, but that the foregrounds have distinct frequency dependence as compared to the CMB. This figure is inspired by Fig. 51 from the reference.

1.3 Instrumentation for CMB Polarimetry

As elaborated above, the anisotropy signals we intend to study in the CMB are minute when compared to the blackbody emission spectrum of the background at 2.73 K. Additionally, they can be masked by astrophysical foregrounds that require sophisticated analyses to remove. In order to recover the non-galactic anisotropy signal, extremely sensitive receivers must be coupled to wide field-of-view, high-throughput telescope

optics, while also considering many types of complex instrumental systematic errors in the design. In this section, we discuss developments in CMB instrumentation which have enabled the ever-improving sensitivity of CMB instrumentation. As we proceed, relevant instrumental systematics will be discussed.

1.3.1 Telescope Designs

High-throughput telescope designs, where throughput equals $A\Omega$, with A the effective area and Ω the solid angle over which the apertue illuminates the effective area, have been devised for CMB telescopes from among a few fundamental designs. Reflector designs can be well suited to experiments designed to be sensitive to small scales, where refracting optical elements are often too large to be reliably fabricated. Off-axis Gregorian designs avoid losing field-of-view to optical elements in the path of light while maintaining good systematics [93]; crossed-Dragone designs satisfy conditions which ensure minimal polarization systematics (mainly, the cross-polarization) [89] [25]. Refractor designs are also in use for telescopes with larger beam size [1] [110] and as part of reimaging optics in large-aperture telescopes [125]. Examples of instruments using both reflector designs mentioned above will be discussed in Sec. 1.4.

1.3.2 Cold and Warm Optical Elements

The position of the focus and/or $f\#$, where the latter is the ratio of the focal length of the telescope to the aperture diameter, of a particular reflector design is often not well-suited to coupling to the detector array. Reimaging optics are then used, as these enable control of coupling between arrays of detectors and the telescope itself. Making these elements cryogenic to reduce loss, and using high refractive-index materials to make the receiver compact and reduce emission from the thinner lenses thus designed, is a major focus of CMB instrumentation work. Development of

silicon [19] and alumina [1] lenses has enabled receiver designs which take advantage of high-performing arrays and telescopes.

Additional optical elements in the cold stages of a receiver include IR-blocking filters, the most common being metal-mesh patterned onto millimeter wave-transparent plastics [126]. These can be though of as optical low-pass filters. Additionally, this technique can be used for band definition. A metal-mesh filter suspended in front of a detector array can define the bandpass or the upper band edge to which the detector will be sensitive. In the latter case, the lower band edge can then be defined by some waveguide-like element, or by on-wafer transmission-line filters.

Finally, the use of polarization modulation as a systematic control element has become an important consideration for CMB experiments in search of B-mode signals, or other polarization signatures at degree angular scales and above. Once it is decided to peform such modulation, the use of a half-wave plate (HWP), either stepped or continuously-rotating, can be compared to other modulators, variable-delay polarization modulators (VPM) [50] or even rapid rotation of the telescope boresight [95]. We will discuss the use of continuously-rotating HWPs (CRHWPs) throughout Ch. 4. Without modulation, it is difficult to account for and deproject the contamination sourced by combinations of low-frequency signals in the instrument and in the atmosphere.

1.3.3 Milllimeter-Wave Focal Planes

The use of cryogenic detectors to improve detector sensitivity has led to major efforts in CMB instrumentation and its coupling to advancing cryogenic technologies. When incoherent detectors like bolometers can be held at low temperatures to reach sufficently good sensitivity, they present an attractive technique for recording the signals of the CMB. The generic scheme for a bolometer is discussed in Sec. 2.1. Initial devices were based on doped semiconductors [87], but these evolved with the

implementation of sensitive temperature-sensitive resistors (thermistors) based on superconductors [57] [75]. These latter were more easily multiplexed [20] [72], and have been highly developed over the last ∼20 years.

Improvements to detector sensitivity well below the photon noise background, considered as the sum of shot noise and coherent wave noise, do not improve the overall sensitivity of a CMB instrument. Once this limit began to be achieved, the paramount improvement for CMB-instrument focal planes became to place as many background-limited detectors in a focal plane as possible. On the detector side of the instrumentation, this necessitated:

- dense fabricaton of millimeter-wave structures and highly-uniform detectors on silicon substrates;
- multiplexing techniques able to scale to readout of these dense arrays without overloading the cryogenic stages of the receivers;
- high-yield array assembly techniques to assure that the maximum number of detectors are usable in the field.

Throughout this process, requirements on device sensitivity (i.e. reaching the background limit of photon-induced noise) have been balanced against the need for detectors to operate as stably and linearly as possible. As this work discusses, superconducting sensors in most CMB experiments today, especially ground-based experiments, are in complex thermal environments and can only be treated as approximately linear. Their electrical readout is also sensitive to possible oscillatory effects which must be accounted for in the design.

Not yet discussed are the on-chip millimeter-wave transmission and filtering elements, which have been critical in enabling more control over the definition of millimeter-wave bands over which incoherent detectors like bolometers can absorb power. In addition, such elements can be used to define multiple sub-bands after the

millimeter-wave signal is coupled to the detector arrays via superconducting antennae [88] [94] [67]. Such "multichroic" designs have arisen in response to the enhanced understanding of the strength and complexity of foreground signals, in addition to their ability to maximize use of the limited focal plane area. These foregrounds, as well as any time-varying sources of sky signal, are best constrained and removed by simultaneous measurement across multiple frequency bands, which is most compactly performed in instruments featuring multichroic focal planes.

1.4 CMB Experiments in this Work

In this section, we introduce the experiments that are studied in the body of this work. Each features a millimeter-wave reflector-design telescope, but there are many differencess in their design and history. We seek to provide the relevant background for the chapters dealing with work on the Atacama Cosmology Telescope (ACT) [Chs. 3, 4] and the Atacama B-Mode Search (ABS) [Ch. 5]. We feature citations to the main results achieved by these experiments where appropriate.

1.4.1 Atacama Cosmology Telescope

ACT is a two-reflector millimeter-wave telescope with an off-axis Gregorian design, a $\sim$6 m primary mirror, and a 2 m secondary mirror. This gives a beam full-width half-maximum of 1.4 arcmin at 150 GHz, and a field of view of 3° as defined by a cold aperture stop inside the receiver. Details of the optical design can be found in Fowler et al., 2007 [35]. Sited at 5190 m in the Atacama Desert near Cerro Toco, Chile, the mirrors of the telescope are fixed to a frame movable in azimuth and elevation, with a co-moving metallic ground-screen also built on this frame. This robotic mount,

fabricated by Kuka Robotics[1] allows the telescope to slew rapidly in azimuth, with a rate during observations of 1.5°/s [122].

Since the first camera, the Millimeter Bolometric Array Camera (MBAC), was mounted on the telescope in 2007, reimaging optics have been used in the cryogenic receiver to maximize the number of sensors in the telescope focal plane. These reimaging optics are placed in "optics tubes" within the body of a larger cryogenic receiver. Elements in the optics tubes are cryogenically cooled, with IR-blocking and GHz low-pass filters at warmer (40 K) stages cooled by pulse tube coolers, cryogenic lenses at liquid helium temperature (4 K) or lower also cooled by closed-cycle coolers, and a Lyot stop defining the illumination of the array from the telescope focus. In MBAC, the cryogenic arrays of "pop-up" bolometers [85] were cooled by helium-3 sorption fridges [73] [122] to a base temperature of 300 mK. These were single-color arrays with bandpasses centered at 145, 217, and 265 GHz.

The MBAC arrays were not polarization-sensitive, but coupled to free space using an absorber structure. In the ACT Polarimeter (ACTPol) receiver upgrade, a new cryogenic receiver was designed to accomodate a custom dilution refrigerator (DR) designed by Janis[2]. Details on this new cryogenic platform may be found in Thornton et al., 2016 [125]. We emphasize that the three-tube configuration used for MBAC was maintained in the ACTPol upgrade. New lenses featuring metamaterial AR coatings were developed for these tubes [19].

In addition, given the greater base temperature and cooling power of the DR, more detectors could be read out and run with lower bath temperatures, enhancing their sensitivity. The resulting set of arrays featured pixels developed through the TRUCE collaboration [135], which developed a planar orthomode transducer (OMT) made from superconducting niobium fed by a corrugated silicon platelet feedhorn. The OMT enabled the TRUCE pixels to define the polarization sensitivity of a given

[1] https://www.kuka.com/en-us
[2] 225 Wildwood Ave, Woburn, MA 01801

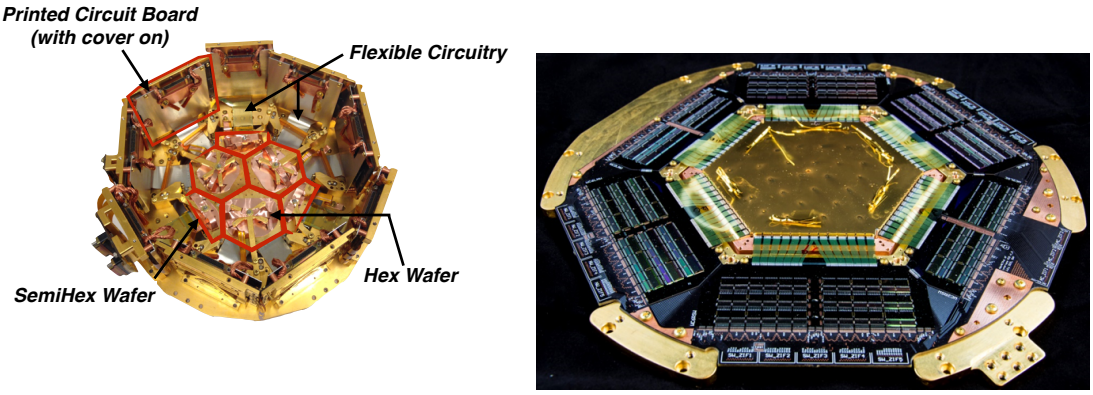

Figure 1.3: *Left:* The ACTPol dichroic 90/150 GHz array viewed from behind looking toward the sky. The labels indicate subcomponents including the component hexagon ("hex") and semi-hexagon ("semihex") wafers. Figure reproduced from [53] with permission of the author. *Right:* The AdvACT HF 150/230 GHz array with detector wafer at center. More details on the subcomponents may be found in Ch. 3. Courtesy R. Soden.

bolometer. The TRUCE design was also used in science-grade arrays for SPTpol [2] and ABS [29].

Among the ACTPol arrays, two included single-color pixels with a pair of orthogonally polarization-sensitive transition-edge sensor (TES) bolometers with a common bandpass centered at 145 GHz [45]. The first of these arrays deployed in 2013. The final array was dichroic, with four TES bolometers per pixel and bandpasses centered at 90 and 150 GHz. The dichroic array featured on-chip microwave filtering to define the band edges near the channel crossover within each pixel [18] [53]. This array was used in celestial observations beginning in 2015.

The Advanced ACTPol (AdvACT) project is an ongoing upgrade to the instrumentation developed for ACTPol, with greater array density thanks to a simplified array design. In ACTPol, three-inch silicon wafers cut into hexagons were used in the fabrication of the pixels and their bolometers; these were then tiled into a larger configuration using four and a half hexagons (three full hexagons, three semi-hexagons) to fill the focal plane area of the ACTPol reimaging optics. In the case of AdvACT, a single six-inch (150 mm) silicon wafer forms the center of a planar array design

that greatly simplifies assembly and maximizes the number of working channels in the completed array. Figure 1.3 shows the two array designs looking from behind the detector array toward the sky. Not seen in either of these views are the feedhorn arrays, which feed the pixel optics (OMT + microwave lines), and which became a spline-profiled design for AdvACT [118].

In addition to this major development, a new TES fabricatiion process was developed [78] that produced large arrays with uniform detector parameters across the larger-diameter wafers. This improvement was mainly due to replacing a proximity-effect bilayer-design TES, which is difficult to control, with a doping and heat-treating scheme for aluminum using manganese. More details on these devices follows in Ch. 3.

In short, AdvACT was designed to take full advantage of greater wafer area and uniformity by fabricating high-density, dichroic arrays. Each array thus features bolometers that are sensitive to two distinct bandpasses. The high-frequency (or HF) array features detectors with bandpasses centered at 150 and 230 GHz; the mid-frequency (or MF) arrays, of which there are two, features 90 and 150 GHz bolometers; and the low-frequency (or LF) array features 27 and 39 GHz bolometers. We collect the preceding information about the three array types in Tab. 1.1, along with the nominal number of TES bolometers available in each array for observations.

Finally, AdvACT was designed concurrently for use with broad-band silicon metamaterial HWPs, building off the AR-coating treatment used on ACTPol and AdvACT lenses [13]. We report on this work, and the analysis of the data acquired with AdvACT arrays and these HWPs, in Ch. 4.

1.4.2 Atacama B-Mode Search

The ABS telescope built off technology developed for MBAC (the helium sorption-fridge system) and TRUCE (early polarization-sensitive pixels with OMTs), function-

Array	Channels (GHz)	N TES	Beam Sizes (arcmin)	Status
HF	150/230	2024	1.4/0.9	Deployed 6-2016
2×MF	90/150	1716	2.3/1.4	Both Deployed 4-2017
LF	27/39	276	7.8/5.4	Awaiting Deployment

Table 1.1: Summary of the AdvACT arrays, including their channels (identified by central frequency of the bandpass), the number of detectors coupled to the sky (split evenly among the channels), and their status as of this writing.

Figure 1.4: Picture of the ABS receiver during its final observing season in 2014. The blue structure is aluminum hexcell placed in a square mount to act as a reflective ground screen. The conical baffle and supporting shipping container can also be seen.

ing as a pathfinder for forward-looking technology like a warm, continuously-rotating HWP [69]. The feedhorn design was developed for the 145 GHz single-channel detectors in order to be fabricated using the Princeton machine shop [128].

Sited within the same compound as ACT, ABS deployed a crossed-Dragone design telescope with 32 arcmin FWHM beams for TES bolometers at 145 GHz [28]. The total field of view for the ABS focal pane was 22°. The $\sim$ 1 m cryogenic receiver contained the entire optics system, with mirrors cooled to 3.8 K beneath a series of filters, and the HWP at ambient temperature above the aperture defined by the

cryostat window. The HWP sat at the bottom of a conical reflective baffle that was intended to prevent ground signal from reaching the focal plane.

This receiver was hoisted into position through a hole in the roof of the shipping container in which ABS was delivered to the site. A rectangular prism-shaped ground screen was mounted on the receiver to complement the conical baffle. Figure 1.4 shows a picture of the receiver during its final observing season (2014). ABS performed azimuth scans at constant elevation, covering multiple science fields.

ABS demonstrated the successful use of the HWP as a polarization modulator in its first result paper [68]. We will return to the details of ABS' unique design, and its science achievements, throughout this work, and especially in Ch. 5.

1.5 Structure of this Work

This dissertation will proceed as follows: in Ch. 2, we introduce the techniques used to model TES bolometer response and noise properties. This includes an introducton to the practical measurement methods used to recover fundamental parameters describing the bolometers. These results apply generally to the detectors used in both AdvACT and ABS, but they will be most relevant with regard to the detailed studies carried out as part of laboratory testing of the AdvACT arrays.

This testing is further described in Ch. 3. We begin by giving a detailed overview of the components of the AdvACT arrays and their interconnections, all of which enable the measurement of bolometer signals. We then describe the noise performance of the HF and two MF arrays, as well as data acquired to study the impedance of individual bolometers. Using a separate system for testing bolometers at NIST Boulder, we uncover evidence that high-frequency anomalies in the impedance data can explain the excess noise seen at low frequencies in AdvACT bolometers in the

arrays. We conclude by commenting on array performance in the field for these deployed arrays.

As part of the season following the deployment of the two MF arrays, three HWPs designed for the appropriate bands of each array were rotated continuously in order to modulate incoming polarization to the AdvACT arrays. We describe the principle of this technique, its history with ABS, and preliminary studies of its performance in the AdvACT project. This concludes our look into AdvACT specifically.

With regard to ABS, we present the maximum-likelihood analysis implemented to produce the final EE and BB bandpower error bars, as well as the published likelihood on the tensor-to-scalar ratio r. We introduce the MASTER pipeline [52] used in ABS to produce many Monte Carlo simulations that makes it possible to accurately model the statistics of crucial variables like r by efficiently computing hundreds of experimental simulations.

Finally, we conclude with a presentation of ongoing work on developing an understanding of, and tools for dealing with, the nonlinearity of TES bolometer signals in response to slowly-varing, large amplitude fluctuations sourced by instrument $1/f$ noise. These preliminary results include simulations indicating that this effect can leak large-scale models, and excess noise, from intensity to polarization during CMB observations. We point to ways to track the susceptibility of a given array of bolometers over time using standard bolometer calibration procedures, and then conclude.

Chapter 2

Electrothermal Models of Bolometers

In this chapter, we present the concepts and the first-order coupled differential equations describing the electrothermal behavior of their electrically-biased thermal sensors. We begin with general concepts relevant to all bolometer thermal architectures, then focus on the case relevant to AdvACT transition-edge sensor (TES) bolometers.

2.1 Basic Model

The bolometric detection concept [71] can be summarized as the detection of thermal power produced by incident electromagnetic (EM), or optical, power. This process is broadband and can easily record brightness temperatures, as compared to photon fluxes.

Absorbing elements to convert optical power into thermal power can be designed across much of the electromagnetic spectrum, though bolometers are most easily optimized from millimeter-wave to infrared wavelengths [108], where the limiting sources of noise arising in the bolometer have been well-understood for the past 35 years [86]. At high energies, measuring individual photon pulses and converting these

to photon energies may be more appropriate, and the bolometer becomes a calorimeter [44] [63].

Regardless of the frequency band over which the bolometer is sensitive, these devices can usually be fully described by i) their thermal architecture and ii) their electrical architecture. The former is generated through a lumped-element represetation of heat flow in the bolometer, with distinct thermal "blocks" representing isothermal components of the bolometer with heat capacities C_i and temperatures T_i. The latter generally applies to a distinct sensor, usually a thermistor (temperature-sensitive resistor), which converts the bolometer thermal signal into an electrical signal. In both cases, we use circuit diagrams to represent the relevant aspects of each architecture.

Figure 2.1 shows the simplest thermal circuit diagram, a single block with temperature T and heat capacity C. The figure also shows a single resistive element (R) schematically representing an unspecified electrical circuit. As this figure indicates, the two circuits are coupled due to the thermal power $P_{\rm bias}$ produced by current flow through the thermistor. In order to thermalize the sum of $P_{\rm bias}$ and the optical signal P_γ, heat flows across the thermal impedance connecting the thermal block to a bath at temperature $T_{\rm bath} < T$. In the analysis of small transient signals, we will label this thermal impedance as a thermal conductance G to the bath. However, for constant P_γ and $P_{\rm bias}$, we instead refer to a power to the bath $P_{\rm bath}$ related to G and satisfying the following equation:

$$P_{\rm bath} = P_\gamma + P_{\rm bias} \tag{2.1}$$

which we refer to as the "power balance equation." This equation forms the basis for the linear, small-signal model which allows us to describe the bolometer response to electrical and optical excitations given a steady-state $P_{\rm bias}$ and predefined $P_{\rm bath}$.

In essence, the bolometer always satisfies this equation. In the appropriate small-signal limit, expansion of the nonlinearities hiding in terms like $P_{\rm bias}$ to first order result in a set of coupled equations, where the coupling occurs due to the thermistor

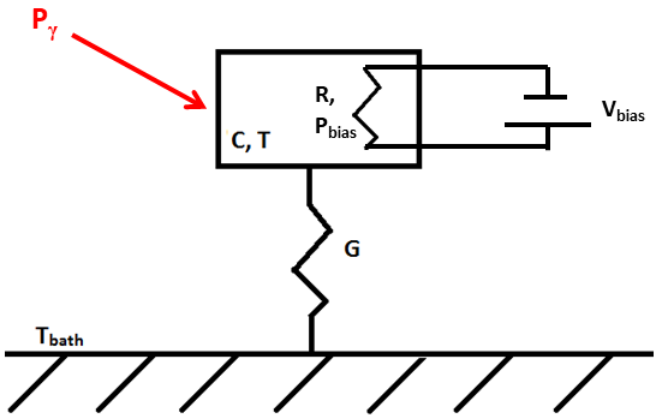

Figure 2.1: Thermal circuit diagram of the simplest bolometer model. A single thermal element, or "block" with heat capacity C and temperature T sees incoming power $P_{\rm bias} + P_\gamma$. This is balanced by the outgoing power flowing to the cold thermal bath, $P_{\rm bath}$.

resistance depending on the temperature, and the bolometer temperature on the resistance due to the $P_{\rm bias}$ term. Since these equations are linear, it is natural to write them in a matrix formalism. Solving for the current (δI) and temperature (δT) fluctuations driven by incoming voltage (δV) and millimeter-wave power (δP_γ) fluctuations, we can write the equation as:

$$\begin{pmatrix} \delta I \\ \delta T \end{pmatrix} = M^{-1} \begin{pmatrix} \delta V \\ \delta P_\gamma \end{pmatrix}. \tag{2.2}$$

We discuss this matrix, hereafter called the "coupling matrix", in detail for various sensors throughout this work. One effect which is hidden in the matrix formalism is the use of passive negative feedback in the electrothermal circuit. By this we mean ensuring that changes in P_γ an be compensated by opposite changes in $P_{\rm bias}$, since $P_{\rm bath}$ is fixed. The use of this effect is ensured by sending constant current to thermistors with negative dR/dT, and constant voltage to thermistors with positive dR/dT. An example of the latter will be discussed in Section 2.3.

2.2 Extensions to the Basic Model

In this thesis, we consider extended thermal models of bolometers. These are characterized by additional thermal "blocks" with distinct temperatures T_i, heat capacities C_i, and thermal conductances G_i, where we use i to specify these as internal to the bolometer island. The latter may include a separate connection to the thermal bath. In any model, including the simplest, we assume that Joule heating affects only the single block representing the part of the bolometer nearest the thermistor, including the thermistor itself.

We can understand the possible need for such extensions by considering the limit of a thermally large bolometer, in which heat takes an appreciable time to raise the temperature of the thermistor. Since the thermistor internal temperature is "read out" as the only signal, we expect that high-frequency power fluctuations far away from the sensor will be filtered out according to an internal time constant within the bolometer. We will then see a bolometer response that is quite complex compared to the simple model derived from Fig. 2.1.

However, if we model this thermal transfer as occuring between the thermistor block and a distinct, second block, with the two connected by an internal thermal conductance, we can model the bolometer response with an extra equation describing the thermal and power fluctuations at the second block.

The coupling matrix M, or its inverse M^{-1}, in Eq. 2.2 is always an $N+1$ by $N+1$ square matrix, where N is the number of blocks used to model the bolometer thermal structure. We will consider extended models with a second thermal block floating from the thermistor block and independent of the bath (hereafter called the "hanging" model). In the limit of large coupling conductance G_i, this model reduces to the simplest one-block model. Figure 2.2 shows schematic representations for both the series and hanging model.

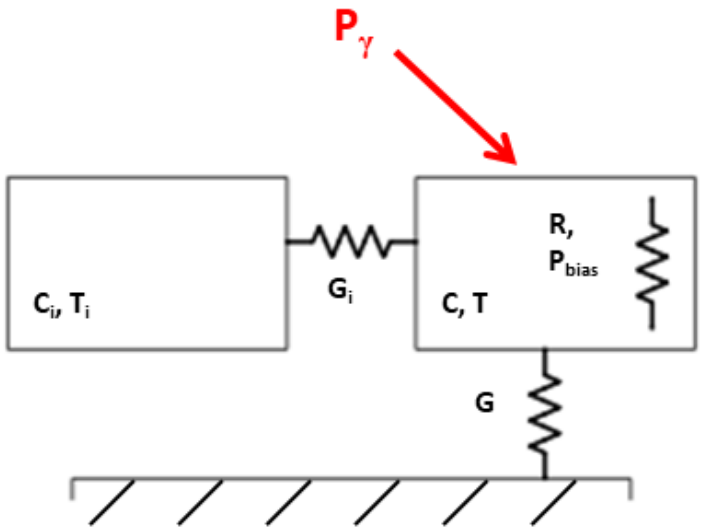

Figure 2.2: *Left:* A schematic of the hanging electrothermal model for bolometers, with parameters for the second block written with subindices i. Not shown is the voltage source producing the power P_{bias} in the thermistor with resistance R. *Right:* Electrothermal schematic for the intermediate electrothermal model.

2.3 Models for Transition-Edge Sensor Bolometers

We now briefly review the main features of the bolometer small-signal model for the case of a TES thermistor under voltage bias. Discussions of bolometers featuring alternative thermistors can be found in [38] [87]. The discussion below is heavily based on the chapter describing the simple TES model and its features in the book chapter by K. Irwin and G. Hilton [58].

By necessity, this model simplifies the response of the TES to recover analytic expressions for the bolometer response. The TES itself is a superconducting thin film held on its resistive transition by a bias voltage. The steepness of the transition with temperature, $R(T)$, acts as a transducer to enable the electrical readout of the incoming thermal signals. We identify the film's critical temperature T_c, with the temperature of the TES in operation, such that the steady-state temperature $T = T_c$

in all bolometer equations involving TES thermistors. We are validated in doing this due to the narrow range ($\mathcal{O}(1\%)$ of T_c) of temperatures within the transition. Another important value for these devices is their normal state resistance, R_{N}, which determines the scale of the thermistor resistance in operation R. We often write achieved values of R in operation as fractions or percentages of R_{N}.

When operating TESes in their transition, a stiff bias voltage provides the negative feedback required to use these high open loop gain sensors without railing, which in this case is termed "thermal runaway." A heuristic to see how bias voltage provides the correct feedback is to consider an increase in optical power, which increases the sensor temperature. This increase in TES temperature increases the TES resistance, which reduces the Joule heating P_{bias} since $P_{\mathrm{bias}} = V^2/R$, where V is the constant bias voltage.

For our purposes, the TES is represented by the following equation, describing the resistance fluctuations δR induced by thermal fluctuations δT and current fluctuations δI:

$$\delta R = \frac{R}{T}\alpha\delta T + \frac{R}{I}\beta\delta I. \tag{2.3}$$

From the above one can see that $\alpha = \frac{dln(R)}{dln(T)}$ and $\beta = \frac{dln(R)}{dln(I)}$. These parameters, also called the "sensitivites" of the TES to temperature and current fluctuations for α and β respectively, are instrumental in determining the overall detector sensitivity and stability within the coupled electrothermal equations.

We now discuss the expressions for the thermal and electrical architectures of a simple TES bolometer. The first equation expands Eq. 2.1 to first order in δT, where the time-dependent temperature $T(t) = T_c + \delta T(t)$. We also add a term for power induced by the changing temperature of the heat capacity C:

$$C\frac{d\delta T}{dt} = V(2+\beta)\delta I + (P_{\mathrm{bias}}\alpha/T_c - G)\delta T + \delta P_\gamma, \tag{2.4}$$

where all δ terms are time-dependent, the conductance $G = dP_{\rm sat}/dT|_{T_c}$, and $P_{\rm sat}$ is defined as the total power incident on the bolometer (the sum of $P_{\rm bias}$ and P_γ) required to drive the detector into its normal state. Looking back at Eq. 2.1, we see that $P_{\rm sat}$ is then nearly equal to the term $P_{\rm bath}$. The approximation of $P_{\rm bath}$ as $P_{\rm sat}$ will apply to all discussions of TES bolometers. For definiteness, we specify the common power-law model used to describe $P_{\rm sat}$ that defines the parameters determining G:

$$P_{\rm sat} = \kappa(T_c^n - T_{\rm bath}^n), \tag{2.5}$$

so that $G = n\kappa T_c^{n-1}$. We note, finally, that the sharpness of the resistive transition in TES temperature also leads to a very sharp $R(P)$ curve. Therefore, the total power on the TES during operation is usually within 10% of $P_{\rm sat}$.

We now define an open loop gain under constant-current (hard current bias) conditions using the term multiplying δT in Eq. 2.4: The result will be hereafter referred to as "loop gain" $\mathscr{L}$:

$$\mathscr{L} = \frac{P_{\rm bias}\alpha}{GT}. \tag{2.6}$$

For large loop gains, the TES sensor has a faster and more linear response across a wider range of signal amplitudes. This is not evident from the bare equations, but results from considering some limiting cases of the equations above. For instance, under hard current bias, δI goes to zero and the time-domain equation for the TES temperature fluctuation is directly integrable. Instead of a bare thermal time constant $\tau = C/G$, which would occur for $P_{\rm bias} = \mathscr{L} = 0$, we follow Irwin and Hilton, 2005 [58] and define a new time constant:

$$\tau_I = \frac{\tau}{(1 - \mathscr{L})}. \tag{2.7}$$

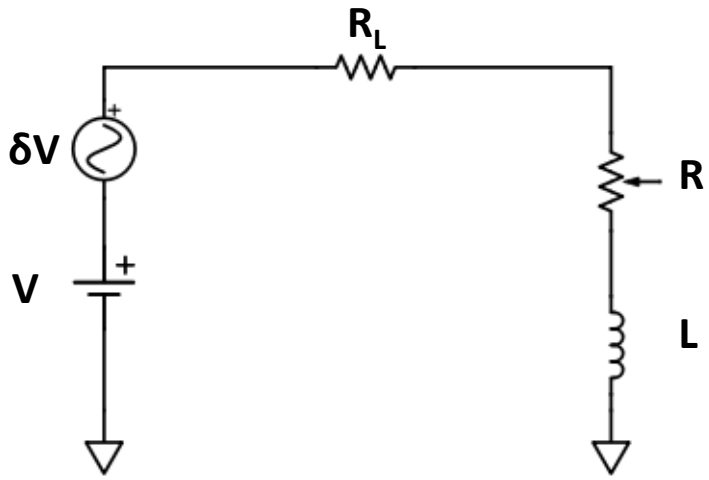

Figure 2.3: A schematic of the conceptual TES electrical bias circuit used in Eq. 2.8. Here, $R_L \sim R_{\rm sh}$. A more detailed circuit appears in Fig. 3.3.

In the electrical circuit, we account for a TES under a voltage bias V with fluctuations $\delta V(t)$. The TES is in series with an impedance R_L, the Thevenin-equivalent impedance of other elements in the TES bias circuit, and an inductance L:

$$L\frac{d\delta I}{dt} = -\left[R_L + R(1+\beta)\right]\delta I - \frac{V\alpha}{T}\delta T + \delta V. \tag{2.8}$$

These components are schematically represented in Fig. 2.3.

This equation by itself can be used to define a new time constant in the system when we set $\delta T = 0$. In this case, the equation for the time-domain behavior of the current fluctations is independent of δT. We then define the time constant determining the decay of current in the TES bias circuit as a response to some δV:

$$\tau_{\rm el} = \frac{L}{R_L + R(1+\beta)}. \tag{2.9}$$

With these equations, we can now define the coupling matrix M for the simple model of the TES bolometer. We write these equations keeping the inductance L and heat capacity C as coefficients of the first-derivative terms, as opposed to the format

in Irwin and Hilton, 2005 [58]. We also transform the equations to the frequency domain assuming sinusoidal input signals and responses. Writing the full equations:

$$\begin{pmatrix} i\omega L + R(1+\beta) + R_L & \frac{V\alpha}{T} \\ -V(2+\beta) & i\omega C + (1-\mathscr{L})G \end{pmatrix} \begin{pmatrix} \delta I \\ \delta T \end{pmatrix} = \begin{pmatrix} \delta V \\ \delta P_\gamma \end{pmatrix}. \tag{2.10}$$

Once the coupling matrix is written down, we can define important quantities from its inverse. For instance, the quantity called "responsivity", $s_I = \delta I/\delta P_\gamma$, can be read out as $M^{-1}_{1,2}$, where the subindices specify the row and column, respectively, in the matrix M^{-1}. The responsivity is the frequency-domain filter applied by the TES to incoming power signals. We seek to maximize its amplitude to improve raw TES bolometer sensitivity and maximize signal-to-noise ratios. Another interesting function is the TES impedance $\delta V/\delta I$, which is equal to $(M^{-1}_{1,1})^{-1}$ minus the equivalent impedance of other elements in the TES bias circuit, $Z_{\rm eq}$. Measuring this function in the lab is a useful way to extract TES bolometer parameters.

To begin a discussion of bolometer design, we write the form for the TES bolometer responsivity, s_I, as:

$$s_I \sim -\frac{1}{V_{\rm bias}} \frac{\mathscr{L}}{\mathscr{L}+1} \frac{1}{1+i\omega\tau_{\rm eff}}, \tag{2.11}$$

in the limit of small inductance ($\tau_{\rm el} \ll \tau_{\rm eff}$), small β, and stiff voltage bias ($R_L/R \ll 1$). In practice, all of these conditions hold only imperfectly. For completeness, we do include nonzero β in the formula for $\tau_{\rm eff}$:

$$\tau_{\rm eff} = \tau \frac{1+\beta}{1+\beta+\mathscr{L}}. \tag{2.12}$$

where we have again taken $R_L/R \to 0$. This parameter is an effective time constant in the sense that it arises as the small-inductance limit of one of the eigenvalues of the matrix M. These eigenvalues define "rise" and "fall" time constants in the time-

domain response of the TES current and temperature to a unit impulse. We skip these details and direct interested readers once again to [58].

In the AdvACT project, we used the approximate expressions above describing an "ideal" TES bolometer to understand trade-offs in design. We reiterate that our idealization goes beyond assuming the simplest electrothermal architecture of the bolometer, to assuming ideal bias conditions (i.e. no terms depending on R_L) and insensitivity to bias current fluctuations (setting $\beta = 0$). For such a device, designing a bolometer proceeds roughly as the following:

- Determine the expected power background on the device P_{load} due to incoming radiation and select a P_{sat} target by multiplying P_{load} by a safety factor (~ 2 to 3).

- Select a critical temperature for the TES that, for fixed P_{sat}, optimizes the TES sensitivity.

- Add a tunable-thickness metal film to the bolometer to control the heat capacity of the TES and minimize the time constant τ_{eff} for fast TES response without violating the bound $\tau_{\text{el}} < 5.8\tau_{\text{eff}}$ required for TES electrical stability [46].

The above criteria then determine many of the crucial parameters for an array of TES bolometers: their P_{sat} values, their critical temperatures, and their time constants. Though not mentioned above, the normal resistance R_{N} is an important overall calibration factor that determines the amplitude of the responsivity and plays into expected TES noise behavior.

We conclude this section by providing the matrix equation describing the hanging two-block electrothermal model from Section 2.2. In the 3×3 matrix below, the new parameters C_i and G_i fully parametrize the new components of the extended model,

with δP_i representing the distinct power fluctuations on the hanging block:

$$\begin{pmatrix} i\omega L + R(1+\beta) + R_L & 0 & \frac{V\alpha}{T} \\ 0 & iC_i\omega + G_i & -G_i \\ -V(2+\beta) & -G_i & i\omega C + (1-\mathscr{L})G + G_i \end{pmatrix} \begin{pmatrix} \delta I \\ \delta T_i \\ \delta T \end{pmatrix} = \begin{pmatrix} \delta V \\ \delta P_i \\ \delta P \end{pmatrix}. \tag{2.13}$$

2.4 Verifying TES Bolometer Models and Parameters

Having sketched the equations and results relevant to bolometer design, we now describe practical methods for verifying that any particular electrothermal model captures both the TES bolometer response and noise performance. Specifically, we would like to measure all of the parameters defining the TES bolometer, and then predict the noise spectral density before comparing with data.

2.4.1 Bias Steps

Practically speaking, the parameters $P_{\rm sat}$, T_c, G, and $R_{\rm N}$ that define critical elements of a TES bolometer design can all be measured from a current-voltage, or $I-V$, curve. This measurement involves driving the TES normal via large bias current, stepping this bias current down until the TES enters its resistive transition, and recording the current and voltage at the TES until the TES becomes fully superconducting. We are only able to record the TES current using the AdvACT readout electrronics, which will be further discussed in subsequent sections.

An example dataset, showing characterstic curves for an AdvACT TES with $T_{\rm bath}$ at multiple temperatures, is shown in Fig. 2.4. Here the $I-V$ curves have been converted to $R-P$ curves, where $R = V/I$ and $P = I \times V$. We take $P_{\rm sat}$ to be the

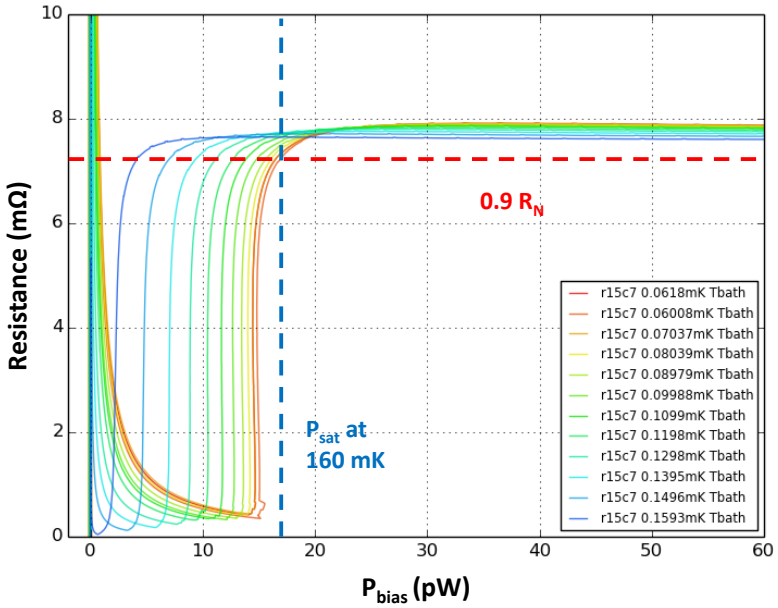

Figure 2.4: Resistance vs. power curves measured for an AdvACT TES bolometer. The color of the solid lines corresponds to measured $T_{\rm bath}$ value before the data was acquired. Temperature increases as color goes from red to violet, and from right to left in the plot. We indicate the % $R_{\rm N}$ used to define $P_{\rm sat}$ as the dashed red horizontal line, while the dashed vertical line indicates $P_{\rm sat}$, the power where the horizontal line and the 160 mK curve intersect.

value of P where $R = 0.9R_{\rm N}$, where $R_{\rm N}$ is the value of the flat portion at the top of the curve.

With this data in hand, it remains to measure the time constants of our devices, where we assume the single time constant $\tau_{\rm eff}$ fully describes the bolometer response to a small, discrete step in the bias voltage ($\mathcal{O}$(few %) of the DC bias level). We use our warm electronics to step between two bias values, and measure the exponential rise and decay of the TES current at each step. When converted to a 3dB frequency $f_{\rm 3dB,eff} = 1/2\pi\tau_{\rm eff}$, our results should behave as: [93] [46] [**?**]

$$f_{\rm 3dB,eff}(P_{\rm bias}) \propto 1 + \frac{\mathscr{L}(P_{\rm bias})}{1+\beta}. \tag{2.14}$$

An example of this fit can be seen in Fig. 2.5.

The constant of proportionality in the above is purely thermal $f_{3\mathrm{dB},0} = 1/2\pi\tau$. If we multiply through by this parameter, we find a line with intercept $f_{3\mathrm{dB},0}$ and a slope that depends on a combination of α, β, T_c, G, and C. We assume the last three parameters have already been measured. In this case, the slope may be used to measure the quantity $\alpha/(1+\beta)$. However, this assumes that these parameters are not themselves a function of P_{bias}, which we know to be false in principle. This approximate expression is thus not able to distinguish the relative sizes of α and β, nor do we expect it to be accurate across wide ranges of P_{bias}.

2.4.2 TES Bolometer Impedance

A more complete understanding of the TES response can be gleaned via measurements of the electrical impedance, Z_{TES} of the sensor. This general technique has been applied before to studies of bolometer electrothermal models [38] [137] [83]. We

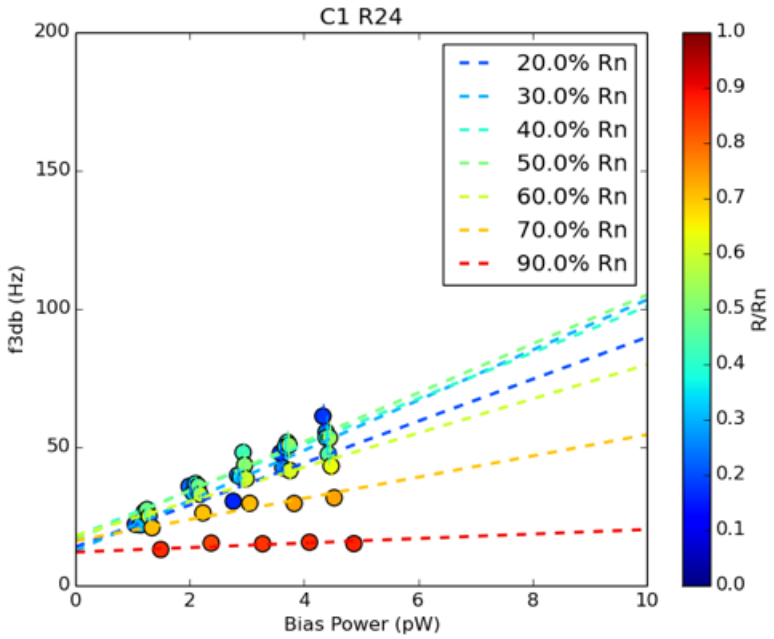

Figure 2.5: Example linear fit to $f_{3\mathrm{dB}}$ versus P_{bias} for an early AdvACT test device. Figure courtesy S.P. Ho, and appeared as part of poster presentation at 36th ESA Antenna (see 0.1).

will provide detailed discussions of the technique as applied to studies of AdvACT bolometers in Sec. 3.4; in this section we simply sketch the key features of how impedance measurements can distinguish α and β, thus providing the complete set of parameters needed to predict TES bolometer noise.

Conceptually, we require measurements of the impedance across the entire electrical bandwidth of the TES ($\sim$ few kHz, usually). We also must calibrate out any frequency dependence of the Thevenin-equivalent bias voltage and the series impedance (including the inductance) in the electrical bias circuit of the TES. Once this is done, acquired data can be fit to the following expression:

$$Z_{\rm TES}(\omega) = R(1+\beta) + \frac{R(2+\beta)\mathscr{L}}{(1-\mathscr{L}) + i\omega\tau}. \tag{2.15}$$

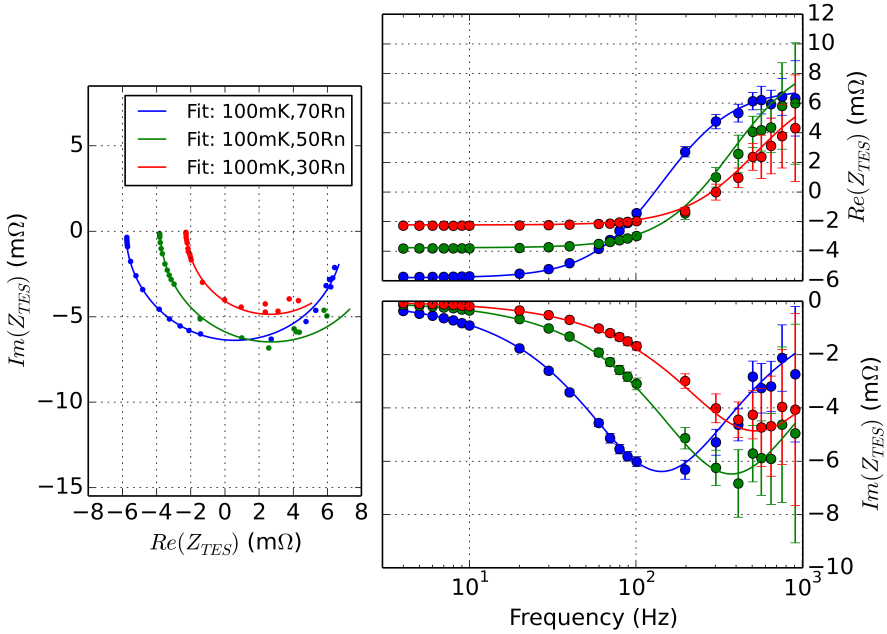

Figure 2.6: Dataset showing AdvACT TES bolometer impedance data (points) and best-fit models (solid lines). These data were taken with $T_{\rm bath}$ of 100 mK and at various TES resistances, written here as percentages of $R_{\rm N}$ = [70,50,30]%. The semi-circular shape of the model is forced by the form of Eq. 2.15.

Derivation of this result in Irwin and Hilton, 2005 [58] proceeds, as mentioned above, by studying the component $M^{-1}_{1,1}$ component of the inverse of the simple model's coupling matrix M. Qualitatively, the resulting equation describes a semicircle in the lower half-plane of the complex plane. In the $\omega \to \infty$ case, the TES responds as a resistor with its dynamic resistance at constant temperature $dV/dI|_T = R(1+\beta)$ instead of R. At low frequencies $\omega \to 0$, in the limit of large $\mathscr{L}$, we recover $Z_{\rm TES} = -R$ From these twin limits, the parameter β can be recovered. If R is known beforehand, from an $I-V$ curve for example, then only the high-frequency limit is required.

Once β is measured, we can extract the constant-current time constant τ_I by recognizing that the imaginary part of the impedance has a minimum at the frequency $\omega_{\rm min}\tau_I = 1$. This quantity is degenerate in the loop gain (or α if we assume the other parameters have been measured via $I-V$ curves) and the heat capacity C. However, $\mathscr{L}$ also factors into the radius of the semicircle, a shape factor which is independent of the way the semicircle is swept out versus frequency. So we may recover β, α, and C separately, with some non-negligible covariance between them. As an example, Fig. 2.6 shows an example impedance data set and best-fit simple-model curve for an AdvACT bolometer. These data are acquired for a constant $T_{\rm bath}$ at various fractions of $R_{\rm N}$.

By doing this for various bath temperatures, or equivalently various $P_{\rm bias}$, and at various points on the TES transition, we may study how these parameters vary. At any given point, we should expect that our set of parameters completely define the electrothermal model, and thus any other dataset acquired for the devices. We choose to study the validity of this assumption using noise data.

2.4.3 TES Bolometer Noise

In this subsection, we describe how to estimate the total noise generated by the TES bolometer in order to confirm that the electrothermal model captures the frequency

dependence of this noise. For a simple TES bolometer, the sources of noise are usually enumerated as:

- Johnson noise from the TES resistor, with a correction to the standard expression due to the $R(I)$ function of the sensor: $S_{V_{\mathrm{TES}}} = 4k_{\mathrm{B}}TR(1+2\beta)$, where k_{B} is Boltzmann's constant and S_V refers to a noise voltage spectral density in units of V^2/Hz;
- Johnson noise from the load resistance in series with the TES, $S_{V_L} = 4k_{\mathrm{B}}T_L R_L$, where we set T_L equal to T_{bath};
- Current noise in the amplification circuit, which we discuss in Section 3.4;
- Phonon noise due to the conductance G at temperature T, $S_{P_{\mathrm{link}}} = 4k_{\mathrm{B}}GT^2 f_{\mathrm{link}}$, where the units here are W^2/Hz, or noise power spectral density.

In reference to the diagram in Fig. 2.3, the Johnson voltage noise terms arise in series with the TES and load resistor, respectively; the current noise is incoherently summed at readout; and the phonon noise generates some spurious δI within the TES that is read out. Both the TES Johnson noise and phonon noise terms contain nonequilibrium corrections to the equilibrium noise quantities. These arise from the current bias present in the TES and the thermal power flowing through the conductance G during noise measurements, coupled to the nonlinearity of the quantities $R(I)$ and $G(T)$ [58].

As stated above, we measure the TES current using our readout system, and can calibrate this to power units using an estimate for the responsivity. When studying the noise spectrum, we prefer to work in terms of each noise source's contribution to the current noise, comparing their incoherent sum to the measured noise current. Any deviations are then due either to i) errors in the sizes and frequency dependence of the terms which convert voltage and power noises to current noise or ii) additional, unmodeled noise sources.

We will now briefly describe the terms that convert the above quantities to current noise, excepting the amplifier noise, which we take to be a current noise in series with noise arising from the bolometer. We have already mentioned the responsivity $s_I = \delta I/\delta P$. The current noise contribution from phonon noise in the conductance G is then $S_{I_{\rm link}} = |s_I|^2 S_{P_{\rm link}}$.

In order to convert the voltage noise terms sourced by the load resistance and the TES itself, we use the expressions for the internal and external admittance, where admittance is the inverse of electrical impedance. The impedance matrix Z can be derived directly from the coupling matrix M once the source fluctuations $(\delta V, \delta P)$ have been converted to the conjugate forces $(\delta V, \delta P/T)$ of the fluctuation-dissipation theorem. This requires dividing the terms in the second row of M by T [58].

The matrix thus formed is $Z^{\rm ext}$, and defines the external admittance $Y^{\rm ext} = (Z^{\rm ext})^{-1}$. It is important to distinguish this from the internal impedance and admittance matrices, in which we must account for the work done on a voltage source internal to the TES. The resulting change only applies to the $2,1$ element of $Z^{\rm ext}$, which becomes:

$$Z^{\rm int}_{2,1} = \left[I(R_L - R) + i\omega L I\right] \frac{1}{T}. \tag{2.16}$$

This results from accounting for the noise voltage present in the TES electrical circuit when calculating the Joule power dissipated in the TES. Rather than assuming some form for this voltage, we set the power at the TES $P_{\rm bias} = IV_{\rm TES} = I\left(IR + V_{\rm noise}\right)$, but replace the TES voltage multiplying I to the sum of the other voltages in the bias circuit:

$$P_{\rm bias} = I\left(V_{\rm bias} - IR_L - L\frac{dI}{dt}\right), \tag{2.17}$$

where $V_{\rm bias}$ is the Thevenin-equivalent bias voltage supplying the TES. Following this expression, equation 2.16 arises as an expansion of the above expression for $I(t) = I + \delta I(t)$.

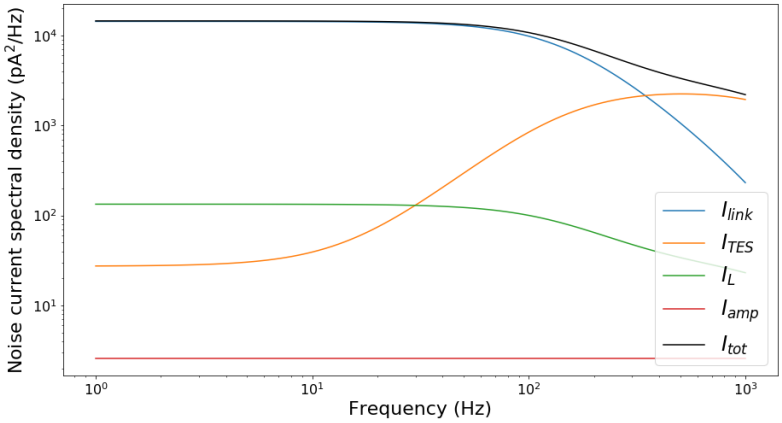

Figure 2.7: Calculated current noise, component by component and coverted to $\mathrm{pA}^2/\mathrm{Hz}$, for the best-fit model to the 50% R_N data shown in Fig. 2.6. Since the crossover between the TES Johnson noise (labeled 'I_{TES}' in this figure) and the thermal link noise 'I_{link}' occurs at 300 Hz, the TES current noise is dominated by thermal link noise out to high frequencies. The small level of amplifier noise 'I_{amp}' is constant with frequency.

Finally, we can calculate the current noise contributed by the TES, S_{I_TES} and the current noise from the load resistor S_{I_L}. Combining all terms, and writing the amplifier current noise as S_{I_amp}, the total current noise is:

$$S_{I_\mathrm{tot}} = S_{I_\mathrm{link}} + |Y^\mathrm{int}_{1,1}|^2 S_{V_\mathrm{TES}} + |Y^\mathrm{ext}_{1,1}|^2 S_{V_L} + S_{I_\mathrm{amp}}. \tag{2.18}$$

Although the current noise is most directly measured in the AdvACT electronics, it can be quickly converted to power units (W^2 / Hz) using an estimate for the responsivity. This quantity, whose square root is defined as noise-equivalent power (NEP), is expressed as:

$$S_{P_\mathrm{tot}} \equiv NEP^2 = \frac{1}{|s_I|^2} S_{I_\mathrm{tot}}, \tag{2.19}$$

where the quantity in the denominator of the right-hand equation is the absolute value of the responsivity in Eq. 2.11. The quantity NEP is most often used when

expressing the sensitivity of a TES. It expresses the EM signal size (in dimensions of power) required to achieve a signal-to-noise ratio of 1. However, in the case when the TES observes the sky, the photon noise term S_{P_γ} must be added to Eq. 2.19. When we speak of a TES bolometer being "background-limited", we mean that the sum of terms in this equation is subdominant to the photon noise, so that the overall detector NEP is dominanted by $\sqrt{S_{P_\gamma}}$.

To make the foregoing discussion more concrete, and to show the relative size of these noise terms for AdvACT TES bolometers, Fig. 2.7 shows the individual current noise terms as a function of frequency for all noise sources except photon shot noise, which was not present for the dark measurements used to estimate these terms. The parameters used to calculate the noise values, responsivity, and relevant components of the admittance matrices are all taken from the best-fit results of the impedance data shown in Fig. 2.6 for 50% $R_{\rm N}$.

We can see that the dominant term for dark noise data is $S_{I_{\rm link}}$, especially at frequencies below $f_{\rm 3dB,eff}$. We note that we have here set the nonlinear term $f_{\rm link} = 1$. Johnson noise from the TES is relevant at higher frequencies, but is strongly reduced by electrothermal feedback due to the the $1/\mathscr{L}$ dependence hidden in $|Y^{\rm int}_{1,1}|^2$.

To summarize, in this subsection we have introduced the noise sources contributing to TES bolometer current and power noise. We have introduced the concepts of internal and external admittances and how they differ, leading to different frequency dependence in the current noise terms associated with internal TES voltage noise and external load resistor voltage noise. We then showed an example of expected TES noise for an AdvACT TES bolometer.

2.4.4 Effects of Extended Models

The effects of adding a second thermal block to our bolometer thermal models is twofold: we add another noise source due to the finite conductance G_i between the

blocks, and we alter the form of the TES bolometer responsivity, impedance, both admittances, and any other quantities derived from the coupling matrix $M = M_{\rm hang}$. In this section, we describe the effect of recalculating the bolometer impedance and the total bolometer current noise for the hanging model, the latter also being the focus (with generic number of additional blocks used to fit excess TES noise) in Gildemeister et al., 2001 [42].

With regard to the new noise source, which we call $S_{P_{\rm hang}}$, its form in units of power is the same as that of $S_{P_{\rm link}}$, except we do not anticipate a need for a corresponding $f_{\rm link}$ because the blocks are isothermal in the steady state. We write:

$$S_{P_{\rm hang}} = 4k_{\rm B}G_iT^2. \tag{2.20}$$

Converting this quantity to a noise current at the TES requires a new function, which can be calculated from the inverse of $M_{\rm hang}$. Before doing so, we review the form of M^{-1} and discuss the new function for TES bolometer impedance.

Recalling Eq. 2.13, we simplify the expression by defining the following functions, each of them an entry on the diagonal of $M_{\rm hang}$:

$$A(\omega) \equiv i\omega L + R(1+\beta) + R_L; \tag{2.21a}$$

$$B(\omega) \equiv i\omega C_i + G_i; \tag{2.21b}$$

$$D(\omega) \equiv i\omega C + G_i + (1-\mathscr{L})G, \tag{2.21c}$$

where we use $D(\omega)$ to avoid confusion with the heat capacity C. Our expression for $M_{\rm hang}$ then becomes:

$$\begin{pmatrix} A(\omega) & 0 & \frac{V\alpha}{T} \\ 0 & B(\omega) & -G_i \\ -V(2+\beta) & -G_i & D(\omega) \end{pmatrix} \begin{pmatrix} \delta I \\ \delta T_i \\ \delta T \end{pmatrix} = \begin{pmatrix} \delta V \\ \delta P_i \\ \delta P \end{pmatrix}, \tag{2.22}$$

where, again due to the assumption of the two blocks being isothermal in the steady state, we have idential terms $-G_i$ as the (2,3) and (3,2) elements in $M_{\rm hang}$.

Now, we can calculate the impedance for the hanging model by calculating the $1,1$ entry of $M_{\rm hang}^{-1}$, inverting it, and subtracting the series equivalent impedance. We take the latter to be $Z_{\rm eq} = R_L + i\omega L$. The result is:

$$Z_{\rm TES,hang} = R(1+\beta) + R(2+\beta)\frac{\mathscr{L}GB(\omega)}{B(\omega)\ D(\omega) - G_i^2}. \tag{2.23}$$

Using this equation, we can extract, or set limits on, the parameters C_i and G_i given an impedance dataset. The effect of their inclusion on the shape of the TES bolometer impedance curve can be seen in Fig. 2.8, which shows the impedance plotted in the complex plane for one value of C_i (where C_i equals the measured best-fit C of the one-block model for Fig. 2.6) and three values of G_i. The main effect is an elongation of the semicircle towards high frequencies, which, because the functional forms for the simple and hanging model have the same high-frequency limit, causes a kink in the curve. We expect this kink to occur above ~ 1 kHz.

We can now investigate the components of $M_{\rm hang}^{-1}$ that are relevant for converting noise powers to noise currents. Assuming zero signal in the inputs δV, δP, and δP_i, and assuming no voltage noise (which we handle separately by recalculating

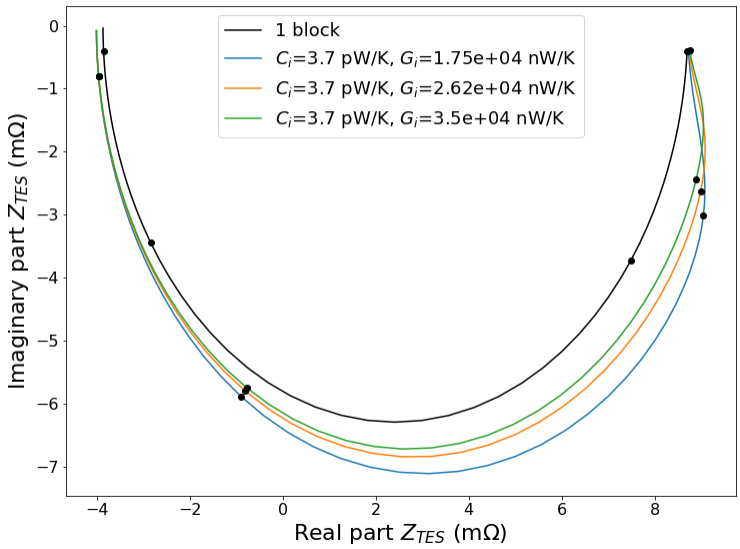

Figure 2.8: Deviations from the best-fit one-block model case according to the hanging-model impedance formula (Eq. 2.23) and values of the new parameters C_i, G_i given in the legend. Solid points indicate frequencies 10, 10^2, 10^3, and 10^4 sweeping from top left to top right. We can see that, up to small (10-20%) deviations from the black curve up to 1 kHz, the definitive feature of the hanging model is the impedance curve moving back towards smaller values on the real axis above 1 kHz.

admittances in the hanging model), we write the following noise vector:

$$\begin{pmatrix} \delta V \\ \delta P_i \\ \delta P \end{pmatrix} \rightarrow \begin{pmatrix} 0 \\ N_{P_{\text{hang}}} \\ N_{P_{\text{link}}} - N_{P_{\text{hang}}} \end{pmatrix} \tag{2.24}$$

where these terms can be thought of as a realization of a noise timestream based on the noise power spectral densities $S_{P_{\text{hang}}}$ and $S_{P_{\text{link}}}$ described above. This vector is then acted upon by M^{-1}_{hang}. Collecting all terms in the first row of the resulting vector, we find a current noise timestream:

$$N_{I_{\text{thermal}}} = (M^{-1}_{\text{hang}})_{1,3} N_{P_{\text{link}}} + \left[(M^{-1}_{\text{hang}})_{1,2} - (M^{-1}_{\text{hang}})_{1,3}\right] N_{P_{\text{hang}}} \tag{2.25}$$

We therefore assume that the absolute square of the factors multiplying $N_{P_{\rm hang}}$ and $N_{P_{\rm link}}$ above will convert $S_{P_{\rm hang}}$ and $S_{P_{\rm link}}$ to their corresponding current noise contributions.

When converting the Johnson voltage noise of the TES and the series load resistance, we follow the same prescription as in the one-block model case. We convert the power fluctuations δP into conjugate forces $\delta P/T$ for both blocks, and divide through by the temperature of the blocks for each term in the second and third rows of $M_{\rm hang}$. We also change the (3,1) component of $M_{\rm hang}$ to the quantity given by Eq. 2.16. This then defines the internal and external impedance matrices. Calculation of the internal and external admittances is identical.

Finally, as in the one-block case, we are able to calculate the noise spectra given a set of input parameters. Figure 2.9 shows the expected contributions of all previous

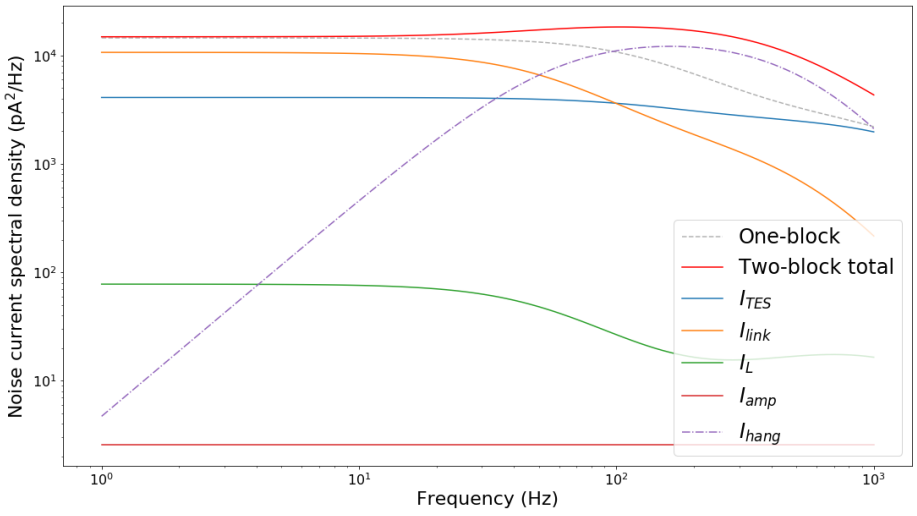

Figure 2.9: Noise contributions to the total current noise in the hanging model of the TES bolometer. All noise sources present in Fig. 2.7 are color-coded as in that figure. The additional noise source, labeled 'I_{hang}', is the pale purple dash-dot line. The previous total current noise for the one-block case is shown in dashed gray. We observe that above ~ 40 Hz, the hanging model predicts an excess of current noise due to the internal thermal conductance. The size of this peak is inversely proportional to G_i.

noise terms, and the additional noise arising from the added thermal link G_i, for one of the parameter cases shown in Fig. 2.8. As described above, those examples feature values of C_i that dominate the sum of the two blocks' heat capacities. This reflects the expected case for the AdvACT bolometers as designed, where the total heat capacity target is tuned using a separate, electrically inert metal film.

We exaggerate the effect of the extra link noise term by making G_i only a factor of 10 larger than G. This is smaller than expected for AdvACT, or in the majority of measurements in [41]. In this reference, an excess heat capacity is placed between the TES and the bath, which differs from the hanging model discussed here. However, for large G_i, they reduce to the same equations [83].

The noise excess is worse for small G_i, despite the noise in power being reduced, due to the coefficient of the power noise in the second term of Eq. 2.25. We expect the actual performance of AdvACT bolometers to lie between this example and the values in the reference.

From the figure, we can see that for this region of parameter space, the hanging model predicts a noise excess caused by the peak of the current noise contribution $S_{I_{\mathrm{hang}}}$. There is also an enhancement of low-frequency Johnson noise as compared to the one-block case due to the differences in the internal admittances for the TES in each model.

To conclude, the effects of a possible hanging heat capacity in the bolometer thermal architecture have been qualitatively described. The presence of such a heat capacity can be observed via impedance measurements at fairly high frequencies, but before the TES bolometer response is rolled off by τ_{el}. Once observed, the distinct kink in the impedance curve can allow us to estimate C_i and G_i and then estimate noise spectra accounting for their presence. The possible excess noise induced by G_i is generally improved for tight coupling (i.e. large G_i), which we may expect given

that the equations for the hanging model exactly reduce to the one-block case for large G_i.

2.5 Conclusion

In this chapter, we have presented an overview of bolometers, and the need for extended electrothermal models in order to fully model the response of bolometers to changing signals. We specifically focused on the parameters and equations describing TES thermistors in order to prepare the reader for the in-depth discussion of the testing and analysis of AdvACT TES bolometers in the coming chapter. However, much of the framework laid out in the preceding pages can be applied to different sensor types; the full equations are still valid assuming we expand a given thermistor's $R(T)$ behavior in terms of α and β. The limits taken to arrive at simple expressions for bolometer response functions like the responsivity are some of the only elements requiring adjustment.

The expressions needed to describe the behavior of a TES bolometer with a second, "hanging" block were reported within the context of measuring their effects on quantities like impedance and noise spectra. Some of the assumptions underlying the hanging block model and their relevance to the actual AdvACT bolometer design have been mentioned; these will be more fully explored in the next chapter.

Chapter 3

AdvACT Detector Testing

In this chapter, we detail the impedance and noise studies performed on AdvACT TES bolometer arrays both in the lab and *in situ* as the focal plane of ACT. Details on the relationship of the AdvACT project to ACT are given in Sec. 1.4.1. We begin by introducing the technologies used in the measurements, and describe the data acquisition methods developed for AdvACT array testing. Our discussion of these acquisitions progresses to providing results for AdvACT array noise. We then turn to an overview of impedance data acquisition and results, and apply these to comparing measured to expected noise spectra over a wide frequency band for impedance data at high excitation frequency. Observed excess noise beyond the simple TES bolometer electrothermal model is observed. Its possible causes are discussed, with the result that the total noise appears to be adequately explained within the context of the hanging electrothermal bolometer model.

3.1 Experimental Setups

In the course of the detector testing to be described in the body of this chapter, we have used a variety of different experimental setups to produce data allowing us to investigate the performance of the AdvACT TES bolometers. The majority of the

tests were performed in the Oxford Instruments Triton 200 [1] dilution refrigerator (DR) at Princeton, backed by a Cryomech PT407 pulse tube[2]. Specialized detector testing was made possible at the Boulder campus of the National Institute for Standards and Technology (hereafter NIST) in a two-stage adiabatic demagnetization refrigerator (ADR) cryostat from High Precision Devices [3]. Finally, the field data to be discussed were acquired with the arrays cooled using a Janis DR designed for the ACTPol experiment [125]. These three cryogenic setups share a common readout architecture known as time-domain multiplexing (TDM) to allow massively-multiplexed readout of hundreds to thousands of TES bolometers. We will shortly discuss in detail the use of this readout scheme as it applies to the detector data under study.

In the sections below, we first describe the array architecture in the AdvACT project, and discuss how the Princeton cryogenic setup allows testing of these high-density bolometer arrays. We will also introduce the state-of-the-art implementation of TDM in use for AdvACT. Subsequent subsections provide brief notes on the other cryogenic systems used to acquire impedance and noise data as discussed later in the chapter.

3.1.1 AdvACT Array Architecture and Laboratory Testing

A single AdvACT array involves many components beyond the silicon wafer on which the bolometers themselves are fabricated. We wish to provide an overview of the components and their conceptual uses in order to simplify more detailed discussion on detector testing below. Detailed description of the assembly protocols and processes may be found in Li et al., 2016 [79]. The assembly of the arrays was undertaken in a collaborative effort by the leading coauthors of that reference, specifically S. Choi, S.P. Ho, Y. Li, and M. Salatino.

[1] https://www.oxinst.com
[2] http://www.cryomech.com
[3] http://www.hpd-online.com

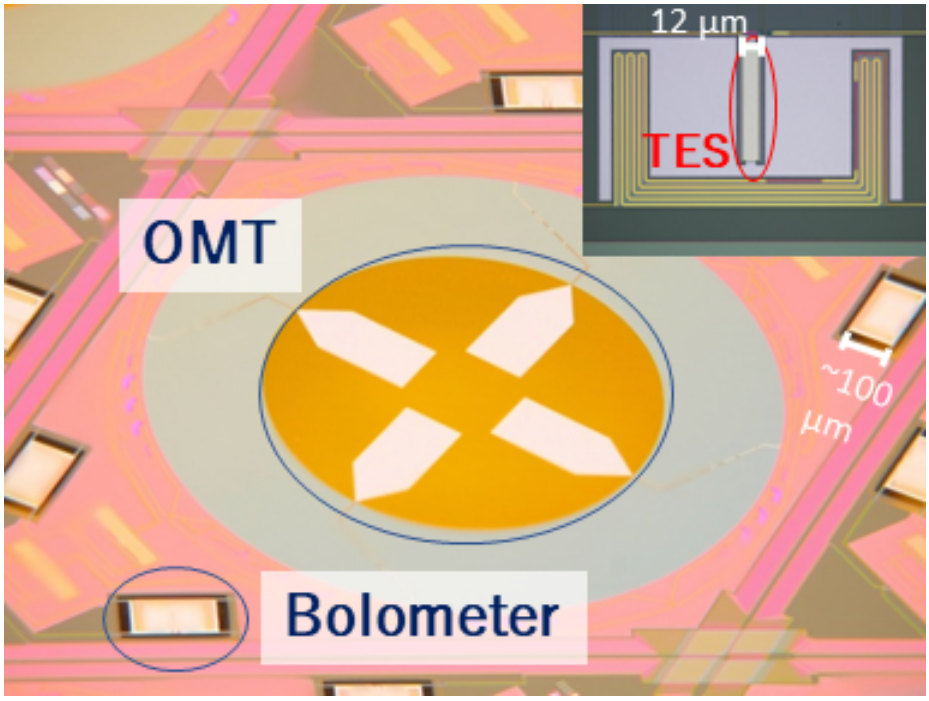

Figure 3.1: Labeled photograph of a single AdvACT pixel within a larger mid-frequency array. The transmission lines can be seen where they attach to the points of the OMT fin. The entire bolometer (circled in blue, bottom left) is suspended from four silicon nitride legs connecting to the bulk silicon wafer. In the inset, a photograph of a bolometer shown, with the 400 nm-thick aluminum manganese TES shown circled in red.

We begin with the silicon "detector wafers." These are fabricated at NIST on 150 mm-diameter silicon wafers [26], allowing more bolometers to be made on a single wafer. This improves array uniformity when measured as the spread in important TES parameters like T_c and $P_{\rm sat}$. It also simplifies assembly, increasing the final yield (often expressed as a percentage) of working detector channels to fabricated channels.

This detector wafer consists of pixels in which four TES bolometers (two polarization pairs sensitive to two distinct millimeter bands) are coupled to the polarization-defining fins of the orthomode transducers (OMTs) that are illuminated by the feedhorns. Each bolometer may be thought of as a silicon "island" suspended on a silicon nitride membrane and connected to the rest of the wafer by four silicon nitride "legs"

that sit at each corner of the rectangular island. Two of these legs carry the bias voltage leads to the TES, and two carry the filtered microwave signals onto the island, where they are dissipated in a lossy gold meander. The leg cross-sectional area and length determine the conductance G between the island and the bath. The TES itself is an AlMn film deposted on top of niobium electrodes, which apply the bias voltage to the superconducting film. Details of the process used to ensure repeatable, precise control of the TES critical temperature T_c and normal resistance $R_{\rm N}$ can be found in [78]. Finally, a separate, normal metal film of PdAu is deposited on the island not covered by the Au meander and the TES. By controlling the thickness and surface area (i.e. the total volume) of this PdAu film, it is possible to tune the heat capacity C of the island when it is viewed as a single thermal block. We will interrogate this assumption using the impedance and noise data of subsequent sections. In Tab. 3.1, we provide details on the leg dimensions and PdAu volume used, in the fabrication design, to target the listed G and C values, for all bolometer channels in the AdvACT arrays. By bolometer "channel" we here mean the frequency band as identified by nominal center frequency in simulations of the pixel microwave filters.

An example pixel, with components identified by text, can be seen in Fig. 3.1. The long dimension of the bolometer is $\sim 100\mu$m, and the entire pixel is approxi-

Array	Center Freq (GHz)	$P_{\rm sat}$ (pW)	Leg Width (μm)	Leg Length (μm)	G (pW/K)	PdAu Volume (μm^3)	C (pJ/K)
HF	150 GHz	12.5	24	61	292	3.61×10^4	3.5
HF	230 GHz	25	48	61	585	6.08×10^4	5.4
MF	90 GHz	11.3	24	61	264	2.15×10^4	2.4
MF	150 GHz	12.5	21.6	61	292	3.61×10^4	3.5
LF	27 GHz	7.8	12.1	61	182	2.74×10^4	2.9
LF	39 GHz	1.5	10	628	35.1	0	0.6

Table 3.1: Summary of bolometer island parameters (SiN leg dimensions, PdAu volume) and their targeted design bolometer parameters $P_{\rm sat}$, G, and C. On all islands, an AlMn film defines the TES and is a base layer on the island above the Nb electrodes. A film of PdAu is added on top of the AlMn film to provide heat capacity. For all bands except the LF 27 GHz, this AlMn film is expected to contribute 0.8 pJ/K to the total heat capacity (rightmost column). For LF 27 GHz channel, the contribution is 0.6 pJ/K due to decreased surface area of the AlMn. This matches the reduced G target for this channel, which is not strongly loaded by the atmosphere.

mately 5 mm between the furthest-separated pair of vertices of the rhombus in which its components are located. The TES is the narrow bar extending along the short dimension of the island. Its width is 12 μm, and its width and length are in a 1:8 ratio. The TES aspect ratio is used to set R_{N}.

The detector wafer is then added into a "wafer stack" by aligning and gluing together the following additional wafers:

- The waveguide-interface plate (WIP), which is the furthest-skyward component of the stack, and promotes good alignment and mechanical spacing between the OMTs in the detector wafer and the waveguide section of the feedhorns;

- The detector wafer, containing the bolometers and OMTs (both suspended on silicon nitride membranes), the microwave transmission circuitry and filters, and the electrical leads for biasing the sensors;

- The backshort cavity, a spacing wafer providing quarter-wavelength separation between the OMT plane and the terminating backshort, with individual apertures cut for each pixel;

- The backshort cap, a wafer with a thin niobium film acting as the backshort. All wafers except the detector wafer are gold coated for improved heat transfer through the silicon and then epoxied together. The exposed perimeter of the non-sky side of the detector wafer is bare silicon, with defined wire bond pads used to connect individual detector bias circuitry in the wafer to external cryo-electronic components.

These additional electronic components define both the readout and TES bias circuitry. Before describing them, we outline the main features of the readout system used in AdvACT arrays, TDM. Details of the design and performance of the overall readout system may be found in [51].

Broadly construed, TDM divides the number N of TES bolometers in an array into an architecture of P columns and R rows. Columns are read out in parallel, and rows are read sequentially. At any one time, only one row in each column is being sampled. This setup reduces the number of cryogenic wires needed to record TES electrical signals from $2N$ to $\sim 4P + 2R$. The additional factor of 2 multiplying P is due to the presence of both bias and feedback lines defined for each column.

The reason for the feedback lines is that the ultimate subunit of the readout is a superconducting quantum interference device (SQUID). Formed from a pair of Josephson junctions oriented in a loop, the dc-SQUID forms a flux-to-voltage transducer with controllable gain. Viewed from the TES bolometer side, the SQUID senses changes in the TES current δI as changes in the flux passing through the loop due to a coupling inductance generating a $\delta\phi$ for the given δI. The SQUID response to such a change in inductance is some δV. For small signals, we thus assume that $\delta V \propto \delta I$. However, the full $V(\phi)$ curve of a SQUID is periodic, as we will see in Sec. 3.2. So, in order to maintain linearity, a compensating feedback flux is applied to the SQUID using a feedback current signal $\delta I_{\rm fb}$. This value becomes the signal, which is recorded by the warm electronics used in AdvACT. Its relation to δI, the original signal at the TES, is:

$$\delta I_{\rm fb} = -M_{\rm rat}\delta I, \tag{3.1}$$

where $M_{\rm rat}$ stands for the ratio of the TES-to-SQUID mutual inductance, which determines the flux signal applied by TES current changes, to the feedback-to-SQUID mutual inductance. We assume $M_{\rm rat} = 24.3$ throughout this work for AdvACT array studies. Thought of in this way, the voltage signal produced by a given channel's SQUID is the error signal in a flux-locked feedback loop on the SQUID.

To implement this flux-locked loop, as well as provide the TES bolometers the appropriate bias voltages, multiple component chips fabricated in silicon must be included in the array. In AdvACT, they include the following:

- silicon wiring chips with niobium circuitry, which route readout and bias signals appropriately from wirebond pads to other silicon subcomponents;
- interface chips containing: fabricated shunt resistors (i.e. in parallel with the TES) to provide bias voltages, and multiple inductors to define the TES electrical bandwidth, with one shunt resistor and inductor for each TES channel;
- multiplexing (mux) chips containing: coupling inductances between the TES electrical circuit and its SQUID, bias and feedback circuitry circuitry for the SQUIDs in a column, and flux-activated switches (FAS) [136] used to define row-switching in the multiplexing scheme.

After being fabricated at NIST, these cold multiplexing components were tested by collaborators at Cornell, who also developed much of the tuning protocol discussed in Sec. 3.2.

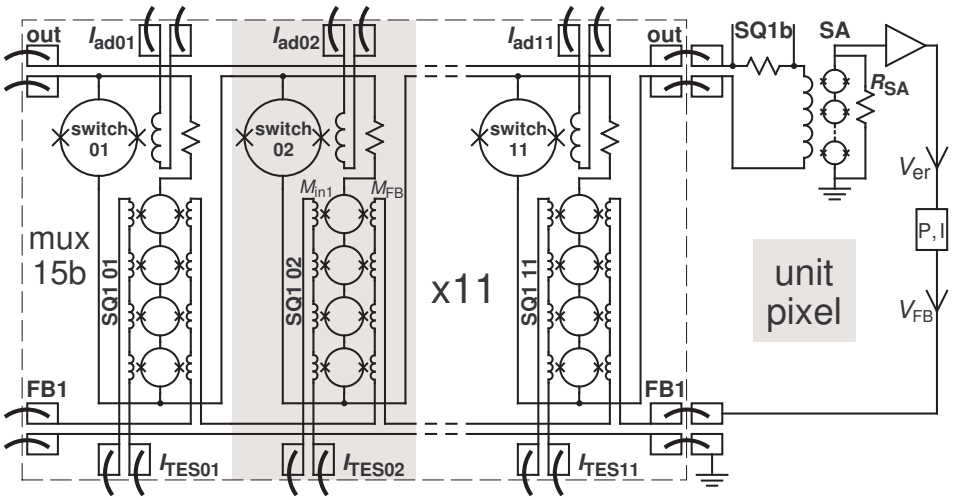

Figure 3.2: Mux15b electrical schematic showing how detector current signals (lines marked I_{TES} along the bottom) couple into the readout architecture of rows (addressing currents, or "I_{ad}" here, which are routed to all columns) and columns (the horizontal axis with defined SQUID bias (SQ1b) and feedback (SQ1) lines). This figure shows a few rows for a single column. Modeled on Fig. 2 from [24], with help and permission of W.B. Doriese.

The final component of the list, the mux chip, is usually identified by a name defining a particular implementation of the SQUID amplifier-based TDM architecture. Specifically for AdvACT arrays, as well as for other experiments using TDM in the field, an architecture known as mux15b is used [24] [1]. The readout circuitry schematic shown in Fig.3.2 presents the main features of this architecture. An array of SQUIDs chained in series forms the first stage of amplification, known as SQ1, which provides the initial error signal from its coupling to the TES current. Additional amplification is provided by a SQUID series array (SA) at warmer cryogenic stages before the SQUID error signal is read out, processed, and converted to an appropriate feedback value, which is recorded as the experimental signal.

With regard to TDM row-switching, a particular row in the column shown in Fig. 3.2 is activated by a current applied through the row addressing ("ad") lines. When no flux is applied, the FAS is closed and the switch superconducting, so all current shunts through the FAS and the SQ1 array is unbiased. However, applying sufficient flux to the FAS via the coupling inductor in the addressing line drives the FAS to a large ($\sim$100 Ω) resistance, at which point current passes through the SQ1 array.

We summarize the overall design of the interface chip in Fig. 3.3. Individual shunt resistors for 22 channels are defined on each chip, as are multiple inductances for each channel which can be selected by the experimenter at the time when she places the aluminum wirebonds used to couple circuitry among discrete silicon chips.

We conclude by describing how all of these components fit together to read out an AdvACT array. A photograph of a completely assembled array is shown in Fig. 3.4, with the central wafer stack resting on the unseen feedhorn array. Beginning at the wafer stack, aluminum wirebonds connect niobium pads at the edge of the detector wafer to aluminum pads on custom-made flexible circuitry, called "flex." The latter consists of aluminum traces terminating in bond pads at either end, and fabricated on polyimide film to provide elastic mechanical coupling between the silicon array and

other parts [98]. The flex mounts to a copper-trace printed-circuit board (PCB) that surrounds the central detector wafer and is mounted to a gold-plated copper support ring. Detector signals leave the flex to a wiring chip glued to the PCB using rubber

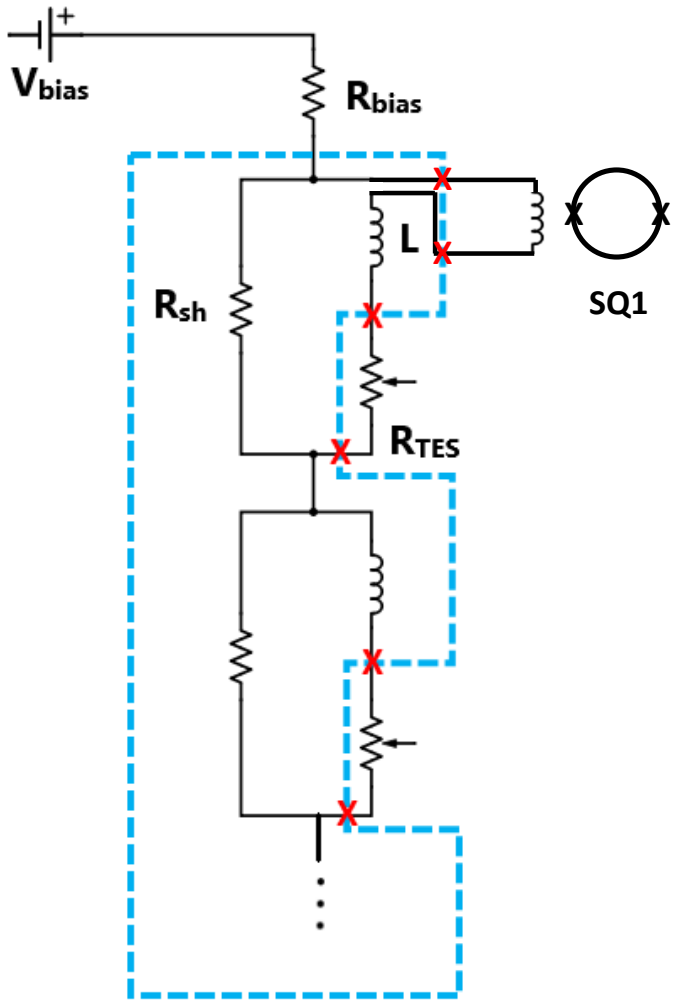

Figure 3.3: Schematic of the bias circuit as fabricated in the AdvACT array interface chips. A voltage V_{bias} is passed across a resistor (R_{bias}) of $\sim 200\ \Omega$. These components in the MCE effectively apply a current bias to the TES channels, which are in series with one another. At least 24 bolometers, and up to 110, share a single bias line depending on the array. A single channel includes the shunt resistor R_{sh}, the inductor L, and the TES itself. Wirebonds are shown with a red X, and the components on an interface chip are inside the dashed border. We indicate the SQUID coupling to the TES bias circuit for the first TES in the bias line.

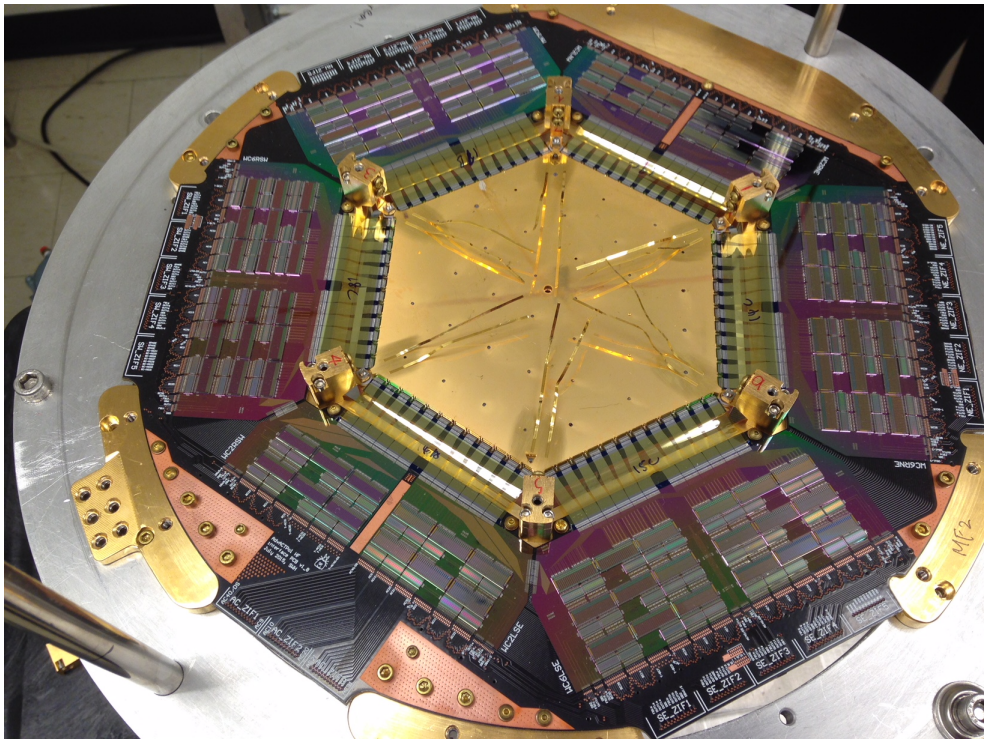

Figure 3.4: The completely assembled cold components of the second mid-frequency array for AdvACT. The central hexagon is the detector wafer stack, with flex attached to each side. These extend outward to the PCB, on which are mounted the wiring chips populated with smaller interface and multiplexing chips.

cement. This wiring chip, as described above, provides the appropriate routing for these detector signals, as well as TES bias signals and all SQUID signals, to discrete mux and interface chips. These smaller chips are stycasted to the wiring chips before bonding proceeds. Additionally, we consider that wiring chips provide a layer of modularity above the PCB, which contains signal traces for all of the lines running from cryogenic stages to room temperature, known as "critical lines" since multiple TES bolometers share each of them.

At the output of the PCB, all critical lines are routed, via ancillary PCBs, to soldered MDM connectors. These connectors interface the complete array package [131] with the warm-stage electronics via NbTi woven-loom cables from Tekdata [4]. The warm-stage electronics are known as Multi-Channel Electronics (MCE) [5]; through

[4]https://www.tekdata-interconnect.com

this system the user controls all critical line bias values while feedback values are recorded and the row switching is performed. We also use the MCE to generate the sine-wave bias signals used for impedance measurements, as discussed in Sec. 3.4.

This description applies to readout of entire AdvACT arrays in both the Princeton laboratory and field cryostats. In the laboratory specifically, we couple the array package (feedhorn array, wafer stack, PCB, and all silicon chips) to the mixing chamber of the DR. This is done via a copper interface plate and mounting brackets that allow us to mechanically suspend the array from the mixing chamber [11]. One additional component, a metal-mesh millimeter low-pass filter, is mounted in front of the sky-side horn aperture to cut any out-of-band radiation.

The DR provides adequate cooling power to allow the array to reach base temperatures of ~ 30 mK. During measurements, we perform proportion-integral-derivative (PID) feedback control to keep the array temperature typically between 100 and 150 mK. In addition to the array, a cryogenic blackbody is suspended from the 4 K stage of the DR. It is used to illuminate one-third of the feedhorns (and thus pixels) of the array for optical tests [12], while the remaining bolometers are assumed to have negligible millimeter-wave loading. On the outside of the cryostat, a cylindrical μ-metal magnetic shield with high aspect ratio (cylinder height to opening diameter) is lifted into place around the outer vacuum jacket of the DR.

3.1.2 NIST Laboratory Tests

When performing TES bolometer testing at NIST in order to achieve high sinusoid input frequencies for impedance studies, many aspects of the above description are simplified. A single PCB supports individual wiring chips, interface and multiplexing chips, and separate silicon die with the devices to be studied. All of these components are rubber-cemented to the board, and connected via wirebonds to provide the appropriate signal routing. This compact package is then mounted to a rod in the adi-

abatic demagnetization refrigerator (ADR) that provides the cooling energy at base temperature. We note that the mux chips used in this package are not mux15b, but a previous generation known as mux11c. This architecture features two cold SQUID amplifier stages before the SA, and row switching is provided not by a shunting FAS but by directly applying bias voltage to SQ1s one at a time. A different M_{rat} is also defined [107]. This technology is identical to that used in previous generations of ACT focal planes, as in [46] [99].

In the NIST ADR used for these measurements, the use of strong magnetic fields in the thermal cycling process has led to two cryogenic shields being placed around the TES bolometer package. The inner shield is a μ-metal shield in two clamshell halves that are bolted together around the detector. The outer shield is niobium, also constructed in two pieces to allow access. Both are cooled to 4 K by the cold stage of a Cryomech PT407 pulse tube. We provide a photograph of the setup before the mounting of the lower halves of both shields in Fig. 3.5.

In this case, soldered MDMs are mounted on the single PCB, and TekEtch cable looms exit the magnetic shielding through small (2 cm by 0.5 cm) gaps in the mounted magnetic shields. These cables then reach a PCB at 4 K that connects them to the SQUID SA amplifiers, before the signals exit the cryostat and connect to the warm electronics. The control electronics here are not the MCE but a distinct set of daughterboards implementing TDM readout [107]. However, nearly all of the details to come on SQUID tuning, TES biasing, etc. applies equally well to both the MCE and the NIST readout electronics.

We tested two types of TES bolometers at NIST. The first kind are "single pixels," standalone versions of the pixels making up AdvACT arrays and featuring identical OMTs, microwave circuits, etc. Such pixels also generally include a dark TES bolometer, not connected to microwave circuits, and a heater resistor for providing thermal signals to the TES bolometer substrate. The second, known as "TES test die," fea-

ture only bolometers and their corresponding bias lines, as well as a heater resistor. These test die contain multiple distinct TES designs, and can be used to determine the effects of design choices on bolometer performance.

3.1.3 AdvACT Field Tests

When the AdvACT arrays are placed in the focal plane of the telescope, they are individually mounted to a fiberglass (G10) support within a module called an "optics tube." The defining elements of an optics tube are the vacuum window, metal-mesh infrared-blocking and low-pass edge-defining filters, the silicon lenses, cylindrical magnetic shields surrounding each array, and the array mounted to a wedge-shaped mount in order to accurately position it with regard to optical components. Each array couples to the mixing chamber of the field DR via a cold strap mounted to a tab on the

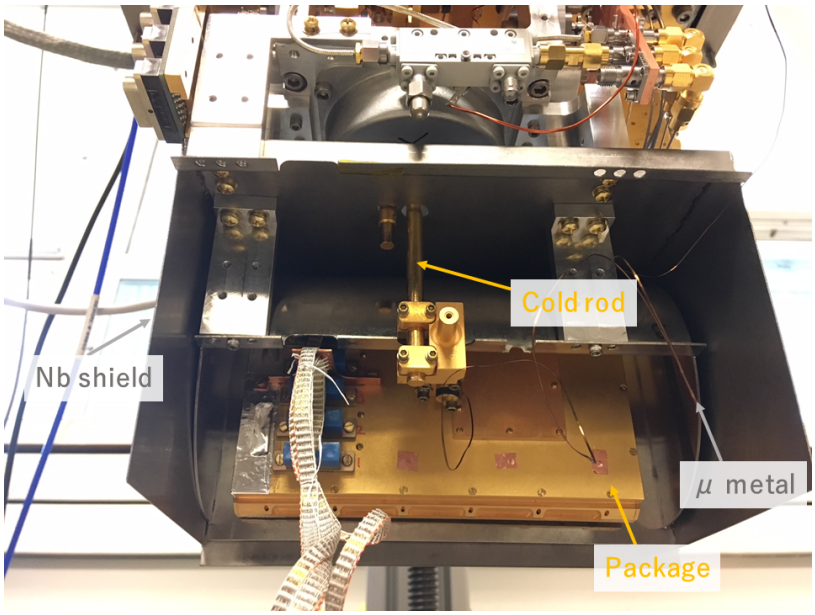

Figure 3.5: Partially-assembled cryogenic setup for NIST laboratory tests. The gold-plated copper package is visible extending below the top half of the μ-metal shield. It attaches, via the square bracket in the center of the image, to a 1 cm-diameter rod that is the ADR system's coldest stage. These components are then surrounded by the open, upper half of the superconducting niobium magnetic shield. The magnet is above this suspended assembly.

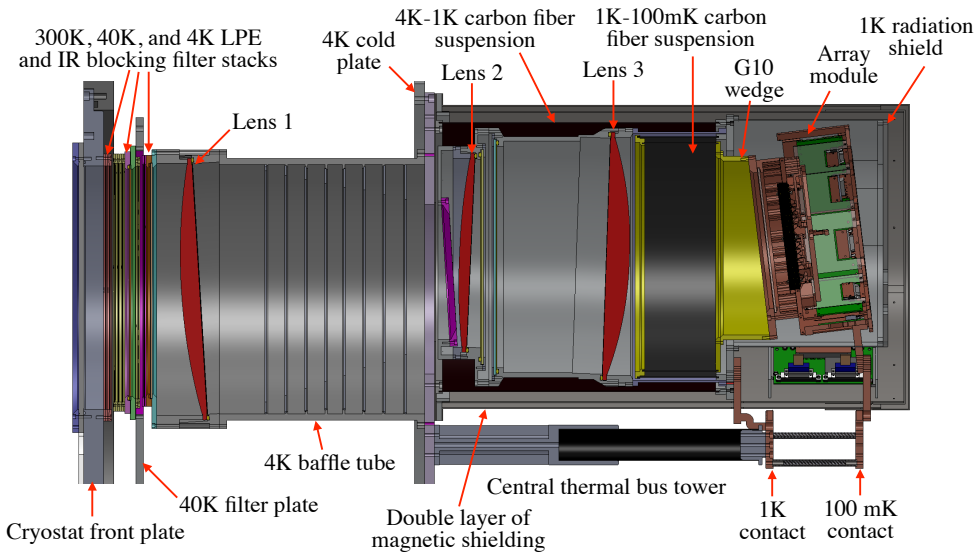

Figure 3.6: Labeled components of an optics tube loaded with an ACTPol array. This schematic drawing is reproduced from Thornton et al., 2016 [125] with permission from the author.

array [125]. Figure 3.6 shows a cutaway drawing of a tube with an assembled ACTPol array in place from Thornton et al., 2016 [125].

We mention these components only to record that the presence of the ambient-temperature window and the cryogenic optics within each tube causes millimeter-wave loading not present in the Princeton laboratory setup. This can be observed even when the arrays are rendered "dark" by covers over the vacuum windows. For the *in situ* tests of the high-frequency array, these covers were aluminum plates with disks of mylar-laminated insulator (MLI) loosely attached to the surface looking in to the DR. This combination should minimize the loading induced by the other elements within the optics tube, but a significant optical power ($\sim>$ 5 pW for150 GHz channels) was recorded during these tests.

3.2 AdvACT Array Data Acquisition

In this section, we discuss the kinds of data acquired for AdvACT array laboratory testing, and the methods used for acquiring them. We also provide results on noise data acquired as part of the chaarcterization routines described below. In some cases, more or less detail on acquisition may be found in the Appendices, especially Appendix A for detailed information on the scripts used to acquire impedance data through the MCE. Specific descriptions of acquisition methods applying to other setups will be discussed in the appropriate sections that follow.

3.2.1 SQUID Tuning and I-V Curves

In the mux11d implementation of TDM, tuning an array of SQUIDs to read out TES bolometers begins by acquiring open-loop $V(\phi)$ response curves for the SA, the warmest SQUID amplifiers. The goal is to maximize the amplitude of the SA curve as a function of the applied bias to the SA. Using automated scripts written for the MCE [5], we perform a sweep of SA bias values and record the optimum bias for subsequent tuning.

With the SA SQUIDs biased, we send a signal into each column sufficient to bias the SQ1 amplifiers. Using the SA feedback loop to keep the output linear, we drive current into the row addressing lines, thus driving flux into the FAS. We record the values of the row bias signal at the minimum and maximum value of the SA feedback. The median of these values across the columns becomes the "row-select" and "row-deselect" values used to drive each row, as in Fig. 3.2 [51].

We now proceed to driving current through the SQ1 feedback lines, while keeping the SA SQUIDs at their lockpoints using the SA feedback. By plotting SA feedback vs. SQ1 feedback, we can optimize the SQ1 response (i.e. maximize the SQ1 $V(\phi)$ curves) independently of the SA response. However, our final operating mode is to

operate on the open-loop output of the SA, the error signal, in order to determine the appropriate SA feedback to keep the SQ1 locked. Thus, the final amplifier gains and readout configuration are best estimated by recording the open-loop signal generated by ramping current through the SQ1 feedback circuit. This is the final component of the SQUID tuning. Numbers relevant for performing the row switching, SQUID biasing, and feedback calculations are all automatically stored in an experimental configuration file read by the MCE.

As a first check of the detectors,we additionally ramp current through the TES bias lines at the end of the automated SQUID tuning. We do so while recording the open-loop error signal through the SQ1 and SA. Using these data, we can identify any issues affecting single detectors (i.e. broken bonds somewhere between the input coil to the SQUID on the mux chips and the detector wafer).

Channels with no response to the TES bias line ramp then have open SQUID inputs, and are known as dark SQUIDs. To be very conservative, we have added such channels to "dead lists," which are used to specify channels for which the MCE should not apply feedback. This is because channels that are not dead-listed can result in large, erroneous values of feedback being sent in by the MCE. This latter scenario would induce leakage as the MCE switches to subsequent rows. Other channels in the dead lists include SQUIDs that cannot be biased or addressed by feedback; these latter are almost always due to failures of critical line bonds, and thus come in groups of tens to hundreds.

Persistence. A second, and pernicious, failure mode involves the FAS in the array readout circuitry being always normal. This induces so-called "persistence" in the column that the FAS occupies. Since the FAS is never in its superconducting state, SQ1 bias current is always shunted to the SQ1 in parallel to the affected FAS. This row then persists through all row switches, and its signals affect the readout of every row in such a column. We expect that such issues are usually caused by magnetic

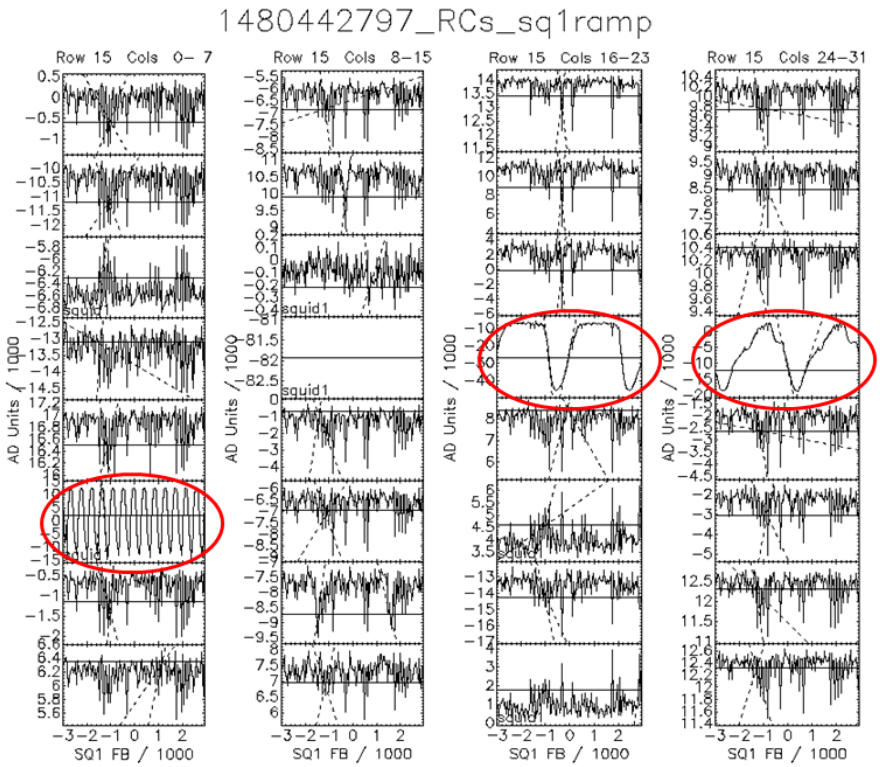

Figure 3.7: A tuning plot produced by MCE control software in a configuration where all panels should be noise. Each panel represents the open-loop response of the SQ1 at row 15 of each of the 32 columns in MF1 while ramping the SQ1 feedback with no flux applied to the FAS. The red ovals indicate the three persistent columns that were present at the time of this test. The noise in the other panel is nominal. SQUIDs with perfectly zero response are connected to columns with open critical lines. Dashed lines in the plot would normally indicate the slope of the error signal at the lock point, a proxy for gain through the entire readout chain. The periods vary among the persistent columns, indicating different states (e.g., possibly superconducting for the short period) of the TES coupled to the problem channel.

flux trapped in the FAS when it is cooled through its transition (for niobium, this is $\sim$ 7 K). However, fabrication failures or handling damage which disconnect an FAS from its SQ1 would produce the same effect.

Persistence in the AdvACT arrays is tested for taking a special set of tuning data, in which the open-loop measurement of ramping current through the SQ1 feedback lines is performed with all rows set to be always off. We do this by setting the row-select value to the row-deselect value, which we expect will cause no signal to be read

at the SA output. If we see any $V(\phi)$-like behavior, we label the column persistent; the severity of the effect is qualitatively proportional to the amplitude of the response. We do not always dead list these columns, though we note them and can attempt to repair the column by replacing a mux chip containing a persistence candidate with another. An example of a dataset in which three persistent columns appear can be seen in Fig. 3.7.

Finally, as discussed in Sec. 2.4, I-V curves are used to study important characteristics of the TES bolometers. These include measurements of $R_{\rm N}$ and $P_{\rm sat}$ across the array. We work to achieve minimal scatter in values of the former across detectors in both bands, while the latter should be tightly distributed within each band. Importantly, analysis of I-V curves requires calibration into physical units. Resistances in the system, constants of the MCE readout hardware, and other relevant parameters are all inputs to these measurements.

System resistances are measured using a specialized card that can allows an external probe to connect pins in the MCE and measure the resistance. Unchanging resistance values in the MCE cards and backplane are taken as given based on known surface-mount components and models and measurements of previous mux chips. However, one crucial parameter, $R_{\rm sh}$, cannot be measured directly by probing. Tests performed prior to the array assembly record typical values of $\sim 200\ \mu\Omega$. This per-channel number thus forms the largest uncertainty in our estimates of $P_{\rm bias}$, $R_{\rm N}$, and other parameters. A brief description of how we estimate these values in AdvACT studies is given in Sec. 3.3.

When acquiring I-V curves, we must account for the fact that the feedback values in the MCE record only relative changes in current at the TES. An overall current offset is thus accounted for when converting to physical units (which are generally linear transformations) by fitting a slope to the normal part of an I-V curve, extrap-

olating this to zero bias voltage, and removing the offset. Previous reports on ACT [137] and ACTPol [46] [99] describe this method in more detail.

We proceed now to describing how we acquire I-V curves, as well as other critical characterization data, at various bath temperatures.

3.2.2 Bath Temperature Ramp Data

In order to stably control the bath temperature and move between temperature setpoints in the laboratory, we use a Lakeshore AC370 [5] readout and control box. This device features multiple readout channels, each using an AC resistance bridge for accurate measurement of the $\sim$ kΩ resistances of ruthenium oxide (ROx) thermometers at the coldest stages of the DR. These thermometers have been calibrated from resistance to temperature using measurements during a common cooldown with a pre-calibrated thermometer at Cornell.

At each bath temperature, we acquire the following datasets:

- I-V curves, in order to recover $P_{\rm sat}$ and measure T_c and G from fits to $P_{\rm sat}$ vs $T_{\rm bath}$ (see Eq. 2.5);
- bias step data, in order to measure $f_{\rm 3dB,eff}$ at various $P_{\rm bias}$ and fit these data to Eq. 2.14;
- DC-biased noise data, in order to determine noise current densities and estimated NEP for all active bolometers.

For the last two items, it is also important to acquire data across the transition. In laboratory testing of AdvACT arrays, we study devices at steps between $0.2R_{\rm N}$ and $0.7R_{\rm N}$, which represents the approximate spread in achieved TES resistance when we bias detectors in the field.

[5] https://www.lakeshore.com

We write a master script to perform the acquisition by first taking an I-V curve, then subsequently analyzing the output to optimize bias values for each bias line based on the data from bolometers that share it. In the HF arrays, up to 110 bolometers can share a bias line. These numbers fall to up to 99 bolometers per bias line for the MF array, and 25 bolometers per bias line for LF. Choosing the best bias involves taking the median of the bias value (in digital-analog converter, or DAC, units) for which each bolometer is closest to the target fractional R_{N}. We use this method to define bias points for multiple % R_{N} targets and record them in separate output files.

Array Heating During testing of the HF array, we found that taking I-V curves for all bias lines at once produced a heating spike of $\sim$ 5mK. This would produce large systematics in our assumed T_{bath} values when fitting out the parameters T_c and G. In order to reduce this, we chose to perform the I-V curve acquisition within a single "quadrant" of the HF and MF arrays. The quadrants are defined as groups of eight columns, contiguous in the MCE readout space, which share MDM cabling and connectors in the completed array assemblies. There are six bias lines per quadrant in the HF and MF arrays. With this method, we reduced the transient heating during I-V acquisition to $\lesssim$ 2 mK. In the field, conversely, we elected to run full-array I-V acquisitions, and instead tune the high-voltage range of the I-V curve to the minimum possible voltage for which we can still recover unbiased estimates for R_{N} and apply the offset correction of the I-V data described above.

We finally use the biases selected for each quadrant to bias the entire array, being careful to drive all detectors normal using high bias voltage applied to the bias line input. This has the effect of applying a current $I > I_c$, the critical current of the TESes. Fig. 3.8 shows the distributions of P_{bias} and fraction of R_{N} across the dark detectors in the second MF array (MF2) based on I-V data taken during a bath temperature ramp. We targeted 130 mK for the bath temperature during this I-V

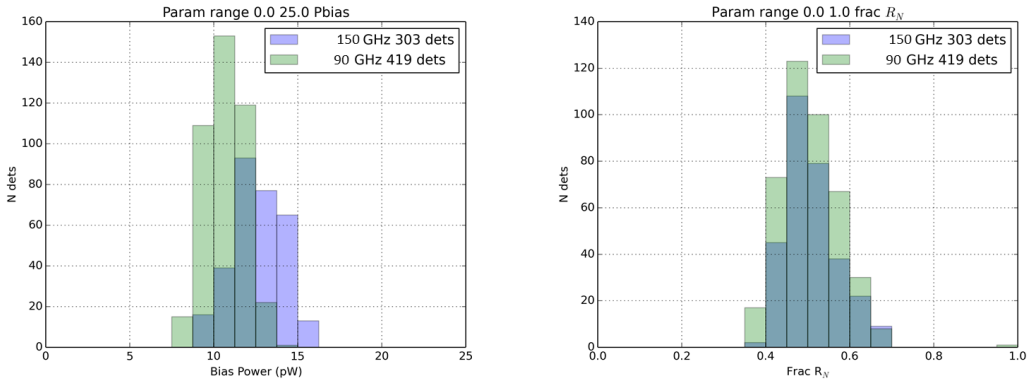

Figure 3.8: Results for bias powers (left) and fraction of R_{N} achieved (right) for an IV taken with $T_{\mathrm{bath}} = 130$ mK on MF2. Only bolometers that do not see the cold load are shown, where the maximum number of such dark bolometers per frequency band is 572. This T_{bath} approximates the loading we expect for MF2 bolometers in the field. The AdvACT bolometer design targets values of $R_{\mathrm{N}} = 8$ mΩ and P_{bias}, which in this case is approximately P_{sat}, of 11.3 and 12.5 pW for 90 GHz and 150 GHz bolometers, respectively. The ranges indicated span either the physical (fraction of R_{N} between 0 and 1) or are sufficiently large to avoid cutting any functioning detectors.

curve acquisition. The ∼2 mK transient heating signal can affect the measurement of P_{bias}, adding variance to the distribution.

When ramping the bath temperature, we span a nominal range of temperatures from 70 mK to 150 mK, usually progressing in steps of 10 mK. Based on our target T_c and P_{sat} values and the expected millimeter-wave loading in the telescope, the temperatures of most interest to us for bias step and noise studies are 100 - 130 mK. Bath temperatures higher than 100 mK, the nominal array temperature during observations, approximate the conditions of loading from the atmosphere and optics tube emissions by reducing the $P_{\mathrm{bias}} \sim P_{\mathrm{sat}}$ values in our laboratory setup.

For noise measurements, our data are obtained by acquiring some number of samples through the MCE after the detectors have been biased. Special, fast-sampled noise on individual detectors was acquired separately, as part of the impedance software suite, and will be discussed further in Appendix A.

3.3 Dark Noise in the AdvACT Arrays

As measured, noise data are recorded as feedback values applied by the MCE for individual bolometers identified by their column and row within the "readout array." Analysis of these data must begin by calibrating them into physical units.

First, the feedback voltage applied in DAC units is converted to volts using our knowledge of the number of bits and maximum voltage for the DAC. We then use the measured resistance of the feedback loop, very close to constant across columns, to convert $V_{\rm fb}$ to $I_{\rm fb}$. This number is ~ 2 kΩ due to bias resistors within the MCE circuitry. Finally, we use Eq. 3.1 to estimate the current fluctuations at the TES.

If we want to convert our measurements to TES voltage or power, we must calculate the bias voltage V on the TES. We do so by assuming the following equation:

$$V = \left(\frac{V_{\rm bias}}{R_{\rm bias}} - I_{\rm TES} \right) R_{\rm sh}, \tag{3.2}$$

where $V_{\rm bias}$ has been converted from the bias DAC value recorded by the MCE, $R_{\rm bias}$ is measured at DC through the bias line and is usually $\sim 200\Omega$, and $R_{\rm sh}$ is an estimated shunt resistance on the interface chip. The parameter $R_{\rm sh}$ is not directly measurable in the fully-assembled array. In separate cooldowns at Cornell, we estimate a per-channel $R_{\rm sh}$, normally about 200 ± 20 $\mu\Omega$ across groups of multiple interface chips by measuring the series resistance of ~ 100 shunt resistors and assigning the average value to all shunt resistors in the group of interface chips. These values are logged and properly assigned to TES channels once the interface chips have been fully assembled in the array.

With the voltage estimated at the TES this way, we assume that the power at the TES is then simply $V \times I$. However, this neglects the internal electrothermal behavior of the TES. We note that, due to the different sizes of the feedback and bias resistances, the latter requires more accuracy when we wish to calibrate TES

signal into units of power. At the same time, details of the bias circuit do not enter our estimates of current noise. We thus generally prefer to compare expected to measured current noise in some of the more detailed noise studies to be described below. However, the more relevant parameter for determining dark array sensitivity relative to photon-induced noise is NEP.

Our results for dark NEP of the HF array come from tests performed *in situ* on the telescope. We did not use laboratory data due partially to early drafts of the bath temperature acquisition code not properly performing the detector biasing scheme, and partially to evidence for excessive pickup in the lab. In the magnetically-shielded optics tube of the telescope, and with aluminum covers over the windows, we anticipated some minimal amount of optical loading P_γ. However, the observed shift in $P_{\rm bias}$ values between the laboratory and the field indicate considerable P_γ in the configuration. Nevertheless, we gathered data as in the lab while ramping the bath temperature, with the exception that there was no PID control loop to regulate the bath temperature during the acquisition.

In Fig. 3.9, we give a range example detector power spectral densities for a single detector in the top panel and summarize our results for NEP, measured in a 2 Hz band (10 Hz $\pm$ 1 Hz) in the array in the bottom panel. The rolloff near $\sim$ 115 Hz is the effect of an antialiasing filter applied to AdvACT data when the $\sim$ 10 kHz readout rate is reduced to $\sim$ 400 Hz in order not to exceed the maximum data transfer and storage rate of the MCE hardware. All of these power spectral densities are estimated using the "welch" function of the scipy scientific-computng package[6]. This function implements the Welch periodogram method of spectral density estimation [134]. It defines segments of a specified length from the input timestream with 50% overlap between segments, applying a Hanning window function, estimating the spectral den-

[6]http://www.scipy.org

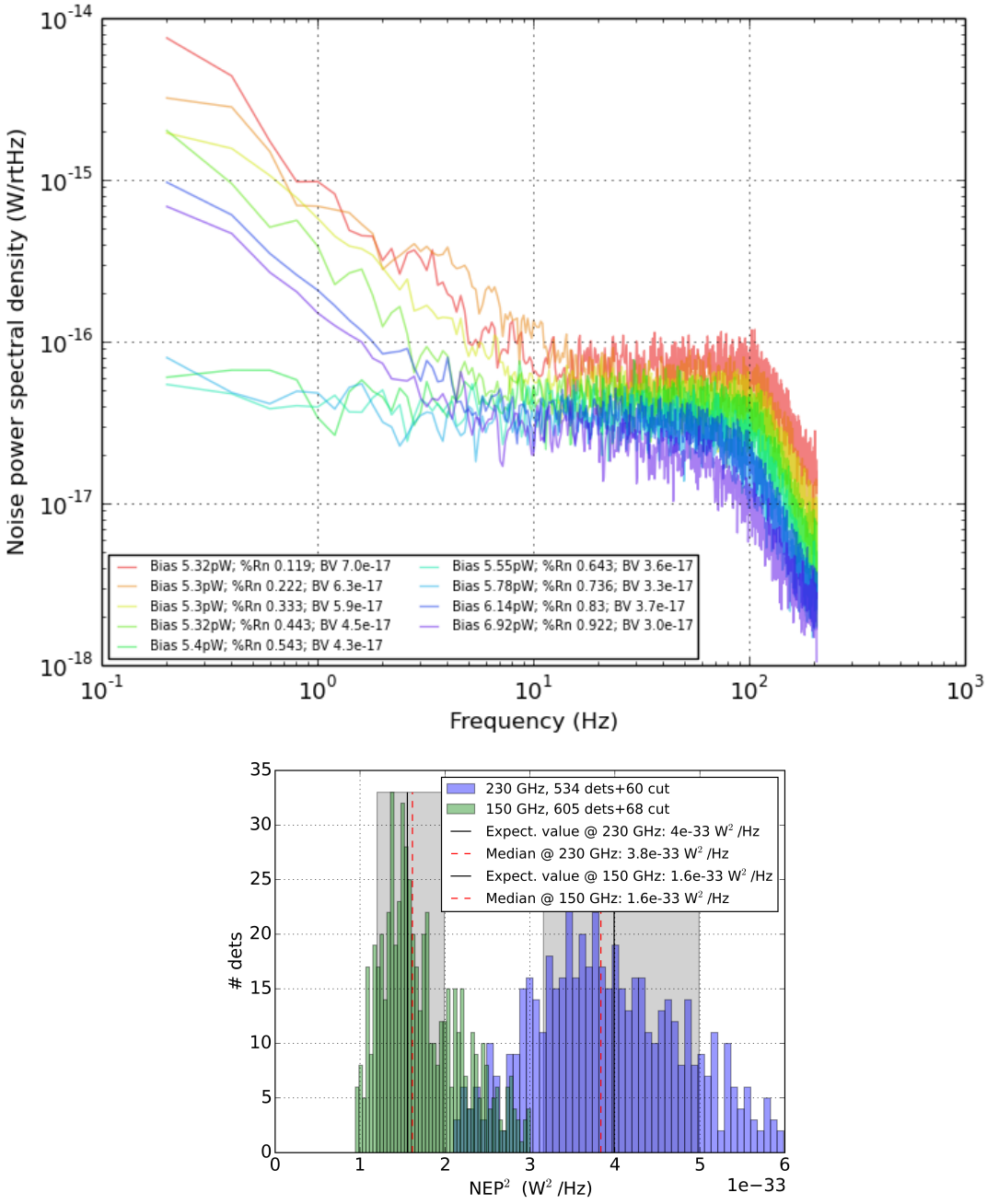

Figure 3.9: *Top*: Example noise power spectral densities (NEP) for a bolometer in the HF array throughout the TES transition and measured on ACT at 120 mK. See text for discussion of trend of increasing NEP with decreasing TES resistance. *Bottom*: Distribution of NEP for bolometers in the HF array as measured on the telescope. The two distributions are blue (230 GHz) and green (150 GHz). The width of the gray band represents systematic errors in the estimation of P_γ due primarily to a possible 5 mK bath temperature miscalibration between the laboratory and the telescope. In addition, the band includes the effect of 5 mK of heating during the unregulated I-V acquisition on the telescope. This panel originally appeared in [15].

sity for each segment after normalizing out the effect of the window function, and averaging the resultant estimates accounting for the common data between segments.

In the top panel, the trend in estimated NEP as a function of different TES resistances R (i.e. different points on the resistive transition) indicates a potential calibration error that is affected by the TES resistance, or a source of constant current noise that is being projected into power. We surmise that this effect is due to excess current noise aliased into the low-frequency band of our devices, an effect which we observe to be TES resistance-dependent in other datasets. This excess is then calibrated into power.

However, when studying the distribution of NEP at 10 Hz across the array for a given target resistance, we are able to qualitatively match the median of the measured distribution to a model of the sum of noise contributions from thermal link and photon noise, with no free parameters. We are able to estimate the photon noise using the observed difference in P_{bias} for detectors in the laboratory and on the telescope, for the same T_{bath} and fraction of R_{N}. Using this technique, we are susceptible to additional uncertainties introduced by heating the array during I-V acquisition and miscalibration of thermometers between the lab and the telescope. These are represented by the widths of the gray bands in the right panel.

Due to the presence of significant photon-sourced NEP, these data are not able to confirm that detector-sourced noise is dominated by thermal link noise, as expected. However, laboratory data from testing the two mid-frequency arrays gave us the opportunity to compare measured NEP values to the expected values for the dark detectors. Again, by "dark detectors" we mean bolometers in array pixels whose feedhorns were covered by the metal-plated silicon mask. We note that studies of the change in P_{bias} for such dark detectors under changes to the cold load temperature point to the true bath temperature of the array being higher than that recorded by the PID control loop [12].

Results for the distribution of dark MF NEP at 120 mK are shown in Fig. 3.10. The top figures in the left (MF1) and right (MF2) columns feature NEP^2 averaged across all detectors. We write the average for a given frequency bin over detectors indexed with i as:

$$NEP_{\rm avg} = \left(\Sigma_i^n \frac{1}{NEP_i}\right)^{-1}. \tag{3.3}$$

We observe a noticeable rise in current noise at $\sim$ 100 Hz and a low-frequency noise, near 10 Hz, that increases inversely with TES resistance R. Both the excess at high frequencies and the changes in noise current at low frequencies remain when the current noise is converted to power. Since these measurements feature no photon noise, this is further evidence of an excess noise source being aliased into the signal band (roughly 1 Hz to 30 Hz) and increasing the dark noise above our expectations.

This excess is clearly seen when comparing the median of the NEP^2 distributions measured at 10 Hz (0.8×10^{-33} and 0.9×10^{-33} W^2/Hz for the 90 and 150 GHz channels, respectively), to the expected values shown by the solid black vertical lines in the middle panels (both about 0.5×10^{-33} W^2/Hz). These plots are also for laboratory data measured at 120 mK, but only for 50% $R_{\rm N}$. Here the gray band represents the characteristic spread in expected NEP values due to variance in the measured conductances G of the bolometers. We estimate an excess of 30-40% from comparing the measured median NEP^2 to the central expected value.

In calculating this expected value, we have also set the dimensionless correction parameter $f_{\rm link}$ applied to the thermal link noise (see Sec. 2.4) equal to one. This parameter varies between about 0.5 and 1. We do this, in the first place, to establish that the difference between measured and expected NEP cannot be explained by miscalibrated temperatures entering the value of $f_{\rm link}$, and secondly because, when plotting measured NEP vs. expected $f_{\rm link}$ across noise measured at different bath temepratures, we do not find a clear trend above the variance in NEP^2. We thus do not have evidence for $f_{\rm link} \neq 1$ in our data, and choose not to include it.

Finally, we provide a plot which projects the measured NEP values to the corresponding pixels in the array. We show only the results for the 90 GHz-band detectors, for which there are more devices measurable in both arrays. The clear high-noise outliers in MF1 were traced to particular readout rows in the array for which high noise was measured in data across bath temperatures and percent R_{N}. We have not confirmed the cause of this, but expect that the conversion between current noise and NEP is not sufficiently well-understood for these devices; thus, it is possible their noise is not aberrantly high.

Aside from the noise floor above 1 Hz and the rise in noise near 100 Hz, we note the presence of $1/f$ in both the HF telescope and MF lab frequency-domain noise spectra figures. In the case of the MF figures, we have incoherently averaged across the bolometers and the $1/f$ signal persists. We investigate this signal in particular noise datasets and find that it is difficult to reduce by assuming a simple common-mode source. Specifically, we construct a sample-by-sample array common mode as the median of all working detector values for that sample. When this template is subtracted from each detector's data, the $1/f$ power is reduced. This can be seen in the side-by-side comparison of Fig. 3.11. We take the constructed common mode to represent a thermal signal sourced by fluctuations of the bath temperature during data acquisition. The residual $1/f$ after this common-mode subtraction is not well-characterized currently.

To conclude, we have presented evidence that the dark bolometer noise in the AdvACT HF and MF arrays, whether calibrated in current or power, cannot be explained by thermal link noise alone. The source of this current excess will be explored with reference to addional noise sources arising from carrier flow and superconducting physics, as well as the effects of the extended electrothermal model introduced in Section 2.2. Before we progress to detailed noise studies, we will introduce our

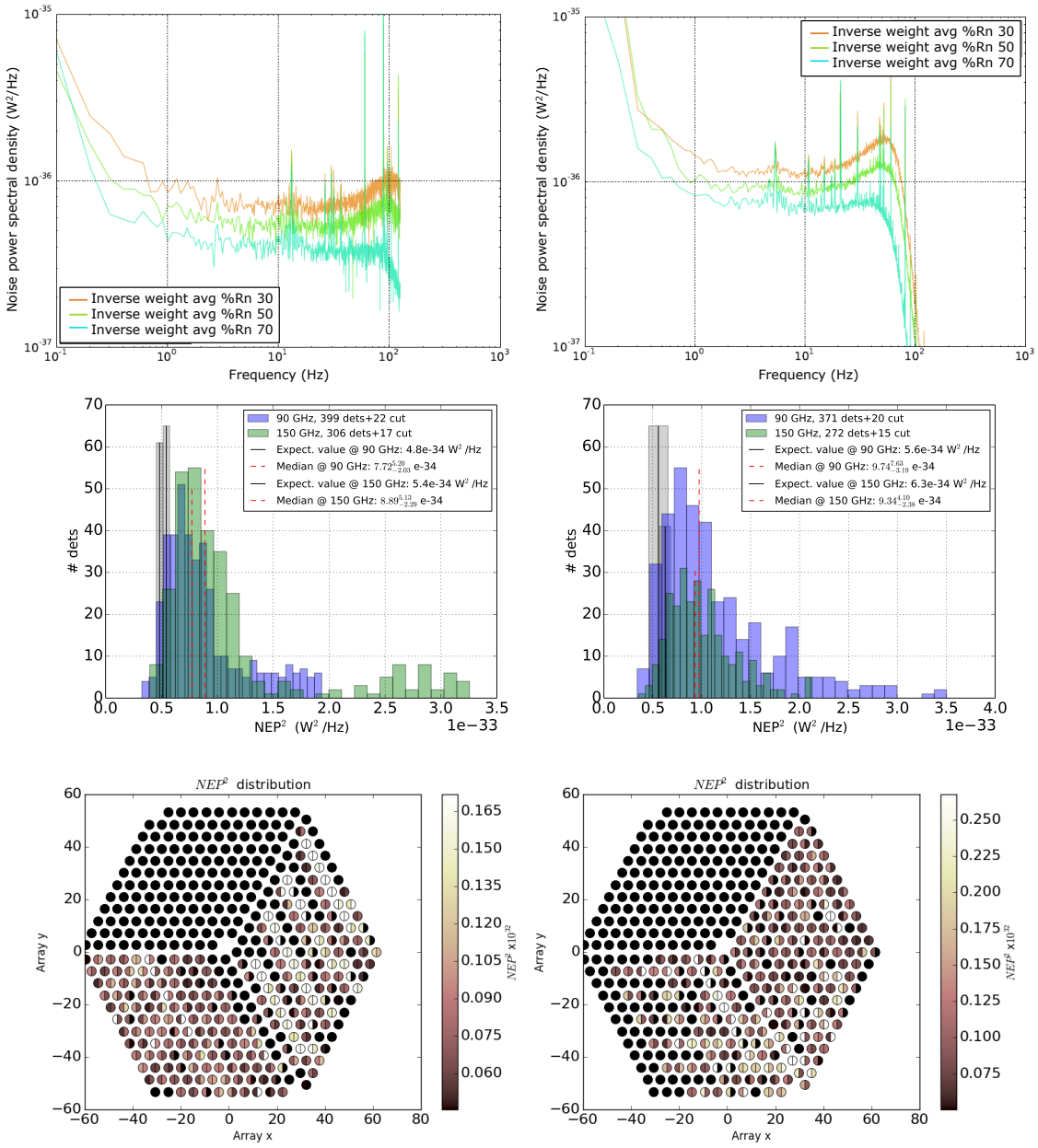

Figure 3.10: All plots in the left column are from laboratory data acquired on the MF1 array; those in the right are laboratory data taken on MF2. *Top row*: Detector-averaged NEP^2 measured at three points in the transition at 120 mK T_{bath}. The MF2 plot has a different antialiasing filter in place, and it has a noticeable effect at frequencies $\gtrsim 90$ Hz. Both sets of data show a prominent noise excess near 100 Hz that increases with decreasing TES resistance (here measured in % R_{N}). The strong lines at 60 and 120 Hz are known line pickup, and are reduced by common-mode subtraction; they also do not dominate in the field. The source of the line at 90 Hz is not known; it is not reduced by common-mode subtraction, but does not appear in the field. *Middle row*: Distribution of NEP^2 measured at 10 Hz for the two arrays, with histogram color corresponding to bolometer channel. The expected values, as shown by the vertical black lines with gray bands indicating expected spread, are below the measured medians (dashed red vertical lines). These panels taken from [14]. *Bottom row*: NEP^2 values plotted in array space for the 90 GHz bolometers. Each circle thus contains two halves for the two bolometers in a polarization pair. Black points are either illuminated by the cold load, or not measurable. The clear pattern of the high-noise (white) points in MF1 were traced to high-noise rows.

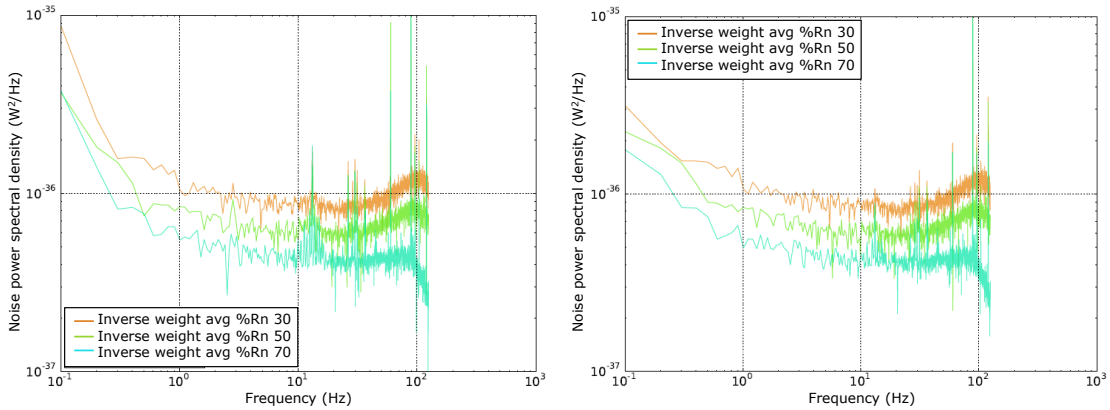

Figure 3.11: Illustration of common-mode subtraction for all MF1 dark bolometers during lab noise measurements at $T_{\mathrm{bath}} = 100$ mK. The left panel shows the inverse variance-weighted average across bolometers without the subtraction, and the right spectra show the results with it. Overall, the $1/f$ signal is not clearly reduced despite the subtraction. However, the narrow features, or spikes, have been reduced. The only spike which is not reduced by the subtraction is the one near 100 Hz, which indicates it is out of phase across the bolometers.

methods for studying bolometer impedance, and the results seen for AdvACT TES bolometers.

3.4 AdvACT Bolometer Impedance

In this section, we describe the main features of the data acquisition and calibration schemes used to produce estimated TES bolometer impedances Z_{TES}, as well as the methods used to extract parameters from them. Our chosen technique is to sweep the frequency of a small-amplitude sinusoid applied to a bolometer bias line from frequencies of a few Hz to the maximum frequency available with the setup in use. For data acquired with the MCE, this high-frequency limit is approximately 1 kHz; for data acquired at NIST, the use of a dedicated function generator to apply the sine wave allows measurements up to 100 kHz. However, in this section we mainly focus on AdvACT array impedance data acquired through the MCE. We begin by summarizing the main features of the data gathered for impedance measurements

in the MCE. Further technical details involved in running the MCE in the special acquisition mode used for these data may be found in Appendix A.

When acquiring a given impedance dataset, we first either bias the TES into its transition with DAC values of $\mathcal{O}(10^3)$, as we described in Sec. 3.2 in our summary of the bath temperature data acquisition, or apply a small DC offset from a DAC value of zero to ensure the sine wave signal does not go negative. In the former case, we will hereafter speak of the "operating condition" of the bolometer during the acquisition, this condition being defined by the achieved % R_{N}, or equivalently the TES resistance R, and the bath temperature of the array at the time of the acquisition. In the latter case, this nearly-zero DC bias is applied when acquiring calibrating data with the TES in its superconducting or normal state. To measure the response of the TES and its bias circuit while superconducting, we do the small-bias frequency sweep with $T_{\mathrm{bath}} < T_c$. For the dataset with the TES in its normal state, we increase the bath temperature to $T_{\mathrm{bath}} > T_c$.

After the TES is biased, we use built-in MCE software to set the MCE bias to digitally approximate a sine wave of a given amplitude and target frequency. Because the MCE can only update its biases in discrete units, and at particular periods set by the row-visiting (or "frame") rate of the MCE, only certain frequencies are accessible, and the digital approximation of the sine wave worsens for high frequencies. When the command is given, the MCE applies the sine wave with a repeatable zero-phase index, measured as number of MCE frames from the start of the acquisition. We thus have confidence that a fit to a sinusoid in the output TES current, when the frames before this zero-phase input index are cut, will recover the correct phase lag produced by the TES and its bias circuit. However, we cannot directly access the MCE input signal after data acquisition, since it is written directly to the TES bias line register.

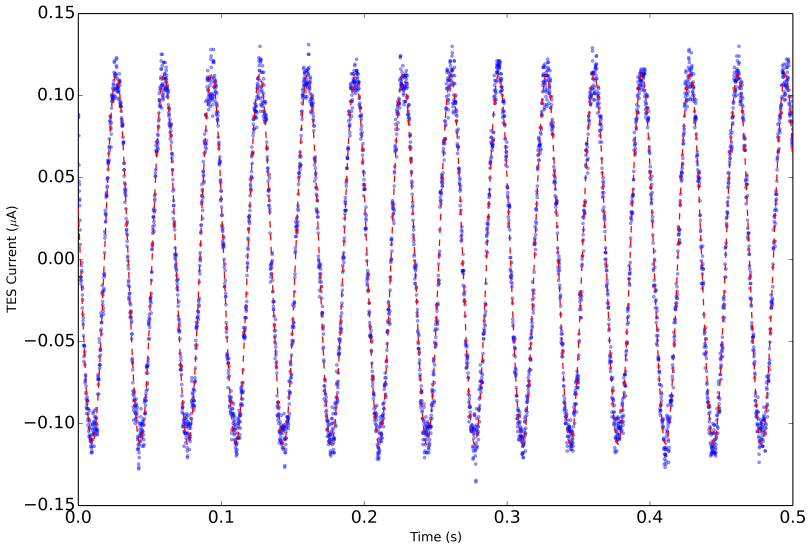

Figure 3.12: Data (blue) and best-fit line (red) acquired for an input sinusoid of f = 30 Hz, T_{bath} 120 mK, and target TES resistance 50% R_{N}. The fit has been performed as described in the text, with an offset applied to make t = 0 the zero-phase point of the input MCE sinusoid. The sample rate is 9.1 kHz.

The final component of the impedance acquisition through the MCE is to set the sampling rate of the MCE to the frame rate. This is done most easily by altering how the MCE delivers its "frames" data. Usually, a frame can be thought of as a matrix populated with the feedback values of individual TES bolometers in their columns and rows. The MCE then reports every Nth frame to the storage computer. However, we fill a frame of some arbitrary size (256 for our measurements) with samples from a single detector. The MCE repeatedly "visits" this row at the frame rate previously used to switch between rows. We thus receive frames with contiguous samples from a singular bolometer at this $\sim$ 10 kHz frame rate. We can now point out that, because the sine wave can only be approximated by discrete steps of the bias voltage at a rate of every two frames, and our readout bandwidth is limited by the same rate, we cannot measure sinusoids at frequencies greater than $\sim$ one-quarter of the frame rate. Thus, somewhere between 1 and 2 kHz, our system loses its sensitivity due to digital effects.

We perform this acquisition for each sine wave frequency desired, over all operating conditions to study. Fig. 3.12 shows the best-fit sinusoid to the MCE data, calibrated to TES current, for a particular input sine frequency. In these fits, we let the sine frequency be a free parameter, and add nuisance parameters for the mean and linear trend of the data. We then perform a least-squares residual minimization of the sum of the linear trend and sinusoid when fitting to the data. The red dashed line in the figure is the resultant best-fit line, and tracks well the blue data in the figure.

We perform a data reduction from the raw feedback data $V_{\rm fb}$ at each frequency to a voltage transfer function $\mathscr{T}(f) = \frac{V_{\rm fb}}{V_{\rm bias}}$ at each operating condition. This transfer function is a complex value at each frequency describing the relative amplitude and phase of the output sinusoid as compared to the input. This transfer function can be converted to $Z_{\rm TES}$ once the Thevenin-equivalent voltage and series impedance present in the TES bias circuit are known. Following the work by [81] [137], we use the voltage transfer functions measured in the superconducting and normal state of the TES to form a quantity proportional to the Thevenin voltage $\tilde{V}_{\rm th}$ and equivalent series impedance $Z_{\rm eq}$ as follows:

$$\tilde{V}_{\rm th} = \frac{R_{\rm N}}{\mathscr{T}_{\rm N}^{-1} - \mathscr{T}_{\rm sc}^{-1}}, \tag{3.4a}$$

$$Z_{\rm eq} = \frac{R_{\rm N}}{\mathscr{T}_{\rm sc}/\mathscr{T}_{\rm N} - 1}, \tag{3.4b}$$

where $\mathscr{T}_{\rm sc}$ and $\mathscr{T}_{\rm N}$ are the transfer functions measured in the superconducting and normal state, respectively. To be explicit, $\tilde{V}_{\rm th}$ is the Thevenin-equivalent voltage divided by the input bias voltage amplitude at the MCE and a calibration factor between TES current and feedback voltage. The latter can differ from the ideal value $\delta I_{\rm TES}/\delta V_{\rm fb} = -M_{\rm rat}/R_{\rm fb}$ due to unmodeled parasitic impedances in the bias circuit. Additionally, we note that the normal resistance is the calibrated physical value used to convert the dimensionless voltage transfer functions back into physical units.

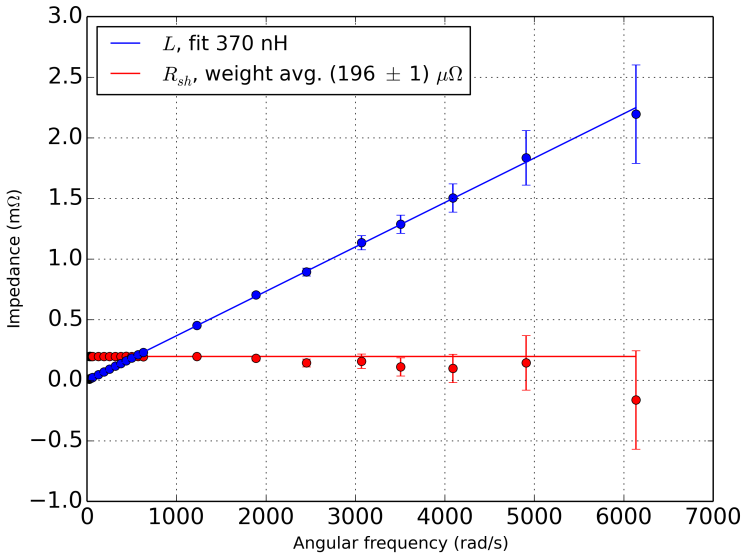

Figure 3.13: Comparison between measured and modeled $Z_{\rm eq}$, where the model is given in the text as the sum of the impedances from the TES shunt resistor and the inductance. We expected inductances of $\lesssim$ 300 nH. Our value of $R_{\rm sh}$ is not independent of the estimate from probe data taken at Cornell, as we have converted the transfer function data to dimensions of impedance using an $R_{\rm N}$ estimated with a pre-existing value of $R_{\rm sh}$. This data was acquired for an HF bolometer during *in situ* measurements; we thus drove the TES normal with a large DC bias current instead of warming $T_{\rm bath}$ above T_c. The best-fit lines and resultant estimated quantities for this bolometer's bias circuit are given in the legend. This image originally appeared in [15].

We can perform a check of the quality of our calibrating transfer functions by plotting the real and imaginary parts of the $Z_{\rm eq}$ as a function of angular frequency ω. We expect the real part to be frequency-independent and equal the resistance $R_L \sim R_{\rm sh}$ defined in the ideal bias circuit of the simple TES bolometer model of Ch. 2. The imaginary part, if dominated as we assume by the inductance L used to limit the bandwidth of the TES noise, should be a straight line. Thus overall we expect $Z_{\rm eq} = R_{\rm sh} + i\omega L$. Fig. 3.13 shows the result of taking the average real part of $Z_{\rm eq}$ and fitting a line to the imaginary part, as compared to the data. Given that the figure shows typical performance of these fits, the results indicate our assumptions are accurate over the range of frequencies probed by the MCE sinusoid.

With $\tilde{V}_{\rm th}$ and $Z_{\rm eq}$, we now calculate the TES impedance as:

$$Z_{\rm TES} = \tilde{V}_{\rm th}\mathscr{T}_{\rm trans}^{-1} - Z_{\rm eq}, \tag{3.5}$$

where $\mathscr{T}_{\rm trans}^{-1}$ is the voltage transfer function for a TES at a given operating point.

For each measured transfer function at each frequency, we estimate the error in the transfer function based on the estimated covariance matrix near the minimum of the best-fit model to the raw TES current data. We simulate multivariate Gaussian draws and take the error as the average of the asymmetric errors, i.e., averaging the difference between the 16th percentile and the median, and the 84th percentile and the median. These errors then propagate to the calibration quantities and $Z_{\rm TES}$ according to analytic estimates. We estimate a single real-valued error for the complex quantity $Z_{\rm TES}$, and assume this total represents the coadded variance of the identical errors in the real and imaginary parts of $Z_{\rm TES}$.

We can now proceed to fitting a model to these data. For AdvACT array data, we have used the model given by Eq. 2.15. We directly fit the parameters C, α, and β, with G and T_c fixed at the values given by the analysis of $P_{\rm sat}$ vs. $T_{\rm bath}$ curves [**?**] with no uncertainty assumed, and $P_{\rm bias}$ and TES resistance R determined from the I-V curves used to bias the TES before the impedance data were taken. When fitting, we find it convenient to apply two minimization routines in tandem. A rough minimization of the χ^2 function, with analytic error estimates at each frequency, is performed by the scipy "minimize" wrapper of the Nelder-Mead minimization algorithm. Since we are minimizing the deviation of a complex quantity from a complex-valued model, we choose a scheme where the quadratic-coadded deviation between the model and data for the real and imaginary parts is treated as the random variable. We can consider this to mean that we treat the sum of the absolute distances between the model and the data at each frequency as a χ^2.

Parameter	Median	Typical Uncertainties (%)	Spread (Max - Min)
C [pJ/K]	3.8	2	1.51
G [pW/K]	300 (90); 390 (150)	–	–
α	114	6	63
β	1.6	14	0.9
$\mathscr{L}$	21	6	16
$f_{\mathrm{3dB,\ eff}}$ [Hz]	130	4	69

Table 3.2: Summary of TES parameters measured using complex impedance data in the MF arrays for $T_{\mathrm{bath}} \in [120, 130]$ mK and fraction of $R_{\mathrm{N}} = 0.5$. These values come from eight bolometers total, across both arrays and frequency channels. With alternate measurement techniques, only the parameter $f_{\mathrm{3dB,\ eff}}$ is recovered at each operating condition. These results are to be published in [14].

After the scipy function finds a preferred minimum, we use the iminuit Python wrapper [7] of the MINUIT minimization library [59] to reanalyze the function and estimate parameter errors after renormalizing the error bars to ensure reasonable reduced χ^2 values. Using the "minos" function in iminuit, we can fully explore any nonlinearities near the minimum to ensure our parameter errors are conservative. These errors are the basis of the results in Tab. 3.2. In that table, we record details about the parameters recovered from fitting the impedance data of bolometers across both MF arrays and both frequency channels, in various operating conditions. We additionally include derived parameters like $\mathscr{L}$ and the $f_{\mathrm{3dB,eff}}$. The errors on the former are scaled from the estimated error on the TES α, while for the latter we draw realizations from the multivariate Gaussian described by the MINUIT-estimated covariance and take the spread as an error estimate.

As an added consideration, we find it necessary to impose certain constraints on the fit parameters in order to avoid a proliferation of degrees of freedom and to break possible degeneracies. For these data, the main feature is that impedance data at different % R_{N} and common T_{bath} are fit with a common heat capacity C for the bolometer. This improves the substantial degeneracy between C and α. Thus, only the TES sensitivities α and β are fit for each operating condition. Unfortunately,

[7] https://github.com/iminuit/iminuit

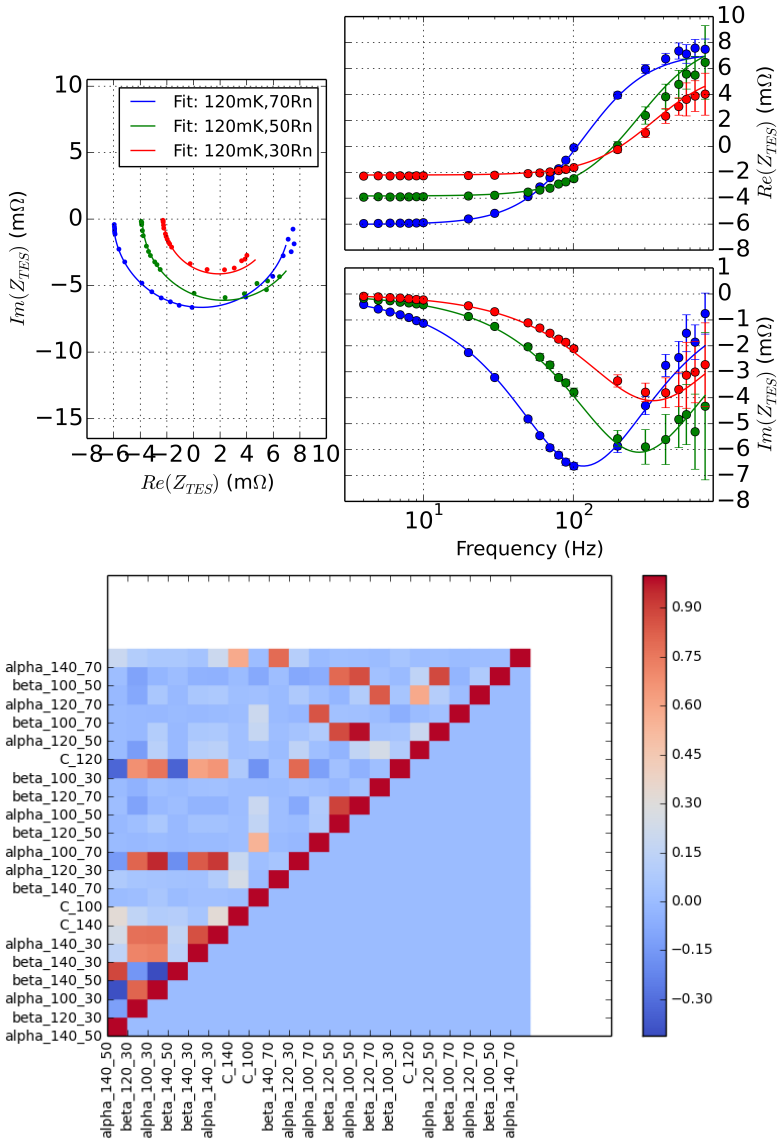

Figure 3.14: *Top*: Impedance data for an MF1 90 GHz-channel bolometer at 120 mK $T_{\rm bath}$ and all three resistances in the transition. The left panel shows the data in the complex plane, while the right column shows the real (top) and imaginary (bottom) part of $Z_{\rm TES}$ per frequency. We observe the frequency response bandwidth of the TES increase as % $R_{\rm N}$ decreases, as seen in the position of the minimum of the imaginary part. The simple model adequately explains these data. This image originally appeared in [14]. *Bottom*: The covariance matrix of the 21 parameters (α, β in 9 operating conditions, C at three bath temperatures) used to fit $\sim 12 \times 20$ data points for the same bolometer shown in the top three-panel image. The data cover all operating conditions used to study this device. Covariances between α and β for a given operating condition dominate the off-diagonal elements; this covariance increases with the $f_{\rm 3dB}$ of the device, and thus inversely with the % $R_{\rm N}$ of the operating condition. This α-β covariance is consistent across the eight bolometers studied in the laboratory. Other important covariances, like between the largest α and C at a given $T_{\rm bath}$, are not as consistently strong.

the limits of the sinusoid frequency (or equivalently, the sampling) mean that for fast devices, we are not able to strongly constrain β from the high-frequency limit of the impedance. In this case, α and β become strongly covariant.

In Fig. 3.14, we include an example covariance matrix (bottom panel) for the bolometer with example impedance data shown as the top panel. The top panel shows the operating-condition data for all % R_{N} at 120 mK for an MF1 90 GHz bolometer, while the bottom shows the estimated covariance when all datasets in 12 operating conditions (30%, 50% and 70% R_{N} at 100, 120, and 140 mK) are used to fit the 21 parameters describing the impedance. Though most covariances between fit parameters are $\sim 30\%$, we find strong coupling between α and β, with covariances as high as 95%. We note that all errors estimated using MINUIT properly account for these covariances.

All of the above measurements have been interpreted in the context of the simple bolometer electrothermal model. However, we expect a correlate in the impedance data for the excess noise discussed above. This is observed using data acquired at NIST, and is most apparent in MF bolometers fabricated as part of a wafer of single pixels in 2016. When fitting these data, we find it useful to perform the following processes in our numerical studies:

- Select a break frequency f_{split}, where for frequencies below f_{split} we estimate single-block model parameters as described above;
- Open the fitting regime to a wide range of frequencies up to $\sim$ 20-30 kHz, where impedance data at these frequencies are acquired with optimized SQUID feedback parameters;
- Use these parameters in an initialization array for a Markov Chain Monte Carlo (MCMC) sampler (implemented in the emcee [34] Python package), to be discussed further below;

- Take the median value sampled by the MCMC chain for each parameter as our best-fit value, and estimate errors according to percentiles in the marginalized parameter distributions.

We switch to MCMC sampling as we expand our possible degeneracies when fitting the hanging model. When fitting this model, we alter our constraints such that all thermal parameters C_i, G_i, and C are held constant across all operating conditions, i.e., for all data. We find empirically that this improves the sampler performance.

In addition, due to the way the NIST data are acquired using a software lock-in, we are not able to estimate errors in the same way as in the MCE measurement case. We follow the analysis provided in Lindeman et al., 2007 [81], altering their error estimate to take as input the RMS TES current fluctuations. We note that in the Thevenin-equivalent circuit, the TES current goes as $V_{\rm th}/(Z_{\rm TES} + Z_{\rm eq}$. Assuming a fiducial $\Delta I_{\rm TES}$ estimated from thermal-link noise converted to current only by the bias voltage, and thus independent of frequency, we write a real-valued error $\Delta Z_{\rm TES}$ representing the coadded real and imaginary error as:

$$|\Delta Z_{\rm TES}| = \left|\frac{dZ}{dI}\right| \Delta I_{\rm TES} = \left|\frac{(Z_{\rm TES} + Z_{\rm eq})^2}{V_{\rm thev}}\right| \Delta I_{\rm TES}, \tag{3.6}$$

where we convert $V_{\rm thev}$ estimated from the function calculated in Eq. 3.4a to proper voltage units using the ideal conversion $-M_{\rm rat}/R_{\rm fb}$. This equation applies at each frequency.

As a final caveat, we have found it necessary to carefully tune the parameters of the NIST SQUID feedback circuit to ensure good high-frequency response of the feedback signal. Our focus was mainly on changing the P and I parameters of the feedback together to ensure frequency-independent response of the superconducting transfer data at frequencies above 10 kHz. Altering these numbers affects the shape of the high-frequency impedance data, but we strongly expect that properly calibrating

these data as described above will not produce bias. This is because the transfer functions should capture the effects of the feedback.

With the errors estimated and the minimization routine ready, it is now possible to explore the results of fitting the two-block model to data up to tens of kilohertz. Figure 3.15 shows the measured data and MCMC-preferred model results for two MF single-pixel bolometers, the top panel for a 150 GHz-channel bolometer and the bottom a 90 GHz-channel bolometer. It is clear that the model is able to describe the "turnover" in the data, and in doing so, recover a large G_i. For the bolometer in the top panel, the ratio of G_i/G at 40% $R_{\rm N}$ is 110; for the bottom, it is 120.

This behavior persists, in this case, across operating conditions ($T_{\rm bath}$ and % $R_{\rm N}$), though the extremity of the feature (i.e. the change in the real part of $Z_{\rm TES}$ at high frequencies) is reduced at higher $T_{\rm bath}$, and thus lower $P_{\rm bias}$ and $I_{\rm TES}$. Due to the form of the equations describing the hanging model, this is not necessarily a surprise – the severity of both the distortion to the impedance and, as will be shown, the noise spectral densities, is enhanced for large $P_{\rm bias}$ and large loop gain $\mathscr{L}$. In general, we find that the hanging model is able to account for large deviations from the simple model. We plan to quantify the improvement further by studying $\delta\chi^2$ performance between the models across many different devices, perhaps after carefully checking the assumptions in the $Z_{\rm TES}$ error estimates.

In Fig. 3.16, we show the parameter distributions of the MCMC chain across all parameter pairs, as well as the 1-D reduced distributions, for the same bolometer as highlighted in the bottom panel of Fig. 3.15. The strong covariance of α and β parameters across operating conditions, especially bath temperatures, is due to their mutual covariance with the thermal parameters, especially in the case of α and G_i. These results highlight that the equations describing TES bolometer impedance feature strong parameter degeneracies. Nevertheless, we can place few-percent errors on

these parameters even while accounting for these covariances, and better understand how real devices perform with regard to the models in use.

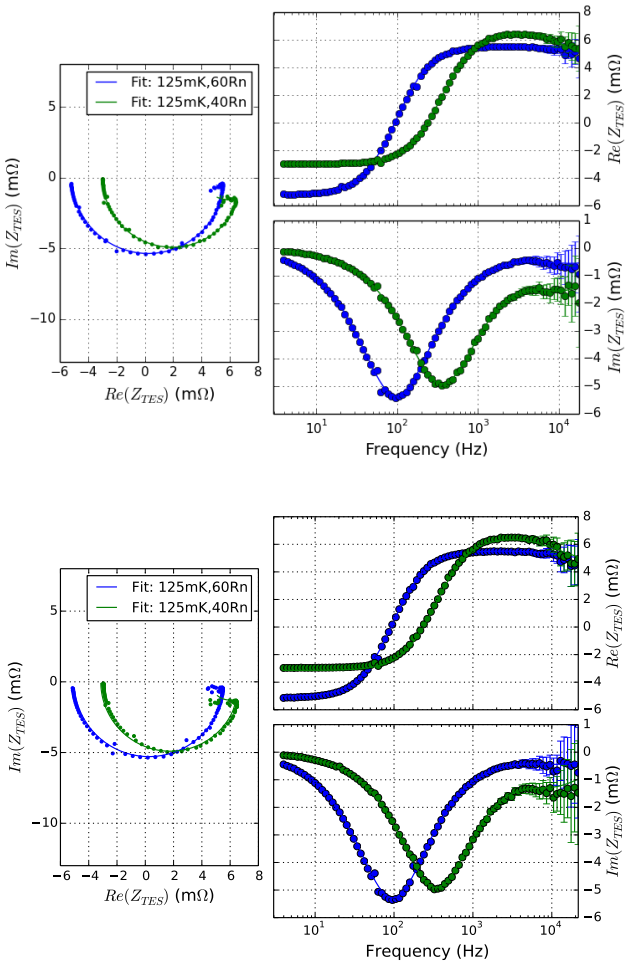

Figure 3.15: Plots of complex impedance data and fits. On the left in each plot are data in the complex plane while plots of the real and imaginary parts versus frequency are shown at right. *Top*: Two-block model fit results to impedance data for a 150 GHz AdvACT TES bolometer measured at NIST on a single pixel. The solid line represents the model calculated from the median values of all fit parameters in the MCMC chain. We observe that the feature at high frequency (best visible as the deviation of the real part of $Z_{\rm TES}$ above 3 kHz from a straight line– see upper-right panels) is well-described with this model. *Bottom*: Data and two-block model estimate for a 90 GHz AdvACT TES bolometer on a single pixel. Again, the result of using the hanging two-block model is an improved fit to the data.

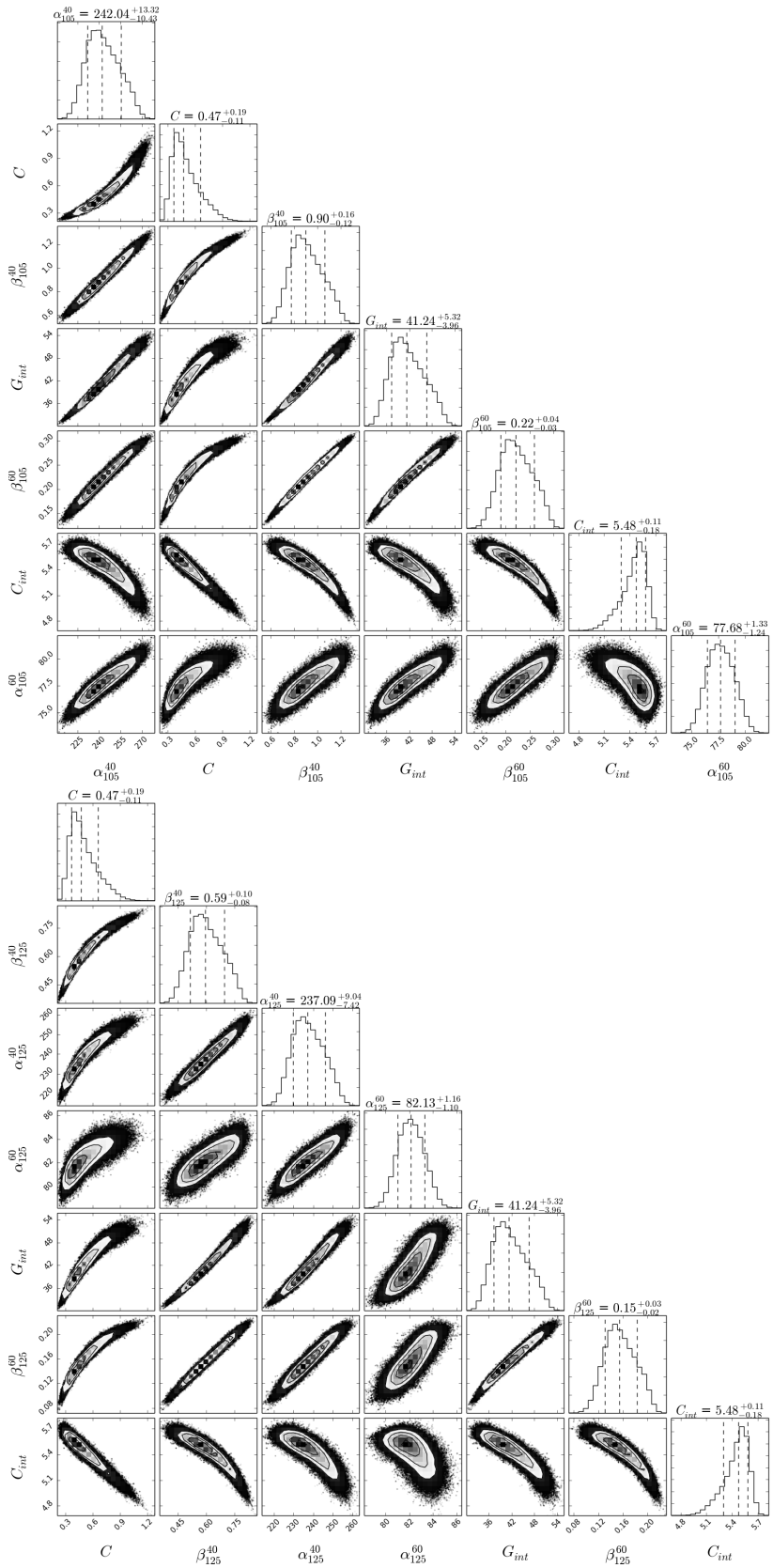
$\alpha_{105}^{40} = 242.04^{+13.32}_{-10.43}$
$C = 0.47^{+0.19}_{-0.11}$
$\beta_{105}^{40} = 0.90^{+0.16}_{-0.12}$
$G_{int} = 41.24^{+5.32}_{-3.96}$
$\beta_{105}^{60} = 0.22^{+0.04}_{-0.03}$
$C_{int} = 5.48^{+0.11}_{-0.18}$
$\alpha_{105}^{60} = 77.68^{+1.33}_{-1.24}$
α_{105}^{40}
C
β_{105}^{40}
G_{int}
β_{105}^{60}
C_{int}
α_{105}^{60}
$C = 0.47^{+0.19}_{-0.11}$
$\beta_{125}^{40} = 0.59^{+0.10}_{-0.08}$
$\alpha_{125}^{40} = 237.09^{+9.04}_{-7.42}$
$\alpha_{125}^{60} = 82.13^{+1.16}_{-1.10}$
$G_{int} = 41.24^{+5.32}_{-3.96}$
$\beta_{125}^{60} = 0.15^{+0.03}_{-0.02}$
$C_{int} = 5.48^{+0.11}_{-0.18}$
C
β_{125}^{40}
α_{125}^{40}
α_{125}^{60}
G_{int}
β_{125}^{60}
C_{int}

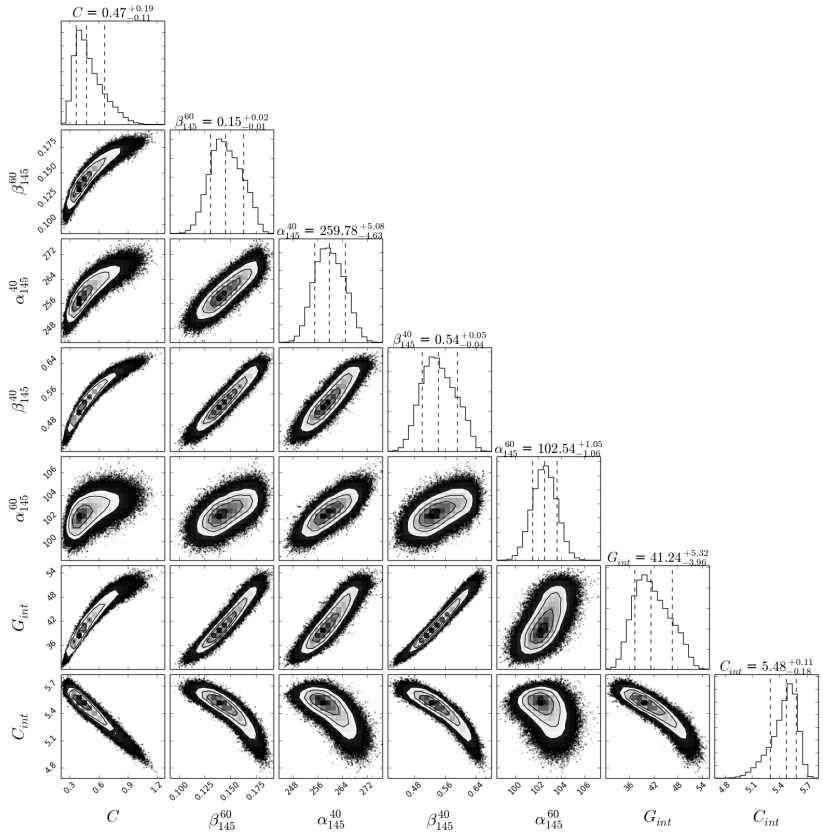

Figure 3.16: Overview of the MCMC chain for data across all operating conditions. These results correspond to the fit to the impedance data in the bottom panel of Fig. 3.15. Vertical lines in the 1-D distributions indicate the 16th, 50th, and 84th perentiles, used to form asymmetric 1-σ errors. These distributions are the marginalized one-parameter distributions from the full MCMC chain. The subplots are in order of increasing $T_{\rm bath}$ from 105 mK (top, previous page) to 125 mK data (bottom, previous) and 145 mK (this page). The strong covariances among α and β parameters across temperatures is due to the mutual dependence of all of these parameters on the common thermal parameters C, C_i, G_i. Further strong covariances between β and hanging-model parameter G_i likely results from their main effect on $Z_{\rm TES}$ occurring at high frequency, in a non-linear way.

Before concluding, we comment that it is instructive to compare the recovered C_i and C parameters of the two-block model to the estimations of PdAu and AlMn heat capacities on the island. We note first that C_i and C are both allowed sufficient space in their priors to "trade places" as to which forms the dominant heat capacity. The MCMC studies uniformly prefer large C_i and small C. If we identify the AlMn metal film with C and the PdAu film with C_i, we find that overall the TES capacity C is a

factor of 2 below ($C \sim 0.4$ pJ/K) the estimated value (0.8 pJ/K, as mentioned in Tab. 3.1). We also find larger-than-expected C_i, by about a factor of 2 ($C_i \sim 5$ pJ/K) for both 90 GHz and 150 GHz devices, where our estimated PdAu heat capacity is derived from measurements in Laufer and Papaconstantopoulos, 1987 [74]. It is possible that other elements of the island are altering the evidence for a physical picture of the source of the hanging model. We discuss this possibility in the context of a unique bolometer below.

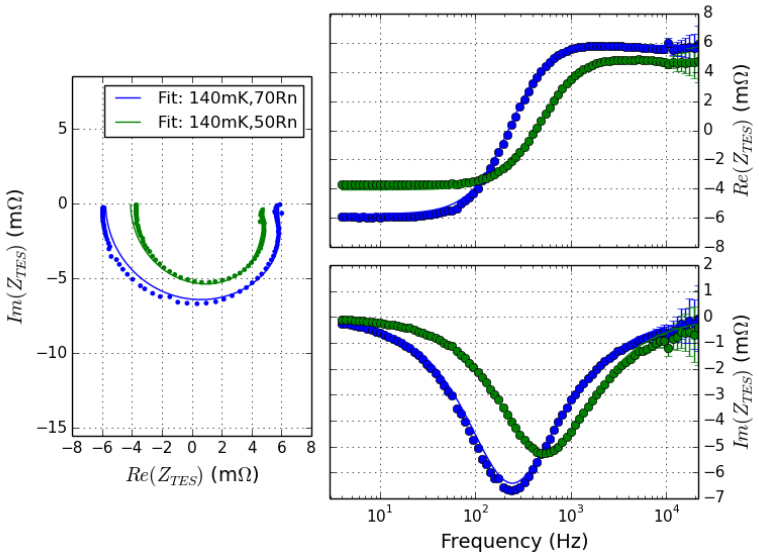

Figure 3.17: Data and modeled two-block impedance for an AdvACT bolometer with low G, no PdAu, and reduced AlMn. The data are described with the hanging model, despite the absence of PdAu which we had identified with C_i. The result is in acceptable agreement for these particular data, but this does not translate to the shape of the noise spectra for this bolometer.

For a particular set of TES test die, a very low heat capacity was designed to match the low G targets needed to maximize sensitivity of the AdvACT LF bolometers. An example bolometer, one with the minimum AlMn deposit needed (i.e., just to define the TES) and no PdAu on the island, was studied using the hanging model. For this device, the data indicate a broadening of the semicircle in the complex plane, rather than the localized feature at high frequency seen in Fig. 3.15. Fig. 3.17 shows

impedance data and MCMC-prefered models for this bolometer, as well as the best-fit simple model curves in gray. The latter are only fit using data up to 1 kHz; the resulting deviation at high frequencies indicates the need for some form of extended model. However, we do not yet have a way to ascertain whether this is the hanging model or an alternative. With these data, we find that $C \sim 0.3$ pJ/K, $C_i \sim 0.2$, and the ratio G_i:G is 25. The smaller value of C is qualitatively consistent with a reduction in the total volume of AlMn in this device, but we would expect a total heat capacity due to the AlMn that is smaller by a factor of 2-3 (AlMn $C \sim 0.1$ pJ/K). We do not have a strong intuition for any feature on the bolometer island to identify with the smaller C_i. However, we wish to state this bolometer's deviation from the simple model at high frequency indicates that an extended model may need to be applied even to a seemingly simple bolometer.

We can now progress to the test of the model via comparison of expected to measured noise spectra.

3.5 Model Studies with Dark Noise Spectra

We introduced noise sources and their current-referred contributions to the total bolometer noise budget in Sec. 2.4. The enumerated noise sources were thermal link (also called phonon, or G) noise, Johnson noise in the TES, Johnson noise in the shunt resistor, and current-referred noise in the SQUID amplifier chain. However, we now know that the data indicate an excess both in the mid- to high-frequency range of the TES band, and at low frequencies, likely due to aliasing. In this section, we will explore this claim, and the possible sources for the excess noise, before presenting the evidence for the hanging model based on these data.

Excess noise in TES bolometers has been observed in the literature for over a decade. The excellent review by Ullom and Bennett, 2015 [127] summarizes the

features of this excess. It has been found to increase with α, the TES sensitivity to temperature. Measures to reduce α by adding normal-metal features on top of the electrically-active areas of the TES have been found to reduce the excess.

To explain the excess, additional sources of noise, possibly in the TES itself, have been proposed. They include a modeling of a Weidemann-Franz thermal resistance (equivalent, in inverse, to a thermal conductance) to match the quasiparticle electrical resistance. This internal conductance, thought of as a thermal coupling of the electron population to the phonons in the TES, would then source noise [55]. In principle, the fluctuations in the number of Cooper pairs near T_c should also result in resistance fluctuations that would be measured as noise [113]. However, this latter noise source is assumed to be below the noise floor sourced by the thermal link noise, for instance, and thus is negligible.

Modeling of TESes as superconducting weak links [111] [66] has added the possibility of noise sourced by the stochastic generation of "phase slips," or 2π wrappings of the superconducting order parameter within the TES between its superconducting leads. Fraser, 2004 [36] gives a detailed presentation of this concept, along with equations useful for estimating the size of this noise source based on experimentally-accessible TES parameters. In his work, the claim is that phase-slip "shot noise" can replicate the main qualitative features of TES excess noise seen in detailed device studies in the literature.

However, the notion of extended electrothermal models sourcing excess noise [137] [42] [43] has generally allowed sufficient freedom to reproduce the spectral and operating condition-dependent features of excess TES noise. In both of the latter two references, the notion of indefinite numbers of thermal blocks in series arises naturally from studying the generic features of N block models. In the first reference, [137], as in this reference, we prefer to extend the model to a definite number of blocks and determine the validity of this extension, in order to elucidate the possible causes

for the excess in the detector architecture. Though this ambitious goal is not easily accomplished, it is a strong desideratum to only extend the bolometer model to a physically-motivated degree.

In initially investigating the excess noise, we proceeded along the lines of [60], in which a similar excess is studied by assuming it is an enhancement of the TES Johnson noise. In the regime of AdvACT detectors, with α well over 100 and large $P_{\rm bias}$ and TES current at the sensor, we assumed that some element of the equilibrium form of the Johnson noise may not be valid. This would be beyond the correction outlined in [58] where a nonequilbrium factor of $(1 + 2\beta)$ is a coefficient of the Johnson noise. We have included that term throughout this work.

We found that this hypothesis is not satisfactory with respect to more than two or three of the ten MF bolometers studied with impedance and noise acquisitions. However, in the cases where some semblance of agreement is found, we were able to use the modeled bolometer noise to predict the effect of aliased noise. To be explicit, our noise model is written:

$$S_I^{\rm tot} = S_I^{\rm thermal} + S_I^{\rm sh} + (1 + M^2)S_I^{\rm J} + S_I^{\rm SQUID}, \tag{3.7}$$

where each of these terms is the current-referred noise associated with the noise source. We choose this parameterization so that the factor multiplying $S_I^{\rm J}$ is positive-definite and is significant if it deviates from zero.

When we discuss "aliasing" in the TDM context relevant for AdvACT, we mean that frequencies above the row-visit rate (7.5 kHz for HF, 9 kHZ for MF, 15 kHz for LF) will be mixed into the band up to the Nyquist frequency (half of the above frequencies). We perform this aliasing explicitly for all the noise projection curves in Fig. 3.18 up to a maximum frequency of 1 MHz, near which the MCE readout has a final rolloff of the signal bandwidth. In this figure, the parameters used to describe the

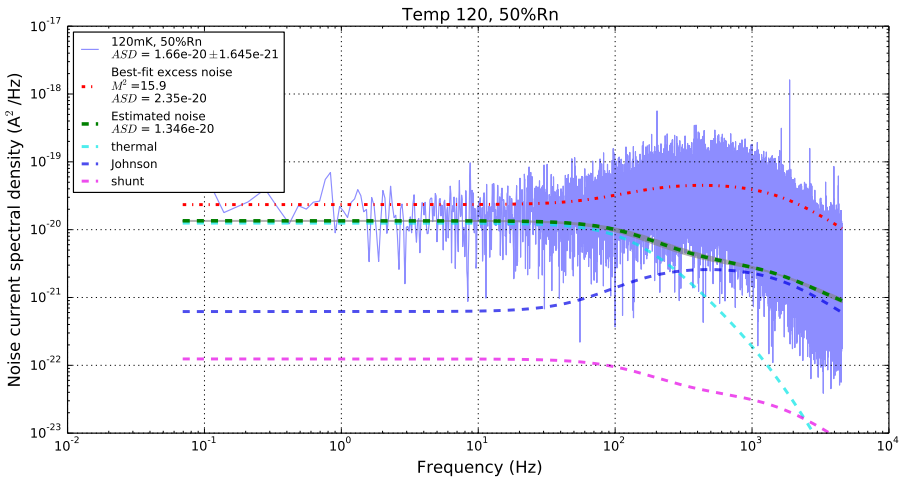

Figure 3.18: Measured noise current spectral density (blue) compared to the one-block model expectation derived from parameters measured via impedance data (green dashed) and with the addition of scaled TES Johnson noise (red dot-dashed). All model lines include the effects of aliasing from the Nyquist frequency up to 1 MHz. Aliasing is responsible for the difference between the green model and the red-dash dot for frequencies below 100 Hz. The width of the green line is roughly equal to the 68% CL (gray band) based on 100 multivariate-Gaussian drawns on the Minuit-estimated covariance. These data will be published in [14].

impedance data seen in Fig. 3.14 would predict the green dashed line after aliasing is factored in. The gray band around this line represents the approximate 68% CL band for the noise spectra given the covariances among the fit parameters. It is clear that there is a 50% excess of current noise at 10 Hz, where the noise values in the legend are estimated. However, the red dashed line represents a fit (with aliasing included) of the noise data to M, resulting in an excess factor of ~ 9 for the Johnson noise. This is the median best-fit value of the quantity $(1 + M^2)$ across the detectors used to produce Tab. 3.2. With this fitted result, the modeled and measured noise now agree to $\sim< 10$ %.

However, in other cases the excess cannot be well-described by the scaled Johnson noise factor, and M^2 does not deviate from zero. In addition, it is possible that the model misestimates the aliased component at high frequencies. To explore this effect, we reconfigured the MCE row-visit rate by forcing it to switch between the row of

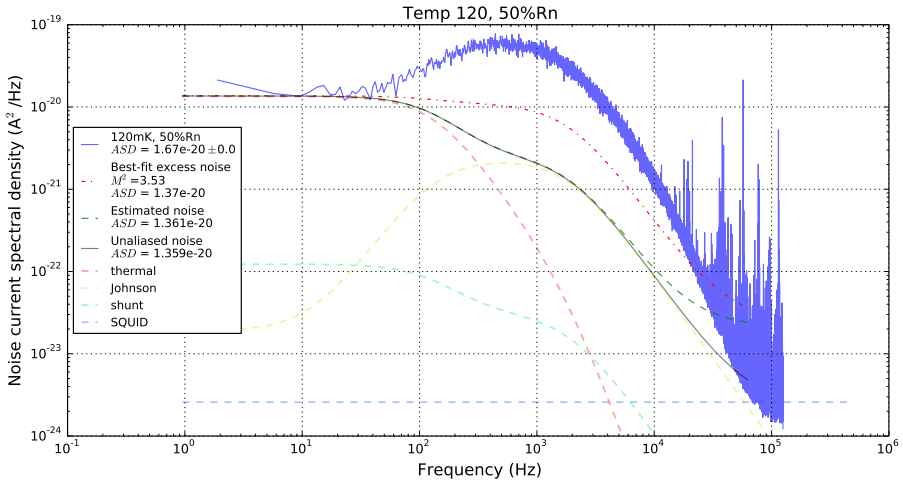

Figure 3.19: Measured noise current spectral density (blue) and models as in Fig. 3.18 but with data acquired to higher frequencies. Here we also plot unaliased source-by-source noise curves (colored dashed). The red curve is the best-fit excess Johnson noise model, and is not able to adequately represent the frequency position and amplitude of the excess.

interest and a dummy row. By this means, a sample rate of 250 kHz is achievable, similar to that used in NIST testing.

We acquired noise data in this configuration, at detector biases identical to those used in impedance data acquisition, for three detectors in MF1. Figure 3.19 shows the results for the MF1 bolometer with noise data shown in 3.18. We have here plotted the individual contributions of the various noise sources (unaliased) as well as the aliased total without excess Johnson noise (green dashed) and the best-fit excess Johnson noise result (red dot-dashed) with aliasing on. In particular, for the SQUID current noise value, we have calculated this directly from the quoted performance of the mux11d amplifier chain in Doriese et al., 2016 [24], converting this to current as follows:

$$S_I^{\mathrm{SQUID}} = S_\phi^{\mathrm{SQUID}} \left(P_{\phi,\,\mathrm{DAC}} \frac{dV}{d\mathrm{DAC}} \frac{1}{R_{\mathrm{fb}} M_{\mathrm{rat}}} \right)^2 , \tag{3.8}$$

where S_ϕ^{SQUID} is the SQUID noise density in flux quanta, $P_{\phi,\,\mathrm{DAC}}$ is the SQUID period (representing one flux quantum) in MCE DAC units, and the final factors convert DAC units to volts $\left(\frac{dV}{d\mathrm{DAC}}\right)$ and volts into TES current $\left(\frac{1}{R_{\mathrm{fb}}M_{\mathrm{rat}}}\right)$.

It is clear that the amplitude of the excess cannot explain the broad rise without affecting the estimate of the low-frequency noise data. Thus we are led to the conclusion that the hypothesis of excess Johnson noise is not supported. It would be preferable to run the impedance acquisition at the 250 kHz rate achieved for static noise bias, but limitations of the MCE firmware and hardware did not currently allow this. We next turn to estimating two-block hanging model noise values, and comparing them to noise data, acquired at NIST.

Fig. 3.20 shows noise data acquired at 125 kHz sample rate for the devices corresponding to the top and bottom panels of Fig. 3.15. The operating conditions are for the same T_{bath} as in that figure, and 60% R_{N}. We can see immediately that, qualitatively, the broad features of the excess are recreated, without resorting to a scaling factor. We calculate the square root of the median square residual between model and data to avoid being biased by narrow lines in the frequency domain. We find values of this root-median-square of $5.5\times\ 10^{-21}$ A^2/Hz (24% of the noise current density at 10 Hz) and $5.2\times\ 10^{-21}$ A^2/Hz (29% of the 10 Hz current noise) for the top and bottom panels, respectively. We note that we have not estimated a SQUID current noise for these data, partially explaining the deviation of the model below the data at high frequencies.

According to this model, then, the Johnson noise of the AdvACT TES devices is strongly suppressed, even with respect to the one-block model at these large ($\sim>$ 10) loop gains $\mathscr{L}$. The important second source of noise, then, is that sourced by the internal conductance G_i. Understanding how this noise excess varies under different operating conditions then becomes critical. Instead of the large-$\mathscr{L}$ suppression of Johnson noise, we find that for both larger α (smaller % R_{N}) and larger P_{bias} (smaller

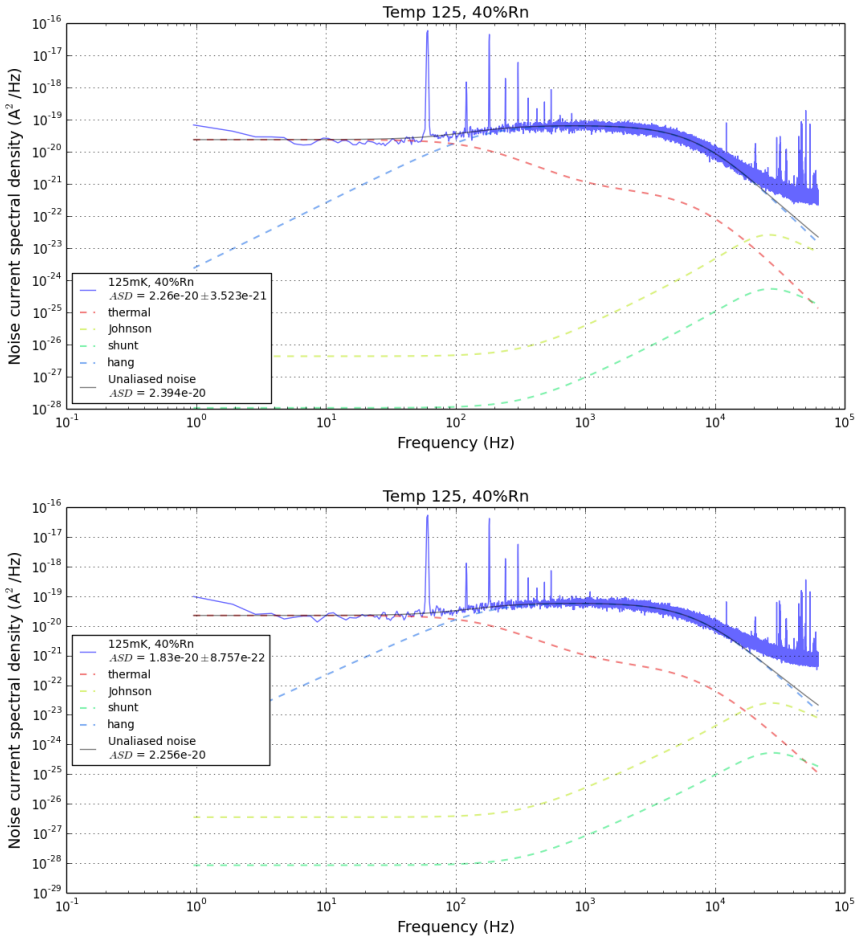

Figure 3.20: Noise data corresponding to the 150 GHz (top) and 90 GHz (bottom) bolometers for which impedance data were shown in Fig. 3.15, with all models unaliased and noise components separated by noise source. This model does not include SQUID amplifier noise, which we expect to be the component responsible for the noise floor above 20 kHz. We find the root median square deviation of model from data to be $\sim 30\%$ of the low-frequency noise value. We reiterate that these values are not a fit, but a prediction based upon the parameters determined from the MCMC exploration of the posterior (see Sec. 3.4).

T_{bath}), the excess appears more clearly in the current noise. This is despite the current noise induced by the smaller conductance to bath, which continues to dominate at frequencies below $\sim$ 50 Hz, also increasing for smaller % R_{N}. In general, then, the behavior of this excess is as described by [Ullom], but we argue that it can be completely attributed to a thermal noise source connecting to a hanging heat capacity in an extended model. We note that this line of reasoning cannot be completely

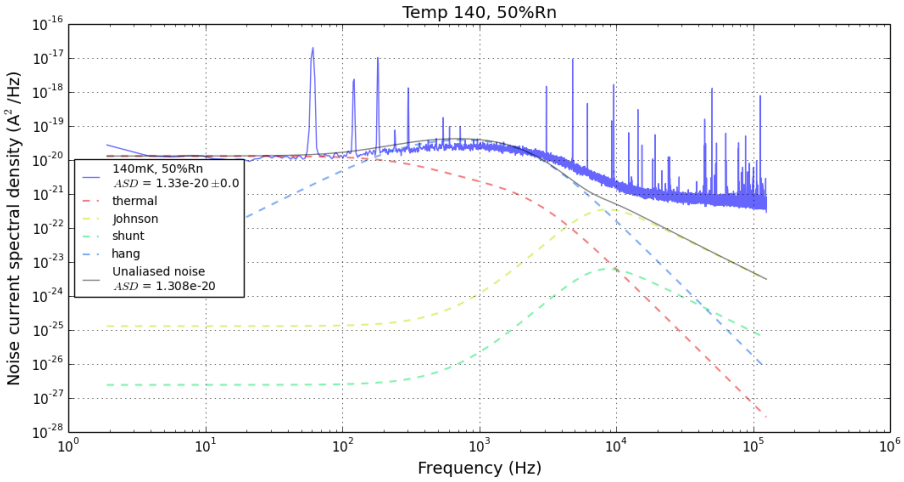

Figure 3.21: Noise current spectral density data, by-source noise estimates, and total noise estimates for the hanging model as applied to the detector with impedance data shown in Fig. 3.17. In this case, the hanging model does not accurately describe the broad features in the noise spectra. We do not yet have a model to describe this observed behavior.

proven, given issues seen in fitting the hanging model to data at 20% and 30% R_{N}. In general, concerns about TES instabilities near these resistances makes them less likely to be used during normal observations.

As a final point of interest, we conclude this section by including the estimated noise for the unique low-G bolometer studied in Fig. 3.17. Fig. 3.21 indicates that the resulting total noise estimate cannot replicate the frequency-domain shape of the data, as opposed to the MF case. This is more evidence that the hanging model may not be applicable here, and moving to a new model is motivated.

3.6 Field Performance of Arrays

As a result of the array tests above and others described elsewhere [54] [12], the first three AdvACT arrays were deemed ready for use in observations. The high-frequency (HF) array was installed on the telescope in summer 2016, and observed for six months along with the previously-installed ACTPol arrays. After an inter-

season break, telescope operations resumed in May 2017 after the installation of the two MF arrays in April 2017. In this section, we describe the performance of the three AdvACT arrays during their simultaneous observations throughout the 2017 season (referred to as "s17" hereafter).

Yield. Before celestial observations can begin, the arrays must be tuned and studied to understand the presence of possible issues like open lines, persistence, etc. This array commissioning in s17 proceeded by:

- Tuning the array and finding readout channels with problematic or no SQUID response.
- Testing for persistence and noting for which columns and whether it can be allayed.
- Taking I-V curves across the array to determine working detectors.

The response to each type of issue is, in the case of open SQUID response, to add the channel to a "deadlist" for which the MCE feedback loop will not be applied. This avoids the possibility of the MCE ramping the feedback DAC through its entire dynamic range in search of a faulty lock point. For MF1 and MF2, the majority of bad readout channels were isolated and seemingly random, with one broken column in MF2. In HF, critical line electrical failures preventing signal passes has greatly reduced the number of working detectors. We cannot ascertain the cause of these failures until the array is removed from the field.

In the case of persistence, we found four weakly persistent and two strongly persistent columns in MF2, and none in HF and MF1. We believe that, by underbiasing the SQ1 in the affected columns, we have reduced the persistence in the weakly-persistent columns to acceptable levels. Detectors in the two strongly-persistent columns, which have now observed for a year, have not been fully vetted, but it appears their I-V characteristics deviate from expectations significantly.

Finally, for detector channels which do not respond to I-V curves, which we assume indicates a failure of a wirebond somewhere in the TES readout circuit, we create lists of non-working detectors in order to prevent their data from being used to determine applied voltages to the TES bias lines. This is convenient with the MCE configuration files describing each array's bias line configuration.

We estimate our yields with respect to the number of optically-active TES bolometers for the arrays (2024 in HF, 1716 in MF). Fig. 3.22 shows the trend of number of well-biased detectors for each of $\sim$ 500 I-V datasets vs. the estimated precipitable water vapor (PWV), a proxy for atmospheric loading in power, divided by sin(el), where el is the elevation of the telescope during the observation. These results are taken across the entirety of s17. The three plots cover each array (HF, MF1, MF2 from left to right). We observe that the MF arrays are fairly static with respect to atmospheric brightness. This is partially due to the atmospheric loading on the 90 GHz detectors being minimal when compared to their $P_{\rm sat}$ targets. In HF, the more complex response is likely due to the dichroic nature of the arrays, with the 230 GHz-channel bolometers being especially sensitive to atmospheric loading, and some saturating between 1 mm and 2 mm PWV.

Transforming these numbers into yields, we recover that at 1.5 mm loading, the HF yield is 66% (1326 detectors), the MF1 yield is 94% (1612 detectors), and the MF2 yield is 83% (1432 detectors).

1/f Noise. A major difference between detector studies in the laboratory and *in situ* on ACT is the presence of additional sources of noise. We expect that thermal fluctuations will be larger, due to the lack of focal plane temperature regulation. In addition, it is believed that the motion (specifically the acceleration) of the telescope can induce additional array heating through mechanical vibrations. As the telescope scans, the harmonics of the scan frequency rise above the noise background, and can play a significant role in determining the low-frequency noise properties of the arrays

in the field. Finally, the strong correlated noise induced by changing atmospheric fluctuations, with spatial coherence lengths on the order of one-quarter to one-half of the array, results in $1/f$ modes that must be understood.

Other ACT-related studies have described how array-scale common modes induced by the atmosphere can be used to determine a flat field for the array [27] [82]. This flat field will partially prevent the correlated modes of the assumed-unpolarized atmosphere from leaking into polarization. However, once this is done, we may be concerned that other correlated noise sources, like bath temperature fluctuations, will become the dominant mode.

In the ACTPol context, we explored trying to recover information about possible correlations between timestreams from the thermometers used to record array temperatures and the correlated noise in the TES bolometer timestreams. This has been observed in other references for the ACTPol receiver [99]. The results of this study were inconclusive, and we instead present a comparison of parameters describing the shape of the correlated noise component in the array-averaged noise spectral densities. Here, "array-averaged" is in the same inverse-variance sense as in Eq. 3.3. Our model for the shape of the noise spectral density is:

$$SD = A\left(\frac{f_k}{f}\right)^{\eta} + w, \tag{3.9}$$

where A is a fluctuation amplitude at the knee frequency f_k, η is an explicitly positive-definite exponent, and w is some white noise level. We thus have a four-parameter family of curves to describe the shape of the array-averaged spectral density.

Previous studies of these parameters, especially the exponent η [27], have shown that it should be near either the 2D ($\eta = 8/3$) or 3D ($\eta = 11/3$) limit of the Kolmogorov turbulence expressions, as used to describe the fluctuations of air in the atmosphere. These studies were done specifically with the telescope stationary (i.e.

a "stare" dataset). In Fig. 3.23, we give a side-by-side example of fitting the array-averaged spectral density in CMB temperature units K^2/Hz for the 90 GHz and 150 GHz-channel bolometers separately (top row, left and right panels, respectively) on MF1. These data have been resampled to an 80 Hz sample rate using repeated nearest-neighbor averaging, in order to speed computation. The calibration is provisional, and based on a pW-to-K conversion number measured early in the season from planet studies [12]. We perform this fit with the scipy "optimize" wrapper of the Nelder-Mead algorithm [40], with a data-weighting scheme designed to prevent localized noise spikes from affecting the fit while also ensuring the few points at low frequency are considered important in the minimization.

In the top row, the plots are for a specific $\sim$ 10-minute section of scanning data called a time-ordered dataset (TOD). We also studied the distribution of the shape parameters f_k and η across a set of multiple TODs, as seen in the bottom row. Specifically, we are interested in their possible dependence on atmospheric loading. The results indicate a distinct η for the 90 GHz and 150 GHz channels, and some mild dependence on atmospheric loading. In general, we expect detectors in different bands to have different sensitivites to atmosphere, different heights at which they are exploring the turbulent atmosphere, and different white noise levels affecting f_k. We also show our fit results for TODs acquired at the same time on the HF array (bottom row of 3.23) with the 150 GHz and 230 GHz devices separated.

In order to determine a baseline level of *in situ* 1/f noise, we performed the same type of fitting on stare data on days with very little atmospheric loading for MF1. Initial results indicate $\eta \lesssim 2.0$ during August 2017 stare observations at PWV < 1.5 for the 90 GHz-channel bolometers, which are less sensitive to atmosphere.

NEP In Field. To conclude our discussion of array performance in the field, we wish to determine the possible effect of the excess in-band (i.e. below $\sim$ 30 Hz) dark noise as seen in the laboratory. First, because the arrays now receive photon

NEP from both the sky and the emissive components within the cryostat, there is an additional source of noise which may dominate the total optical power-referred bolometer noise. We expect that this additional NEP should obey the following equation [70] [138] given some incoming P_γ:

$$NEP_\gamma^2 = 2h\nu_c P_\gamma + 2\frac{P_\gamma^2}{\delta\nu}, \tag{3.10}$$

where ν_c is the central frequency of the bolometer microwave band, ν is the width of this band, and h is Planck's constant.

Our studies of NEP in the field proceed by adding the measured median array dark NEP to the above Eq. 3.10. We then have a model for $NEP_{\rm tot}^2$ as a function of P_γ. We take $P_\gamma = \mathscr{P} - P_{\rm bias}$, where $\mathscr{P}$ is effectively some array-wide saturation power. We can then fit for $\mathscr{P}$ for each channel in each array with the dependent variable being the array median NEP^2 for each TOD, and the independent variable being $P_{\rm bias}$. Through this study, we wish to determine if this NEP^2 model describes the data. We do this as a function of median $P_{\rm bias}$, rather than atmospheric loading; this means that loading decreases from left to right (i.e. as $P_{\rm bias}$ increases).

Our results are shown in Fig. 3.24. These data are converted to power units using an estimated responsivity $1/V_{\rm TES}$ as estimated from I-V curves. Thus individual detectors have not yet been flat-fielded. However, the subpanels, which span HF, MF1, and MF2 from left to right, indicate that the non-90 GHz channels see appreciable P_γ-dependent effects that are well described by the model with its one free scaling parameter. The observation-to-observation variance in the 90 GHz channels appears to dominate the expected trend, and we may be concerned particularly at the apparently flat trend of the MF1 90 GHz median NEP^2 on the high $P_{\rm bias}$ (or low loading) side. In these conditions, it is possible that some intrinsic bolometer noise is the most important noise source.

Array/Channel	Dark NEP Contribution (%)
HF/230 GHz	23
HF/150 GHz	32
MF1/150 GHz	31
MF1/90 GHz	38
MF2/150 GHz	26
MF2/90	42

Table 3.3: Contribution, in %, of the median array dark NEP^2 to the total estimated NEP^2 for the arrays based on the fits in Fig. 3.24.

With these data, it is possible to determine the contribution of the measured laboratory dark NEP to the total NEP seen in the field for raw PWV values near 1.0 mm. In this regime, near the approximate median value for CMB observations in Chile, we find that the noise contributions of the dark noise appear as in Tab. 3.3.

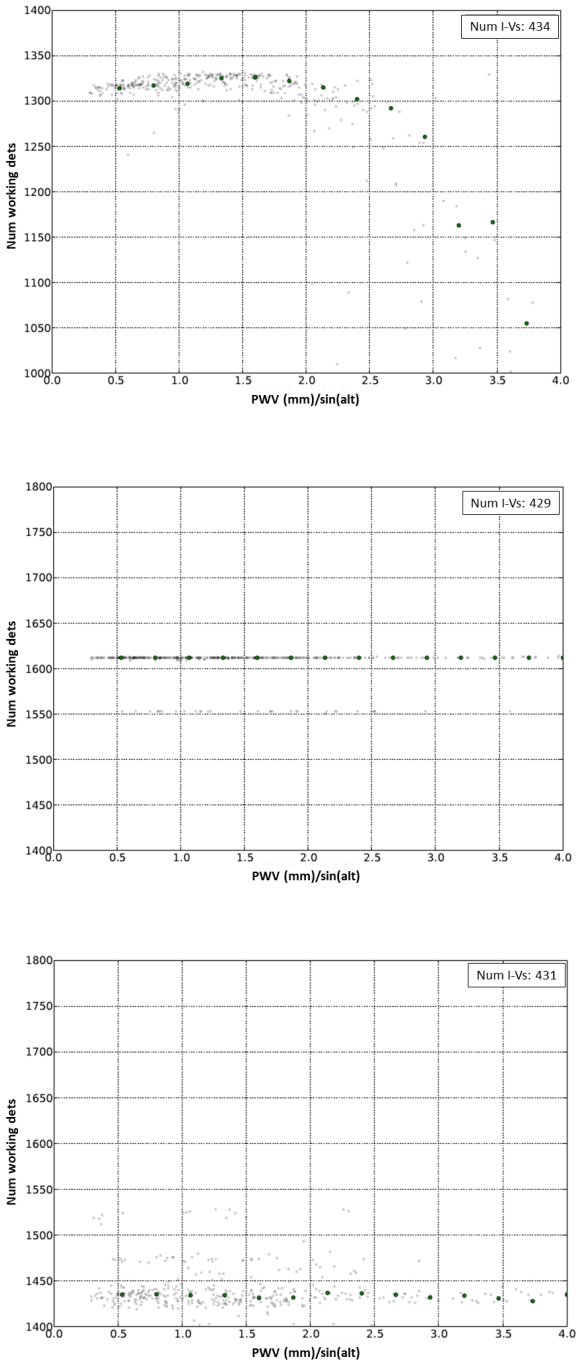

Figure 3.22: Number of well-biased detectors vs. atmospheric loading proxy (PWV/sin(el)) for the HF, MF1, and MF2 arrays (top, middle, and bottom respectively). The darker dots represent median values within a bin. These data show that only the HF array is strongly affected by changing atmospheric conditions, mostly due to saturated detectors in the 230 GHz-centered channel. The overall level of functioning in detectors is most reduced in HF, and is independent of the atmospheric loading, rather being due to cryogenic opens in the array readout.

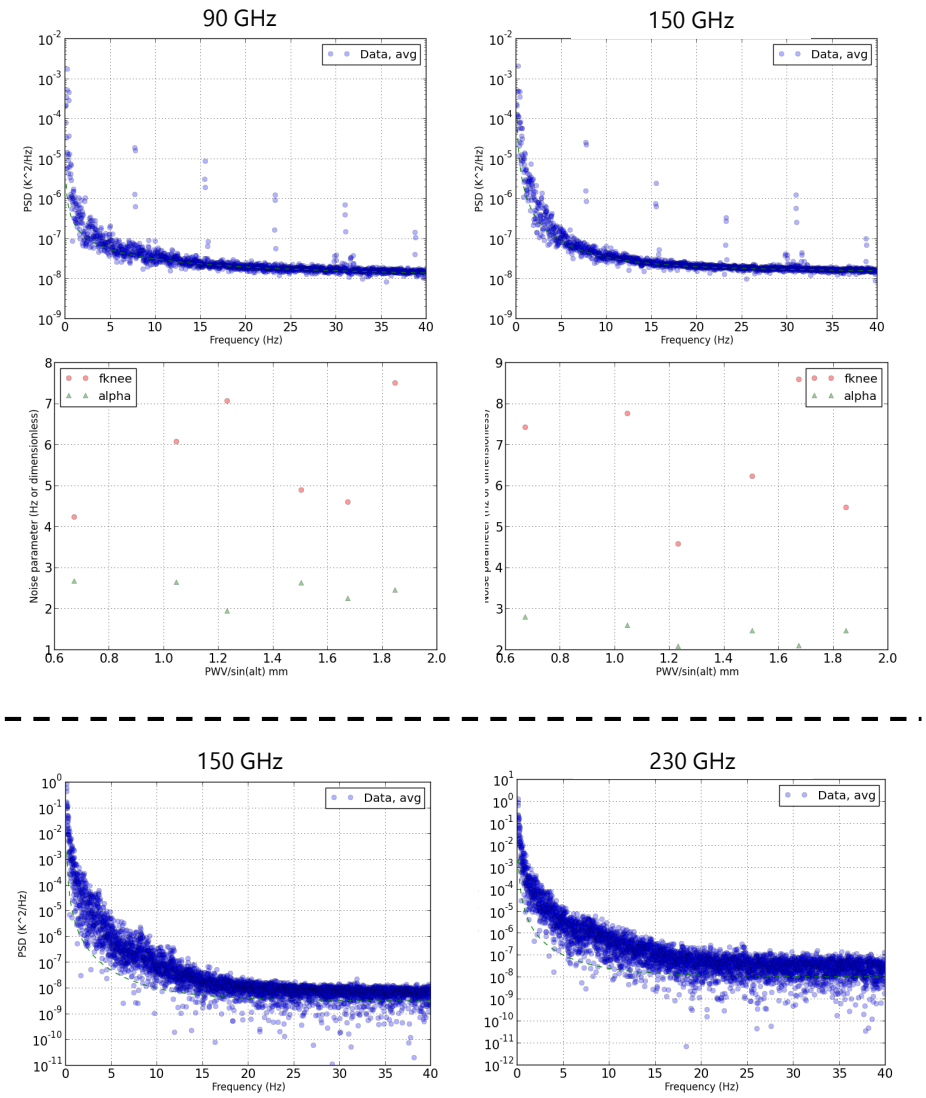

Figure 3.23: Examples for fitting the correlated+white noise model to field data for MF1 (top row) and HF (bottom row). The differences in noise amplitude and f_k can be seen clearly. The lines at harmonics of ∼8 Hz in the top row are consistent from observation to observation in this period, but not yet understood. In the middle row, fit parameters f_k and η for a set of 6 TODs spanning two dats of observations are included for MF1 with 90 GHz data on the left and 150 GHz on the right. These show no clear PWV dependence, though more statistics must be gathered to bolster this conclusion.

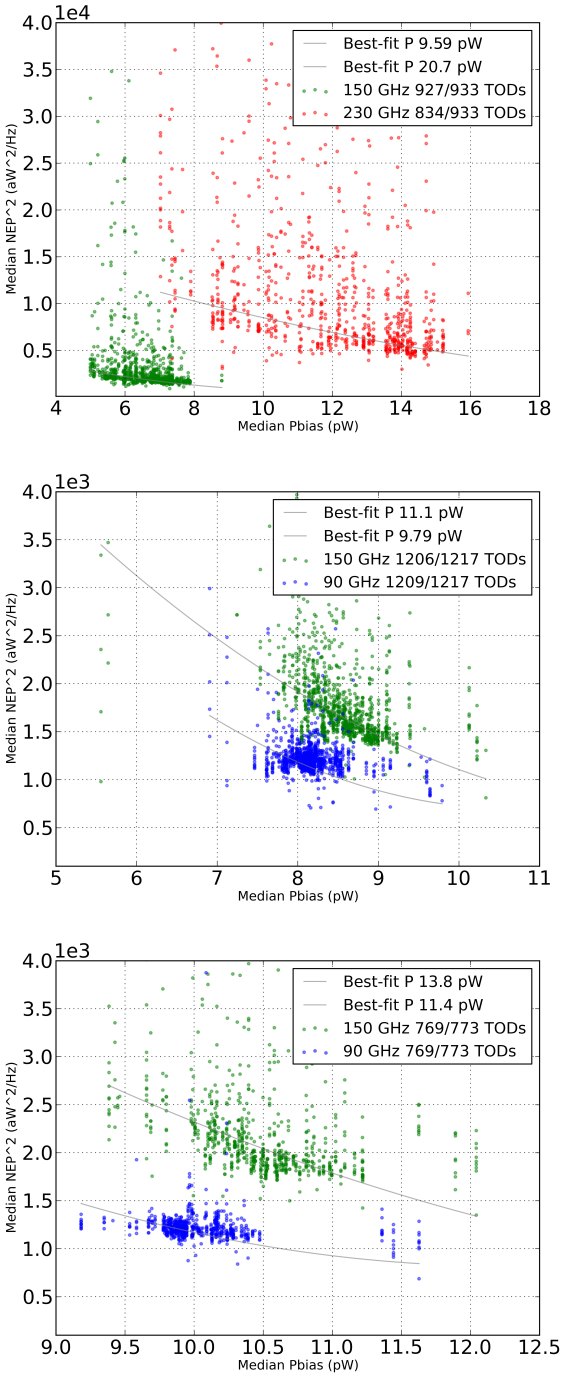

Figure 3.24: From top to bottom: Median NEP^2 across working detectors in HF, MF1, and MF2, versus the median array $P_{\rm bias}$. We expect the NEP^2 to follow the form of Eq. 3.10, with an offset provided by the median dark array noise at 50% $R_{\rm N}$. The former is the target for all detectors in the field. The gray lines for each channel represent the best-fit to an overall offset between $P_{\rm bias}$ and P_γ. Except for the 90 GHz channels, specifically on MF1, this model appears to explain the observed NEP trends in the field. These data span three weeks of observations during s17.

3.7 Conclusion

In this chapter, we have presented an overview of the noise performance and bolometer response characteristics of the three fielded AdvACT arrays as of summer 2018. In these studies, it has been determined that a dark noise excess in the region of ~ 100 Hz can be described according to the hanging two-block electrothermal model of a TES bolometer. We further have initial evidence for the identification of the second thermal lumped element with the layer of PdAu used to control the heat capacity of the AdvACT bolometer island.

We have further described details of data acquisition with the MCE, which AdvACT uses to implement its time-domain multiplexing in the laboratory and the field. Complete studies of the TES bolometer impedance necessitated special data acquired with an earlier, less-complex system that allowed for simple, fast (i.e. > 100 kHz) sampling of the TES response to sinusoid signals. It is these data that lend the strongest support to the hypothesis that the two-block hanging model can adequately describe the TES bolometers in AdvACT, especially in the MF arrays.

As a result of this excess, additional aliased noise is introduced into the frequency band most relevant to CMB studies. This excess is seen when comparing the expected dark noise in the arrays to measurements. However, we find that results in the field indicate that AdvACT bolometers are dominated by photon noise induced by cryostat loading and atmosphere, an important criterion for ensuring the detector arrays are as sensitive as possible. Thus we believe that the AdvACT bolometer arrays, though exhibiting interesting deviations from the simple bolometer model, are validated for sensitive CMB observations.

Chapter 4

AdvACT Polarization Modulation Studies

In this chapter, we describe the implementation of a continuously-rotating half-wave plate (CRHWP) polarization modulator as part of the AdvACT project, and initial analysis of the resulting detector data. We begin by providing a conceptual overview of the modulation scheme, and the usefulness of modulation in general. We progress to describing the HWP-synchronous signal that arises in detector timestreams, which we henceforth refer to as $A(\chi)$. We then discuss the use of a warm CRHWP in ABS, followed by the implementation in AdvACT and initial description of the $A(\chi)$ signal seen in a special observing run during October 2017 during which all three deployed AdvACT arrays had achromatic CRHWPs deployed in their optical paths. We then progress to discussion of the HWP performance and usefulness of the data from this special run, and conclude with a presentation of how $A(\chi)$ signals can be used to inter-calibrate detectors and track changes in their complex-valued response to incoming signals.

4.1 CRHWP Modulation: An Overview

As discussed in the last section of Ch. 3, the noise properties of the AdvACT TES bolometers during observations differ from the white noise due to the presence of $1/f$ noise derived from atmospheric brightness fluctuations in the detector optical band, thermal drifts of the bath temperature of the arrays, and possibly other "noise" sources. Here the quotes refer to the fact that these noise terms are in fact signals, but ones that obscure the incoming CMB polarization and make understanding the CMB at large scales from the ground a challenge.

We can understand the promise of modulating incoming polarization signals into a frequency band where atmospheric signals do not dominate by considering the following model for a TES timestream:

$$d(t) = s(t) + n_{\mathrm{white}}(t) + n_{\mathrm{corr}}(t), \tag{4.1}$$

where $s(t)$ is the CMB signal we wish to recover, and the other two are noise terms, with n_{corr} representing noise with a non-zero autocorrelation within $d(t)$ on long timescales and the characteristic frequency-domain shape of a power law, with exponent η, as given in Eq. 3.9. In addition, we expect n_{corr} to be correlated across detectors in the focal plane due to the spatial coherence scale of the atmospheric fluctuations.

If we take the Fourier transform of the above equation, which we will indicate using $\tilde{s}(\omega)$, and assume that our polarization signal as measured at the detector has been shifted to $\tilde{s}(\omega + \omega_{\mathrm{mod}})$, we can imagine filtering in a narrow band around ω_{mod} and demodulating our data at that frequency in order to recover a timestream that is free of long-timescale correlated signals.

Multiple experiments spanning more than a decade [61] [124] [69] have used CRHWPs to achieve this polarization signal modulation ahead of the detectors in the

optical path. Other experiments have used "stepped" HWPs in place of boresight rotation in order to improve observing strategy relevant for polarimeter studies, and to mitigate polarization systematics [9]. The signal description of a warm CRHWP has been described in detail in Kusaka and Essinger-Hileman et al., 2014 [69], which we draw from broadly in the following.

First, we must introduce the concept of a HWP itself. A generic HWP can be considered as a disc, made of a birefringent material, in the $x-y$ plane. We may imagine that the HWP is positioned such that its strongly refracting (called "extraordinary") axis points along x and the orthogonal, more weakly refracting ("ordinary") axis is along y. A polarized plane wave traveling in the $-z$ direction towards the HWP with linear polarization angle θ from the $x-$axis will leave the HWP with polarization angle $-\theta$. This is because waves polarized along the different axes of the disc travel at different speeds, producing an overall relative phase change between the x and y components of the incoming wave's polarization. This change is equivalent to the polarization vector being rotated. Since the polarization is rotated by 2θ, for rotation frequency $\dot{\theta}/2\pi = f_r$, this effect and the spin-2 symmetry of polarization produces a polarized signal at $4f_r$ in the detector. This physical picture is summarized in Fig. 4.1.

We represent the CRHWP-modulated timestream as the following:

$$d_m(t) = I + I_{\rm atmo} + \epsilon \mathrm{Re}\left\{\left[e^{2\phi-4i\chi}\left(Q+iU\right)\right]\right\} + \mathrm{A}(\chi), \tag{4.2}$$

where we have suppressed the time dependence of $\chi, I, I_{\rm atmo}, Q$, and U. The exponential factor multiplying the complex polarization value contains both a detector polarization angle ϕ, which we take to zero for clarity in this case, and the time-domain modulation as χ rotates. We write this as $m = e^{-4i\chi}$. The factor ϵ is termed a "modulation efficiency", the fraction of incoming polarized signal that is fully trans-

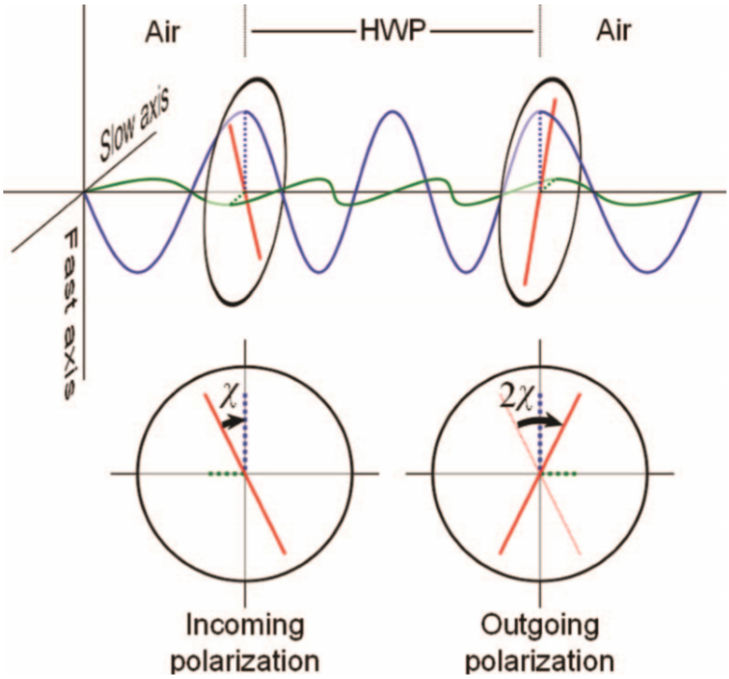

Figure 4.1: A sketch of how the HWP enables polarization rotation. The slow axis is the extraordinary axis in sapphire. The number of wavelengths in the figure is not meant as a realistic depiction of a real HWP. This figure is from [69]

mitted to the detectors through the CRHWP and other optical components. Finally, we note that $\mathrm{A}(\chi)$ can be generically decomposed in a Fourier series in χ, which we discuss further in Sec. 4.1.1.

Acting with a demodulation factor $m^* = e^{4i\chi}$, the unpolarized components of the Eq. 4.2 are shifted to 4 f_r. Components of $\mathrm{A}(\chi)$ are also folded onto harmonics of f_r in the demodulated timestream. If the odd harmonics are small, as we may expect from the discussion in Sec. 4.1.1, then the Fourier transform of the demodulated timestream will have a peak at 2 f_r. Filtering the demodulated timestream before this peak is then sufficient to recover a clean, pure-polarization timestream with only sky Q as the real part timestream and sky U as the imaginary part. After filtering, we find:

$$d_d(t) = \frac{\epsilon}{2}\left(Q + iU\right) \tag{4.3}$$

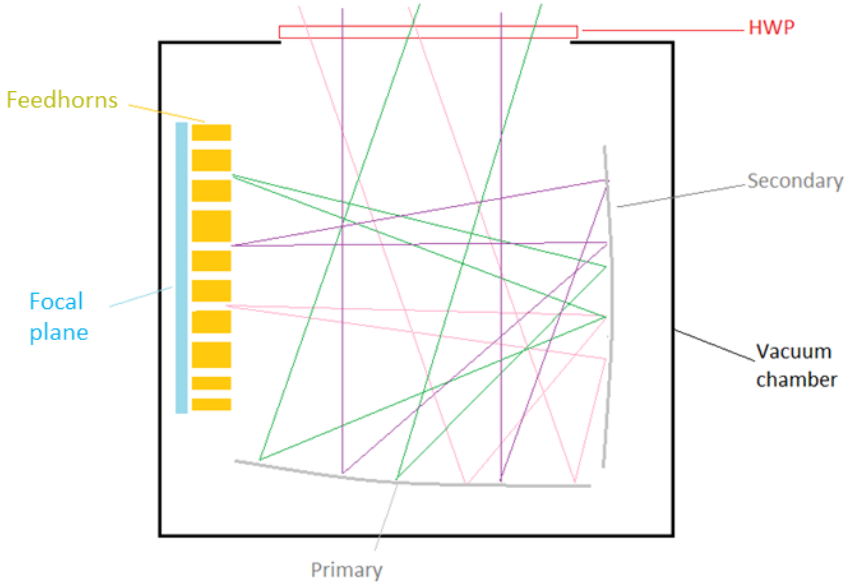

Figure 4.2: A cartoon of the ABS optical setup. Shown are the HWP in red at the top aperture of the vacuum system, which holds the cryogenically cooled mirrors (at 4K) as well as the feedhorns and detectors (at 300 mK when observing). The ray traces are not accurate, but meant to guide the eye through the crossed-Dragone configuration and the fact that detectors are mapped to plane waves arriving from infiinity at various angles of incidence. These illuminate nearly the full HWP for each detector.

We briefly review the way that CRHWP data analysis proceeded in ABS, and the important differences between the ABS and AdvACT cases. In ABS, the HWP was the most skyward element. A cartoon of the ABS optical design can be seen in Fig. 4.2. This results in the valid assumption that any modulated signal at $4f_r$ must be from outside the instrument, with the minor systematics discussed above. Since the CRHWP was also at the exit aperture, every detector saw the entire ABS HWP in its field-of-view, making the detectors less sensitive to small features on or int the HWP itself.

With these considerations, the analysis scheme of ABS data required only a band-pass filter around $4f_r$ at $\pm$ 1.1 Hz, demodulation using the factor m^* and the dedicated

χ measurement from a precision glass-slide encoder, and a subsequent, complementary low-pass filter acting on the demodulated data [68]. This scheme resulted in major reduction in the $1/f$ of the demodulated timestreams, as measured by knee frequencies, and systematics well below the level of the statistical noise at scales above $\ell = 30$. The effective limit of the sensitivity of ABS to large scales came from details of the scan strategy and pickup of scan-synchronous signal [68]. In addition, detectors could be calibrated relative to each other using the essentially common CRHWP signal.

In the AdvACT optics, the CRHWPs are in a very different position than in the case of ABS. The CRHWPs sit just above the cryostat window, between the secondary mirror of the Gregorian telescope and the cold stop at 4 K inside the receiver. Figure 4.3 shows the labeled location of the HWP on a ray trace of the optics from ACT into an ACTPol optics tube. At this point in the optics, rays are converging through the stop, and the beams of individual detectors see small areas of the HWP. Thus, we may expect the CRHWP, or equivalently the A(χ), signal in AdvACT to differ considerably from detector to detector based on their location in the focal plane.

Importantly, due to space constraints on the front side of the receiver, the AdvACT χ readout system is more complex. Ref. [132] provides details on the LED and

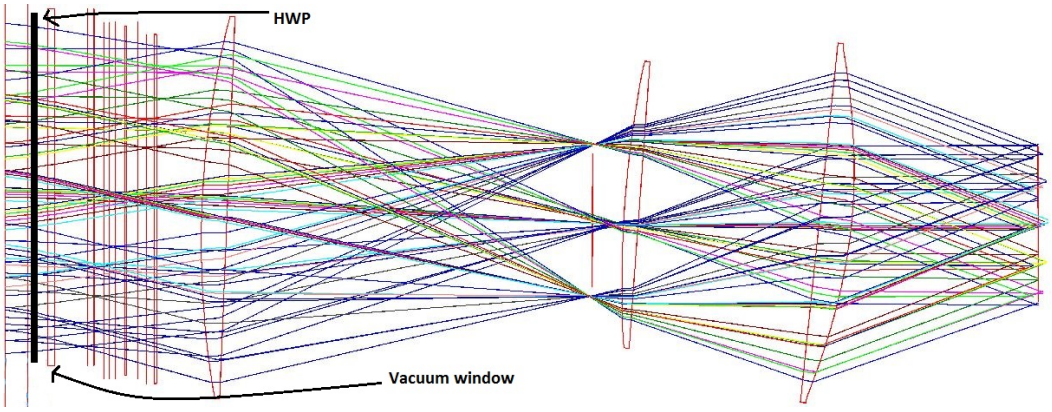

Figure 4.3: A ray-tracing simulation of the optics tube design for ACTPol, with the rough position and diameter of the HWP overlaid in solid black. This figure is meant to indicate how ACTPol detectors and ABS detectors see their respective HWPs differently. Courtesy M. Niemack.

photodiode apparatus, and the encoder ring that contains precisely-placed holes separated by degree. These allow reconstruction of CRHWP position but require a careful analysis of the fast-sampled voltage signal coming from the photodiode receptor.

With these differences in mind, we move to a discussion of the recovery of $\mathrm{A}(\chi)$ using a Fourier-series analysis.

4.1.1 CRHWP Synchronous Signal

When studying the signal injected by the CRHWP into the detector timestreams, what we have called $\mathrm{A}(\chi)$, we assume the following:

- The signal is periodic in χ;
- The shape of the signal may drift within or across TODs;
- The dominant harmonic of f_r visible in $\mathrm{A}(\chi)$ should be at $2f_r$.

In some sense, the first and the second are contradictory. What we mean is that the $\mathrm{A}(\chi)$ signal should be modeled as being periodic in χ, but its harmonic content can change over sufficiently long timescales. The converse of this is that the signal we care about is itself changes to the $4f_r$ harmonic at all timescales. Thus, estimating $\mathrm{A}(\chi)$ and deprojecting or removing it is complicated by the desire to preserve all information at $4f_r$.

Given the periodicity of the signal, we proceed in our study of $\mathrm{A}(\chi)$ by decomposing it into its Fourier series components up to the nth harmonic:

$$\mathrm{A}(\chi) = \sum_{m}^{n} a_m \cos(m\chi) + b_m \sin(m\chi) = \sum_{m}^{n} \tilde{Q}_m e^{im\chi}. \tag{4.4}$$

The above equation schematically represents the Fourier series (or discrete Fourier transform) of $\mathrm{A}(\chi)$ in the variable χ. Here we use $\tilde{X}$ to identify a complex number.

We can further decompose the complex amplitude of a given harmonic, $\tilde{Q}_m$, into a sum of terms:

$$\tilde{Q}_m = \tilde{\mathscr{A}}_m + \tilde{\sigma}_m, \tag{4.5}$$

where $\tilde{\mathscr{A}}_m$ describes a roughly constant amplitude and phase for the mth harmonic sourced by slowly-varying instrumental elements, and $\tilde{\sigma}_m$ describes a more rapidly time-varying complex amplitude, with a timescale of tens of seconds to minutes, possibly driven by long-timescale fluctuations identical to those that source $1/f$ noise.

In general, we expect that different components of the instrument will source nonzero $\mathrm{A}(\chi)$ components at different harmonics. We do not *a priori* anticipate large odd-harmonic components in $\mathrm{A}(\chi)$. However, in the case of the term $\tilde{\mathscr{A}}_2$, we assume that the differential emission along the axes of the CRHWP will dominate. A time-varying component of $\tilde{\sigma}_2$ is sourced by differential transmission of any intensity signals arising skyward of the CRHWP. This term should be most strongly sourced by the changing atmospheric loading.

At $4f_r$, a component of $\tilde{\mathscr{A}}_4$ arises from any $I \rightarrow P$ leakage of optical components skyward of the CRHWP. These are usually induced by polarized emission of the mirrors, a finite-conductance effect of any real metal. Any nonzero $\tilde{\sigma}_4$ sourced by the instrument is indistinguishable from signal on the relevant timescales. Concerns about non-sky, or even non-optical, effects inducing a signal that survives filtering and demodulation is a primary concern of CRHWP experiments. Averaging over many scans to recover only the celestially-fixed signal can reduce the significance of these leakages, but only if the variation is independent of telescope position. An important effect that has recently been elucidated is the fact that any gain variations of the detector or readout backend acting upon a nonzero $\tilde{\mathscr{A}}_4$ [123] [23] produce a signal in the demodulated timestream. In the case of detector nonlinearity, this variation is driven mainly by unpolarized $1/f$. We discuss studies of TES bolometer nonlinearity in Ch. 6.

Overall, these considerations demand that CRHWP experiments develop pipelines to remove A(χ), including any non-zero $\tilde{Q}$ contributions to the signal at $4f_r$. In addition, the relative size of the static and time-varying terms can have important effects on the required complexity of the removal pipeline.

4.2 ABS CRHWP Results

In this section, we will present a brief overview of the performance of a warm CRHWP in ABS. We have already discussed some assumptions and features of the ABS science-level analysis of demodulated CRHWP data. We now discuss aspects of A(χ) studies that benefited the understanding of ABS data, as an example of the possible uses of these concepts for both AdvACT and future experiments.

First, we describe the ABS CRHWP. The narrow-band design, meant to be optimum at the center of the ABS band $\sim$ 150 GHz, is fabricated from 31.5-cm thick sapphire, and is 33 cm in diameter. A laminated anti-reflection (AR) coating was used to improve the ABS sensitivity [69]. The CRHWP rotated at $f_r = 2.55$ Hz, in order for the $4f_r$ signal to be at 10.2 Hz, a clean part of the frequency domain in ABS observation noise spectra.

We now discuss the A(χ) subtraction pipeline implemented for ABS time-ordered data. Over the course of a full ABS constant-elevation scan (CES), an observation lasting for $\sim$ 1 hr, each bolometer's timestream is binned by χ value. The resulting binned data is averaged within each bin to produce an estimated A(χ) "template" for each ABS bolometer. This template is then decomposed into a truncated Fourier series with components as in Eq. 4.4, with the terms from $m = 0$ (the mean of the A(χ) signal, which was not removed from the timestream before binning) to $m = 19$ being removed. In this description, the majority of the A(χ) amplitude is found in the second harmonic, with a small additional component at the fourth harmonic.

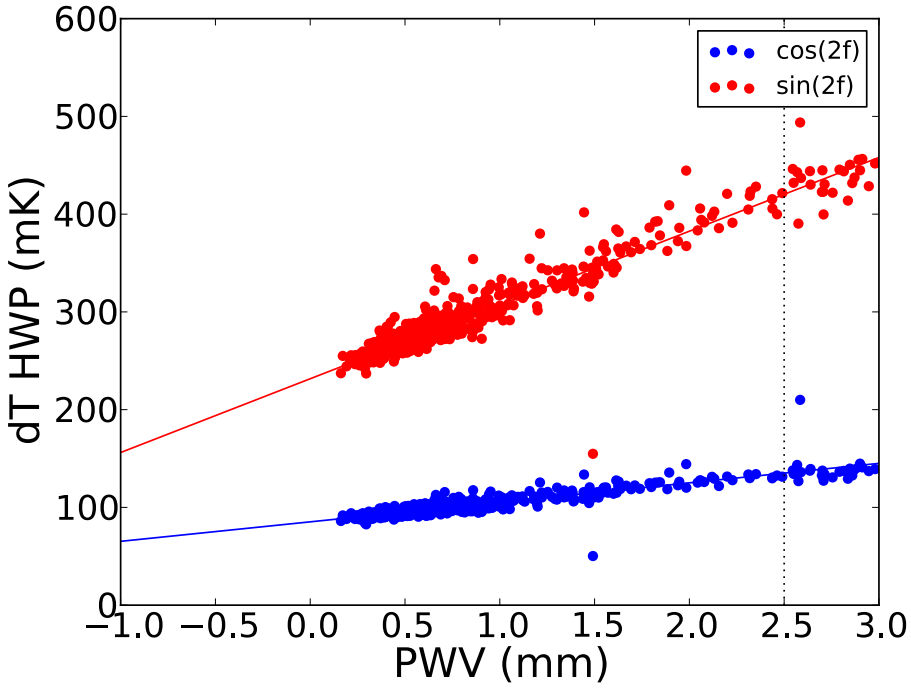

Figure 4.4: Per-CES measurements (circles) of a_2 and b_2, defined in Eq. 4.4, for an example ABS TES bolometer across the first season of observations. The best-fit line (solid) is used to make a data-selection threshold for CES which deviate excessively. The fit is restricted to the inner 95% of the a_2 and b_2 distributions. These data were gathered at the ABS observing elevation of 45°. Figure appeared previously in [116] and is reproduced here with permission of the author.

As this is performed for every CES, details of the variation of the harmonic components of $\mathrm{A}(\chi)$ can be studied across entire seasons. Simon et al., 2016 [116] describes how the differential transmission-dependent component of the $m = 2$ harmonic, what we have called $\tilde{\sigma}_2$, can be used as a bolometer responsivity tracker. As an example, Fig. 4.4 shows a linear fit to the measured $m = 2$ cosine and sine components of $\mathrm{A}(\chi)$ across many CESes. The linear increase as a function of atmospheric loading is an indicator that differential transmission is driving the environmentally-dependent effects on $\mathrm{A}(\chi)$.

In the final ABS analysis [68], the tracking of the amplitude of the $m = 2$ harmonic allowed discrete responsivity epochs to be identified, data-selection criteria to be developed, and a relative responsivity number for each bolometer in each CES to be

determined. We note that the use of the $2f_r$ signal for responsivity calibration across the entire array is only valid given that all ABS bolometers see the entirety of the CRHWP at the exit aperture. The ABS CRHWP also provided a path to measure the DC optical efficiencies and time constant response of the bolometers to a changing optical signal, based on inputting a roughly constant polarized signal and varying the CRHWP rotation rate [117].

This pipeline was vetted in the time and Fourier domains by studying the achieved $1/f$ suppression after filtering and demodulation [69]. Additionally, a dedicated study of $I \rightarrow P$ through the entirety of the ABS optics measured via studying maps of demodulated data during observations of Jupiter [30] agreed with detailed physical models of the CRHWP transmission and reflection components. These and other similar point-source data were used to characterize the ABS beam, with the important factor ϵ, the modulation efficiency, also being derived from these studies [68].

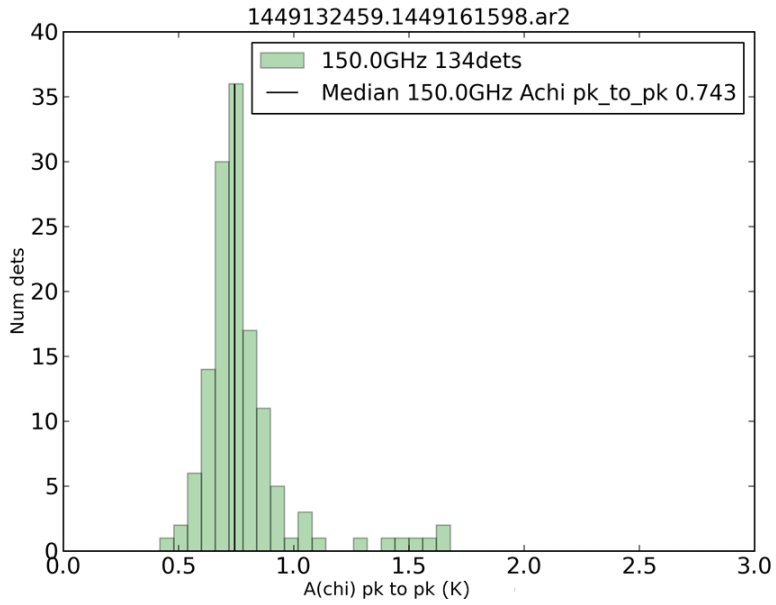

Figure 4.5: Calibrated A(χ) peak-to-peak amplitude of the sapphire CRHWP from ABS for a special ACTPol TOD in which it was present in the optical path for an ACTPol 150 GHz array. The median value of 0.74 K is in reasonable agreement with measurements of the A(χ) amplitude of the same CRHWP measured by ABS.

As a cross-check, we treat the amplitude of the $m = 2$ harmonic from the data in Fig. 4.4 as the total amplitude of A(χ). For PWV = 1 mm, we estimate $\sim 2 \times\sqrt{(300mK)^2 + (100mK)^2} = 0.6$ K. For a period of $\sim$ three weeks in 2015, the ABS sapphire HWP was placed in front of an ACTPol array, called PA2, which was also an array of single-band detectors with a band central frequency of 150 GHz. Figure 4.5 shows a histogram of the measured value of A(χ) peak-to-peak for a TOD on ACT with the sapphire CRHWP present. We take the 20% error to indicate that the particular calibration to $T_{\rm CMB}$ in use here is reasonable. By the latter, we refer to converting an optical power fluctuation to a brightness temperature fluctuation given the full Planck expression for the blackbody brightness spectrum when we integrate over the band of millimeter-wave frequencies to which the bolometer is sensitive. We take $T_{\rm CMB} = 2.73$ K. This is in distinction to the Rayleigh-Jeans brightness temperature, where the function integrated over the bolometer bandpass is the low-frequency (long-wavelength) approximation to the Planck brightness spectrum.

For reference, in Fig. 4.6 we show example per-detector TOD timestreams as injected by the ABS sapphire CRHWP (top subplot), and those seen by HF (upper middle), MF1 (lower middle), and MF2 (bottom) with their respective CRHWPs present. As discussed in Sec. 4.3 below, the large amplitude of the signal in MF1 is traceable to a defect on the outer surface of the HWP itself. The other metamaterial HWPs source A(χ) signals of between 0.2 and 1 K in peak-to-peak amplitude. Distributions across the arrays can be seen in Fig. 4.9.

4.3 AdvACT HWP Overview

We now introduce the hardware and software used in the 2017 special observing run of AdvACT with three CRHWPs present for all three arrays.

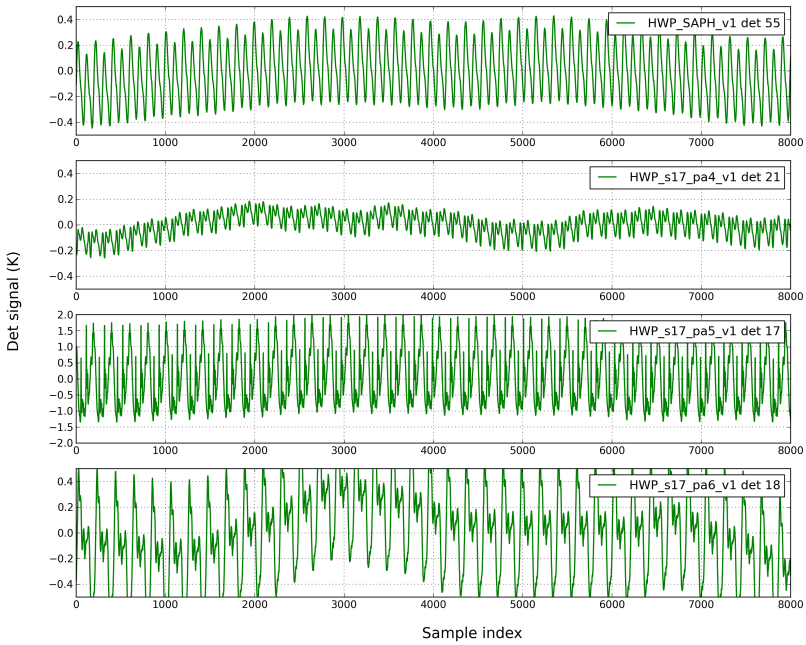

Figure 4.6: Example detector timestreams during observations with (in order, from top down): ABS sapphire on ACTPol array PA2; AdvACT silicon metamaterial on HF; MF1; and MF2, respectively. We have removed the linear trend of the raw data for clarity. The sharp features in the MF1 data are known to be sourced by a defect in the HWP. We see also that the sapphire HWP signal (top panel) is smooth and at low harmonics. All TODs have visible $1/f$ noise driving the baseline of the A(χ) signal.

4.3.1 AdvACT HWP Instrumentation

We begin by describing the HWPs themselves. Based on work done to fabricate metamaterial anti-reflection (AR) coatings for the ACTPol silicon lenses [19], designs for silicon metamaterial HWPs had been planned for AdvACT since the beginning of the project. In order to properly modulate polarization across the wide range of frequencies to which the dichroic pixels are sensitive, the HWP follows a stacked design, as laid out in Pancharatnam, 1955. [97] These HWPs are called "achromatic" for this reason. In addition to providing a birefrigent metamaterial, the technique of controlling the dielectric constant by changing the surface geometry, what we mean by "metamaterial," is also used to define AR coatings for the HWPs. Developing

silicon achromatic HWPs has thus far culminated in the successful fabrication of HWPs for the HF (with high modulation efficiency and low reflectance spanning over an octave in millimeter-wave frequency from $\sim$ 130 GHz to $\sim$ 280 GHz) and for the MF (similarly broad, from 60 GHz to 170 GHz) arrays. More detail may be found in Coughlin et al., 2018 [13].

We pass over the details of the air-bearing and drive system for the AdvACT HWPs. Information on the ABS air bearing system may be found in [69]. Details may be found in [132]. We wish to briefly review the main features of the readout system that is used to recover the HWP position. We have not yet discussed the importance of an accurate, relatively precise estimate of the χ timestream in order for the estimated $\mathrm{A}(\chi)$ template to be successfully used in removing the measured signal in the TOD. If there is effective jitter σ_χ in the χ timestream, this can directly add to the variance of both $\mathrm{A}(\chi)$-subtracted and demodulated timestreams as:

$$\sigma_{\mathrm{A}(\chi)} \sim \frac{d\mathrm{A}(\chi)}{d\chi}\sigma_\chi, \tag{4.6a}$$

$$\sigma_{m^*} \sim -4\sigma_\chi, \tag{4.6b}$$

where m^* is the demodulation factor introduced in Sec. 4.1 that is applied to our $\mathrm{A}(\chi)$-subtracted TODs in the pipeline to be described in Sec. 4.3.2. Though we can reduce the effective jitter in our $\mathrm{A}(\chi)$ estimate by binning, binning also has the effect of introducing signal variance from any drifts of the $\mathrm{A}(\chi)$ harmonics.

The hardware used for recording χ data in AdvACT first uses precisely-placed holes on an encoder ring which is at the edge of the HWP rotor assembly. The holes on this encoder ring are intended to be placed as accurately as possible on the same diameter, with separation of exactly 2°. A single hole, offset at a slightly larger radius, is read out as the "home hole" and is used to indicate the direction of rotation of the HWP, being slightly closer to a particular degree hole, as well as being

an absolute angle reference. It has been found that the natural variance in their achieved separation can be an important template to remove from the final angle solutions through a kind of remapping. However, we generally work with an angle solution that ignores this effect.

The operating principle of the photointerruptor encoder is that a red light-emitting diode (LED) sits below the encoder ring, at the edge of the HWP assembly and safely removed from the moving parts. Above it is a well-aligned phodiode designed to receive a strong signal when an encoder hole passes between the source and the detector. The voltage signal of this photoreceptor is read out at a sample rate of 40 kHz; these data are multiplexed in order to be merged into the ACT TOD file format, which includes critical housekeeping data as well as encoder positions for the telescope boresight and the detector TOD. A digital design for this processing was led by M. Hasselfield for the ACT collaboration, building from the previous-generation design by J. Ward, who was also responsible for much of the mechanical design in the rotor and bearing systems.

Usefully, an algorithm has been developed by M. Hasselfield and described in a publication in preparation [Ward et al. in prep] whereby this signal can be used to estimate χ. The raw encoder signal is first downsampled to 3.2 kHz, and then processed to find the large-amplitude photodiode response to the LED using an empiricially determined threshold. Timestamps for the degree-hole peaks are then analyzed to produce an angle timestream, which accounts for the home hole by using its recorded peak timestamp as the $\chi = 0$ point. These timestamps are synchronous with the "sync box" used to keep detector data synchronized with samples of the ACT azimuth and elevation encoders. This analysis is performed in real time, and the estimated χ timestream is then stored with the full AdvACT TOD for later access.

To characterize jitter after the χ estimate has been acquired, we analyze the χ timestream as follows:

- Bound full rotations of the HWP by finding large negative jumps (i.e. from high to low χ);
- Subtract an estimated χ template assuming constant rotation speed over the entire rotation, taking as input the mean sample time and mean rotation speed over the entire TOD;
- Study the residuals from this model.

An example for a particular TOD is shown in Fig. 4.7. Here the red line indicates a maximum-likelihood Gaussian fit to the residuals, whose distribution is approximated by the histogram in cyan. The distribution of the data is slightly skewed toward positive residual values, but the estimated σ_χ of 0.03° accords well with the results of studies based on power spectra of the χ timestream.[1]

4.3.2 A(χ) Estimation, Decomposition, and Subtraction

To estimate A(χ), we first high-pass filter the detector TOD at 1 Hz using a digital four-pole Butterworth filter. We do so to avoid biasing our estimate of A(χ), which is constrained to be at frequencies greater than $f_r = 2$ Hz, with $1/f$ drifts. This also has the effect of removing the mean of the TOD, which is therefore not present in our estimated A(χ) or its Fourier series approximation. We apply the filter in a "forward-backward" configuration in order to avoid introducing a phase from the filter to the timestream.

We then group detector samples in a TOD into bins according to the χ value at the timestamp of the sample. These bins are of arbitrary size. The pipeline first defines the bin edges according to the desired number of bins, then uses a fast function, "bincount", in numpy [96] to compute the sum of the detector samples within a given χ bin, finally dividing by the number of counts in the bin using the same function.

[1] M. Hasselfield, private communication.

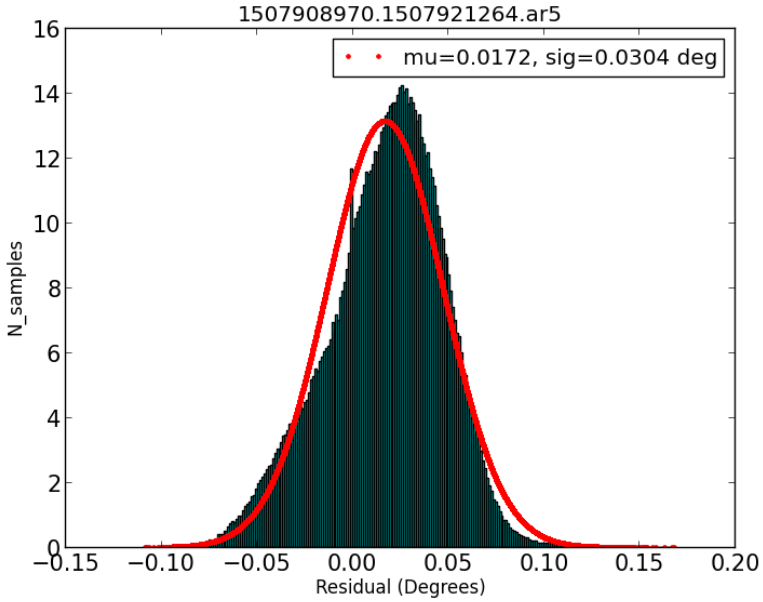

Figure 4.7: Distribution of χ residuals and preferred Gaussian to describe it for an AdvACT TOD from the 2017 CRHWP observing season. We do not yet have an explanation for the apparent skewness of the histogram. The label indicates the recovered mean and standard deviation of the distribution, with the latter being an estimate of σ_χ. The recovered value of 0.03° is consistent with estimates based on the noise spectral density of χ.

Once we have the estimated value of A(χ) at a series of χ bins, we multiply the $N_{\rm det} \times N_{\rm bin}$ matrix thus estimated on the right with an $h \times N_{\rm bin}$ matrix, labeled $\boldsymbol{H}$, in order to represent the data in terms of its Fourier coefficients. We form H as:

$$\boldsymbol{H} = \frac{1}{N_{\rm bin}} \begin{pmatrix} e^{-i\chi_1} & e^{-2i\chi_1} & \dots & e^{-hi\chi_1} \\ e^{-i\chi_2} & e^{-2i\chi_2} & \dots & e^{-hi\chi_2} \\ \vdots & \vdots & \ddots & \dots \\ e^{-i\chi_n} & e^{-2i\chi_n} & \dots & e^{-hi\chi_n} \\ & & & \end{pmatrix}, \tag{4.7}$$

where $N_{\rm bin}$ is the number of χ bins and h is the number of harmonics used in the Fourier series decomposition. Generically, we set $N_{\rm bin} = 720$ for 0.5° bin width. The maximum harmonic for the ACT f_r of ~ 2.0 Hz that is below the Nyquist frequency

of our detector TOD sampling is $h = 100$. We commonly carry all 100 harmonics to describe $\mathrm{A}(\chi)$ on a per-TOD timescale, and fewer for studies of variability.

The resulting complex-valued matrix $\mathscr{H}$, with dimensions $N_{\mathrm{det}} \times N_{\mathrm{harmonic}}$, has components which we label $\tilde{\mathscr{H}_m}$ that are related to the Fourier series parameters a_m, b_m in Eq. 4.4 as:

$$\mathrm{Re}\left\{\tilde{\mathscr{H}_m}\right\} = \frac{1}{2}a_m; \tag{4.8a}$$

$$\mathrm{Im}\left\{\tilde{\mathscr{H}_m}\right\} = -\frac{1}{2}b_m. \tag{4.8b}$$

We can account for these conversions when we convert this matrix into an $\mathrm{A}(\chi)$ template matrix, $\boldsymbol{T}$, with dimension $N_{\mathrm{det}} \times N_{\mathrm{sample}}$, where N_{sample} is the number of samples in the entire timestream. We perform this conversion again using linear algebra, and an analog to H which performs the inverse function, $\boldsymbol{I}$:

$$\boldsymbol{I} = 2\begin{pmatrix} e^{i\chi(t_1)} & e^{i\chi(t_2)} & \dots & e^{i\chi(t_p)} \\ e^{2i\chi_1} & e^{2i\chi_2} & \dots & e^{2i\chi(t_p)} \\ \vdots & \vdots & \ddots & \dots \\ e^{hi\chi(t_1)} & e^{hi(t_2)} & \dots & e^{hi\chi(t_p)} \\ & & & \end{pmatrix}, \tag{4.9}$$

where we have represented the timestream as having p samples, $\{t_1, \cdots, t_p\}$. We then determine our template, $\boldsymbol{T}$, as:

$$\boldsymbol{T} = \mathrm{Re}\left\{\mathscr{H}\boldsymbol{I}\right\}. \tag{4.10}$$

We note that this formalism does not take into account the variance within each bin. Instead it is simply a series of linear transformations on an assumed-unbiased estimate of the $\mathrm{A}(\chi)$ signal as a result of the filtering and binning operations. In

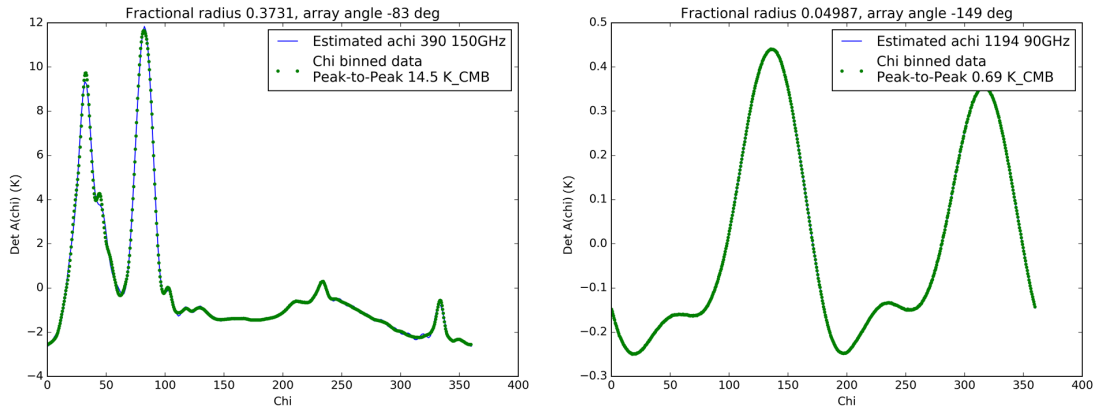

Figure 4.8: Estimated A(χ) (green points) and a reconstruction based on Fourier components (blue line) for different detectors in the same TOD as recorded for MF1 (left) and MF2 (right). The sharp features of MF1 have been confirmed from optical inspection and other analyses to correspond to a long, narrow scratch visible on the outer layer of the CRHWP. We treat the mean $\langle$ A(χ) $\rangle$ as equal to zero throughout our analysis. The data have been high-pass filtered prior to binning and template estimation.

our work, we then subtract T from the original, unfiltered TOD, doing so for every detector simultaneously.

We now turn to studying the model's performance, as well as the performance of the AdvACT CRHWPs. In the following results, we have converted the raw DAC units of a TOD to T_{CMB}, in Kelvin, using a provisional calibration that first calculates TODs in pW using I-V responsivity estimates, and then converts these pW to Kelvin using observations of Uranus. These are based on Uranus measurements discussed in [11].

In Fig. 4.8, we show the estimated A(χ) and the reconstructed model based on a Fourier series with $h = 100$ for a single detector in a single TOD for the two MF arrays. The smooth, $2f_r$-dominated A(χ) on the right is characteristic of the CRHWP that was used in tandem with MF2. With regard to the sharp, narrow features in the MF1 example A(χ) on the left, we were able to determine their correspondence to a physical feature on the CRHWP. As for the HF CRHWP, we found good performance for pixels near the center of the array, but apparently unphysical, large values of the

$A(\chi)$ deviation near the edge. This effect can be seen in Fig. 4.9, where we have provided histograms of the peak-to-peak amplitude of the measured $A(\chi)$ and views of these data in the focal plane space for the 150 GHz channels. We applied weak cuts based on detector properties and timestream quality before studying $A(\chi)$. In these results, we can observe the difference between the $A(\chi)$ amplitude in HF (top row) and the other AdvACT arrays. It is still uncertain how much of the observed effect, i.e. the extended population of HF detectors at peak-to-peak values at and above 10 K, is due to detector effects, miscalibration, and/or specific issues with the CRHWP used in the field.

Model Cleaning. We conclude this section by discussing how we have assessed the signal removal quality of our modeled TOD template T. We generate plots comparing the power before and after subtraction of T in particular frequency regions. Those within $\pm$ 0.1 Hz of an $A(\chi)$ harmonic, identified as a multiple of the estimated CRHWP rotation rate f_r, will be classified "HWP"-affected frequencies. This range of frequencies overestimates the width of the harmonic peaks, but avoids biasing the calculation of power in the "non-HWP" frequencies, i.e. all other frequencies above 1 Hz, where we expect the TOD to be roughly white for these arrays.

We then produce multi-panel plots in which, for a given panel, the x-axis represents the mean power in a single detector's power spectral density, in K^2/Hz, before the subtraction of $A(\chi)$, and the y-axis represents the same quantity after. The separate HWP and non-HWP frequencies are then shown in different colors. The distinct panels refer to a division of the full frequency range, which runs from 1 Hz to above $m = 20$ harmonic at 41 Hz, into subregions from [1,11] Hz (top left panel), [11,21] Hz (top right panel), and [21, 41] Hz. The bottom right panel then represents a histogram view of the mean power before (dashed outline) and after (solid color) $A(\chi)$ subtraction, for the HWP frequencies only. The colors then refer to which subband of frequencies the histogram belongs. Finally, the colored vertical lines show

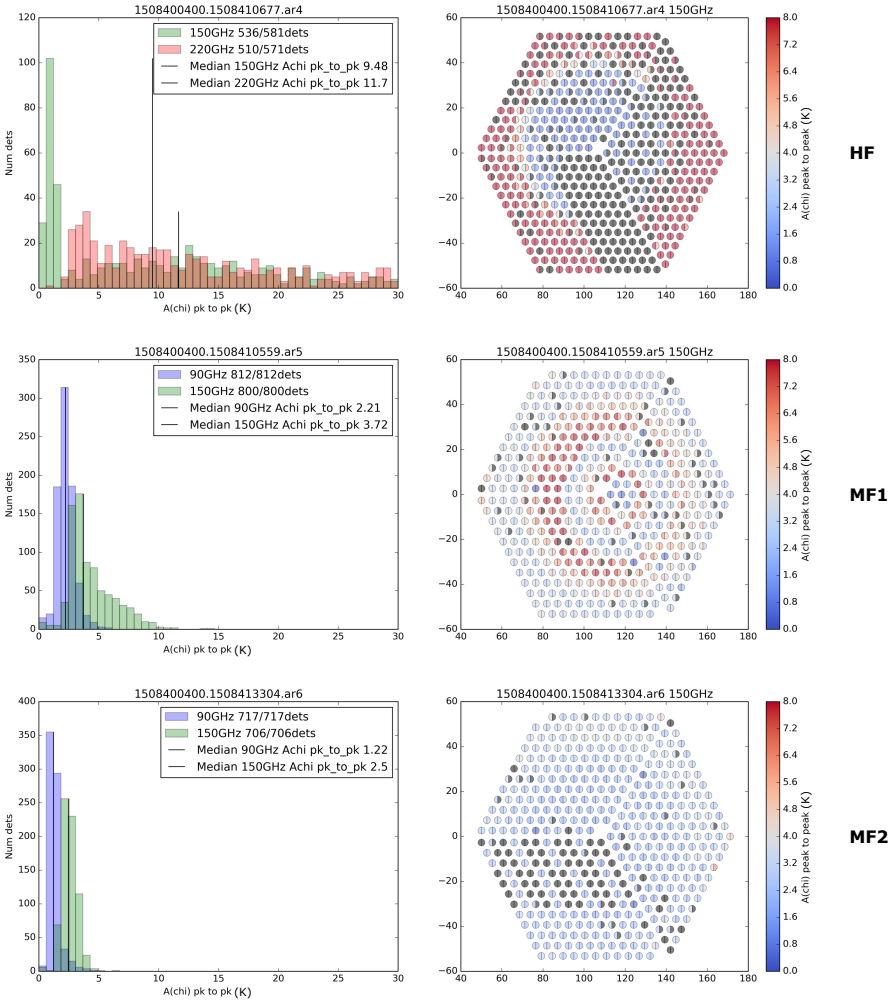

Figure 4.9: Characteristic A(χ) amplitude, measured in peak-to-peak K, for a specific TOD across all three AdvACT arrays with their CRHWPS, with HF (top), MF1 (middle), and MF2 (bottom). In the left column, black lines indicate the per-channel median given in the legends. The right column shows the A(χ) peak-to-peak amplitude as a function of detector position in the array for the 150 GHz detectors, with dark gray indicating detectors that have been cut. The physically-identified feature of MF1 is apparent in the 150 GHz peak-to-peak array (middle right) as the contribution above 5 K. Detectors at the same radius scan across the feature as the HWP rotates.

the median value across detectors of the non-HWP frequencies. For the lowest band of frequencies (upper-left panel in both the top and bottom plots), we see that the A(χ)

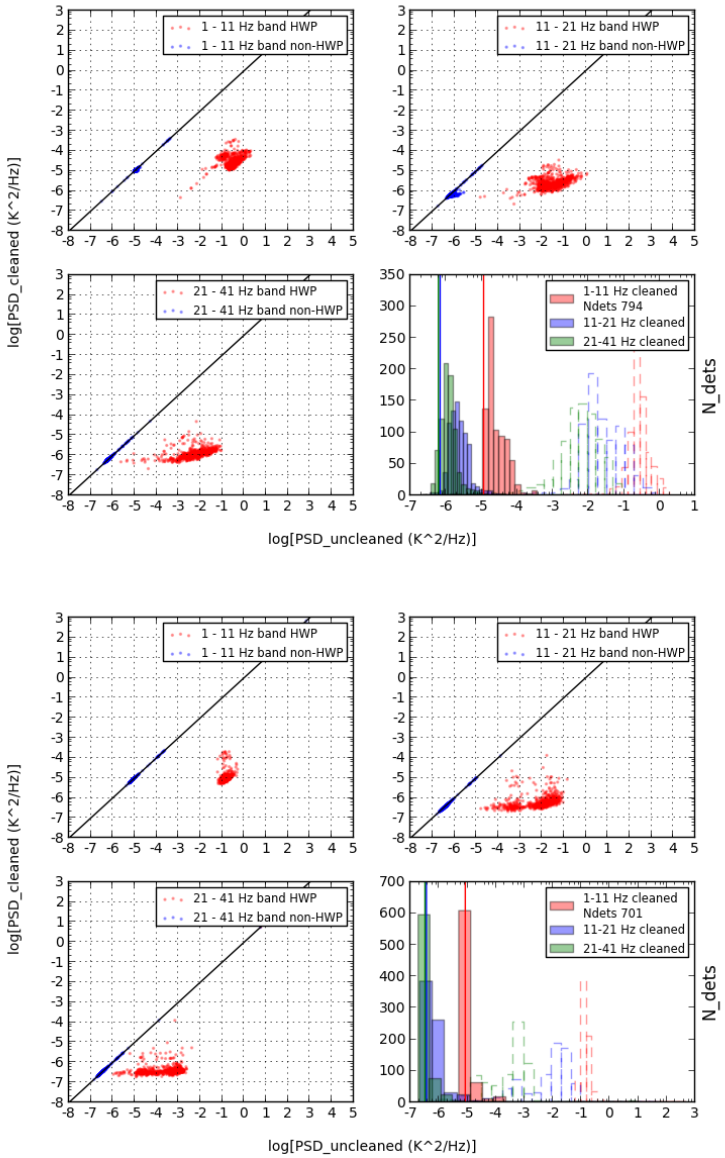

Figure 4.10: Summary of power removal through A(χ) subtraction for a TOD from MF1 (top) and MF2 (bottom). For the two upper panels and bottom-left panel in each plot, we show the average spectral density across frequency samples which are considered to be part of the HWP harmonics (red) or outside them (blue) for 150 GHz detectors in the array. These panels represent data in three ranges of frequency: 1-11 Hz (upper left), 11-21 Hz (upper right), and 21-41 Hz (bottom left). To confirm A(χ) removal performance, we look for equality of the ordinate of the red points, which have had power removed by the subtraction, to those of the blue points. In the bottom-right panel, we show histograms of the average power in the HWP harmonic frequenices before (dashed) and after (solid) removal. The solid vertical lines indicate the white noise floor as estimated from the mean of the non-HWP frequencies.

subtraction has removed 99.99% of the power, on average, in the CRHWP harmonics in this band.

In the results shown in Fig. 4.10 which again are for the 150 GHz channel, we see that for this TOD, the subtracted A(χ) residuals approach the median noise floor level even for the lowest harmonics. In addition, the subtraction is not affecting the non-HWP frequencies, a crucial sanity check achieved by checking that the non-HWP points (in blue) lie along the $y = x$ line in black. We interpret any excess residual to be due to unmodeled drifts of A(χ) on the timescale of the TOD.

Finally, we discuss demodulation performance of our pipeline. Thanks to the small beam ($\sim$ 1.4 arcmin at 150 GHz) and relatively rapid scan speed (2 °/s), the HWP modulation frequency sits below the characteristic frequency with which the beam samples the sky. Thus, demodulation at $4f_r$ convolves multiple pixels, forming a new, extended beam along the scan direction. Given this effect, mapping with demodulated data in AdvACT would require new techniques, which are beyond the scope this work.

However, we can study the demodulated noise properties of our A(χ)-subtracted data. To do so, we bandpass-filter the subtracted timestream around $4f_r$, with a filter width of $\pm$ 1.5 Hz. We then apply m^* to each detector's timestream, multiply by 2 to recover the true Q and U signal (Eq. 4.3), and record the inverse variance-weighted spectral density as in Sec. 3.3. We also do so for the raw TOD and the A(χ)-subtracted TOD. Our results for the TODs with cleaning performance shown above in Fig. 4.10 are in Fig. 4.11. Demodulating this data has drastically reduced noise power on large scales. The presence of residual $1/f$ has not been fully explored, but we estimate a knee frequency of $\sim<$ 50 mHz for the demodulated data of the two arrays.

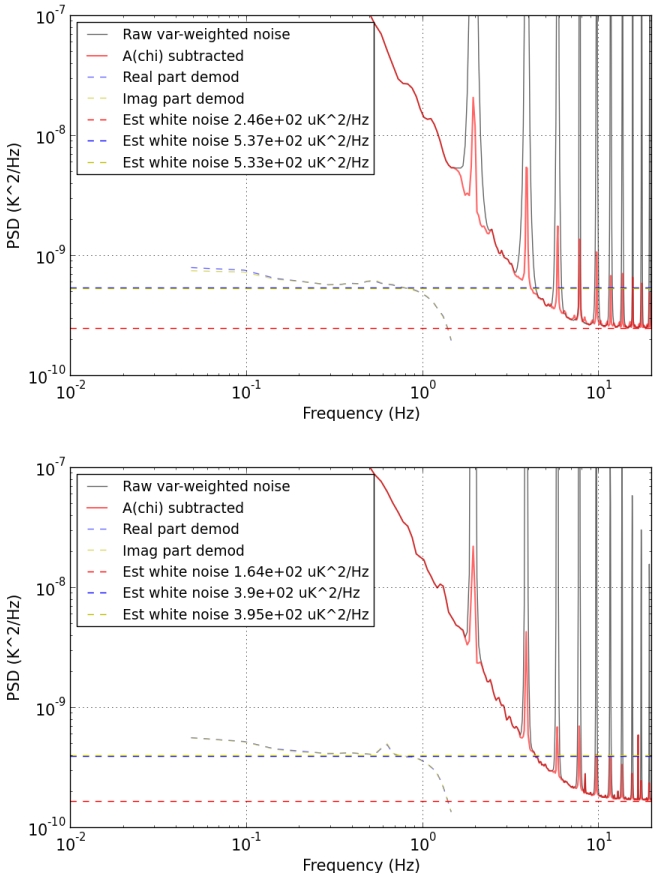

Figure 4.11: Noise spectra for raw TOD (black), A(χ) subtracted TOD (red), and the two components of the complex demodulated spectrum (real, blue; yellow, imaginary). We observe a large reduction in $1/f$ noise due to the bandpass filter and demodulaton technique. The white noise level of the subtracted and demodulated timestreams are indicated by the horizontal dashed lines. with the lines for the real and imaginary components being almost identical. The observed factor-of-two enhancement in the demodulated noise floor is expected due to splitting the raw white noise power between the real and imaginary parts.

4.4 A(χ) Fourier Mode Stability

Given that we can estimate the Fourier series components of A(χ) for every TOD, we now turn to studying how they vary with telescope pointing, time of day, and PWV. These are expected to be the dominant environmental effects which drive changes in A(χ), due to changes in atmospheric loading, changing ambient and CRHWP

temperatures, changes in the telescope optics with the sun, and possible effects from UV illumination.

As shown in Fig. 4.4, we expect a linear change in the $2f_r$ harmonic due to increasing PWV based on ABS. This effect depends on a constant, small value for the differential transmission through the CRHWP of the unpolarized sky intensity. As a reference, we provide a histogram of recovered PWV values for the 75% of the CRHWP period studied in the datasets below, in Fig. 4.12.

It is important to note that, compared to the case with ABS, relative calibration of the AdvACT detectors using the A(χ) values measured in this way is no longer valid. Individual detectors in AdvACT do not see the same incoming signal from the CRHWP due to the details of how their beams pass through the HWP aperture.

However, given this caveat, we have produced a similar data reduction for the CRHWP AdvACT data from MF1 and MF2 in order to determine the level of re-

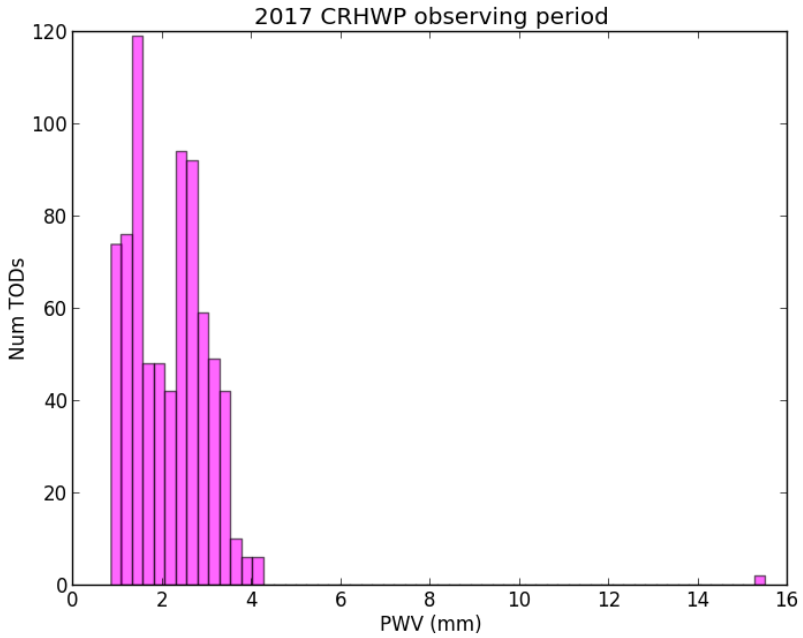

Figure 4.12: Histogram of PWV values estimated by the ALMA weather station [3] for the TODs of the 2017 CRHWP observing period. More commonly used are the measurements from the APEX satellite weather station, which was down during this time.

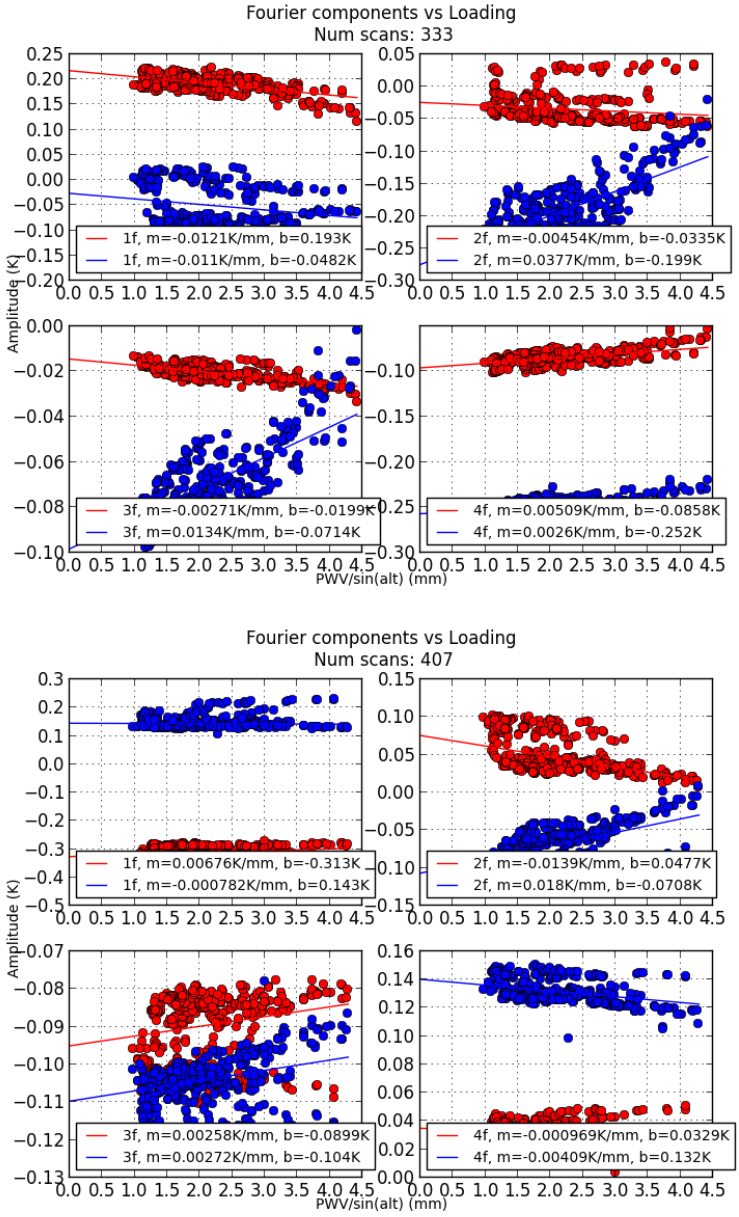

Figure 4.13: A(χ) harmonic response to changing atmospheric loading, measured as PWV/sin(boresight elevation), for an MF1 (top) and an MF2 (bottom) detector, both of them identified as column 4, row 13 in their respective arrays. Each panel in the two subplots corresponds to one of the first four harmonics, with a_m in red and b_m in blue, in the nomenclature of Eq. 4.4. Solid lines indicate the best-fit line for each component, with the parameters given in the legend. Here the intercept "b" is affected by our placement of a pivot scale at loading equal to 2 mm.

sponse to changing loading for different harmonics. We have calibrated these values to K as discussed in Sec. 4.3.2, but have further applied a provisional series of sample

cuts and detector TOD cuts in order to remove detectors with low correlation with the array common mode, and especially readout glitches affecting a small number of samples which could otherwise bias our A(χ) reconstruction when processing $\sim$ 1,000 TODs.

In Fig. 4.13, the results for the first four harmonics of one detector from each of MF1 and MF2 are shown over the four panels of each plot. Comparing the harmonics, it is clear that the $4f_r$ response is smallest, as measured by the slopes given in the legend of each panel. The result further gives evidence for two populations of detector response at $1f_r$, which additionally produces more scatter at $3f_r$ and possibly the other harmonics. We note that the total number of TODs here is somewhat reduced by a lack of PWV data for parts of the 2017 CRHWP observing period. In general, when these data are transformed to harmonic amplitudes by summing the squares of the cosine and sine components, we find that some of these amplitudes decrease with increasing loading. This effect must be further investigated.

The existence of this downward slope with loading, as well as the scatter of the data in Fig. 4.13, presents a difficulty for understanding these data as a data selection tool. However, we investigated the behavior of the first two harmonics as a function of time-of-day, wrapping harmonic amplitudes for all detectors onto an hour axis in UTC. The $1f_r$ result of Fig. 4.14 clearly shows an increase in the A(χ) component amplitude after UTC = 11, which is in the morning in telescope local time.

It appears that we may expect A(χ) amplitudes to rise either as a result of changes to the ACT optics during daytime, or possibly to warming of the HWP in the sun. However, the fact that this affects a harmonic of A(χ) is of great interest. Though it does not appear to affect all detectors, it may be the case that the increase is hidden by another source of variance for detectors where the day-night difference does not appear obvious.

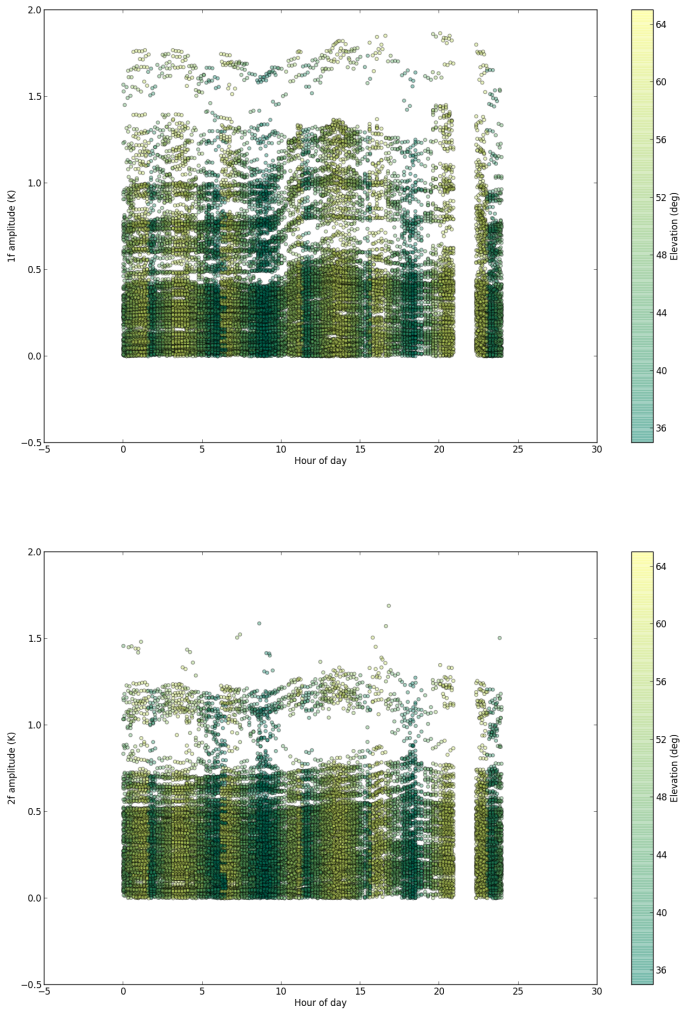

Figure 4.14: Amplitude of the $m = 1$ (top) and $m = 2$ (bottom) harmonics of $\mathrm{A}(\chi)$ (equivalent to $|\tilde{Q}_m|$) vs. UTC hour for all detector TODs across the MF1 CRHWP period. Local time at the telescope was UTC - 3 during these observations. Each point is color-coded by the boresight elevation of the TOD from which it was measured, with overplotting darkening the resulting figure. The vertical stripes result from the AdvACT observing strategy. We are working to further understand the strong step-like behavior of the top panel.

We see similar results, though with a less step-like transition from day to night, with CRHWP data from MF2. In this case, nearly all detectors follow a uniform trend of $\mathrm{A}(\chi)$ harmonic amplitude in the $m = 1$ harmonic, and this is weakly duplicated in the $m = 2$ data. These results are in Fig. 4.15.

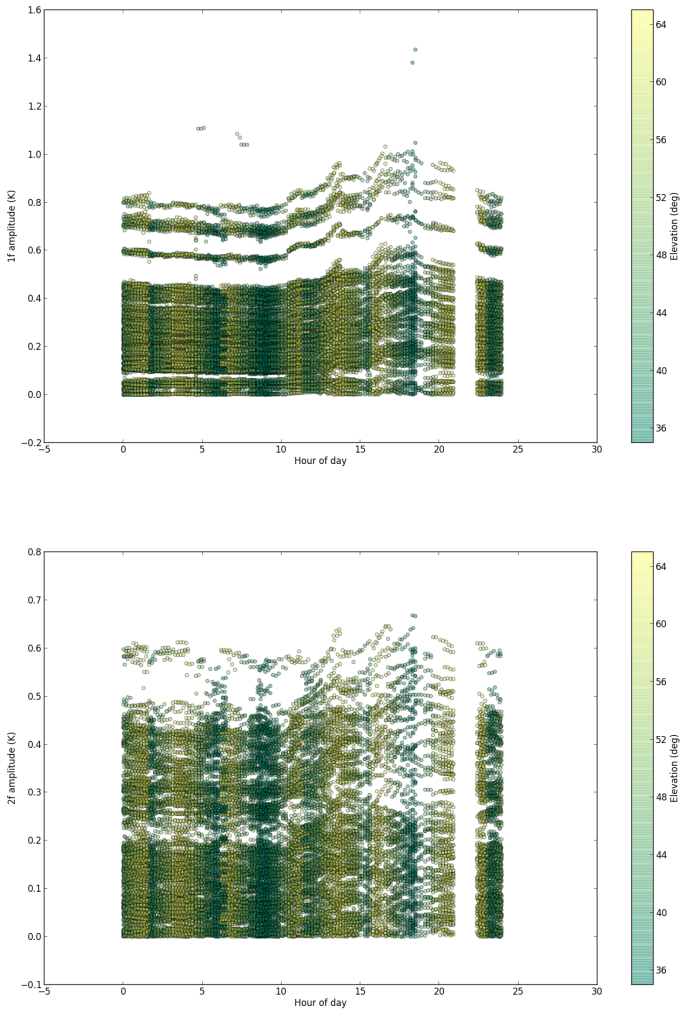

Figure 4.15: Amplitude of the $m = 1$ (top) and $m = 2$ (bottom) harmonics of $A(\chi)$ (equivalent to $|\tilde{Q}_m|$) vs. UTC hour across the MF2 CRHWP observing period. Local time at the telescope was UTC - 5 during these observations. Each point is color-coded by the boresight elevation of the TOD from which it was measured.

Given this hour- or day-timescale dependence of the amplitudes, the investigation of the time variability of our $A(\chi)$ harmonic modes within TODs has been an important part of the larger pipeline development, specifically for the more difficult-to-remove $A(\chi)$ contamination sourced in CRHWP-observing periods with ACTPol arrays prior to 2017. On the other hand, the successful removal of excess power using the estimated $A(\chi)$ from Sec. 4.3.2 indicates this may no longer be as strong a

priority. We leave such a study to future work with the rich CRHWP dataset of 2017 for AdvACT.

4.5 Relative Calibration Using A(χ) Templates

As discussed throughout this chapter, the usefulness of A(χ) harmonic amplitudes for calibrating AdvACT detectors is made more difficult by any nonuniformity of the CRHWP. Imperfections will be observed by detectors within an annulus within the array as the CRHWP spins (see Fig. 4.9). However, this implies that we should expect detectors within annuli to agree on the size and main features of A(χ). An open question is what the relevant annuli size should be, and what to do with detectors at small radius. However, in this section we give some preliminary results and considerations of how to expand this project to further understand the CRHWP data for AdvACT.

First, we anticipate the need to correct a given detector's A(χ) signal for its angular position in the array. We measure this angle from the horizontal axis when looking through the array (i.e. from behind) or into it (i.e. from above, or the sky). Angles increase counterclockwise when viewed from the sky. To correct for this, we essentially shift the argument of A(χ) from χ to $\chi - \gamma$, where we label the angular position of the detector in the focal plane γ.

Second, we correct for the polarization angle of individual detectors being distinct. This was a non-existent effect in the ABS relative calibration of detectors based on harmonic amplitudes, where the different phases of polarization pairs were not a factor.

We can do the above by multiplying element-wise the A(χ) Fourier series components $\tilde{\mathscr{H}}_m$, in an $N_{\rm det} \times N_{\rm harmonic}$ matrix, with a matrix of identical dimension, R. In this matrix, for the detector in row i, with harmonic j+1 corresponding to each

column and with position angle and polarization angle γ_i and ϕ_i respectively, we write the elements to multiply its coefficients by as:

$$R_{i,j} = [\gamma_i, 2\gamma_i + 2\phi_i, 3\gamma_i, 4\gamma_i + 2\phi_i, \cdots]. \tag{4.11}$$

Only the even harmonics are acted on by the polarization-angle correction, as we assume that only power at $m = 2$ or 4 result from polarized interactions. Again, this correction is applied after the individual detector A(χ) bin values and coefficients have been estimated, essentially when the A(χ) per-bin values are reconstructed from a Fourier series using the coefficients.

A first test of this result is provided by plotting the rotated A(χ) estimates, after calculating only the first eight harmonics, in radial annuli. In this case, we have calibrated these detectors using the same values as in previous sections. Since γ_i requires information on the position of individual detectors in the array, e.g. as $\gamma_i = \arctan(y/x)$, it is easy to divide the detector A(χ) into groups using the radius $\sqrt{x^2 + y^2}$. An example for an MF2 TOD is shown in Fig. 4.16 for a group of detectors closest to the center.

After the transformation is performed, a common template can be formed from the A(χ) of detectors in a radial bin. This is best done for detectors at exactly equal radius. We define "equal radius" in this case as those detectors with equivalent radii when rounded to 0.01 level. In Fig. 4.16, we show the new function $A(\chi - \phi)$ for a set of detectors in MF2 at a middle radius on the array (light colored lines), and the common mode indicated in solid black. We have used the same color for polarization pairs (detectors at identical array position in the same frequency channel). These data have been transformed to equivalent optical power in pW, with this conversion estimated from an I-V curve taken before the observation. This avoids pre-applying a calibration through the conversion to Kelvin. However, we have assumed a nominal

direction for the detector response to optical changes, either positive or negative with respect to incoming δP_γ. The common mode here is determined by an average across all detectors at each χ angle defined when generating the transformed $A(\chi)$.

In this figure, the common mode appears to mainly recover unpolarized, odd harmonics. However, we confirm visually that pairs have been corrected to agree on the sign of the large $m = 2$ harmonic mode in individual detector $A(\chi)$. Thus, there must be a reason that the even harmonics are not agreeing between pairs. This may require correction by a sign parameter determined from the response of indivdiual detectors to changing $m = 2$ amplitude with changing atmospheric loading, something we have access to via the studies of Sec. 4.4.

We conclude this section by showing the measured correlation coefficient between the common mode and the detectors at this radius in Fig. 4.17. We plot the coefficient as a scatter versus $A(\chi)$ peak-to-peak in pW (blue circles), with the common mode indicated at 1 on the ordinate axis (black star). These results indicate that the estimates of $A(\chi)$ coming from the largest peak-to-peak detectors are indeed dominating the common mode. Scaling the detectors with smaller peak-to-peak values up, or vice versa, should allow flat-fielding once we are confident in our transformation and common-mode estimation.

4.6 Conclusion

In this chapter, we have presented the concepts and signal processing schemes relevant for understanding and removing the $A(\chi)$ signal due to CRHWPs. We have then applied these to the study of TODs from the special observing run of AdvACT with three silicon metamaterial HWPs. A fast algorithm for estimating the individual-detector $A(\chi)$ signal across the thousands of detectors in an AdvACT HF and MF array has been presented. We have further presented evidence for the significant cleaning per-

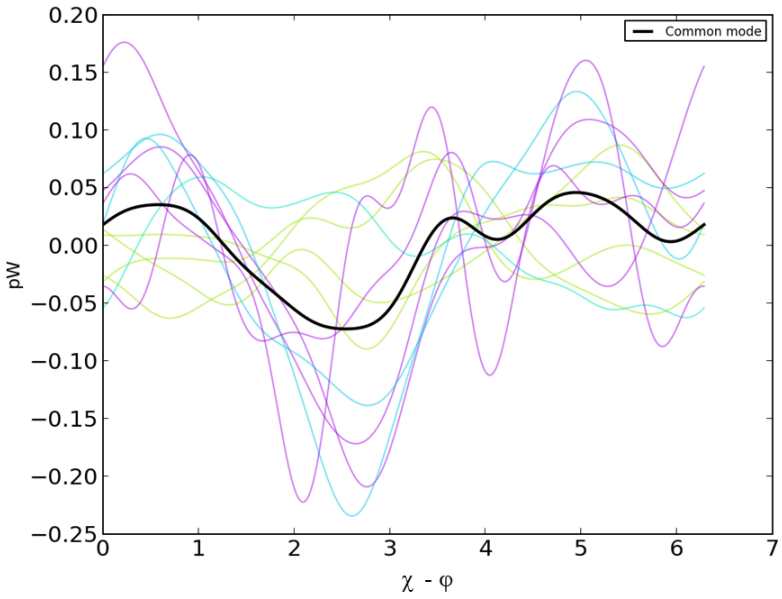

Figure 4.16: Values of the adjusted $A(\chi - \phi)$ function in units of equivalent optical power, in pW, for a set of eight pairs of detectors near the center of MF2 during a CRHWP observation. We are here interested in pW since we hope this technique could yied estimates of the relative gain of these bolometers before we convert pW to K. Again, ϕ is the angle of the plotted detector pair, increasing counterclockwise from the horizontal. Each pair has a common color determined by its horizontal position in the array. The common mode (solid black) appears visually to be dominated by odd-harmonic modes like $1f$ and $3f$. This may be due to differences in the polarized $\mathrm{A}(\chi)$ components between pairs. There then must be some effect spoiling the expected sign change between $\mathrm{A}(\chi)$ measured across polarization pairs. We are working to improve this study for future use.

formed by this pipeline (10^4 in power) as well as the power of demodulating these data for reducing the knee frequency of $1/f$ noise in the polarized timestreams.

Finally, we have described preliminary results on the dependence of $\mathrm{A}(\chi)$ Fourier series components on environmental factors like atmospheric loading, using PWV as our proxy, as well as describing a possible method by which the similar $\mathrm{A}(\chi)$ signals present for detectors at the same radius in the array can be used to relatively calibrate these devices.We plan to continue our study of these observations in order to maximize the understanding of the performance of the AdvACT CRHWP system, as well as to achieve our science goal of allowing ACT to study large-angular-scale sky modes.

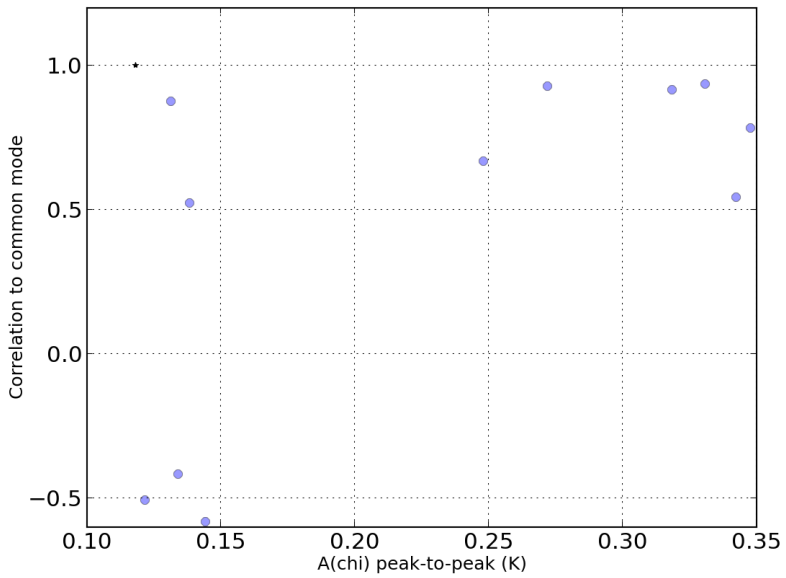

Figure 4.17: Pearson correlation coefficient estimated for the detectors with transformed A(χ) shown in Fig. 4.16. These data are plotted versus the transformed A(χ) peak-to-peak value, which is equal to the size of the untransformed A(χ) signal. These results are preparatory to determining a flat-field correction based on the CRHWP signal. We note that the presence of detectors with correlations < 0 is tentative evidence for a need for an apparent sign correction for these bolometers, or the possible presence of a second mode that dominates A(χ) for some pairs.

Chapter 5

Maximum-Likelihood Studies of CMB Results

In this section, we describe the power spectrum estimation pipeline used in the reduction of data from ABS. The instrument was introduced in Sec. 1.4.2. Here we present a brief introduction to the analysis scheme used by ABS to estimate power spectra, based on the MASTER pipeline [52]. We then describe the construction of likelihood functions based on parametric descriptions of the probability density functions of polarization spectra bandpowers and the scalar-to-tensor ratio r. These results are based on Monte Carlo simulations of ABS observations, which simulations are critical to the pipeline. We conclude by presenting the errors on the measured ABS bandpowers and the upper-limit determination on r derived from the likelihoods. A final comment concerns the effect of estimated foreground power at large scales and its possible effects on these results.

5.1 ABS CMB Power Spectra Pipeline

In the field of studies of the CMB, the mathematical operations involved in reducing many channels of time-domain detector samples into sky signal maps and spherical

harmonic power spectra have been well-studied [104] [10] [90]. However, practial considerations applying to real observations often introduce processing steps or observational constraints that complicate the reduction process. Generally, the most critical effects are due to i) observation of a small patch of sky ("Field A" in [68] is 2400 $\deg^2$), and ii) filtering operations on the detector timestreams (for ABS, these occur in the HWP demodulation scheme and in scan-synchronous signal subtraction, for instance). Accounting for the effects of these operations in the mapmaking equation and power spectrum estimators often results in computationally-intensive pipelines.

An alternative is to create a Monte Carlo (MC) simulation pipeline that can itself feed into the data reduction pipeline of an experiment, just as the real field data. This requires drawing realizations of a CMB sky based on input power spectra, which can represent a ΛCDM universe or a generic functional form. The simulated CMB sky is then "observed" by a representation of the ABS instrument that must capture all relevant details of the experiment, including, for example observation strategy, noise properties, and bad samples. However, the simulated pipelines may then be treated just as the real data are, and reduced using a simplified, compact pipeline that can afford to be naive. By performing this operation hundreds of times, the statistical properties of important quantities like the C_ℓ of the power spectra can be captured.

The use of this process to calibrate out the effects of naive reduction on real CMB instrument data is discussed in detail in [52]. In ABS, the pipeline was designed by A. Kusaka building from work on the QUIET experiment with K. Smith [105], with a power spectrum estimation code used in studies of both simulation and data developed from the QUIET pipeline by S. Choi [11]. As applied in ABS, the pipeline begins by making a weighted-average map based on the value of each detector sample that is not cut due to the data selection criteria. The weight applied is the assumed inverse

variance, taken from the white noise level of the relevant detector's demodulated timestreams.

Once the map is constructed, the pseudo-C_ℓ power spectrum, [130] [119] so called due to the individual C_ℓ containing contributions from noise modes, is estimated from it. This spectrum is known to be biased by the effects mentioned above. We write the relation between the true sky variance at scale ℓ, $\langle C_\ell \rangle$, and the estimated value $\langle \tilde{C}_\ell \rangle$, as:

$$\langle \tilde{C}_\ell \rangle = \sum_{\ell'} M_{\ell\ell'} F_{\ell'} B^2_{\ell'} \langle C_{\ell'} \rangle, \tag{5.1}$$

where the angled brackets imply an ensemble average, $M_{\ell\ell'}$ describes all mode-mode couplings due to the geometry and weighting applied to the Field A map, F_ℓ is the signal transfer function that captures the signal loss due to timestream-level filtering, and B_ℓ is the harmonic-space window function induced by the ABS beam geometry and pixelization effects. This equation is simplified due to the rejection of noise bias in the ABS spectra resulting from constructing $\langle \tilde{C}_\ell \rangle$ from cross-spectra of spherical harmonic coefficients $\tilde{a}_{\ell m}$ derived from maps estimated from disjunct three-day subsets of the ABS observations.

As said above, the MASTER pipeline scheme is to determine the effective values of the unknown quantities $M_{\ell\ell'}$ and F_ℓ at all scales. We assume that removing the effects of the C_ℓ beam bandpower is done not through comparing simulation to signal, but from direct experimental calibration. Before estimating the other biasing parameters, the pseudo-C_ℓ powers are binned in ℓ. This produces a power spectrum estimator indexed by bin number b, $\tilde{C}_b$, where we may acceptably treat each bandpower as an independent random variable. An unbiased power spectrum estimator, $\hat{C}_b$, is finally calculated as:

$$\hat{C}_b = B_b^{-2} F_b^{-1} \sum_{b'} M^{-1}_{bb'} \tilde{C}_{b'}. \tag{5.2}$$

As a practical matter, the estimator for F_b^{-1} is determined by drawing sky from white-noise C_ℓ spectra with unit power. The resulting estimated power spectra $\hat{C}_b$ are then a direct measurement of F_b, and can be divided out from all subsequent estimates.

We conclude this section by noting that, though ABS works with a pipeline that requires careful, accurate simulations for debiasing, the quick processing of any needed simulations (from fiducial ΛCDM signals, to mapping noise-only data, to turning on and off systematic mitigation schemes and filters) gives the pipeline a large amount of flexibility. This, and its relative computational cheapness, make it a very useful tool for CMB data reduction. In addition, as described in the next section, we can numerically estimate errors for power spectra bandpowers, and other quantities derived from them, using ensembles of MC realizations generated by the pipeline. This can be done by taking either the standard error over the ensemble, which is used in ABS for null test studies, or by constructing a likelihood for the given quantity assuming some parametrized form for the probability density function (PDF). In the next section, we describe the first part of the latter process: estimating the PDF of the quantity from the ensemble results.

5.2 Probability Density Function Estimation

In this section, we describe the application of techniques developed for the QUIET experiment [105] to the estimation of PDFs for i) the CMB spectral bandpowers measured by ABS for EE and BB, and ii) r, the scalar-to-tensor ratio.[1] Since the former is the canonical case, we introduce the formalism first with regard to bandpowers before describing its application to estimating a PDF (and, thus, a likelihood) for r.

[1]This work is also indebted to the QUIET internal study on maximum-likelihood analyses by A. Kusaka.

The functional form used to describe the bandpower PDF is a scaled χ^2 distribution with number of degrees of freedom ν and an independent parameter, σ, defining its standard deviation. This captures the known skewness in the bandpower PDFs, which have also been studied by assuming a log-normal PDF [8]. In our case, we additionally shift the modified χ^2 such that its mean is zero. Writing this function a conditional probability $P(a|b)$, which we read as "the probability of a given b," and writing the original χ^2 PDF as P_{χ^2}, we define our shifted, scaled version as:

$$P^M_{\chi^2}(x|\nu,\sigma) = \frac{\sqrt{2\nu}}{\sigma} P_{\chi^2}\left(\nu\left[\sqrt{\frac{2}{\nu}}\, x/\sigma + 1\right] \mid \nu\right). \tag{5.3}$$

This general probability distribution can be used to define the conditional probability of observing $\hat{C}_b$ given an input C_b:

$$P(\hat{C}_b|C_b) = P^M_{\chi^2}\left(\frac{\hat{C}_b + N_b}{C_b + N_b} - 1|\nu,\sigma\right)/(C_b + N_b). \tag{5.4}$$

The random variable x of Eq. 5.3 is now a function of C_b, $\hat{C}_b$, and a quantity termed the "noise bias" N_b. The ratio taken in this argument ensures our likelihood for C_b will always peak at $\hat{C}_b$, with N_b determining how the distribution width may scale with the recovered $\hat{C}_b$. Because the suite of MC ensembles run through the simulation pipeline includes noise-only simulations, we are able to estimate N_b directly from the bandpowers of the noise-only spectra. In order to estimate N_b from signal simulations, we require simulations with two different C_b input values. This is a natural requirement for the r pipeline, and therefore also for BB bandpowers. However, in general, we take N_b as given.

We have written a script to perform a negative log-likelihood minimization over ensembles of MC realizations produced using the CMB Boltzmann solver CAMB [77], with each realization providing a value for $\hat{C}_b$, in order to estimate the parameters σ and ν for each bandpower. In fact, we choose to minimize the function with respect to

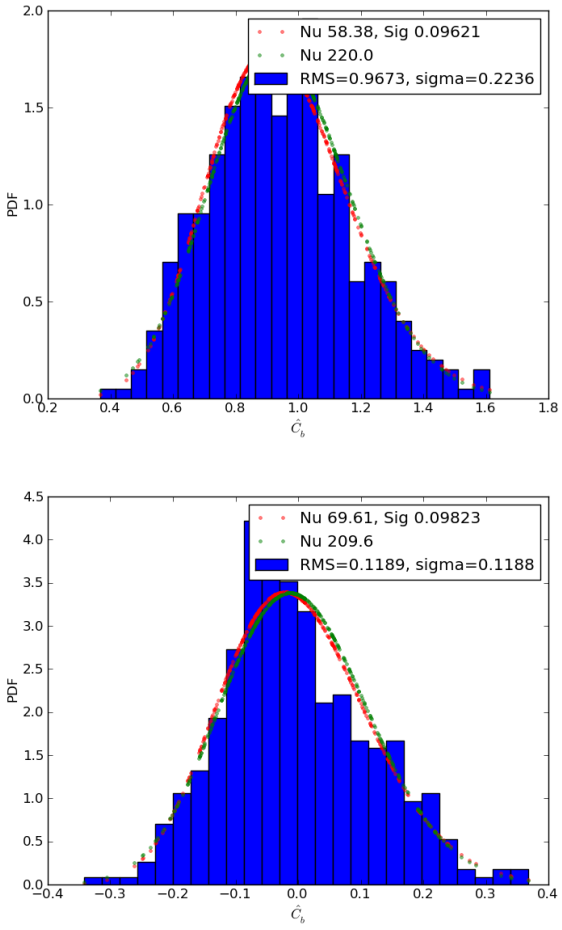

Figure 5.1: *Top*: Distribution of fiducal MC ensemble (400 simulations) generated by ΛCDM simulations for the EE bandpower covering ℓ in [101,130]. The two sets of dotted points indicate the best-fit PDF functions for free σ, ν parameters (red) and a reduced model, equivalent to a scaled χ^2 translated to have zero mean, achieved by setting $\sigma = \sqrt{2/\nu}$ (green). The best-fit parameters, and some statistics of the MC ensemble, are in the legend, with the parameter N_b being estimated directly from the mean of noise-only MC ensemble results for this bandpower. *Bottom*: Best-fit results for the same models, matched to the same colors, for the BB bandpower over the same range of ℓ. Here the fiducial model is zero bandpower input, hence the distribution being centered around zero.

the parameter $\sqrt{2/\nu}$, which instead of diverging as the PDF function approaches the normal distribution, trends smoothly to zero. We perform the minimization of the negative log-likelihood with the iminuit Python wrapper of the "migrad" algorithm in the C package Minuit [59]. Again, this assumes C_b and N_b are known.

Figure 5.1 shows the fit to the bandpower ensembles for the bandpower bin $\ell \in [101, 130]$ for the EE (top) and BB (bottom) spectra over 400 fiducial realizations. For EE, the fiducial model is a full ΛCDM sky realization. For BB, the fiducial input spectra is zero everywhere. Each dot represents a single MC realization, and the blue histogram of the ensemble $\hat{C}_b$ values is purely for qualitative comparison. The histogram has been normalized to produce a true PDF. We provide some sample statistics for the ensemble in the legend.

In this case, we see that the green points, representing a scaled, shifted χ^2 achieved by setting $\sigma = \sqrt{2/\nu}$, is quite close to the best-fit two-parameter distribution. This indicates that we are very close to the regime where the bandpower estimators are distributed exactly as χ^2 variables formed from the sum of the individual, Gaussian-distributed harmonic powers.

As an example of the possible effect of estimating N_b, Fig. 5.2 shows the same fiducial distribution (i.e. $C_b = 0$ for BB) for the same bandpower as show in Fig. 5.1. In order to do so, we must jointly fit the PDF model of Eq. 5.4 to two MC ensembles. The first is the fiducial BB ensemble already discussed, and the second takes bandpowers determined by the bandpowers of summed BB lensing and non-zero r bandpowers. In these simulations, we set $r = 0.9$ based on initial estimates of the sensitivity to r of the ABS data. Though this was an underestimate, we can still constrain N_b in this way.

For certain bandpowers in both the EE and BB spectra, we find that the minimization prefers very small values of the quantity $\sqrt{2/\nu}$ which we use in our fit function. We confirm that there is no clear minimum for non-zero values of this parameter by running a one-dimensional minimization of the function with respect to σ for fixed values of $\sqrt{2/\nu}$. If the negative log-likelihood trends monotonically towards smaller values as the parameter approaches zero, we take there to be no reasonable constraint on the parameter.

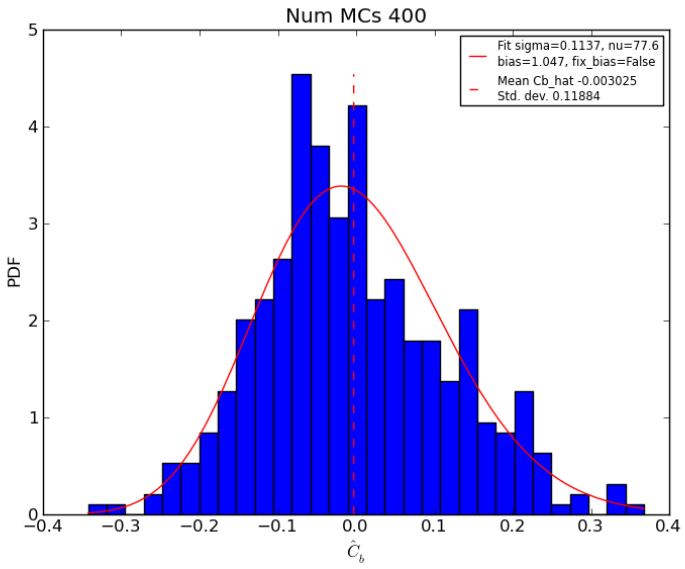

Figure 5.2: The same fiducial BB MC ensemble shown in the right panel of Fig. 5.1, but with N_b a free parameter. The constraint on N_b comes from jointly fitting the model of Eq. 5.4 for two MC datasets: the BB fiducial ensemble and an ensemble with $r = 0.9$. The recovered bias on the bandpower N_b is 20% smaller when compared to the estimate from noise-only simulations, $N_b = 1.21$.

When this is the case, we assume a Gaussian distribution for the PDF (the result of taking $\nu \to \infty$) with zero mean, and then estimate the variance σ in order to define the bandpower PDF. We set an upper limit on the parameter $\sqrt{2/\nu}$ using the value of the parameter for which the negative-log likelihood increases above the minimum by one. Figure 5.3 shows a check on the trending of the parameter toward zero for a particular EE bandpower. The color bar encodes the likelihood value and the two axes show the fixed parameter (x-axis) and the free parameter to be minimized, σ (y-axis).

Taking the foregoing discussion into account, we provide in Tab. 5.1 and Fig. 5.4 the results for fitting ν and σ to the EE and BB band powers over the first nine ell bins in ABS. Errors are here estimated from the covariance matrix reported by Minuit at the minimum, except for the upper bounds on $\sqrt{2/\nu}$ (one-sided error bars in the plots), which are discussed above. Partially due to the issues with the ensembles for

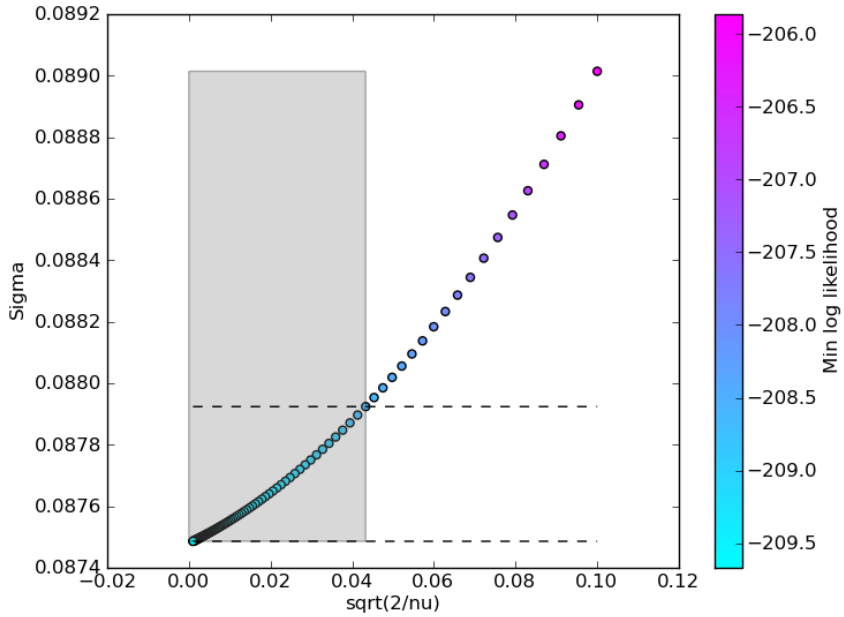

Figure 5.3: The minimum negative log-likelihood (colormap) when the PDF of the fiducial MC ensemble of the fourth EE bandpower is minimized with respect to σ for various values of $\sqrt{2/\nu}$. The σ values minimizing the function are plotted on the y-axis. There is no minimum found above the bottom-leftmost point closest to $\sqrt{2/\nu}$ = 0. The shaded region defines the 1-σ upper-limit on the $\sqrt{2/\nu}$ parameter, while the dashed line shows the estimated 1-σ error bar on the σ parameter. We do not use this minimization in this case, but instead revert to fitting a Gaussian PDF to the distribution (see text).

	EE		BB	
ℓ Range	σ	ν	σ	ν
41-70	0.16	190	0.16	180
71-100	0.12	340	**0.12**	**130**
101-130	0.10	60	0.10	70
131-160	0.08	80	**0.09**	**260**
161-190	0.07	600	0.08	1.0×10^5
191-220	0.07	200	0.07	290
221-250	0.06	160	**0.06**	**500**
251-280	0.06	370	0.06	220
281-310	**0.05**	**670**	0.06	790

Table 5.1: Estimated values for σ and ν when fitting Eq. 5.4 to the values of $\hat{C}_b$ over the MC ensemble used in ABS science analysis. Bolded values indicate PDFs estimated according to the single-parameter prescription, where we set $\sigma = \sqrt{\frac{2}{\nu}}$.

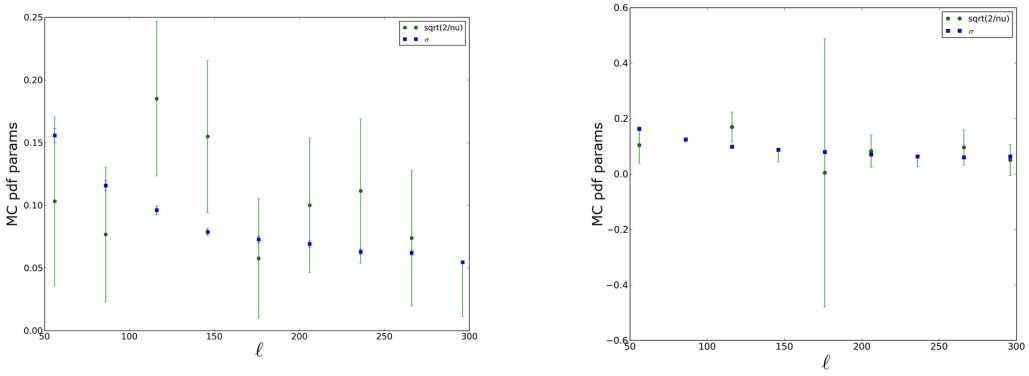

Figure 5.4: *Left*: Best-fit values and estimated errors for the PDF parameters σ and $\sqrt{2/\nu}$ across the first 9 EE bandpowers for ABS. See text for discussion of the one-sided error bars. *Right*: Best-fit values for the PDF parameters for the first 9 BB bandpowers.

certain bandpowers discussed above, our final bandpower PDFs are determined using the single-parameter (i.e., setting $\sigma = \sqrt{2/\nu}$) best-fit χ^2 distributions. It is these which will go into the likelihood used for error estimation in Section 5.3.

We now progress to a discussion of how this formalism can be used to describe the PDF of r. We use the same PDF expression but replace bandpowers (both estimates and known theory values) with r. We also introduce a parameter r_b, analogous to N_b in the bandpowers:

$$P(\hat{r}|r) = P^M_{\chi^2}\left(\frac{\hat{r}+r_b}{r+r_b} - 1|\nu,\sigma\right)/(r+r_b). \tag{5.5}$$

However, as opposed to the case for N_b, which was estimated from noise-only simulations, we recover r_b using the joint-fit technique for ensembles describing fiducial ($r = 0$) and signal ($r = 0.9$) power spectra.

Before we can apply our PDF fitting technique, we must generate the distribution of estimated r values $\hat{r}$. To do so, we use a χ^2 minimization pipeline that takes as input the bandpowers of an individual MC realization, the assumedly Gaussian errors derived from the sample standard deviation of the bandpowers in the ensemble, and

a theory curve. We form the theory curve by summing the mean bandpowers from 100 noiseless simulations of $r = 0.9$ simulations, where the simulations are scaled to produce an r signal curve for $r = 1$, and noiseless simulations ΛCDM lensed BB bandpowers. An estimated $\hat{r}$ is then recovered by letting the fit parameter scale the r =1 contribution to the bandpowers. We perform this fit over both the first three and first four bandpowers in separate trials as an attempt to determine the statistical weight of random fluctuations in the fourth ℓ bin.

Before working with the resulting distributions of $\hat{r}$, we confirm that any bias introduced by the fitting choices are negligible. This can be seen in the two panels of Fig. 5.5, which show the recovered $\hat{r}$ distributions for the two ensembles (zero and non-zero r) in the two columns, with rows showing the resulting distributions of $\hat{r}$ when fitting the first three (left) or the first four (right) bins. These panels also show the best-fit PDF involving three parameters in each row: σ, ν, and the common bin parameter r_b. We find r_b is fairly large, implying a slightly impaired sensitivity to r. We also decide to use the first three bins for all subsequent r analysis, in order to avoid the influence of excess fluctuations as ABS loses sensitivity with increasing ℓ.

With these parameters in hand, we have thus numerically estimated the PDF of the scalar-to-tensor ratio r as seen by ABS. We then proceed to construct the likelihoods for the bandpowers and for r.

5.3 Bandpower and r Likelihoods

Before detailing the method for recovering likelihoods from the best-fit PDFs derived from ABS MC ensembles, we mention that the intention in determining these likelihoods is to set the most accurate possible error bars on the key values estimated by the ABS analysis. With the likelihoods in hand, we are quickly able to define 1-sigma errors and 2-sigma 95% confidence levels by applying Wilks' theorem, associating

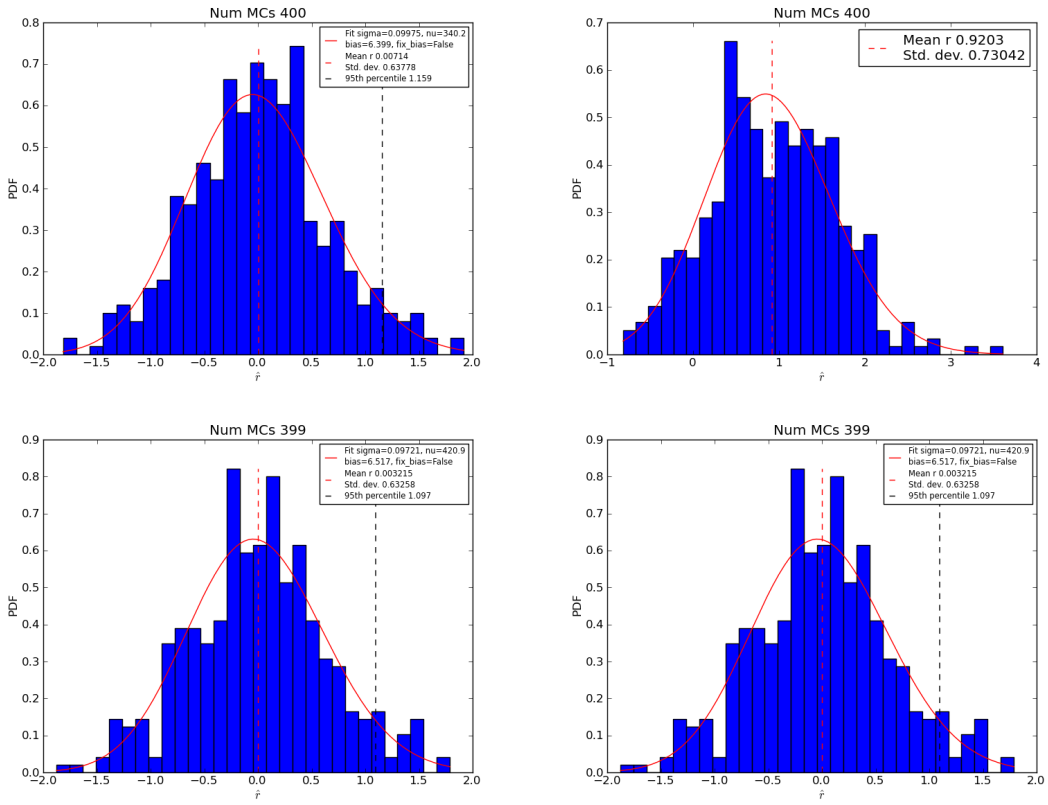

Figure 5.5: *Top row*: Distributions of $\hat{r}$ and the best-fit parameter PDF using a joint fit across the fiducial (left, $r = 0$) and signal (right, $r = 0.9$) ensembles. Each ensemble has 400 MC realizations, where $\hat{r}$ for each realization is estimated from fitting to the first three bandpowers, as discussed in the text. We note that the bias, estimated from the difference between $\langle \hat{r} \rangle$ and r, is small in both cases, thus validating our minimum-χ^2 pipeline. *Bottom row*: The same as for the top row, except the fit used to recover $\hat{r}$ uses the first four bins.

these limits with the the parameter values for which the log likelihood decreases from its maximum by 1 and 4, respectively.

We now define the likelihood used for the individual bandpowers C_b, taking the prescription of Hamimeche and Lewis, 2008 [49] with the caveat that we assume negligible covariance between bandpowers. This also distinguishes the ABS likelihood analysis from that used in [105]. This results in the following:

$$\mathcal{L}_{C_b} = P(C_b|\hat{C}_b) \propto P^M_{\chi^2}\left(\frac{\hat{C}_b + N_b}{C_b + N_b} - 1|\nu, \sigma\right)/(C_b + N_b). \tag{5.6}$$

In essence, we have simply inverted the parameter of interest in our already-measured PDF. We have not applied Bayes' theorem (i.e. defined a prior), but these will be additive constants to the log-likelihood and can thus be ignored in our $\Delta\mathcal{L}$-based analysis. We note that this "change of views" does not mean that $\mathcal{L}_{C_b}$ as a function of C_b is identical to the the PDF as a function of $\hat{C}_b$. Given the places of these terms in the denominator and numerator, respectively, of our random variable in Eq. 5.4, and the extra scaling factor outside of the χ^2 function, the likelihood has a distinct shape. We must also take, as input to $\mathcal{L}_{C_b}$, a value for $\hat{C}_b$, since changing this parameter will affect the errors and upper limits derived from the likelihood.

The argument above applies equally to the likelihood for r, $\mathcal{L}_r$. Figure 5.6 shows the impact of this perspective change, by plotting $2ln(\mathcal{L}_r)$ vs. its dependence on values of r (red) or $\hat{r}$ (green), which share a common axis. When the one parameter is being varied, the other is set to zero. The increase in the width of the distribution for theory r is expected since the random parameter explores the skewed high side of the approximately χ^2 PDF. The true likelihood, assuming ABS measured an $r = 0$, would be the red curve.

However, an additional complication arises due to calibration uncertainty in the BB bandpowers. Capturing this effect requires marginalizing over a Gaussian-distributed calibration factor s, with $\mu = 1$ and σ_s. The likelihood $\mathcal{L}_r$ then becomes [39]:

$$\mathcal{L}_{r,\mathrm{corr}} = \int_{-\infty}^{\infty} \mathcal{L}_r(s \times r) \frac{1}{\sqrt{2\pi}\sigma_s} e^{-\frac{(s-\sigma_s)^2}{2\sigma_s^2}} ds. \tag{5.7}$$

When this is done, the resulting two-sigma upper limit on r has been mildly increased. The final result for the ABS upper-limit on r, shown in the left panel Fig. 5.7, shows both the original and calibration error-convolved curves for estimated $\hat{r}$ of 0.65. The fit producing this estimate of $\hat{r}$ is shown in the right panel of the figure.

Having derived the upper limit on r, we move to bandpower error estimation. In determining 1-σ bandpower errors, we remind the reader that we have taken the

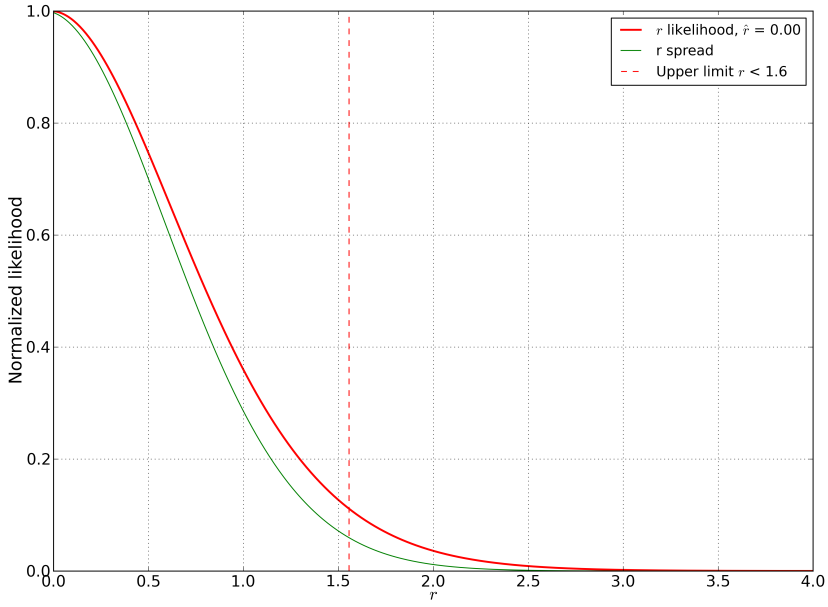

Figure 5.6: Correct likelihood for r (red) given $\hat{r} = 0$ compared to the plotting the PDF as a function of $\hat{r}$ when $r = 0$. The plot demonstrates the change in the function shape depending on whether we study the PDF or $\mathcal{L}_r$.

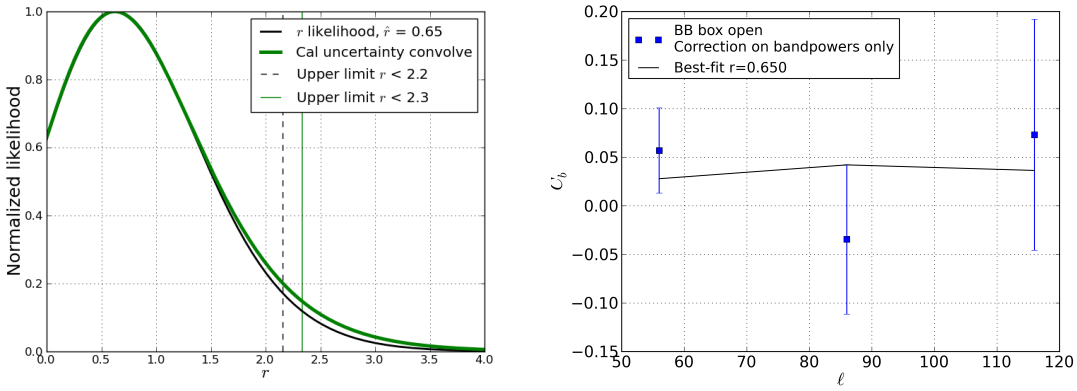

Figure 5.7: *Left*: ABS likelihood for r without (black) and with (green) the convolution of a Gaussian term describing the calibration uncertainty. The upper limits indicated are the points where $\Delta\mathcal{L}_r = ln(\mathcal{L}/\mathcal{L}_{\max} = -4$. Previously published in [68]. *Right*: ABS data and the best-fit theory spectrum for the first three bandpowers. This defines the $\hat{r}$ we assume in the likelihood at left.

simplifying assumption of setting $\sigma = \sqrt{2/\nu}$ when fitting our PDF functional form to the MC distributions. The derived likelihoods and vertical lines indicating separately

the upper and lower 1-σ errors on the same bandpowers whose PDF fits we showed in Fig. 5.1 are shown in Fig. 5.8. Again, the results for the EE bandpower are shown in the top panel and those for the BB bandpower are shown in the bottom.

We note that as we move to bandpowers at larger ℓ, we expect the number of degrees of freedom to increase. This has the effect of causing the PDF functions to approach Gaussian distributions, for which we would expect the likelihood errors to be more symmetric. Tab. 5.2 collects the ABS bandpowers estimated from data, the

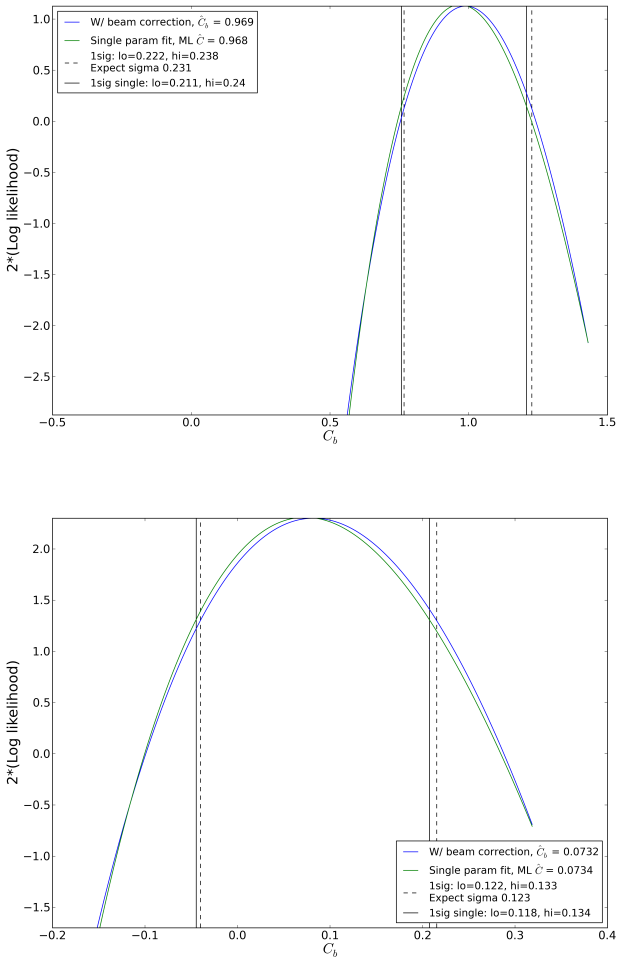

Figure 5.8: *Top*: Likelihood for the EE bandpower spanning $\ell \in [101, 130]$. The two curves show likelihoods with and without a final beam correction based on cross-correlation of ABS spectra with Planck [68]. Our results assume the green curve and dashed one-σ upper and lower error bars. *Bottom*: BB bandpower likelihood for the same ℓ span as int he left panel.

	EE			BB		
ℓ Range	Bandpower	ML Error	ν	Bandpower	ML Error	ν
41-70	0.33	+0.10/-0.09	80	0.06	+0.06/-0.05	80
71-100	0.47	+0.15/-0.13	150	-0.03	+0.08/-0.07	130
101-130	0.97	+0.24/-0.21	220	0.07	+0.13/-0.12	210
131-160	0.59	+0.25/-0.22	330	0.13	+0.21/-0.19	250
161-190	0.25	+0.30/-0.28	380	0.21	+0.32/-0.28	310
191-220	0.5	+0.5/-0.4	420	-0.2	+0.4/-0.4	400
221-250	1.2	+0.7/-0.7	510	-0.5	+0.6/-0.5	490
251-280	2.3	+1.1/-1.1	520	-0.3	+0.9/-0.8	560
281-310	5.1	+1.7/-1.6	660	0.1	+1.5/-1.4	500

Table 5.2: Results by band for measured ABS bandpower, asymmetric error bars deduced from the likelihood given the single-parameter fit to the MC ensemble of $\hat{C}_b$, and the parameter ν, the single parameter used to describe the scaled-χ^2 fit.

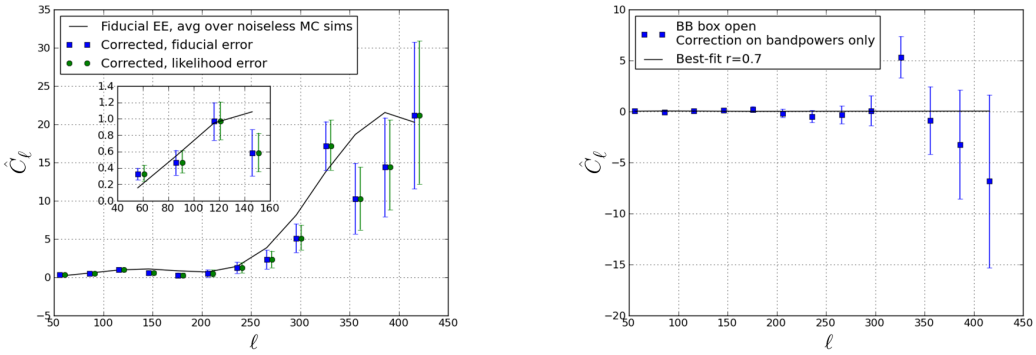

Figure 5.9: *Left*: ABS measured EE spectra with maximum-likelihood, asymmetric error bars (green points) determined as in the text, and fiducial error bars (blue) determined solely from the spread of the bandpower values across the MC realizations. The first 13 bandpowers are shown, with their values and errors, along with other details, in Tab. 5.2. Due to null test failures, only the first 9 bandpowers are provided in the table, and in the result paper (Kusaka et al., 2018 [68]). *Right*: ABS measured BB spectra, with error bars as at left, except the blue points are now the full maximum-likelihood error bar points.

likelihood-derived asymmetric error bars for these bandpowers, and the degrees of freedom fit parameter of their corresponding PDF distributions for the fiducial MC ensembles.

Finally, we show the EE and BB spectra measured by ABS, with appropriate error bars from the table, in Fig. 5.9. The theory curves indicate i) for EE, the average

of the noiselessΛCDM simulations discussed in Sect. 5.2, and ii) for BB, the theory curve used in our minimum-χ^2 fitting pipeline.

5.4 Conclusion

We conclude this chapter, having provided the detailed prescription used to generate the main results of this likelihood pipeline. The ABS upper limit on r is thus revealed to be carefully estimated, but almost three times as large as the estimated r level used in generating the non-zero r MC ensemble. We do not expect this to introduce considerable issues unless an MC ensemble at $r = 2$ were to prefer much different estimate for the PDF bias parameter r_b.

Chapter 6

Future Work: Detector Nonlinearity

We conclude this thesis by discussing additional possibilities for TES bolometer characterization relevant to better understanding performance in the field. Particularly, we focus on concerns about TES nonlinearity when coupled to the HWP harmonic $\tilde{\mathscr{A}}_4$ to produce a spurious signal in the demodulated timestream of CRHWP experiments [123], [23]. We also provide initial simulations used to study this effect in a generic time-domain simulation framework, *s4cmb* in a distinct case, where no CRHWP is present but the TES nonlinearity sources leakage of atmospheric intensity signals due to intensity-driven gain mismatch between detector polarization pairs.[1]

To be explicit, our model for TES nonlinearity can be written as a reobserving function on the input data $d(t)$. Assuming we are only interested in low frequencies in our timestream, we choose to write the nonlinearly-distorted timestream $d'(t)$ as [123]:

$$d'(t) = [1 + g_1 d(t)] d(t - \tau_1 d(t)), \tag{6.1}$$

[1] J. Peloton, https://github.com/JulienPeloton/s4cmb.

where the parameters g_1 and τ_1 would be zero for an ideal detector. These parameters can be estimated by expanding the ordinary differential equations outlined in Ch. 2 to second order. Expressions are recovered that depend on parameters like τ, $\mathscr{L}$, and other familiar components of the simple, and extended, TES bolometer models [123]. We are interested in constraining these parameters in a controlled, calibrated way, preferably *in situ* on the telescope.

6.1 Direct Measurement of Nonlinearity

As a first attempt to probe nonlinearity in AdvACT TES bolometers, we performed a test data acquisition in December 2017 during downtime from observations. We use the MCE to send in digitally-approximated sinusoids of various frequencies to 10 TES bias lines on a common MCE "bias card" in use on the AdvACT HF and two MF arrays. We then look for pickup at twice the input frequency, where if we label this frequency f_s, we expect to see a signal proprtional to g_1, since:

$$d'(t) \sim d(t) + g_1 d^2(t), \tag{6.2}$$

based on simplifying Eq. 6.1 for a measurement where we ignore the phase-lag effects of nonzero τ_1. Such a probe is provided by comparing the amplitude of the discrete Fourier transform at f_s to that at $2f_s$. Assuming a purely sinusoidal input, the ratio of these two is an estimate of the g_1 we wish to determine if we assume some input signal size to convert the dimensionless ratio to something like %/K.

To see the effect of nonlinearity in the frequency domain, Fig. 6.1 shows three current spectral densities (solid curves) measured at three separate input sinusoid amplitudes, in DAC. This is an MF1 detector studied with a reflective cover over the aperture of the receiver window. We can clearly see the increase of the height of the largest peak from green (20 DAC amplitude) to red (160 DAC amplitude), as

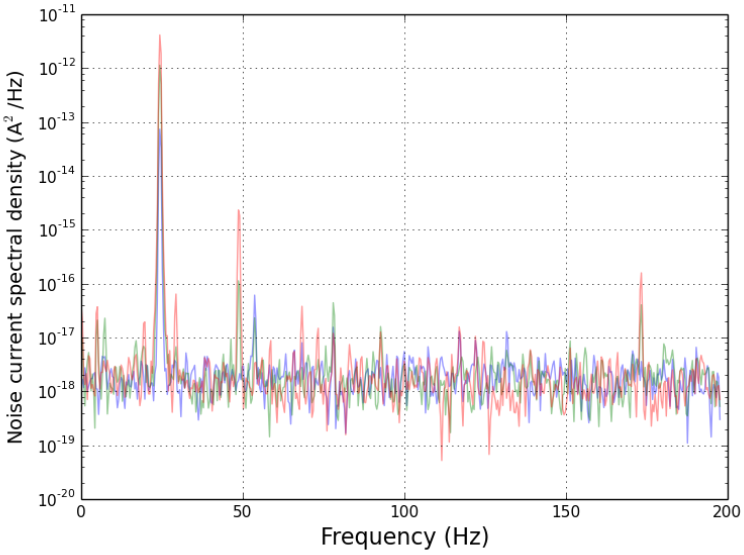

Figure 6.1: An example current spectral density for an MF1 detector on a bias line receiving the MCE digital approximation of a 28 Hz sine wave (main peak). The second peak at 56 Hz is clearly visible, along with other peaks possibly resulting from intermodulation with existing frequency spikes. Colors match to bias sine-wave amplitude, with red = 160 DAC units, green = 80 DAC, and blue = 20 DAC.

well as the increase of the peak at twice this frequency. When we study this effect across many detectors, we find a confirmation of the qualitative behavior we expect. According to the equations provided in Takakura et al., 2017 [123], the nonlinearity should decrease as $1/\mathscr{L}$. From our previous studies, we expect $\mathscr{L}$ to increase low on the transition. Therefore, we would anticipate that data taken with the largest targeted TES resistance would show the largest ratio of amplitude at $2f_s$ to the amplitude at f_s. We also expect that increasing the modulation frequency makes the nonlinearity terms larger.

In Fig. 6.2, we plot the ratio of the amplitudes of the second to the first harmonic of f_s as a function of input sinusoid amplitude. The two panels correspond to f_s = 11 Hz (left) and f_s = 28 Hz (right). In this plot, the colors correspond to the % R_{N} which was targeted during the data acquisition. In this plot, we have ignored devices where the value of the ratio at the smallest amplitude (20 DAC) is above

10%, as these essentially did not show any response to the sine wave. Additionally, this cut ignores devices that were driven into unstable regimes of the transition due to the excitation amplitude. This is an important effect that will likely determine how usefully we may use this technique in the future. We were left with about 1/3 of the MF1 array available to study, those addressed by the 10 bias lines to which we directed the sinusoid.

While our model would predict g_1 to be independent of the input amplitude, we find that for the 160 DAC amplitude, a signficant increase in this ratio is observed. Of course, we may have expected that we were exercising a higher-order nonlinearity given the presence of higher-order harmonics in Fig. 6.1.

If we take the middle amplitude, 80 DAC, and convert this to a bias voltage on the TES, we recover 3 nV. This would then correspond to a current signal of 0.7 pA assuming a TES resistance of 4 mΩ (50% R_{N} and $R_{\mathrm{N}} = 8$ mΩ). Finally, we convert this to a power fluctuation by multiplying the two (equivalently, dividing by the naive estimate of the responsivity), and convert to a brightness temperature fluctuation assuming a rule-of-thumb found for ACTPol and AdvACT of ~ 10 K/pW. This results in assuming our input, if considered as a temperature difference, is ~ 30 mK, and we thus roughly estimate $g_1 \sim 0.1$ %/mK.

This should be compared to the estimate in Takakura et al., 2017 [123] of an expected range for the absolute value of g_1 from 0.2 to 0.4 %/K. There an assumed modulation frequency of 8 Hz was input to the parameter estimates; higher modulation frequencies should increase the terms, but not sufficiently to explain the discrepancy. This is also concerning given the high expected loop gains for AdvACT devices. However, we stress that this study is preliminary. We hope that this probe may be developed in future to provide quick checks of device linearity in the field.

6.2 Simulations of Nonlinearity in Observations

Given the presence of nonlinearity in TES bolometers (Eq. 6.1), it is imperative to understand how this simple model for signal-dependent gain effects may contribute to spurious signal in upcoming CMB instruments. This model arose in Takakura et al. 2017 [123] as a way to explain leakage of an unpolarized atmosphere signal into the demodulated timestream of the POLARBEAR experiment with a CRHWP. However, we also expect that for telescopes without polarization modulators, differences between the nonlinearity coupling values, especially g_1, across different TES polarization pairs may produce a significant leakage of general sky intensity (CMB + atmosphere) I into recovered polarization P.

To get an upper bound on this effect size, we have begun running simulations using a CMB instrument systematic error pipeline available publicly, *s4cmb*. Initial results for this work are presented in Crowley, Simon, Silva, and Goeckner-Wald et al., 2018 [16]. As discussed in that text, various aspects of the design of the Simons Observatory (SO), a project which will span multiple telescopes to be sited near the Simons Array and AdvACT in Chile, were included in the simulations. However, many aspects of the instrument design and observing strategy have not been confirmed within the SO technical team.

Further, the simulation was made more tractable by taking only 32 detectors in 16 pairs, sampled at 32 Hz, and using an effective description of atmospheric noise power as measured by the noise power spectra of existing ACTPol datasets. We modeled the nonlinearity parameters g_1 and τ_1 by calculating them based on current optimum bolometer design parameters for SO, then putting a 10% spread on these parameters, a lower-bound estimate of expected fabrication variance of the bolometers. Finally, the level of nonlinearity was varied between simulated observations by scaling these numbers with estimated changes of $P_{\rm bias}$, assuming a fiducial $P_{\rm sat}$ and changing P_γ due to changing PWV.

We wish to emphasize that these results were achieved with an explicit pair-differencing pipeline, in which sky polarization is recovered at each pixel by subtracting the timestream of one detector from its orthogonally-polarized pipeline. In general, weighting of each detector's sampling of a sky pixel by that detector's polarization angle can more cleanly recover polarization in a map. However, as stated above, pair-differencing represents a "worst-case" leakage, especially when nothing has been done to attempt the mitigate the presence of the effects of nonlinearity.

Our results indicate that, in combination with large, long-timescale, unpolarized signals, the differential nonlinearity of detector pairs can leak an appreciable signal into the recovered maps of polarization (here in Stokes Q and U). We confirm that this is due entirely to nonlinearity by:

- setting sky Q and U to zero so that any signal in these maps is due to noise or systematic effects;
- comparing the result with nonlinearity (Case I) to that without, where $1/f$ noise is still present (Case III), and to pure signal + white noise simulations (Case II).

We include the results for a putative "deep" observing strategy, in which 1% of the sky is mapped in a repeating 12-day pattern of observations. These observations are four-hours azimuthal scans of the sky at constant elevation, and occur once a day, to mimic having only 20% observing efficiency. This number is a convenience of the split of 24 hours into four and 20; current experiments like ACT achieve higher ($\gtrsim$ 40%) during the active observing season.

The result for Case I (left column) for sky I (top row), Q (middle) and U (bottom) indicates that including nonlinearity in the systematics of the telescope can produce signals at the ~ 1 μ K level. Case II and III (middle and left columns, respectively) confirm that what is seen in Case I is not the result of issues with the simulation

of white or correlated noise. We thus confirm that the systematic defined and discussed in this chapter should be carefully considered, along with any unmodeled gain drifts, out of concern for leakage of the bright atmopshere and CMB temperature anisotropies into the low signal-to-noise-ratio channels of Q and U, which we transform directly into the E- and B-modes discussed in Ch. 1.

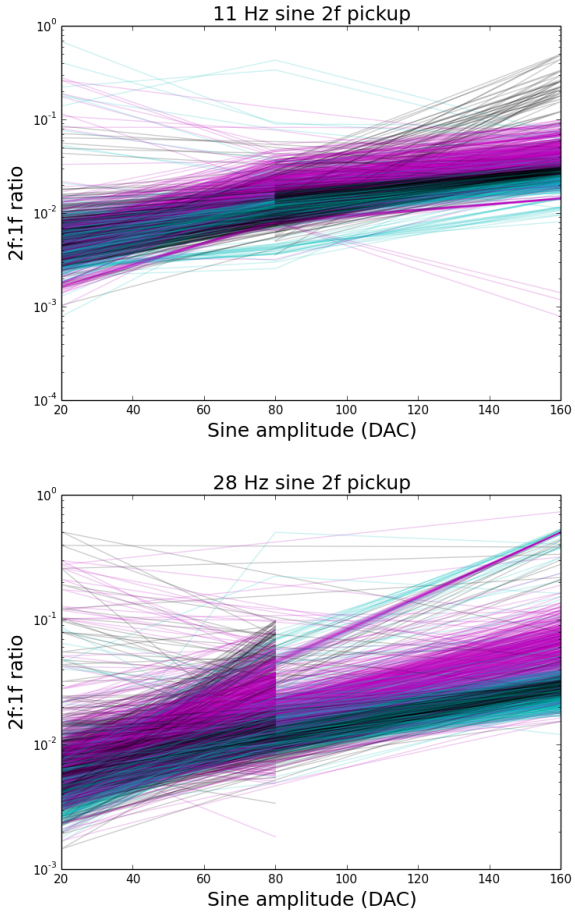

Figure 6.2: Results for study of pickup at twice the frequency of a bias-input sine wave for $f_s = 11$ Hz (top) and $f_s = 28$ Hz bottom across ∼1700 responsive detectors in MF1. We note that a majority of detectors, across the transition, respond to increasing excitation amplitude with increasing signal at $2f_s$. The model used in this chapter is valid for the case when this increase is a linear function of amplitude, though this function may change with bolometer operating condition.

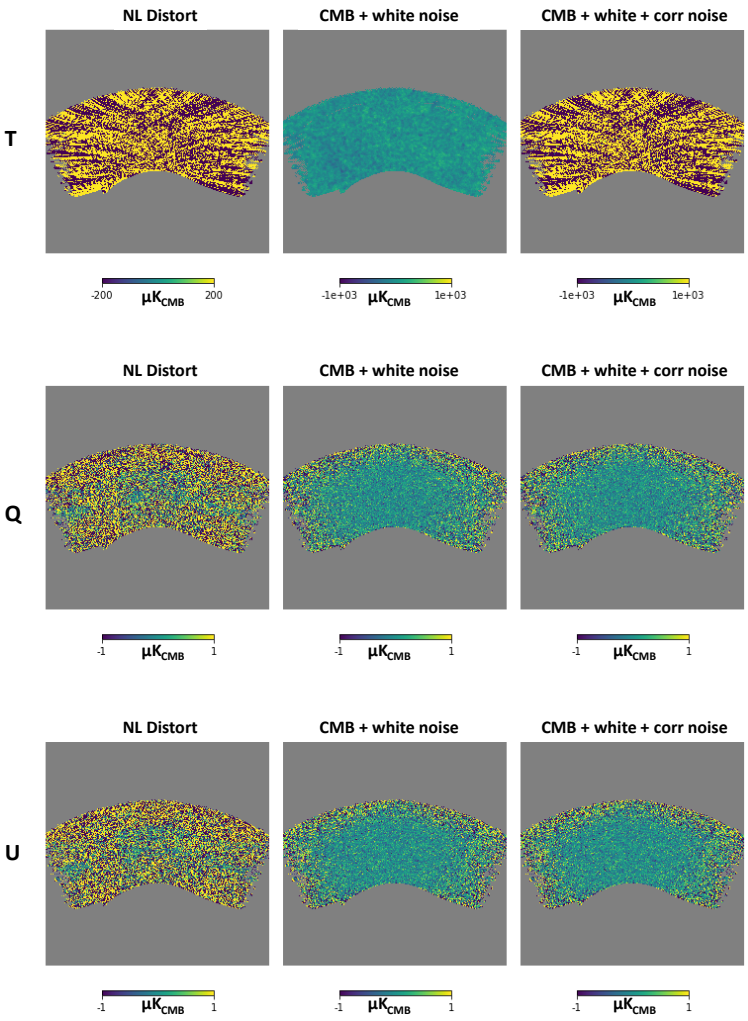

Figure 6.3: In this figure, Case I (labeled "NL Distort") has its three nonzero Stokes vector components (I, Q, and U) in rows, respectively, for the column at left. The apparent excess noise, and large-scale features, should be compared to the polarization plots (i.e. last two rows) for Case II (middle column, labeled "CMB + white noise") and Case III (right column, "CMB + white + corr noise"). These features are thus directly the result of differential nonlinearity within pairs of TES bolometers. Originally appeared in [16].

6.3 TES Loop Gain from I-V Curves

The loop gain $\mathscr{L}$ of a TES bolometer was introduced in Ch. 3 as a parameter describing the strength of the electrothermal feedback supplied by the voltage biasing of the TES. This directly impacts measurable parameters like the TES effective time constant τ_{eff}, as seen in Eq. 2.12. Finally, as discussed in Sec. 6.1, it reduces the size of the second-order nonlinearity terms [123].

Therefore, it is of interest to measure $\mathscr{L}$, and to do so regularly. However, the probes most commonly used, bias steps and swept-sine impedance datasets, cannot be used straightforwardly to track a TES bolometer's loop gain *in situ*. Instead, the results must be calibrated and processed, then interpolated to account for the actual TES operating conditions and how they might differ from those during the tests.

A preferable method would involve studying the I-V characteristic curves of bolometers to recover an estimate of $\mathscr{L}$ that could be recovered on the $\sim$ few-hour timescales between calibrating I-V curves taken during AdvACT observations. We consider the logarithmic derivative of TES resistance R with respect to the bias power P_{bias}. We recall a few initial facts about our approximate description of the TES as a temperature sensor, specifically involving the parameters α and β:

$$dR = R/T\alpha dT + R/I\beta dI. \tag{6.3}$$

We then write our parameter of interest:

$$\frac{dlnR}{dlnP_{\text{bias}}} = \frac{P_{\text{bias}}}{R}\frac{dR}{dP_{\text{bias}}} = \frac{P_{\text{bias}}\alpha}{T}\frac{dT}{dP_{\text{bias}}}, \tag{6.4}$$

where the TES temperature T has entered when replacing dR/R with $\alpha dT/T$, and assuming $dI = 0$. We recover the exact expression for loop gain $\mathscr{L}$ if we assume that

the bolometer is in the dark, where $\mathrm{d}P_{\mathrm{bias}} = \mathrm{d}P_{\mathrm{bath}}$. In that case, $\frac{dT}{dP_{\mathrm{bias}}} = \frac{dT}{dP_{\mathrm{therm}}} = 1/G$.

We have attempted to estimate $\mathscr{L}$ based on a detector's I-V curve after converting the latter into units of resistance R vs. bias power P_{bias}. We approximate the derivative at any point on the R-P curve using the midpoint method, where, assuming a sequence of samples indexed by an integer i, we estimate the derivative as:

$$\left.\frac{dR}{dP_{\mathrm{bias}}}\right|_i = \frac{R_{i+1} - R_{i-1}}{P_{i+1} - P_{i-1}}. \tag{6.5}$$

We expect that the resulting numerical estimate should be always positive, i.e. R always decreases as P_{bias} decreases. However, we find an interesting effect in which the $R(P)$ curve of the TES bolometer is not single-valued. At some resistance and P_{bias}, the sign of the derivative is reversed. Near this point, the derivative as approximated above becomes very large, as will be seen in figures below. We do not yet have a proposal for the cause of this curvature, and are content to take the absolute value of the above derivative when estimating $\mathscr{L}$, since this estimate is defined as an explicitly positive quantity.

Once the derivative is estimated, we can calculate our loop gain estimate by multiplying the derivative by the factor P/R. We also attempt to estimate the TES current sensitivity β analogously to $\mathscr{L}$, approximating the derivative dR/dI and multiplying by I/R. This may help in estimating an "effective loop gain" $\mathscr{L}/(1+\beta)$, which arises when one compares the thermal time constant, transformed into a bare bolometer $f_{\mathrm{3dB}} = G/(2\pi C)$, to the feedback-derived quantity $f_{\mathrm{3dB,eff}}$ which is estimated by bias steps.

In Fig. 6.4, we show two panels with the same data, showing the result of our estimate versus P_{bias} as the independent variable (left panel), where the curvature of the magenta points indicates the issue with non-single-valuedness. We also show the

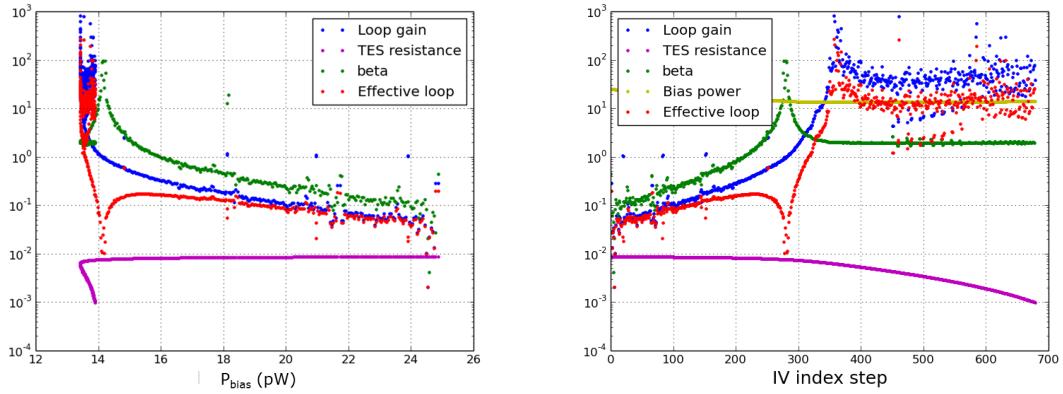

Figure 6.4: Loop gain $\mathscr{L}$ (blue) estimated from the I-V data based on Eq. 6.4. Other data include $P_{\rm bias}$ (yellow) and R (magenta) an estimate of β based on the derivative of dR/dI (green); and an effective loop gain $\mathscr{L}/(1+\beta)$ (red). The left panel does not show $P_{\rm bias}$ because we use it as the independent variable there.

same data, where for clarity in showing the range of loop gain values, we have used simply the I-V curve step index, which counts the number of steps from the initial data point. The position of the cusp in the blue and red data indicates the turnover point after which the sign of $dR/dP_{\rm bias}$ changes. The cusp in the estimate for β is a result of a similar turnover in the TES $R(I)$ curve. This is for an example detector that was studied using dedicated impedance data in laboratory tests of MF1.

If we compare the loop gain estimated here to that recovered from the impedance fit, we find $\mathscr{L}_{\rm I\text{-}V} \sim 50$ and $\mathscr{L}_{\rm imped} \sim 20$. Understanding the cause of this discrepancy, as well as the issues causing the noisy effects on this estimator at I-V steps after the turnover, must still be studied.

6.4 TES Bolometer Systematics and Modeling in the Future

As a conclusion to this work, we wish to summarize the main findings presented therein. These, in our estimation, are that TES bolometers are often more compli-

cated in their internal thermal (and electrothermal) architectures than the simplest, single-block model assumes. As experiments begin to push on maximizing the number of detectors to meet ambitious sensitivity targets, it is important to not neglect attempts to detect excess noise, understand its source, and control any possible enhancement in the CMB signal band.

Additionally, it is potentially dangerous to assume that these bolometers can be treated as linear-gain devices for ground-based CMB observations. We emphasize "ground-based," since it is the pernicious presence of atmospheric fluctuation-induced $1/f$ noise that generates spurious polarization signals. Mitigating this after the fact using observed unmodulated timestreams to clean the estimated polarization timestreams, as in Takakura et al., 2017 [123] is one possible path. However, for experiments without the presence of CRHWPs, and even for those using them, it is important to consider that systematics control can be balanced against ambitious sensitivity gains. Given that enhancing the loop gain parameter $\mathscr{L}$ by increasing the bias power P_{bias} applied during observations is always a potential choice, we are also in need of a model for the effect that can be usefully compared against enhancing noise levels by making these bolometers as sensitive as possible. This will be the continuation of the work presented in this chapter.

Finally, we presented multiple elements of a preliminary study of the performance of a CRHWP at a part of the optics where the HWP-synchronous signal ($\mathrm{A}(\chi)$) may alter between detectors and with time in complex ways. Producing science from this data, when CRHWPs are used to observe on a telescope sensitive to small sales, cannot proceed exactly as in previous experiments [69]. We will continue to explore this rich dataset, taking advantage of the good sensitivity and performance of the AdvACT bolometers as built, to attempt to push the sensitivity of the AdvACT project to larger scales. TES bolometers reacting to these signals demonstrate the complex

interplay between aspects of instrumentation that have enabled current progress on the study of the CMB, and will continue to do so in future.

Appendix A

Impedance Data Acquisition and Analysis Code

This appendix is meant to serve as a brief overview of the codebase used in the impedance measurements reported in Ch. 3. We separate individual scripts or modules based on whether they are used for acquisition or analysis.

A.1 Acquisition Scripts

input_sine.py This script initiates the data-taking for the impedance measurements. It has the following argument format:

input_sine.py -m <marker> -cr <col/row numbers> -bc <bias_card> -adc <adc_offset> -rc <readout_card> -f <frequencies> -o <offset> -a <amplitude> -t <temperature> -fr <frames> -ramp <max_frequency> -start <min_frequency> -Rn <percR_{N} > -bl <bias_line> -n <noise_frames>

The "marker" argument ensures that data generated as part of a single call to this script has a common prefix, for simpler analysis.

It instantiates a loop over detectors in the array, identified by MCE column and row number. It then instantiates an inner loop over frequencies, either provided as a

command line argument ("frequencies" taken as a Python list) or given as a beginning ("start") and ending ("ramp") frequency. If the script generates the frequencies automatically, then the step size is the power of 10 of the previous frequency. We have generally run the acquisition between 4 Hz and 1 kHz. Based on the frequencies requested, the script requires some hard-coded information about the MCE frame (or row-visit) rate in order to accurately estimate the true frequency of the sine wave as approximated by the MCE.

This script is relatively informed about how to properly DC bias a TES bolometer. Both an "offset" and a "percR_{N} " (or percent R_{N}) parameter should be provided. If the former is non-zero and the latter is 0 (i.e., superconducting), then no DC bias is applied. For any other "percR_{N} " parameter, the TES is driven normal by the default normal bias in the *array.cfg* file, before the DC bias is set to the value of the "offset" argument. The script reads local configuration information (with hardcoded paths) in order to determine which bias line on which bias card corresponds to the detector under test. This functionality is provided by helper modules *read_bias_lines.py* and *bias_card_finder.py*. With regard to determining the DC bias, we have used a secondary script (*Psat_script.py*) to estimate this quantity for each target percent R_{N}. This secondary script reads I-V curve data in for the detector under test.

This script is also used to communicate with the MCE to set up the sine wave input for later transmission to a particular target register. The argument "adc_offset" is a toggle which determines whether the sine wave signal will go to the TES bias card specified by the argument "bias_card," or to the ADC register specified by the argument. As mentioned above, the script determines the appropriate bias card and bias line based on MCE column and row number. If the detector is not targeted by the bias card requested in the argument, the script overrides the "bias_card" argument.

Once the target is set, the script calls the MCE utility function "mce_internal_ramp_setup." This function, and the general characteristics of an internal ramp, are described on

the public MCE wiki. [1] This ramp is hardcoded to update every two MCE frames, where the timespan of a frame is set by the details of the multiplexing setup, and a minimum step size of 1 DAC unit.

Once this internal ramp register is set aside by the MCE, we define the sine wave using a second MCE utility function, "mce_awg_setup." This script accepts arguments defining the shape of the excitation (we specify "sine"), a DAC offset and amplitude for the sine wave, and the number of ramp steps N to be used in defining the sinusoid period. For each frequency, N is determined in order to most closely match the frequency requested by the user. Once the two setup scripts have been run, the script *collect_sine* is called.

When this is complete, input_sine.py assumes the sine wave bias is no longer running. It then rebiases the detector, and takes a number "noise_frames" of DC-biased noise with the multiplexing set up in *collect_sine*.

Throughout, individual log files for each acquisition are written to a specified directory, and a running log of sine-wave data taken is written in the folder where the data are stored.

collect_sine This is a Bash executable script written to perform the actual MCE acquisition commands needed to send the sine wave. It takes a series of arguments, all generated inside *input_sine.py*. The argument structure is:

collect_sine <filename> <column> <row> <frames> <readout_card> <datarate> <bias_card> <bias_line> <noise>

This script sends the bias sine wave to "bias_line" on "bias_card," as determined by *input_sine.py*. It sets up a rectangle-mode acquisition on the MCE, in which a single detector is sampled repeatedly, rather than switching between rows. This fills up a dummy frame of some specified number of rows and columns (currently hardcoded to be 32×8=256), which then is read out at the rate specified by the "datarate"

[1] https://e-mode.phas.ubc.ca/mcewiki/index.php/Main_Page

argument. This argument should always equal the total number of samples in a frame.

Although the "row" argument of a particular detector is unique, we note that the "column" argument in this script is relative to the RC card specified by "readout_card," and thus can only span [0-7]. Thus, the global column 12 must be addressed as column 4 on readout card 2. Similarly, the bias line of a particular detector in the array must be mapped into the "bias_line" index for the particular bias card set by "bias_card" in order for the sine wave to be properly addressed.

Once the rectangle mode is enabled and the sine wave bias is set to appear only on the appropriate bias line (using MCE command "enbl_bias_mod"), the sine wave is started, a number of rectangle-mode frames is acquired according to the argument "frames," and the sine wave is then turned off. If the argument "noise" equals the string "y," the sine wave bias is not enabled, and rectangle-mode noise is acquired instead.

impedance_noise_acqscript.py Due to some of the need for secondary analysis to feed to the acquisition scripts, we have written a set of wrapper scripts where analysis of I-V curves can be performed, proper naming conventions for the different kinds of data can be enforced, and a separate external loop over detector column and row numbers can be performed. In this way, we can study each detector at bias values that are closest to the target percent R_{N} for each individual bolometer. This script also ensures that any on-transition data are marked by the filename of the I-V curve taken before the sine wave data was acquired.

A.2 Analysis Scripts

transfer_function.py Raw data are read into this file, which searches according to a regular-expression pattern-matching module in Python. An argument "marker"

identical to the one used in the acquisition of the data should be provided to ensure all frequencies are found. Additional identification of specific files is performed by specifying the MCE column and row numbers, and the target percent R_{N} used in determining the DC bias applied during the acquisition.

Once the files specifying a dataset are found, they are looped over. First, the mce_data module for Python is used to properly read the data (in feedback DAC unnits) from binary flatfile in which they are stored. Information about the MCE sample rate stored in the runfile (an auxiliary file associated with the data file) is used to generate a vector of times assuming constant sample rate. The original vector of MCE samples is also shifted so that the fiirst 262 samples are cut. We have found that this precise sample index is the zero-phase point for the input sine wave, so in order to recover phase information from our studies, we shift our output by this amount. An "array" argument is used to specify a bias line configuration file, which is read to determine if the feedback signal has positive or negative response to changing TES current signals.

This data is then fit to a five-parameter model for the data:

$$y_i = a + b\sin(c + 2\pi d t_i) + e t_i. \tag{A.1}$$

This fit is performed by the "curve_fit" function in the scipy.optimize module. We take the best-fit sinusoid frequency d to be the true frequency of the sine wave. This function provides an estimated covariance matrix along with the best-fit parameters. This matrix is used to generate error bars for the parameters of interest (amplitude b and phase c) using 300 draws of a covariance matrix appropriately scaled such that the best-fit parameters produce a reduced χ^2 of 1. These errors are propagated to all other quantities estimated from the best-fit amplitude and phase at each frequency.

The appropriately-scaled transfer function is then estimated using calibration constants within the MCE, a command line argument specifying the sine wave amplitude in bias DAC units, and the measured amplitude and phase of the feedback signal. This data can either be plotted for inspection, or written to a file (with filename specified by the "out" argument) for later use.

analyze_transfer.py This script performs the calibration of the transfer function into physical units, as well as the calculation of the complex calibration numbers $V_{\rm th}$ and $Z_{\rm eq}$ as in Ch. 3. Together, these values can be used to estimate $Z_{\rm TES}$. This is usually done for a single detector, whose column and row number is specified on the command line. The script has been designed to work with demodulated lock-in data stored in the NIST Python dictionary format, or with the transfer functions saved as Python Pickle files, as written by *transfer_function.py*.

In order to perform the calibration in either case, an I-V curve or set of I-Vs must be specified to be studied. The code must be told what set of operating conditions (combinations of $T_{\rm bath}$ and % $R_{\rm N}$) to try to process. Then the number of I-Vs provided as a command line argument should generally match the number of bath temperatures to be studied. For each operating condition, a given I-V is studied to determine the TES resistance at the applied bias, the bias power, and the normal resistance of the device. The value of $R_{\rm N}$ is required to calibrate the impedance data to Ohms [81] [137], and relies on the shunt resistance assumed in its estimation. The TES resistance in transition and the bias power are assumed to be exactly known, and are required for extracting parameters in the fit. The TES thermal conductance G estimated from I-V curve data at different $T_{\rm bath}$ is also necessary. Information on the applied bias is stored either in the .info files written by input_sine.py (MCE data) or in the NIST-style dictionary for each frequency sweep. The user can specify a shunt resistance mapping file to apply a particular shunt value for the detector studied.

I-V curves from MCE acquisitions are studied by a separate script, *iv-plot_princeton.py*. This code writes the physically-relevant quantities mentioned above to a lcoal file, where analyze_transfer knows to look for them. These numbers are then loaded and used to perform the conversions (e.g., Eq. 3.5) needed to recover Z_{TES}. Errors are either estimated from the magnitude and phase errors estimated by transfer_function.py, or for NIST data, following Eq. 3.6. The resulting data and errors are stored in a Python dictionary for passing to the final analysis module, to be discussed below.

minuit_contact.py As one may imagine, this module contains all connections between the data provided by *analyze_transfer.py* and the minimization algorithms to be applied in fitting the model. An added layer of complexity comes from the choice of total parameter numbers. Both *analyze_transfer.py* and *minuit_contact.py* need it specified which parameters will be fit with unique values at all operating conditions, and which will be held common across datasets. There are two categories of the latter: those held constant across all percent R_{N} studied ("rat_hold") and those held in common across all data sets, and thus across bath temperatures ("temp_hold"). Initial values for the relevant parameters must be specified in *analyze_transfer.py* in order for *minuit_contact.py* to generate the appropriate description of the parameters to fit.

In addition, as discussed in Ch. 3, the simple and hanging bolometer models were fit with differences in which parameters are held constant. Both the analysis script and the fitting module refer to these models as "one_block" and "two_block," in reference to the number of electrothermal elements. Beyond these various levels of customization, a call to instantiate a "minimizer", an object class defined to determine which parameters to define and to perform the fit, requires specifying which minimization scheme to use. The options are: the SciPy minimization using Powell's method; Minuit; a combination scheme where Minuit is called after the SciPy min-

imization succeeds essentially in order to properly estimate errros; and the MCMC implementation using Emcee.

In the two-block model fitting case of NIST data, we have implemented a hybrid approach where certain parameters are first estimated for a reduced set of frequencies, where the one-block model would appear valid. These estimates are then used to set the initialization for the MCMC exploraton an extended frequency range using the hanging model. In the one-block model fitting case, we tend to use the combination of SciPy for initial minimization, and Minuit for robust error estimation.

The final parameters estimated by the minimization routines in the "minimizer" class can then be plotted against the data using the "plot_results" function of the class. This function has many options for how to plot the impedance results, whether and how to load noise data and process it, estimation of noise curves with and without aliasing, etc. This code is fairly complicated since it must handle many choices with regard to what is plotted. Writing a new, more modular version of these functions would be a worthy follow-up to the initial establishment of this code base.

Appendix B

Semiconductor Bolometer Tests for PIXIE

The PIXIE experiment [65] is a proposed Explorer-class satellite designed to accurately measure any distortions of the CMB spectra arising from physics before and after recombination. This science goal is served by an instrument design in which various systematic contaminants in the timestream cancel at first order [92]. A two-port Fourier Transform Spectrometer (FTS) is used to observe either the same sky patch with two co-pointed beams, or to observe with one port filled by an isothermal, highly emissive blackbody. The design for the optical components gives PIXIE sensitivity to celestial emission over 2.5 decades in frequency, from 15 GHz to 6 THz. The movable mirror component enables the time-dependent path length difference within the spectrometer to sample this frequency range in bins of 15 GHz.

At the detection port for the interferometer, two single-polarization detectors are placed back-to-back to record the signals from the interferometer. The individual crystalline-silicon devices are optically and thermally large, with an optically-active area of 13 mm$\times$13 mm [91]. Thin, free-standing wires of silicon, called "harpstrings", are degenerately doped with phosphorous to be metallic. They are arrayed at reg-

ular intervals in order to achieve an effective impedance matched to free space to optimize absorption of incoming radiation. This radiation deposits energy as heat in the wires through Joule heating, with only the polarization parallel to the harpstrings contributing. This heat is conducted to two "end banks" at either end of the harpstrings, which feature two doped silicon thermistor at the top and bottom of the end bank, and a gold bar running along the end bank to ensure good conduction of heat from the harpstrings. These end banks are weakly coupled to the larger silicon frame by multiple silicon legs, which define the conductance to bath that each thermistor sees. In effect, then, these devices feature four bolometers (consisting of the thermistors and their legs) which couple to light through the harpstring-absorber structure. This construction is summarized in Fig. B.1. These devices were designed and fabricated by collaborators at Goddard Space Flight Center.

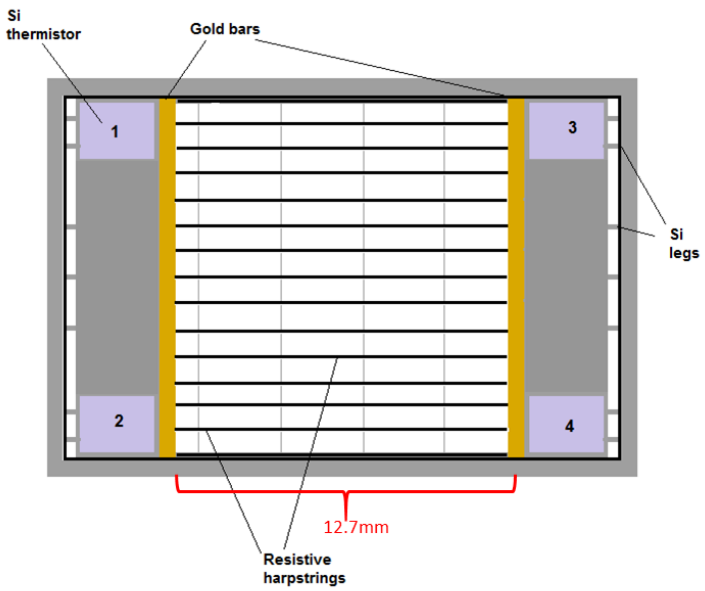

Figure B.1: Labeled diagram of a PIXIE detector. The harpstrings are the darker lines in the central absorber area. The lighter lines indicate support wires. The direction of polarization sensitivity for this device would be horizontal, parallel to the harpstrings.

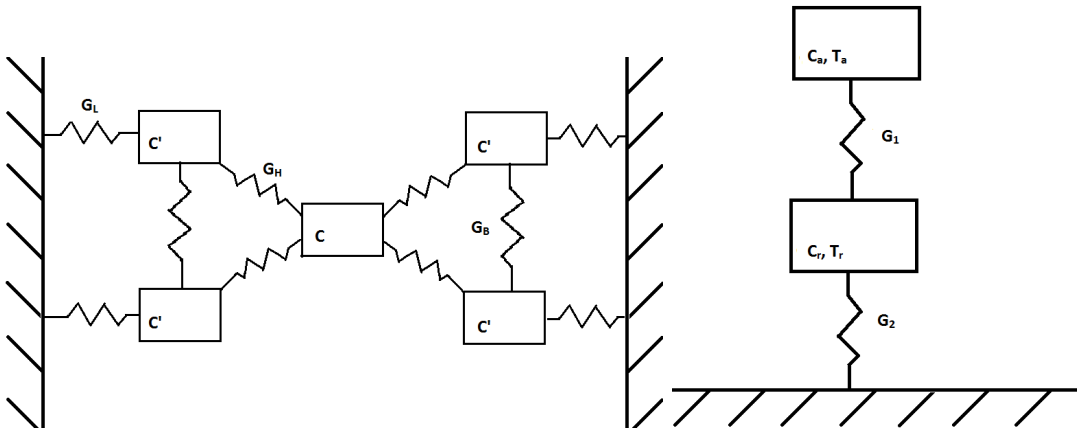

Figure B.2: Models used to describe the PIXIE detector. *Left*: The five-block model, where each block corresponds to a physical component on the PIXIE detector (C' for the thermistors, C for the absorber). Each thermistor is coupled to other blocks by three conductances: G_L, the conductance to bath, G_B, the end bank conductance, and G_H, the harpstring conductance. *Right*: The two-block model, reduced from the five-block model in the case of isothermal thermistors. The absorber block C_a at temperature T_a couples to a resistor block C_r at temperature T_r through conductance G_1. G_2 is then the effective conductance to bath for the entire frame.

In studying this bolometer, we worked with two extended electrothermal models. The first is motivated by the layout of the physical bolometer, and represents each thermistor and the absorber as individual thermal elements. This "five-block" model is shown schematically in Fig. B.2 in the left panel. We represent each thermistor's conductance to bath as G_L, conductance along end banks as G_B, and conductance to the harpstring absorber as G_H. For simplicity, we have assumed that each thermistor has identical heat capacity C', and the absorber has heat capacity C.

The second, which we considered to be motivated in the case of optical tests, is a two-block model distinct from the hanging model. It is shown in the right panel of Fig. B.2. The absorber C_a at temperature T_a passes heat through conductance G_1 to the block C_r at temperature T_r, which conducts it to bath through conductance G_2. This effective model is assumed to derive from the full five-block model in the case that all thermistors are isothermal with each other. This never exactly applies,

but the absorber is expected to be much warmer than the silicon end banks when illuminated due to its effective coupling, in a naturally broad-band way, to free space.

Optical Testing. At Princeton, tests were carried out to illuminate the PIXIE detector with a broad-band millimeter-wave source. These tests were performed with the source outside the cryostat, shining on the 300 mK PIXIE bolometer through a vacuum window, three millimeter-wave filters, and a coupling horn attached just above the harpstring absorber surface.

By coupling the source to a Faraday rotator fed by a square wave, we could chop the illumination at a set frequency and determine single thermistor responses at that frequency. These data could then be compared to the assumed optical responsivity of the thermistor element C_r in the two-block model, or to the standard simple bolometer responsivity from Ch. 2. This responsivity takes the form:

$$S(\omega) = \frac{\Gamma}{\mathscr{G}} \frac{1}{B + i\omega(\tau_1 + \tau_2) - \omega^2 \tau_1 \tau_2}, \tag{B.1}$$

where Γ is a unit conversion factor; $\mathscr{G}$ is the sum of G_1, G_2, and an effective conductance G_{ETF} that is analogous to the role of the loop gain $\mathscr{L}$ of a TES; B is the ratio of $G_2 + G_{\mathrm{ETF}}$ to $\mathscr{G}$, and so should be between 0 and 1; and $\tau_1 = C_a/G_1$ and $\tau_2 = C_r/\mathscr{G}$.

Given our ability to control the chopped source by input square wave and record a copy of that trigger, we were able to perform a kind of software lock-in measurement, comparing the thermistor response to the input signal. Figure B.3 shows, on the left, the best-fit results for a single-block (dashed red) and the two-block (solid green) model to the data for responsivity magnitude versus frequency, and on the right, the same fits to the phase data. Firstly, these data indicate that discrimination between the models using the difference in the responsivity magnitudes is quite difficult. However, the expected phase behavior of the single-block model is clearly violated by the

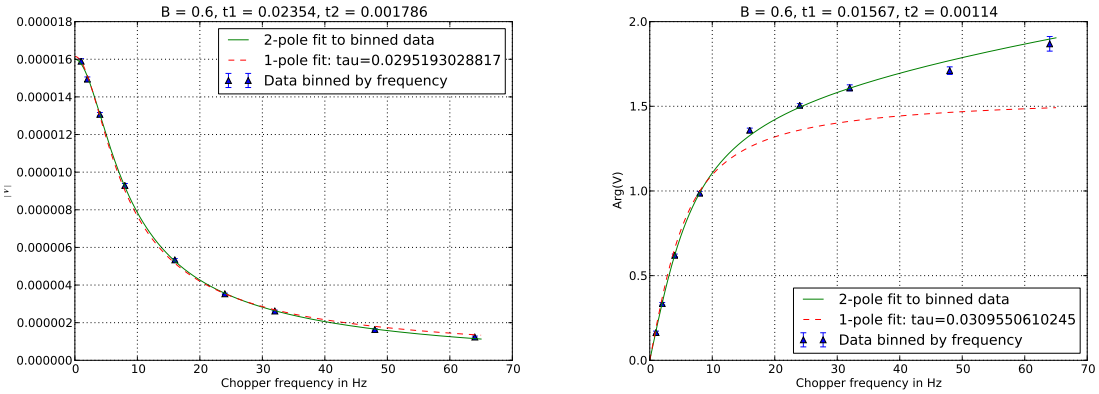

Figure B.3: Tests of broad-band illumination of PIXIE detectors by a warm, chopped source. *Left*: Best-fit model and parameters recovered for fitting the magnitude of the thermistor response to the chopped source versus frequency. The solid green fits the two-block form of Eq. B.1, the dashed red fits using the simple bolometer model where the only degree of freedom aside from a normalization is the time constant. No strong preference is exhibited by the data. *Right*: Best-fit model and parameters for fitting phase versus frequency. Solid green and dashed red lines correspond to models as in the right panel. The two-block model is able to handle the rise of the phase to values above $\pi/2$, and prefers a fast transfer of heat to the bath (small τ_2), as compared to transfer between the absorber and thermistors (larger tau_1).

data. Adding a second block has enabled us to fit the data out to much higher frequency, and recover two time constants of very different order. Specifically, the slower time constant here corresponds to heat transfer between the harpstring absorber and the thermistors. This is supported by other measurements of the version of the PIXIE detectors tested at Princeton at this time, with evidence to be discussed below.

Thermal Transfer. In order to explore the full set of conductances coupled to each thermistor, we carried out a campaign of measurements to fully characterize each thermistor on a different PIXIE detector than the one which was optically tests. We began by estimating the parameters that define the $R(T)$ curve of semiconductor thermistors, as well as the total conductance seen by each thermistor. The resistance of these devices is understood in the context of a variable-range hopping model (for

more, see [87]). It is assume to have the effective form:

$$R(T) = R_0 e^{\sqrt{\frac{T_0}{T}}}. \tag{B.2}$$

We note that the above form implies a negative value of α for these devices. Thus negative feedback is achieved with a current bias, in this case by putting a large resistance in series with the thermistors.

We estimate R_0, T_0, and a sum of the conductances G_L, G_B, and G_H from measurements of the thermistor resistance at various bath temperatures with small bias excitations. We can further attempt to estimate the individual component conductances by recording the resistance change at one thermistor when another on the same end bank, or across the harpstrings, is excited. This work produced estimates of the thermistor conductances as follows: $G_L \approx 1$ nW/K, $G_B \approx 0.1$ nW/K, and $G_H \approx 5$ pW/K. To produce this estimate, we have assumed that each G_H is the same across the four thermistors when estimating the temperature of the absorber through which the cross-harp heat transfer must occur.

These DC thermal transfer values are well-augmented by an AC measurement, which seeks to measure the response of a thermistor to a neighboring thermistor being used as a heater. If the frequency with which the heater thermistor is excited is $f_{\rm heat}$, and the readout frequency is $f_{\rm read}$, then this signal appears in the readout thermistor timestream at frequency $2f_{\rm heat} + f_{\rm read}$. Rather than record how this signal varies with heater frequency, we have measured the signal at this frequency to the self-heating of the thermistor, where its Joule heating at $2f_{\rm read}$ is sensed as power in the third harmonic, $3f_{\rm read}$.[1] This ensures that any parasitic elements of the electrical bias circuit used to provide a current bias to these devices is, if common to the bias circuits of the two thermistors, cancelled in the ratio. We avoid pileup of the two signals by detuning $f_{\rm heat}$ from $f_{\rm read}$, and can do so either with $f_{\rm heat} < f_{\rm read}$, or

[1] This method developed by A. Kusaka at Princeton.

$f_{\rm heat} > f_{\rm read}$. In what follows, the former are called "left" points, and the latter are called "right" points.

We show in Fig. B.4 the results when the ratio of the amplitude of the two peaks is used. The green line represents our fit to an approximately single-block responsivity form:

$$\text{ratio}(f) = \frac{1}{\sqrt{1 + \left(\frac{f}{f_{\rm 3dB}}\right)^{\nu}}}, \tag{B.3}$$

where we would usually force $\nu = 2$. In this case, the green line is the result for $\nu = 3.4$, the preferred value. The magenta fit is an exponential decay functional form that was used to understand devices tested at Goddard. For both fits, the timescale of thermal transfer through the harp is 1 Hz, well below the record > 100 Hz $f_{\rm 3dB}$

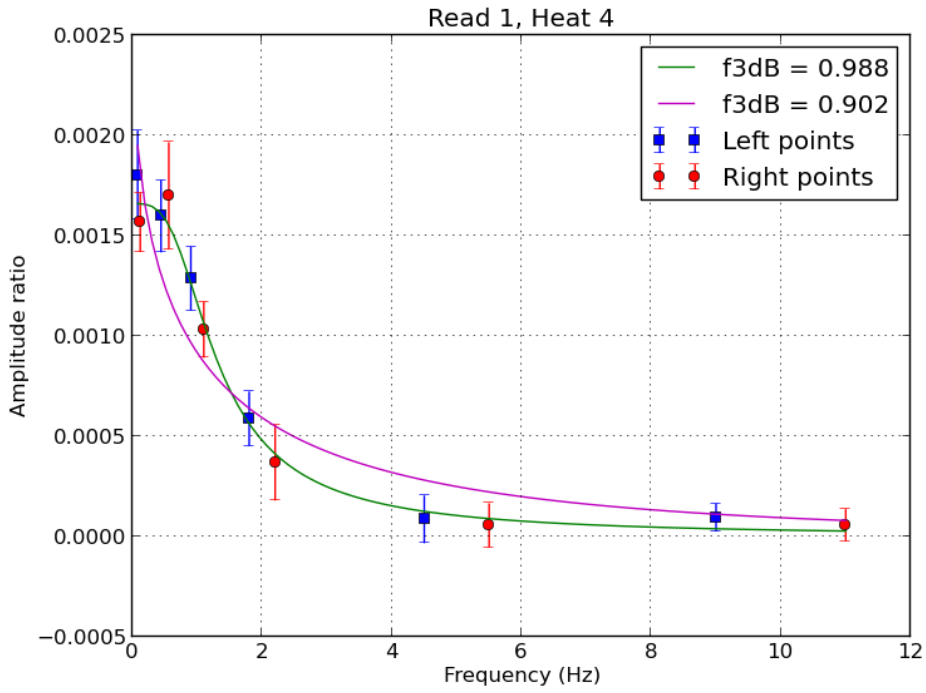

Figure B.4: Results for the ratio of the amplitude of the signal produced by heat transfer to that of self-induced heating. The transfer is between thermistors across the harpstring (thermistors 1 and 4 in Fig. B.1). The fit form of Eq. B.3 recovers a very slow characteristic frequency of 1 Hz, a number well below the design value. This tested detector was part of an earlier generation of devices designed for PIXIE.

values measured at Goddard. This result should not be taken to represent the final measurement on this aspect of PIXIE detector performance.

A new generation of PIXIE detectors has been designed and fabricated at Goddard, and tests are in progress, with future plans including similar AC-biased studies of thermistor heat transfer.

Appendix C

Time-Varying Scan-Synchronous Signal in ABS

A major systematic error issue for ground-based observations of the CMB is pickup of signals synchronous with the scan but not produced in the sky. Sources of such signals may include scattering or far beam sidelobes in the instrument and magnetic pickup by the cryogenic SQUID amplifiers. Though we expect that it will not add coherently in maps produced from many scans, we prefer to remove an estimate for this signal in order to avoid any artifacts. The baffle and ground screen for ABS were designed to prevent this pickup, but additional methods to handle any such signals were also instituted.

As part of the TOD processing for the ABS science analysis, a template of the per-CES scan-synchronous signal (SSS) was estimated and removed. The template itself refers to defining 1°-wide bins in boresight azimuth and averaging detector samples across the $\sim$ 1-hour CES within those bins. This template was removed using a model built from a linear combination of the first 20 Legendre polynomials. The template estimation and removal process was done separately for the real and imaginary parts of the demodulated timestream.

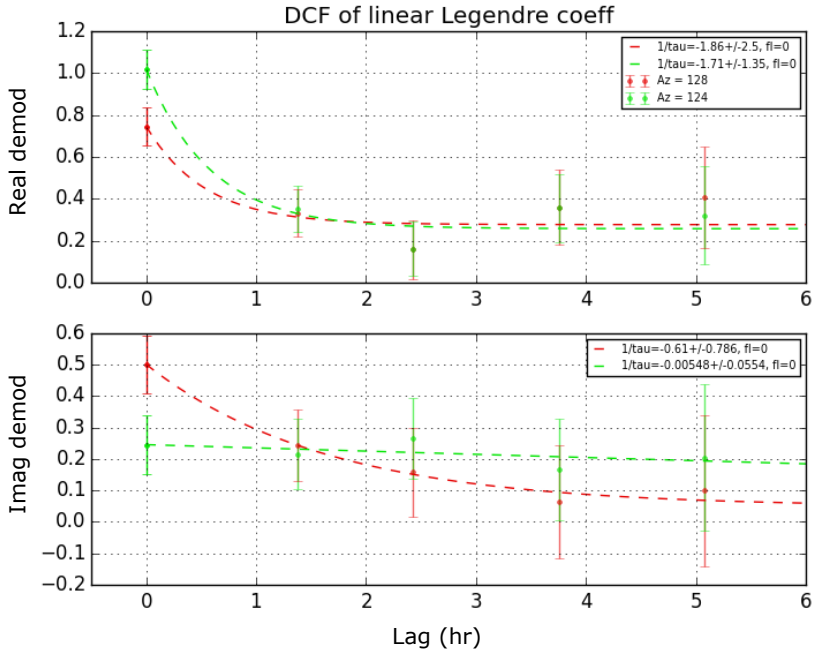

Figure C.1: Example DCF for the linear Legendre coeffienct of an ABS detector across the second observing season. The green and red dashed lines correspond to data and best-fit models for the scan patterns centered at 233° and 229°, respectively. The model given by Eq. C.1 is shown, with the reported $1/\tau$ values equal to b. This detector shows clear evidence for an exponential decay in the DCF.

A data selection criteria was further placed on the residuals of this subtraction being sufficiently small, specifically in the sum of the estimated χ^2 of the residuals from both the real and imaginary timestreams, $\chi^2_{\rm cut} = (\chi^2_{\rm real} + \chi^2_{\rm imag})$. In the frequency domain, we expect this removal to manifest as a reduction of power around the scan frequency $f_{\rm scan}$. A complementary selection criteria was put in place to reject per-detector CES data based on measured power in a band within ± 12 % of $f_{\rm scan}$. This second criterion should have also removed detector-CES timestreams with excessive variation of the SSS, which we expect to appear as a broadening of the peak at $f_{\rm scan}$. Such a signal could be produced by the source of the SSS changing, or the detector responsivity changing on sub-CES timescales. Both are expected to contribute.

In our work, we developed a separate method to search for time-varying SSS. We began by performing the Legendre decomposition of the per-CES templates up to the

fifth Legendre polynomial. Our early results indicated that the linear term, the first Legendre polyomial, had the largest coefficients and varied the most. We thus elected to focus our study on it.

Once we estimated the coefficient of this first-degree polynomial for the template of each detector-CES, we calculated the discrete autocorrelation function (DCF) of this set of coefficients k_i as a function of time between CES, in hours, across the entire first and second seasons of ABS observations. We defined the time of each CES as the midpoint of the scanning period to define the set of times t_i. Our DCF estimator used binning individual DCF samples in bins of width 1.2 hours to reduce variance. However, the reduced number of CESes in the first season resulted in a lack of sensitivity to possible correlations due to fewer samples in the bins. We therefore narrowed our analysis to the second observing season of ABS.

We did this separately for the four scanning patterns which ABS used to observe the main field used for CMB science. We refer to them by their central azimuth, with two in the west (centered at az = 229° and az = 233°) and two in the east (centered at az = 128° and az = 124°). We then fit the DCF to the following decay function:

$$A(l) = c\delta(l) + ae^{bl}, \tag{C.1}$$

where l is the bin lag time in hours, a, b, and c are fit parameters, and b free to be positive or negative. An example of a dataset for an ABS detector across the east set of scans is shown in Fig. C.1. This detector shows evidence for an exponential decay of the DCF in its real component with time constant $\tau = 1/b \sim 0.5$ hours.

In order to determine whether a given detector's full-season DCF indicated possible variations on timescales shorter than a CES, we defined a frequency ω_{eq} at which the white noise of the SSS variation (estimated from the lag = 0 point of the DCF) equals any $1/f$-like noise from the fit parameters for the exponential decay. Taking

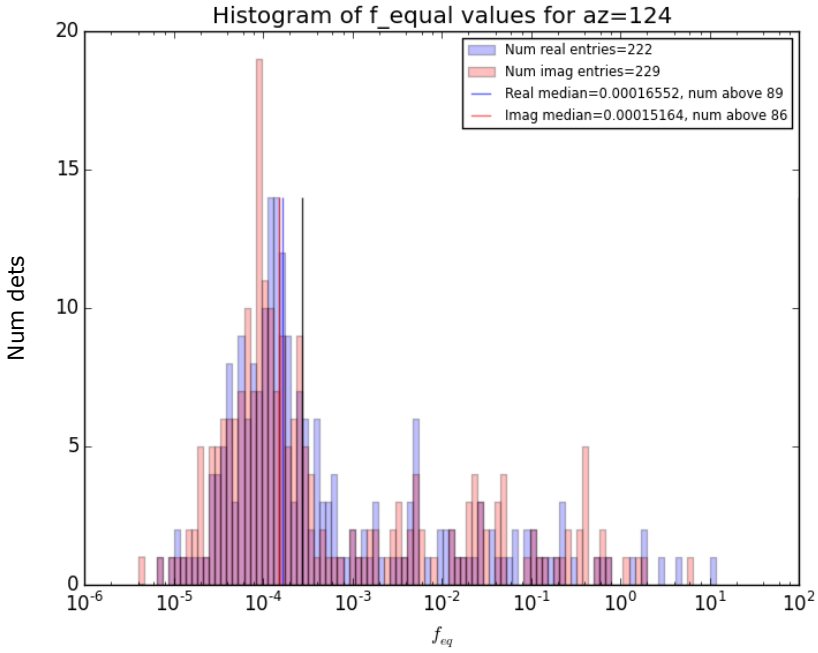

Figure C.2: Histogram across ABS detectors for $f_{\rm eq}$ estimated from the best-fit parameters to the detector correlation functions over the az $= 124°$ scanning pattern. The blue histogram represents the distribution of $f_{\rm eq}$ for the real-part DCF, and the red shows that for the imaginary-part DCF. Colored vertical lines indicate the distribution medians given in the legend. The solid vertical black line is the selection criterion for $f_{\rm eq}$. Above thiss line, the detector is assumed to have time-varying SSS on sub-CES timescales.

the Fourier transform of Eq. C.1 after explicitly assuming $b < 0$ and squaring to recover the power, we find:

$$|\mathscr{F}\{A\}(\omega)|^2 = c^2 + \frac{2abc + a^2}{b^2 + \omega^2}. \tag{C.2}$$

This allows us then to write $\omega_{\rm eq}^2$ as:

$$\omega_{\rm eq}^2 = \frac{a^2}{c^2} + \frac{2ab}{c} - b^2, \tag{C.3}$$

By calculating the quantity in Eq. C.3 for each detector's DCF across all four scanning patterns, we could determine if certain detectors could be considered to have evidence for time-varying SSS on timescales shorter than a CES. We found it useful to take the square root of $\omega_{\rm eq}^2$ and divide by 2π, recovering an $f_{\rm eq}$ for each detector for each scanning pattern. The histogram of $f_{\rm eq}$ for the az $= 124^\circ$ scanning pattern is shown in Fig. C.2. We note that this analysis made use of all other data selection criteria before the DCF were calculated, such that any additional criteria associated with this analysis would not be affected by known problematic detectors. We find a large (~ 90) number of detectors with possible contamination on sub-CES timescales, indicated here as frequencies greater than the vertical black line at $f_{\rm eq} > (1\ \ {\rm hour})^{-1}$.

However, we found that fewer of those detectors had DCFs with possible sub-CES contamination across multiple distributions. Eight totall distributions were defined: the real and imaginary demodulated components across all four scanning patterns. Our suggested criteria was to reject detectors that had $f_{\rm eq} > (1\ {\rm hour})^{-1}$ for three out of the possible eight distributions. This list of 55 detectors was studied in the ABS systematic error tests [68] by running the ABS pipeline with and without these detectors. The results indicate that their effect on the ABS results is negligible, and any possible residual arising from including them is below the level of the statistical noise in the BB power spectrum.

Bibliography

[1] Z. Ahmed, M. Amiri, S. J. Benton, J. J. Bock, R. Bowens-Rubin, I. Buder, E. Bullock, J. Connors, J. P. Filippini, J. A. Grayson, M. Halpern, G. C. Hilton, V. V. Hristov, H. Hui, K. D. Irwin, J. Kang, K. S. Karkare, E. Karpel, J. M. Kovac, C. L. Kuo, C. B. Netterfield, H. T. Nguyen, R. O'Brient, R. W. Ogburn, C. Pryke, C. D. Reintsema, S. Richter, K. L. Thompson, A. D. Turner, A. G. Vieregg, W. L. K. Wu, and K. W. Yoon. BICEP3: a 95GHz refracting telescope for degree-scale CMB polarization. In *Millimeter, Submillimeter, and Far-Infrared Detectors and Instrumentation for Astronomy VII*, volume 9153 of *Proc. SPIE*, page 91531N, August 2014.

[2] J. E. Austermann, K. A. Aird, J. A. Beall, D. Becker, A. Bender, B. A. Benson, L. E. Bleem, J. Britton, J. E. Carlstrom, C. L. Chang, H. C. Chiang, H.-M. Cho, T. M. Crawford, A. T. Crites, A. Datesman, T. de Haan, M. A. Dobbs, E. M. George, N. W. Halverson, N. Harrington, J. W. Henning, G. C. Hilton, G. P. Holder, W. L. Holzapfel, S. Hoover, N. Huang, J. Hubmayr, K. D. Irwin, R. Keisler, J. Kennedy, L. Knox, A. T. Lee, E. Leitch, D. Li, M. Lueker, D. P. Marrone, J. J. McMahon, J. Mehl, S. S. Meyer, T. E. Montroy, T. Natoli, J. P. Nibarger, M. D. Niemack, V. Novosad, S. Padin, C. Pryke, C. L. Reichardt, J. E. Ruhl, B. R. Saliwanchik, J. T. Sayre, K. K. Schaffer, E. Shirokoff, A. A. Stark, K. Story, K. Vanderlinde, J. D. Vieira, G. Wang, R. Williamson, V. Yefremenko, K. W. Yoon, and O. Zahn. SPTpol: an instrument for CMB polarization measurements with the South Pole Telescope. In *Millimeter, Submillimeter, and Far-Infrared Detectors and Instrumentation for Astronomy VI*, volume 8452 of *Proc. SPIE*, page 84521E, September 2012.

[3] N.A. Bahcall. Clusters and cosmology. *Physics Reports*, 333-334:233–244, 2000.

[4] E. Battaner and E. Florido. The Rotation Curve of Spiral Galaxies and its Cosmological Implications. *Fundamentals of Cosmic Physics*, 21:1–154, 2000.

[5] E. S. Battistelli, M. Amiri, B. Burger, M. Halpern, S. Knotek, M. Ellis, X. Gao, D. Kelly, M. Macintosh, K. Irwin, and C. Reintsema. Functional Description of Read-out Electronics for Time-Domain Multiplexed Bolometers for Millimeter and Sub-millimeter Astronomy. *Journal of Low Temperature Physics*, 151:908–914, May 2008.

[6] BICEP2/Keck Collaboration, Planck Collaboration, and et al. Joint Analysis of BICEP2/Keck Array and Planck Data. *Physical Review Letters*, 114(10):101301, March 2015.

[7] D. Blas, J. Lesgourgues, and T. Tram. The Cosmic Linear Anisotropy Solving System (CLASS). Part II: Approximation schemes. *Journal of Cosmology and Astroparticle Physics*, 7:034, July 2011.

[8] J. R. Bond, A. H. Jaffe, and L. Knox. Radical Compression of Cosmic Microwave Background Data. *Astrophysical Journal*, 533:19–37, April 2000.

[9] S. Bryan, P. Ade, M. Amiri, S. Benton, R. Bihary, J. Bock, J. R. Bond, H. C. Chiang, C. Contaldi, B. Crill, O. Dore, B. Elder, J. Filippini, A. Fraisse, A. Gambrel, N. Gandilo, J. Gudmundsson, M. Hasselfield, M. Halpern, G. Hilton, W. Holmes, V. Hristov, K. Irwin, W. Jones, Z. Kermish, C. Lawrie, C. MacTavish, P. Mason, K. Megerian, L. Moncelsi, T. Montroy, T. Morford, J. Nagy, C. B. Netterfield, I. Padilla, A. S. Rahlin, C. Reintsema, D. C. Riley, J. Ruhl, M. Runyan, B. Saliwanchik, J. Shariff, J. Soler, A. Trangsrud, C. Tucker, R. Tucker, A. Turner, S. Wen, D. Wiebe, and E. Young. A cryogenic rotation stage with a large clear aperture for the half-wave plates in the Spider instrument. *Review of Scientific Instruments*, 87(1):014501, January 2016.

[10] E. F. Bunn and B. Wandelt. Pure E and B polarization maps via Wiener filtering. *Phys. Rev. D*, 96(4):043523, August 2017.

[11] K.H.S. Choi. *Measuring the Cosmic Microwave Background from the Atacama Desert*. PhD thesis, Princeton University, 2018.

[12] S. K. Choi, J. Austermann, J. A. Beall, K. T. Crowley, R. Datta, S. M. Duff, P. A. Gallardo, S.-P. P. Ho, J. Hubmayr, B. J. Koopman, Y. Li, F. Nati, M. D. Niemack, L. A. Page, M. Salatino, S. M. Simon, S. T. Staggs, J. Stevens, J. Ullom, and E. J. Wollack. Characterization of the Mid-Frequency Arrays for Advanced ACTPol. *ArXiv e-prints*, November 2017.

[13] K. P. Coughlin, J. J. McMahon, K. T. Crowley, B. J. Koopman, K. H. Miller, S. M. Simon, and E. J. Wollack. Pushing the Limits of Broadband and High-Frequency Metamaterial Silicon Antireflection Coatings. *Journal of Low Temperature Physics*, May 2018.

[14] K. T. Crowley, J. A. Austermann, S. K. Choi, S. M. Duff, P. A. Gallardo, S.-P. P. Ho, J. Hubmayr, B. J. Koopman, F. Nati, M. D. Niemack, M. Salatino, S. M. Simon, S. T. Staggs, J. R. Stevens, J. N. Ullom, E. M. Vavagiakis, and E. J. Wollack. Advanced ACTPol TES Device Parameters and Noise Performance in Fielded Arrays. *Journal of Low Temperature Physics*, 2018. Accepted for publication.

[15] K. T. Crowley, S. K. Choi, J. Kuan, J. A. Austermann, J. A. Beall, R. Datta, S. M. Duff, P. A. Gallardo, M. Hasselfield, S. W. Henderson, S.-P. P. Ho, B. J.

Koopman, M. D. Niemack, M. Salatino, S. M. Simon, S. T. Staggs, and E. J. Wollack. Characterization of AlMn TES impedance, noise, and optical efficiency in the first 150 mm multichroic array for Advanced ACTPol. In *Millimeter, Submillimeter, and Far-Infrared Detectors and Instrumentation for Astronomy VIII*, volume 9914 of *Proc. SPIE*, page 991431, July 2016.

[16] Kevin T. Crowley, Sara M. Simon, Max Silva-Feaver, Neil Goeckner-Wald, Aamir Ali, Jason Austermann, Michael L. Brown, Yuji Chinone, Ari Cukierman, Bradley Dober, Shannon M. Duff, Jo Dunkley, Josquin Errard, Giulio Fabbian, Patricio A. Gallardo, Shuay-Pwu Patty Ho, Johannes Hubmayr, Brian Keating, Akito Kusaka, Nialh McCallum, Jeff McMahon, Federico Nati, Michael D. Niemack, Giuseppe Puglisi, Mayuri Sathyanarayana Rao, Christian L. Reichardt, Maria Salatino, Praween Siritanasak, Suzanne Staggs, Aritoki Suzuki, Grant Teply, Daniel B. Thomas, Joel N. Ullom, Clara Vergs, Michael R. Vissers, Benjamin Westbrook, Edward J. Wollack, Zhilei Xu, and Ningfeng Zhu. Studies of systematic uncertainties for simons observatory: detector array effects. In *Millimeter, Submillimeter, and Far-Infrared Detectors and Instrumentation for Astronomy IX*, volume 10708 of *Proc. SPIE*, pages 10708 – 10708 – 27, 2018.

[17] R. H. Cyburt, B. D. Fields, K. A. Olive, and T.-H. Yeh. Big bang nucleosynthesis: Present status. *Reviews of Modern Physics*, 88(1):015004, January 2016.

[18] R. Datta, J. Hubmayr, C. Munson, J. Austermann, J. Beall, D. Becker, H. M. Cho, N. Halverson, G. Hilton, K. Irwin, D. Li, J. McMahon, L. Newburgh, J. Nibarger, M. Niemack, B. Schmitt, H. Smith, S. Staggs, J. Van Lanen, and E. Wollack. Horn Coupled Multichroic Polarimeters for the Atacama Cosmology Telescope Polarization Experiment. *Journal of Low Temperature Physics*, 176:670–676, September 2014.

[19] R. Datta, C. D. Munson, M. D. Niemack, J. J. McMahon, J. Britton, E. J. Wollack, J. Beall, M. J. Devlin, J. Fowler, P. Gallardo, J. Hubmayr, K. Irwin, L. Newburgh, J. P. Nibarger, L. Page, M. A. Quijada, B. L. Schmitt, S. T. Staggs, R. Thornton, and L. Zhang. Large-aperture wide-bandwidth antireflection-coated silicon lenses for millimeter wavelengths. *Applied Optics*, 52:8747, December 2013.

[20] P. A. J. de Korte, J. Beyer, S. Deiker, G. C. Hilton, K. D. Irwin, M. MacIntosh, S. W. Nam, C. D. Reintsema, L. R. Vale, and M. E. Huber. Time-division superconducting quantum interference device multiplexer for transition-edge sensors. *Review of Scientific Instruments*, 74:3807–3815, August 2003.

[21] W. de Sitter. Einstein's theory of gravitation and its astronomical consequences. Third paper. *Monthly Notices of the Royal Astronomical Society*, 78:3–28, November 1917.

[22] DES Collaboration. Dark Energy Survey Year 1 Results: Cosmological Constraints from Galaxy Clustering and Weak Lensing. *ArXiv e-prints*, August 2017.

[23] J. Didier, A. D. Miller, D. Araujo, F. Aubin, C. Geach, B. Johnson, A. Korotkov, K. Raach, B. Westbrook, K. Young, A. M. Aboobaker, P. Ade, C. Baccigalupi, C. Bao, D. Chapman, M. Dobbs, W. Grainger, S. Hanany, K. Helson, S. Hillbrand, J. Hubmayr, A. Jaffe, T. Jones, J. Klein, A. Lee, L. Levinson, M. Limon, K. MacDermid, M. Milligan, L. Moncelsi, E. Pascale, B. Reichborn-Kjennerud, I. Sagiv, C. Tucker, G. S. Tucker, and K. Zilic. Intensity-Coupled-Polarization in Instruments with a Continuously Rotating Half-Wave Plate. *ArXiv e-prints*, November 2017.

[24] W. B. Doriese, K. M. Morgan, D. A. Bennett, E. V. Denison, C. P. Fitzgerald, J. W. Fowler, J. D. Gard, J. P. Hays-Wehle, G. C. Hilton, K. D. Irwin, Y. I. Joe, J. A. B. Mates, G. C. O'Neil, C. D. Reintsema, N. O. Robbins, D. R. Schmidt, D. S. Swetz, H. Tatsuno, L. R. Vale, and J. N. Ullom. Developments in Time-Division Multiplexing of X-ray Transition-Edge Sensors. *Journal of Low Temperature Physics*, 184:389–395, July 2016.

[25] C. Dragone. Offset multireflector antennas with perfect pattern symmetry and polarization discrimination. *AT T Technical Journal*, 57:2663–2684, September 1978.

[26] S. M. Duff, J. Austermann, J. A. Beall, D. Becker, R. Datta, P. A. Gallardo, S. W. Henderson, G. C. Hilton, S. P. Ho, J. Hubmayr, B. J. Koopman, D. Li, J. McMahon, F. Nati, M. D. Niemack, C. G. Pappas, M. Salatino, B. L. Schmitt, S. M. Simon, S. T. Staggs, J. R. Stevens, J. Van Lanen, E. M. Vavagiakis, J. T. Ward, and E. J. Wollack. Advanced ACTPol Multichroic Polarimeter Array Fabrication Process for 150 mm Wafers. *Journal of Low Temperature Physics*, 184:634–641, August 2016.

[27] R. Dünner, M. Hasselfield, T. A. Marriage, J. Sievers, V. Acquaviva, G. E. Addison, P. A. R. Ade, P. Aguirre, M. Amiri, J. W. Appel, L. F. Barrientos, E. S. Battistelli, J. R. Bond, B. Brown, B. Burger, E. Calabrese, J. Chervenak, S. Das, M. J. Devlin, S. R. Dicker, W. Bertrand Doriese, J. Dunkley, T. Essinger-Hileman, R. P. Fisher, M. B. Gralla, J. W. Fowler, A. Hajian, M. Halpern, C. Hernández-Monteagudo, G. C. Hilton, M. Hilton, A. D. Hincks, R. Hlozek, K. M. Huffenberger, D. H. Hughes, J. P. Hughes, L. Infante, K. D. Irwin, J. Baptiste Juin, M. Kaul, J. Klein, A. Kosowsky, J. M. Lau, M. Limon, Y.-T. Lin, T. Louis, R. H. Lupton, D. Marsden, K. Martocci, P. Mauskopf, F. Menanteau, K. Moodley, H. Moseley, C. B. Netterfield, M. D. Niemack, M. R. Nolta, L. A. Page, L. Parker, B. Partridge, H. Quintana, B. Reid, N. Sehgal, B. D. Sherwin, D. N. Spergel, S. T. Staggs, D. S. Swetz, E. R. Switzer, R. Thornton, H. Trac, C. Tucker, R. Warne, G. Wilson, E. Wollack, and Y. Zhao. The Atacama Cosmology Telescope: Data Characterization and Mapmaking. *Astrophysical Journal*, 762:10, January 2013.

[28] T. Essinger-Hileman. *Probing Inflationary Cosmology: The Atacama B-Mode Search (ABS)*. PhD thesis, Princeton University, 2011.

[29] T. Essinger-Hileman, J. W. Appel, J. A. Beal, H. M. Cho, J. Fowler, M. Halpern, M. Hasselfield, K. D. Irwin, T. A. Marriage, M. D. Niemack, L. Page, L. P. Parker, S. Pufu, S. T. Staggs, O. Stryzak, C. Visnjic, K. W. Yoon, and Y. Zhao. The Atacama B-Mode Search: CMB Polarimetry with Transition-Edge-Sensor Bolometers. In B. Young, B. Cabrera, and A. Miller, editors, *American Institute of Physics Conference Series*, volume 1185 of *American Institute of Physics Conference Series*, pages 494–497, December 2009.

[30] T. Essinger-Hileman, A. Kusaka, J. W. Appel, S. K. Choi, K. Crowley, S. P. Ho, N. Jarosik, L. A. Page, L. P. Parker, S. Raghunathan, S. M. Simon, S. T. Staggs, and K. Visnjic. Systematic effects from an ambient-temperature, continuously rotating half-wave plate. *Review of Scientific Instruments*, 87(9):094503, September 2016.

[31] D. J. Fixsen. The Temperature of the Cosmic Microwave Background. *Astrophysical Journal*, 707:916–920, December 2009.

[32] D. J. Fixsen, G. Hinshaw, C. L. Bennett, and J. C. Mather. The Spectrum of the Cosmic Microwave Background Anisotropy from the Combined COBE FIRAS and DMR Observations. *Astrophysical Journal*, 486:623–628, September 1997.

[33] D. J. Fixsen, A. Kogut, S. Levin, M. Limon, P. Lubin, P. Mirel, M. Seiffert, J. Singal, E. Wollack, T. Villela, and C. A. Wuensche. ARCADE 2 Measurement of the Absolute Sky Brightness at 3-90 GHz. *Astrophysical Journal*, 734:5, June 2011.

[34] D. Foreman-Mackey, D. W. Hogg, D. Lang, and J. Goodman. emcee: The MCMC Hammer. *Publications of the Astronomical Society of the Pacific*, 125:306, March 2013.

[35] J. W. Fowler, M. D. Niemack, S. R. Dicker, A. M. Aboobaker, P. A. R. Ade, E. S. Battistelli, M. J. Devlin, R. P. Fisher, M. Halpern, P. C. Hargrave, A. D. Hincks, M. Kaul, J. Klein, J. M. Lau, M. Limon, T. A. Marriage, P. D. Mauskopf, L. Page, S. T. Staggs, D. S. Swetz, E. R. Switzer, R. J. Thornton, and C. E. Tucker. Optical design of the Atacama Cosmology Telescope and the Millimeter Bolometric Array Camera. *Applied Optics*, 46:3444–3454, June 2007.

[36] G. W. Fraser. On the nature of the superconducting-to-normal transition in transition edge sensors. *Nuclear Instruments and Methods in Physics Research A*, 523:234–245, May 2004.

[37] A. Friedmann. On the Curvature of Space. *General Relativity and Gravitation*, 31:1991, December 1999.

[38] M. Galeazzi and D. McCammon. Microcalorimeter and bolometer model. *Journal of Applied Physics*, 93:4856–4869, April 2003.

[39] K. Ganga, B. Ratra, J. O. Gundersen, and N. Sugiyama. UCSB South Pole 1994 Cosmic Microwave Background Anisotropy Measurement Constraints on Open and Flat-Λ Cold Dark Matter Cosmogonies. *Astrophysical Journal*, 484:7–30, July 1997.

[40] Fuchang Gao and Lixing Han. Implementing the nelder-mead simplex algorithm with adaptive parameters. *Computational Optimization and Applications*, 51(1):259–277, Jan 2012.

[41] E. M. George, J. E. Austermann, J. A. Beall, D. Becker, B. A. Benson, L. E. Bleem, J. E. Carlstrom, C. L. Chang, H.-M. Cho, A. T. Crites, M. A. Dobbs, W. Everett, N. W. Halverson, J. W. Henning, G. C. Hilton, W. L. Holzapfel, J. Hubmayr, K. D. Irwin, D. Li, M. Lueker, J. J. McMahon, J. Mehl, J. Montgomery, T. Natoli, J. P. Nibarger, M. D. Niemack, V. Novosad, J. E. Ruhl, J. T. Sayre, E. Shirokoff, K. T. Story, G. Wang, V. Yefremenko, K. W. Yoon, and E. Young. A Study of Al-Mn Transition Edge Sensor Engineering for Stability. *Journal of Low Temperature Physics*, 176:383–391, August 2014.

[42] J. M. Gildemeister, A. T. Lee, and P. L. Richards. Model for excess noise in voltage-biased superconducting bolometers. *Applied Optics*, 40:6229–6235, December 2001.

[43] D. J. Goldie, M. D. Audley, D. M. Glowacka, V. N. Tsaneva, and S. Withington. Thermal models and noise in transition edge sensors. *Journal of Applied Physics*, 105(7):074512–074512–7, April 2009.

[44] L. Gottardi, H. Akamatsu, M. P. Bruijn, R. den Hartog, J.-W. den Herder, B. Jackson, M. Kiviranta, J. van der Kuur, and H. van Weers. Development of the superconducting detectors and read-out for the X-IFU instrument on board of the X-ray observatory Athena. *Nuclear Instruments and Methods in Physics Research A*, 824:622–625, July 2016.

[45] E. Grace, J. Beall, J. R. Bond, H. M. Cho, R. Datta, M. J. Devlin, R. Dünner, A. E. Fox, P. Gallardo, M. Hasselfield, S. Henderson, G. C. Hilton, A. D. Hincks, R. Hlozek, J. Hubmayr, K. Irwin, J. Klein, B. Koopman, D. Li, M. Lungu, L. Newburgh, J. P. Nibarger, M. D. Niemack, L. Maurin, J. McMahon, S. Naess, L. A. Page, C. Pappas, B. L. Schmitt, J. Sievers, S. T. Staggs, R. Thornton, J. Van Lanen, and E. J. Wollack. ACTPol: on-sky performance and characterization. In *Millimeter, Submillimeter, and Far-Infrared Detectors and Instrumentation for Astronomy VII*, volume 9153 of *Proc. SPIE*, page 915310, August 2014.

[46] E.A. Grace. *Detector Characterization, Optimization, and Operation for ACTPol*. PhD thesis, Princeton University, 2016.

[47] H. P. Gush, M. Halpern, and E. H. Wishnow. Rocket measurement of the cosmic-background-radiation mm-wave spectrum. *Physical Review Letters*, 65:537–540, July 1990.

[48] A. H. Guth. Inflationary universe: A possible solution to the horizon and flatness problems. *Phys. Rev. D*, 23:347–356, January 1981.

[49] S. Hamimeche and A. Lewis. Likelihood analysis of CMB temperature and polarization power spectra. *Phys. Rev. D*, 77(10):103013, May 2008.

[50] K. Harrington, T. Marriage, A. Ali, J. W. Appel, C. L. Bennett, F. Boone, M. Brewer, M. Chan, D. T. Chuss, F. Colazo, S. Dahal, K. Denis, R. Dünner, J. Eimer, T. Essinger-Hileman, P. Fluxa, M. Halpern, G. Hilton, G. F. Hinshaw, J. Hubmayr, J. Iuliano, J. Karakla, J. McMahon, N. T. Miller, S. H. Moseley, G. Palma, L. Parker, M. Petroff, B. Pradenas, K. Rostem, M. Sagliocca, D. Valle, D. Watts, E. Wollack, Z. Xu, and L. Zeng. The Cosmology Large Angular Scale Surveyor. In *Millimeter, Submillimeter, and Far-Infrared Detectors and Instrumentation for Astronomy VIII*, volume 9914 of *Proc. SPIE*, page 99141K, July 2016.

[51] S. W. Henderson, J. R. Stevens, M. Amiri, J. Austermann, J. A. Beall, S. Chaudhuri, H.-M. Cho, S. K. Choi, N. F. Cothard, K. T. Crowley, S. M. Duff, C. P. Fitzgerald, P. A. Gallardo, M. Halpern, M. Hasselfield, G. Hilton, S.-P. P. Ho, J. Hubmayr, K. D. Irwin, B. J. Koopman, D. Li, Y. Li, J. McMahon, F. Nati, M. Niemack, C. D. Reintsema, M. Salatino, A. Schillaci, B. L. Schmitt, S. M. Simon, S. T. Staggs, E. M. Vavagiakis, and J. T. Ward. Readout of two-kilopixel transition-edge sensor arrays for Advanced ACTPol. In *Millimeter, Submillimeter, and Far-Infrared Detectors and Instrumentation for Astronomy VIII*, volume 9914 of *Proc. SPIE*, page 99141G, July 2016.

[52] E. Hivon, K. M. Górski, C. B. Netterfield, B. P. Crill, S. Prunet, and F. Hansen. MASTER of the Cosmic Microwave Background Anisotropy Power Spectrum: A Fast Method for Statistical Analysis of Large and Complex Cosmic Microwave Background Data Sets. *Astrophysical Journal*, 567:2–17, March 2002.

[53] S. P. Ho, C. G. Pappas, J. Austermann, J. A. Beall, D. Becker, S. K. Choi, R. Datta, S. M. Duff, P. A. Gallardo, E. Grace, M. Hasselfield, S. W. Henderson, G. C. Hilton, J. Hubmayr, B. J. Koopman, J. V. Lanen, D. Li, J. McMahon, F. Nati, M. D. Niemack, P. Niraula, M. Salatino, A. Schillaci, B. L. Schmitt, S. M. Simon, S. T. Staggs, J. R. Stevens, J. T. Ward, E. J. Wollack, and E. M. Vavagiakis. The First Multichroic Polarimeter Array on the Atacama Cosmology Telescope: Characterization and Performance. *Journal of Low Temperature Physics*, 184:559–567, August 2016.

[54] S.-P. P Ho, J. Austermann, J. A. Beall, S. K. Choi, N. F. Cothard, K. P. Coughlin, K. T. Crowley, R. D. Datta, S. M. Duff, M. D. Devlin, P. A. Gallardo, M. Hasselfield, S. W. Henderson, G. C. Hilton, J. Hubmayr, B. J. Koopman,

Y. Li, J. J. McMahon, M. D. Niemack, M. Salatino, S. M. Simon, S. T. Staggs, J. N. Ullom, E. M. Vavagiakis, J. Ward, and E. J. Wollack. Highly uniform 150 mm diameter multichroic polarimeter array deployed for CMB detection. volume 9914, pages 9914 – 9914 – 15, 2017.

[55] H. F. C. Hoevers, A. C. Bento, M. P. Bruijn, L. Gottardi, M. A. N. Korevaar, W. A. Mels, and P. A. J. de Korte. Thermal fluctuation noise in a voltage biased superconducting transition edge thermometer. *Applied Physics Letters*, 77:4422, December 2000.

[56] D. Huterer. Weak lensing, dark matter and dark energy. *General Relativity and Gravitation*, 42:2177–2195, September 2010.

[57] K. D. Irwin. An application of electrothermal feedback for high resolution cryogenic particle detection. *Applied Physics Letters*, 66:1998–2000, April 1995.

[58] K.D. Irwin and G.C. Hilton. *Cryogenic Particle Detection*, chapter Transition Edge Sensors, pages 63–150. Springer Verlag, Berlin, 2005.

[59] F. James and M. Roos. Minuit: A System for Function Minimization and Analysis of the Parameter Errors and Correlations. *Comput. Phys. Commun.*, 10:343–367, 1975.

[60] N. Jethava, J. N. Ullom, K. D. Irwin, W. B. Doriese, J. A. Beall, G. C. Hilton, L. R. Vale, and B. Zink. Dependence of Excess Noise on the Partial Derivatives of Resistance in Superconducting Transition Edge Sensors. In B. Young, B. Cabrera, and A. Miller, editors, *American Institute of Physics Conference Series*, volume 1185 of *American Institute of Physics Conference Series*, pages 31–33, December 2009.

[61] B. R. Johnson, J. Collins, M. E. Abroe, P. A. R. Ade, J. Bock, J. Borrill, A. Boscaleri, P. de Bernardis, S. Hanany, A. H. Jaffe, T. Jones, A. T. Lee, L. Levinson, T. Matsumura, B. Rabii, T. Renbarger, P. L. Richards, G. F. Smoot, R. Stompor, H. T. Tran, C. D. Winant, J. H. P. Wu, and J. Zuntz. MAXIPOL: Cosmic Microwave Background Polarimetry Using a Rotating Half-Wave Plate. *Astrophysical Journal*, 665:42–54, August 2007.

[62] M. Kamionkowski, A. Kosowsky, and A. Stebbins. Statistics of cosmic microwave background polarization. *Phys. Rev. D*, 55:7368–7388, June 1997.

[63] R. L. Kelley, H. Akamatsu, P. Azzarello, T. Bialas, K. R. Boyce, G. V. Brown, E. Canavan, M. P. Chiao, E. Costantini, M. J. DiPirro, M. E. Eckart, Y. Ezoe, R. Fujimoto, D. Haas, J.-W. den Herder, A. Hoshino, K. Ishikawa, Y. Ishisaki, N. Iyomoto, C. A. Kilbourne, M. O. Kimball, S. Kitamoto, S. Konami, S. Koyama, M. A. Leutenegger, D. McCammon, K. Mitsuda, I. Mitsuishi, H. Moseley, H. Murakami, M. Murakami, H. Noda, M. Ogawa, T. Ohashi, A. Okamoto, N. Ota, S. Paltani, F. S. Porter, K. Sakai, K. Sato, Y. Sato, M. Sawada, H. Seta, K. Shinozaki, P. J. Shirron, G. A. Sneiderman, H. Sugita,

A. E. Szymkowiak, Y. Takei, T. Tamagawa, M. Tashiro, Y. Terada, M. Tsujimoto, C. P. de Vries, S. Yamada, N. Y. Yamasaki, and Y. Yatsu. The Astro-H high resolution soft x-ray spectrometer. In *Space Telescopes and Instrumentation 2016: Ultraviolet to Gamma Ray*, volume 9905 of *Proc. SPIE*, page 99050V, July 2016.

[64] Lloyd Knox. Determination of inflationary observables by cosmic microwave background anisotropy experiments. *Phys. Rev. D*, 52:4307–4318, Oct 1995.

[65] A. Kogut, D. J. Fixsen, D. T. Chuss, J. Dotson, E. Dwek, M. Halpern, G. F. Hinshaw, S. M. Meyer, S. H. Moseley, M. D. Seiffert, D. N. Spergel, and E. J. Wollack. The Primordial Inflation Explorer (PIXIE): a nulling polarimeter for cosmic microwave background observations. *Journal of Cosmology and Astroparticle Physics*, 7:025, July 2011.

[66] A. G. Kozorezov, A. A. Golubov, D. D. E. Martin, P. A. J. de Korte, M. A. Lindeman, R. A. Hijmering, and J. K. Wigmore. Microscopic Model of a Transition Edge Sensor as a Weak Link. *IEEE Transactions on Applied Superconductivity*, 21:250–253, June 2011.

[67] C. L. Kuo, J. J. Bock, J. A. Bonetti, J. Brevik, G. Chattopadhyay, P. K. Day, S. Golwala, M. Kenyon, A. E. Lange, H. G. LeDuc, H. Nguyen, R. W. Ogburn, A. Orlando, A. Transgrud, A. Turner, G. Wang, and J. Zmuidzinas. Antenna-coupled TES bolometer arrays for CMB polarimetry. In *Millimeter and Submillimeter Detectors and Instrumentation for Astronomy IV*, volume 7020 of *Proc. SPIE*, page 70201I, July 2008.

[68] A. Kusaka, J. Appel, T. Essinger-Hileman, J. A. Beall, L. E. Campusano, H.-M. Cho, S. K. Choi, K. Crowley, J. W. Fowler, P. Gallardo, M. Hasselfield, G. Hilton, S.-P. P. Ho, K. Irwin, N. Jarosik, M. D. Niemack, G. W. Nixon, M. Nolta, L. A. Page, Jr, G. A. Palma, L. Parker, S. Raghunathan, C. D. Reintsema, J. Sievers, S. M. Simon, S. T. Staggs, K. Visnjic, and K.-W. Yoon. Results from the Atacama B-mode Search (ABS) Experiment. *ArXiv e-prints*, January 2018.

[69] A. Kusaka, T. Essinger-Hileman, J. W. Appel, P. Gallardo, K. D. Irwin, N. Jarosik, M. R. Nolta, L. A. Page, L. P. Parker, S. Raghunathan, J. L. Sievers, S. M. Simon, S. T. Staggs, and K. Visnjic. Modulation of cosmic microwave background polarization with a warm rapidly rotating half-wave plate on the Atacama B-Mode Search instrument. *Review of Scientific Instruments*, 85(3):024501, March 2014.

[70] J. M. Lamarre. Photon noise in photometric instruments at far-infrared and submillimeter wavelengths. *Applied Optics*, 25:870–876, March 1986.

[71] S. P. Langley. The bolometer. *Nature*, 57:620–22, 1898.

[72] T. M. Lanting, H.-M. Cho, J. Clarke, W. L. Holzapfel, A. T. Lee, M. Lueker, P. L. Richards, M. A. Dobbs, H. Spieler, and A. Smith. Frequency-domain multiplexed readout of transition-edge sensor arrays with a superconducting quantum interference device. *Applied Physics Letters*, 86(11):112511, March 2005.

[73] J.M. Lau. *CCAM: A Novel Millimeter-Wave Instrument Using a Close-Packed TES Bolometer Array.* PhD thesis, Princeton University, 2007.

[74] P. M. Laufer and D. A. Papaconstantopoulos. Tight-binding coherent-potential-approximation study of the electronic states of palladium–noble-metal alloys. *Phys. Rev. B*, 35:9019–9029, Jun 1987.

[75] A. T. Lee, P. L. Richards, S. W. Nam, B. Cabrera, and K. D. Irwin. A superconducting bolometer with strong electrothermal feedback. *Applied Physics Letters*, 69:1801–1803, September 1996.

[76] Georges Lemaître. Republication of: A homogeneous universe of constant mass and increasing radius accounting for the radial velocity of extra-galactic nebulae. *General Relativity and Gravitation*, 45(8):1635–1646, Aug 2013.

[77] Antony Lewis, Anthony Challinor, and Anthony Lasenby. Efficient computation of CMB anisotropies in closed FRW models. *Astrophys. J.*, 538:473–476, 2000.

[78] D. Li, J. E. Austermann, J. A. Beall, D. T. Becker, S. M. Duff, P. A. Gallardo, S. W. Henderson, G. C. Hilton, S.-P. Ho, J. Hubmayr, B. J. Koopman, J. J. McMahon, F. Nati, M. D. Niemack, C. G. Pappas, M. Salatino, B. L. Schmitt, S. M. Simon, S. T. Staggs, J. Van Lanen, J. T. Ward, and E. J. Wollack. AlMn Transition Edge Sensors for Advanced ACTPol. *Journal of Low Temperature Physics*, 184:66–73, July 2016.

[79] Y. Li, S. Choi, S.-P. Ho, K. T. Crowley, M. Salatino, S. M. Simon, S. T. Staggs, F. Nati, J. Ward, B. L. Schmitt, S. Henderson, B. J. Koopman, P. A. Gallardo, E. M. Vavagiakis, M. D. Niemack, J. McMahon, S. M. Duff, A. Schillaci, J. Hubmayr, G. C. Hilton, J. A. Beall, and E. J. Wollack. Assembly and integration process of the first high density detector array for the Atacama Cosmology Telescope. In *Millimeter, Submillimeter, and Far-Infrared Detectors and Instrumentation for Astronomy VIII*, volume 9914 of *Proc. SPIE*, page 991435, July 2016.

[80] Andrei D. Linde. A New Inflationary Universe Scenario: A Possible Solution of the Horizon, Flatness, Homogeneity, Isotropy and Primordial Monopole Problems. *Phys. Lett.*, 108B:389–393, 1982.

[81] M. A. Lindeman, K. A. Barger, D. E. Brandl, S. G. Crowder, L. Rocks, and D. McCammon. Complex impedance measurements of calorimeters and bolometers: Correction for stray impedances. *Review of Scientific Instruments*, 78(4):043105–043105, April 2007.

[82] T. Louis, E. Grace, M. Hasselfield, M. Lungu, L. Maurin, G. E. Addison, P. A. R. Ade, S. Aiola, R. Allison, M. Amiri, E. Angile, N. Battaglia, J. A. Beall, F. de Bernardis, J. R. Bond, J. Britton, E. Calabrese, H.-m. Cho, S. K. Choi, K. Coughlin, D. Crichton, K. Crowley, R. Datta, M. J. Devlin, S. R. Dicker, J. Dunkley, R. Dünner, S. Ferraro, A. E. Fox, P. Gallardo, M. Gralla, M. Halpern, S. Henderson, J. C. Hill, G. C. Hilton, M. Hilton, A. D. Hincks, R. Hlozek, S. P. P. Ho, Z. Huang, J. Hubmayr, K. M. Huffenberger, J. P. Hughes, L. Infante, K. Irwin, S. Muya Kasanda, J. Klein, B. Koopman, A. Kosowsky, D. Li, M. Madhavacheril, T. A. Marriage, J. McMahon, F. Menanteau, K. Moodley, C. Munson, S. Naess, F. Nati, L. Newburgh, J. Nibarger, M. D. Niemack, M. R. Nolta, C. Nuñez, L. A. Page, C. Pappas, B. Partridge, F. Rojas, E. Schaan, B. L. Schmitt, N. Sehgal, B. D. Sherwin, J. Sievers, S. Simon, D. N. Spergel, S. T. Staggs, E. R. Switzer, R. Thornton, H. Trac, J. Treu, C. Tucker, A. Van Engelen, J. T. Ward, and E. J. Wollack. The Atacama Cosmology Telescope: two-season ACTPol spectra and parameters. *Journal of Cosmology and Astroparticle Physics*, 6:031, June 2017.

[83] I. J. Maasilta. Complex impedance, responsivity and noise of transition-edge sensors: Analytical solutions for two- and three-block thermal models. *AIP Advances*, 2(4):042110, December 2012.

[84] A. Manzotti, K. T. Story, W. L. K. Wu, J. E. Austermann, J. A. Beall, A. N. Bender, B. A. Benson, L. E. Bleem, J. J. Bock, J. E. Carlstrom, C. L. Chang, H. C. Chiang, H.-M. Cho, R. Citron, A. Conley, T. M. Crawford, A. T. Crites, T. de Haan, M. A. Dobbs, S. Dodelson, W. Everett, J. Gallicchio, E. M. George, A. Gilbert, N. W. Halverson, N. Harrington, J. W. Henning, G. C. Hilton, G. P. Holder, W. L. Holzapfel, S. Hoover, Z. Hou, J. D. Hrubes, N. Huang, J. Hubmayr, K. D. Irwin, R. Keisler, L. Knox, A. T. Lee, E. M. Leitch, D. Li, J. J. McMahon, S. S. Meyer, L. M. Mocanu, T. Natoli, J. P. Nibarger, V. Novosad, S. Padin, C. Pryke, C. L. Reichardt, J. E. Ruhl, B. R. Saliwanchik, J. T. Sayre, K. K. Schaffer, G. Smecher, A. A. Stark, K. Vanderlinde, J. D. Vieira, M. P. Viero, G. Wang, N. Whitehorn, V. Yefremenko, and M. Zemcov. CMB Polarization B-mode Delensing with SPTpol and Herschel. *Astrophysical Journal*, 846:45, September 2017.

[85] T.M. Marriage. *Detectors for the Atacama Cosmology Telescope*. PhD thesis, Princeton University, 2006.

[86] J. C. Mather. Bolometer noise: nonequilibrium thoery. *Applied Optics*, 21:1125–1129, March 1982.

[87] D. McCammon. *Cryogenic Particle Detection*, chapter Semiconductor Thermistors, pages 35–62. Springer Verlag, Berlin, 2005.

[88] J. McMahon, J. W. Appel, J. E. Austermann, J. A. Beall, D. Becker, B. A. Benson, L. E. Bleem, J. Britton, C. L. Chang, J. E. Carlstrom, H. M. Cho, A. T. Crites, T. Essinger-Hileman, W. Everett, N. W. Halverson, J. W. Henning,

G. C. Hilton, K. D. Irwin, J. Mehl, S. S. Meyer, S. Mossley, M. D. Niemack, L. P. Parker, S. M. Simon, S. T. Staggs, C. Visnjic, E. Wollack, K. U.-Yen, K. W. Yoon, and Y. Zhao. Planar Orthomode Transducers for Feedhorn-coupled TES Polarimeters. In B. Young, B. Cabrera, and A. Miller, editors, *American Institute of Physics Conference Series*, volume 1185 of *American Institute of Physics Conference Series*, pages 490–493, December 2009.

[89] Y. Mizugutch, M. Akagawa, and H. Yokoi. Offset Dual Reflector Antenna. *ISA Proceedings*, pages 2–5, 1976.

[90] S. K. Næss and T. Louis. A fast map-making preconditioner for regular scanning patterns. *Journal of Cosmology and Astroparticle Physics*, 8:045, August 2014.

[91] P. C. Nagler, K. T. Crowley, K. L. Denis, A. M. Devasia, D. J. Fixsen, A. J. Kogut, G. Manos, S. Porter, and T. R. Stevenson. Multimode bolometer development for the PIXIE instrument. In *Millimeter, Submillimeter, and Far-Infrared Detectors and Instrumentation for Astronomy VIII*, volume 9914 of *Proc. SPIE*, page 99141A, July 2016.

[92] P. C. Nagler, D. J. Fixsen, A. Kogut, and G. S. Tucker. Systematic Effects in Polarizing Fourier Transform Spectrometers for Cosmic Microwave Background Observations. *Astrophysical Journal Supplement*, 221:21, November 2015.

[93] M.D. Niemack. *Towards Dark Energy: Design, Development, and Preliminary Data from ACT*. PhD thesis, Princeton University, 2008.

[94] R. O'Brient, J. Edwards, K. Arnold, G. Engargiola, W. Holzapfel, A. T. Lee, M. Myers, E. Quealy, G. Rebeiz, P. Richards, H. Spieler, and H. Tran. Sinuous antennas for cosmic microwave background polarimetry. In *Millimeter and Submillimeter Detectors and Instrumentation for Astronomy IV*, volume 7020 of *Proc. SPIE*, page 70201H, July 2008.

[95] S. Oguri, J. Choi, T. Damayanthi, M. Hattori, M. Hazumi, H. Ishitsuka, K. Kiuchi, R. Koyano, H. Kutsuma, K. Lee, S. Mima, M. Minowa, M. Nagai, T. Nagasaki, C. Otani, Y. Sekimoto, M. Semoto, J. Suzuki, T. Taino, O. Tajima, N. Tomita, E. Won, T. Uchida, and M. Yoshida. GroundBIRD: observations of CMB polarization with fast scan modulation and MKIDs. In *Ground-based and Airborne Telescopes VI*, volume 9906 of *Proc. SPIE*, page 99063L, July 2016.

[96] T.E. Oliphant. *A Guide to NumPy*. Trelgol Publishing, 2006.

[97] S. Pancharatnam. Achromatic combinations of birefringent plates. *Proceedings of the Indian Academy of Sciences - Section A*, 41(4):137–144, Apr 1955.

[98] C. G. Pappas, J. Austermann, J. A. Beall, S. M. Duff, P. A. Gallardo, E. Grace, S. W. Henderson, S. P. Ho, B. J. Koopman, D. Li, J. McMahon, F. Nati, M. D. Niemack, P. Niraula, M. Salatino, A. Schillaci, B. L. Schmitt, S. M. Simon, S. T. Staggs, J. R. Stevens, E. M. Vavagiakis, J. T. Ward, and E. J. Wollack.

High-Density Superconducting Cables for Advanced ACTPol. *Journal of Low Temperature Physics*, 184:473–479, July 2016.

[99] C.G. Pappas. *Assembly, Characterization, and Operation of Large-Scale TES Detector Arrays for ACTPol*. PhD thesis, Princeton University, 2016.

[100] P. J. E. Peebles. Large-scale background temperature and mass fluctuations due to scale-invariant primeval perturbations. *Astrophysical Journal Letters*, 263:L1–L5, December 1982.

[101] Planck Collaboration, P. A. R. Ade, N. Aghanim, M. Arnaud, M. Ashdown, J. Aumont, C. Baccigalupi, A. J. Banday, R. B. Barreiro, J. G. Bartlett, and et al. Planck 2015 results. XIII. Cosmological parameters. *Astronomy & Astrophysics*, 594:A13, September 2016.

[102] Planck Collaboration, P. A. R. Ade, N. Aghanim, M. Arnaud, M. Ashdown, J. Aumont, C. Baccigalupi, A. J. Banday, R. B. Barreiro, N. Bartolo, and et al. Planck 2015 results. XIV. Dark energy and modified gravity. *Astronomy & Astrophysics*, 594:A14, September 2016.

[103] Planck Collaboration and et al. Planck 2015 results. X. Diffuse component separation: Foreground maps. *Astronomy & Astrophysics*, 594:A10, September 2016.

[104] D. Poletti, G. Fabbian, M. Le Jeune, J. Peloton, K. Arnold, C. Baccigalupi, D. Barron, S. Beckman, J. Borrill, S. Chapman, Y. Chinone, A. Cukierman, A. Ducout, T. Elleflot, J. Errard, S. Feeney, N. Goeckner-Wald, J. Groh, G. Hall, M. Hasegawa, M. Hazumi, C. Hill, L. Howe, Y. Inoue, A. H. Jaffe, O. Jeong, N. Katayama, B. Keating, R. Keskitalo, T. Kisner, A. Kusaka, A. T. Lee, D. Leon, E. Linder, L. Lowry, F. Matsuda, M. Navaroli, H. Paar, G. Puglisi, C. L. Reichardt, C. Ross, P. Siritanasak, N. Stebor, B. Steinbach, R. Stompor, A. Suzuki, O. Tajima, G. Teply, and N. Whitehorn. Making maps of cosmic microwave background polarization for B-mode studies: the POLARBEAR example. *Astronomy & Astrophysics*, 600:A60, April 2017.

[105] QUIET Collaboration, C. Bischoff, A. Brizius, I. Buder, Y. Chinone, K. Cleary, R. N. Dumoulin, A. Kusaka, R. Monsalve, S. K. Næss, L. B. Newburgh, R. Reeves, K. M. Smith, I. K. Wehus, J. A. Zuntz, J. T. L. Zwart, L. Bronfman, R. Bustos, S. E. Church, C. Dickinson, H. K. Eriksen, P. G. Ferreira, T. Gaier, J. O. Gundersen, M. Hasegawa, M. Hazumi, K. M. Huffenberger, M. E. Jones, P. Kangaslahti, D. J. Kapner, C. R. Lawrence, M. Limon, J. May, J. J. McMahon, A. D. Miller, H. Nguyen, G. W. Nixon, T. J. Pearson, L. Piccirillo, S. J. E. Radford, A. C. S. Readhead, J. L. Richards, D. Samtleben, M. Seiffert, M. C. Shepherd, S. T. Staggs, O. Tajima, K. L. Thompson, K. Vanderlinde, R. Williamson, and B. Winstein. First Season QUIET Observations: Measurements of Cosmic Microwave Background Polarization Power Spectra at 43 GHz in the Multipole Range $25 \geq \ell \leq 475$. *Astrophysical Journal*, 741:111, November 2011.

[106] A. C. S. Readhead, S. T. Myers, T. J. Pearson, J. L. Sievers, B. S. Mason, C. R. Contaldi, J. R. Bond, R. Bustos, P. Altamirano, C. Achermann, L. Bronfman, J. E. Carlstrom, J. K. Cartwright, S. Casassus, C. Dickinson, W. L. Holzapfel, J. M. Kovac, E. M. Leitch, J. May, S. Padin, D. Pogosyan, M. Pospieszalski, C. Pryke, R. Reeves, M. C. Shepherd, and S. Torres. Polarization Observations with the Cosmic Background Imager. *Science*, 306:836–844, October 2004.

[107] C. D. Reintsema, J. Beyer, S. W. Nam, S. Deiker, G. C. Hilton, K. Irwin, J. Martinis, J. Ullom, L. R. Vale, and M. Macintosh. Prototype system for superconducting quantum interference device multiplexing of large-format transition-edge sensor arrays. *Review of Scientific Instruments*, 74:4500–4508, October 2003.

[108] P. L. Richards. Bolometers for infrared and millimeter waves. *Journal of Applied Physics*, 76:1–24, July 1994.

[109] H. P. Robertson. Kinematics and World-Structure. *Astrophysical Journal*, 82:284, November 1935.

[110] M. C. Runyan, P. A. R. Ade, M. Amiri, S. Benton, R. Bihary, J. J. Bock, J. R. Bond, J. A. Bonetti, S. A. Bryan, H. C. Chiang, C. R. Contaldi, B. P. Crill, O. Dore, D. O'Dea, M. Farhang, J. P. Filippini, L. Fissel, N. Gandilo, S. R. Golwala, J. E. Gudmundsson, M. Hasselfield, M. Halpern, G. Hilton, W. Holmes, V. V. Hristov, K. D. Irwin, W. C. Jones, C. L. Kuo, C. J. MacTavish, P. V. Mason, T. A. Morford, T. E. Montroy, C. B. Netterfield, A. S. Rahlin, C. D. Reintsema, J. E. Ruhl, M. A. Schenker, J. Shariff, J. D. Soler, A. Trangsrud, R. S. Tucker, C. E. Tucker, and A. Turner. Design and performance of the SPIDER instrument. In *Millimeter, Submillimeter, and Far-Infrared Detectors and Instrumentation for Astronomy V*, volume 7741 of *Proc. SPIE*, page 77411O, July 2010.

[111] J.E. Sadleir. *Superconducting transition-edge sensor physics*. PhD thesis, University of Illinois at Urbana-Champaign, 2016.

[112] D. M. Scolnic, D. O. Jones, A. Rest, Y. C. Pan, R. Chornock, R. J. Foley, M. E. Huber, R. Kessler, G. Narayan, A. G. Riess, S. Rodney, E. Berger, D. J. Brout, P. J. Challis, M. Drout, D. Finkbeiner, R. Lunnan, R. P. Kirshner, N. E. Sanders, E. Schlafly, S. Smartt, C. W. Stubbs, J. Tonry, W. M. Wood-Vasey, M. Foley, J. Hand, E. Johnson, W. S. Burgett, K. C. Chambers, P. W. Draper, K. W. Hodapp, N. Kaiser, R. P. Kudritzki, E. A. Magnier, N. Metcalfe, F. Bresolin, E. Gall, R. Kotak, M. McCrum, and K. W. Smith. The Complete Light-curve Sample of Spectroscopically Confirmed SNe Ia from Pan-STARRS1 and Cosmological Constraints from the Combined Pantheon Sample. *Astrophysical Journal*, 859:101, June 2018.

[113] G. M. Seidel and I. S. Beloborodov. Intrinsic excess noise in a transition edge sensor. *Nuclear Instruments and Methods in Physics Research A*, 520:325–328, March 2004.

[114] U. Seljak and M. Zaldarriaga. Signature of Gravity Waves in the Polarization of the Microwave Background. *Physical Review Letters*, 78:2054–2057, March 1997.

[115] Uros Seljak and Matias Zaldarriaga. A line of sight approach to cosmic microwave background anisotropies. *Astrophys. J.*, 469:437–444, 1996.

[116] S. M. Simon, J. W. Appel, L. E. Campusano, S. K. Choi, K. T. Crowley, T. Essinger-Hileman, P. Gallardo, S. P. Ho, A. Kusaka, F. Nati, G. A. Palma, L. A. Page, S. Raghunathan, and S. T. Staggs. Characterizing Atacama B-mode Search Detectors with a Half-Wave Plate. *Journal of Low Temperature Physics*, 184:534–539, August 2016.

[117] S. M. Simon, J. W. Appel, H. M. Cho, T. Essinger-Hileman, K. D. Irwin, A. Kusaka, M. D. Niemack, M. R. Nolta, L. A. Page, L. P. Parker, S. Raghunathan, J. L. Sievers, S. T. Staggs, and K. Visnjic. In Situ Time Constant and Optical Efficiency Measurements of TRUCE Pixels in the Atacama B-Mode Search. *Journal of Low Temperature Physics*, 176:712–718, September 2014.

[118] S. M. Simon, J. Austermann, J. A. Beall, S. K. Choi, K. P. Coughlin, S. M. Duff, P. A. Gallardo, S. W. Henderson, F. B. Hills, S.-P. P. Ho, J. Hubmayr, A. Josaitis, B. J. Koopman, J. J. McMahon, F. Nati, L. Newburgh, M. D. Niemack, M. Salatino, A. Schillaci, B. L. Schmitt, S. T. Staggs, E. M. Vavagiakis, J. Ward, and E. J. Wollack. The design and characterization of wideband spline-profiled feedhorns for Advanced ACTPol. In *Millimeter, Submillimeter, and Far-Infrared Detectors and Instrumentation for Astronomy VIII*, volume 9914 of *Proc. SPIE*, page 991416, July 2016.

[119] K. M. Smith. Pseudo-C estimators which do not mix E and B modes. *Phys. Rev. D*, 74(8):083002, October 2006.

[120] Y. Sofue and V. Rubin. Rotation Curves of Spiral Galaxies. *Annual Review of Astronomy and Astrophysics*, 39:137–174, 2001.

[121] P. J. Steinhardt and Michael S. Turner. A Prescription for Successful New Inflation. *Phys. Rev. D*, 29:2162–2171, 1984.

[122] D. S. Swetz, P. A. R. Ade, M. Amiri, J. W. Appel, E. S. Battistelli, B. Burger, J. Chervenak, M. J. Devlin, S. R. Dicker, W. B. Doriese, R. Dünner, T. Essinger-Hileman, R. P. Fisher, J. W. Fowler, M. Halpern, M. Hasselfield, G. C. Hilton, A. D. Hincks, K. D. Irwin, N. Jarosik, M. Kaul, J. Klein, J. M. Lau, M. Limon, T. A. Marriage, D. Marsden, K. Martocci, P. Mauskopf, H. Moseley, C. B. Netterfield, M. D. Niemack, M. R. Nolta, L. A. Page, L. Parker, S. T. Staggs, O. Stryzak, E. R. Switzer, R. Thornton, C. Tucker, E. Wollack, and Y. Zhao. Overview of the Atacama Cosmology Telescope: Receiver, Instrumentation, and Telescope Systems. *Astrophysical Journal Supplement*, 194:41, June 2011.

[123] Satoru Takakura, Mario Aguilar, Yoshiki Akiba, Kam Arnold, Carlo Baccigalupi, Darcy Barron, Shawn Beckman, David Boettger, Julian Borrill, Scott Chapman, Yuji Chinone, Ari Cukierman, Anne Ducout, Tucker Elleflot, Josquin Errard, Giulio Fabbian, Takuro Fujino, Nicholas Galitzki, Neil Goeckner-Wald, Nils W. Halverson, Masaya Hasegawa, Kaori Hattori, Masashi Hazumi, Charles Hill, Logan Howe, Yuki Inoue, Andrew H. Jaffe, Oliver Jeong, Daisuke Kaneko, Nobuhiko Katayama, Brian Keating, Reijo Keskitalo, Theodore Kisner, Nicoletta Krachmalnicoff, Akito Kusaka, Adrian T. Lee, David Leon, Lindsay Lowry, Frederick Matsuda, Tomotake Matsumura, Martin Navaroli, Haruki Nishino, Hans Paar, Julien Peloton, Davide Poletti, Giuseppe Puglisi, Christian L. Reichardt, Colin Ross, Praween Siritanasak, Aritoki Suzuki, Osamu Tajima, Sayuri Takatori, and Grant Teply. Performance of a continuously rotating half-wave plate on the POLARBEAR telescope. *Journal of Cosmology and Astro-Particle Physics*, 2017:008, May 2017.

[124] The EBEX Collaboration, A. M. Aboobaker, P. Ade, D. Araujo, F. Aubin, C. Baccigalupi, C. Bao, D. Chapman, J. Didier, M. Dobbs, C. Geach, W. Grainger, S. Hanany, K. Helson, S. Hillbrand, J. Hubmayr, A. Jaffe, B. Johnson, T. Jones, J. Klein, A. Korotkov, A. Lee, L. Levinson, M. Limon, K. MacDermid, T. Matsumura, A. D. Miller, M. Milligan, K. Raach, B. Reichborn-Kjennerud, I. Sagiv, G. Savini, L. Spencer, C. Tucker, G. S. Tucker, B. Westbrook, K. Young, and K. Zilic. The EBEX Balloon Borne Experiment - Optics, Receiver, and Polarimetry. *ArXiv e-prints*, March 2017.

[125] R. J. Thornton, P. A. R. Ade, S. Aiola, F. E. Angilè, M. Amiri, J. A. Beall, D. T. Becker, H.-M. Cho, S. K. Choi, P. Corlies, K. P. Coughlin, R. Datta, M. J. Devlin, S. R. Dicker, R. Dünner, J. W. Fowler, A. E. Fox, P. A. Gallardo, J. Gao, E. Grace, M. Halpern, M. Hasselfield, S. W. Henderson, G. C. Hilton, A. D. Hincks, S. P. Ho, J. Hubmayr, K. D. Irwin, J. Klein, B. Koopman, D. Li, T. Louis, M. Lungu, L. Maurin, J. McMahon, C. D. Munson, S. Naess, F. Nati, L. Newburgh, J. Nibarger, M. D. Niemack, P. Niraula, M. R. Nolta, L. A. Page, C. G. Pappas, A. Schillaci, B. L. Schmitt, N. Sehgal, J. L. Sievers, S. M. Simon, S. T. Staggs, C. Tucker, M. Uehara, J. van Lanen, J. T. Ward, and E. J. Wollack. The Atacama Cosmology Telescope: The Polarization-sensitive ACTPol Instrument. *The Astrophysical Journal Supplement Series*, 227:21, December 2016.

[126] C. E. Tucker and P. A. R. Ade. Thermal filtering for large aperture cryogenic detector arrays. In *Society of Photo-Optical Instrumentation Engineers (SPIE) Conference Series*, volume 6275 of *Proc. SPIE*, page 62750T, June 2006.

[127] J. N. Ullom and D. A. Bennett. Review of superconducting transition-edge sensors for x-ray and gamma-ray spectroscopy. *Superconductor Science Technology*, 28(8):084003, August 2015.

[128] K. Visnjic. *Data Characteristics and Preliminary Results from the Atacama B-Mode Search (ABS)*. PhD thesis, Princeton University, 2013.

[129] A. G. Walker. On Milne's Theory of World-Structure. *Proceedings of the London Mathematical Society, (Series 2) volume 42, p. 90-127*, 42:90–127, 1937.

[130] Benjamin D. Wandelt, Eric Hivon, and Krzysztof M. Górski. Cosmic microwave background anisotropy power spectrum statistics for high precision cosmology. *Phys. Rev. D*, 64:083003, Sep 2001.

[131] J. T. Ward, J. Austermann, J. A. Beall, S. K. Choi, K. T. Crowley, M. J. Devlin, S. M. Duff, P. A. Gallardo, S. W. Henderson, S.-P. P. Ho, G. Hilton, J. Hubmayr, N. Khavari, J. Klein, B. J. Koopman, D. Li, J. McMahon, G. Mumby, F. Nati, M. D. Niemack, L. A. Page, M. Salatino, A. Schillaci, B. L. Schmitt, S. M. Simon, S. T. Staggs, R. Thornton, J. N. Ullom, E. M. Vavagiakis, and E. J. Wollack. Mechanical designs and development of TES bolometer detector arrays for the Advanced ACTPol experiment. In *Millimeter, Submillimeter, and Far-Infrared Detectors and Instrumentation for Astronomy VIII*, volume 9914 of *Proc. SPIE*, page 991437, July 2016.

[132] J.T. Ward. *Development of Technologies for the Atacama Cosmology Telescope and Next Generation Cosmic Microwave Background Instruments*. PhD thesis, University of Pennsylvania, 2018.

[133] S. Weinberg. *Cosmology*. Oxford University Press, 2008.

[134] P. Welch. The use of fast fourier transform for the estimation of power spectra: A method based on time averaging over short, modified periodograms. *IEEE Transactions on Audio and Electroacoustics*, 15(2):70–73, Jun 1967.

[135] K. W. Yoon, J. W. Appel, J. E. Austermann, J. A. Beall, D. Becker, B. A. Benson, L. E. Bleem, J. Britton, C. L. Chang, J. E. Carlstrom, H.-M. Cho, A. T. Crites, T. Essinger-Hileman, W. Everett, N. W. Halverson, J. W. Henning, G. C. Hilton, K. D. Irwin, J. McMahon, J. Mehl, S. S. Meyer, S. Moseley, M. D. Niemack, L. P. Parker, S. M. Simon, S. T. Staggs, K. U-yen, C. Visnjic, E. Wollack, and Y. Zhao. Feedhorn-Coupled TES Polarimeters for Next-Generation CMB Instruments. In B. Young, B. Cabrera, and A. Miller, editors, *American Institute of Physics Conference Series*, volume 1185 of *American Institute of Physics Conference Series*, pages 515–518, December 2009.

[136] H. Zappe. Josephson quantum interference computer devices. *IEEE Transactions on Magnetics*, 13:41–47, January 1977.

[137] Y. Zhao. *Characterization of Transition-Edge Sensors for the Millimeter Bolometer Array Camera on the Atacama Cosmology Telescope*. PhD thesis, Princeton University, 2010.

[138] J. Zmuidzinas. Thermal noise and correlations in photon detection. *Applied Optics*, 42:4989–5008, September 2003.